

Department of Radiation Therapy and Radiation Oncology
Medical Faculty, University of Saarland
Homburg / Saar, Germany

**Insights into the epigenetic role of H2A.J in radiation-induced
premature senescence**

Cumulative thesis to the Medical Faculty in fulfilment
for the degree of
Doctor of Natural Sciences (Dr. rer. nat.)
Medical Faculty,
UNIVERSITY OF SAARLAND
2024

Submission by: Mutaz A. Abd Al-razaq
Date of Birth: 24.08.1986
Place: Ramtha / Jordan

Date of Promotion: 17.02.2025

Dekan: Univ.-Prof. Dr. Matthias Hannig

Supervisors: Univ.-Prof. Dr. rer. physiol. Carola Meier
Prof. Dr. Eckart Meese

Table of contents

Table of contents	2
1. Summary / Zusammenfassung	6
2. Introduction	11
2.1 Ionizing radiation and its physical properties	11
2.1.1 Linear energy transfer	11
2.2 Radiation induced DNA damage	13
2.2.1 Cellular responses to DNA damage	14
2.2.2 Strategies of DNA double-strand break repair	14
2.2.3 Non-homologous end joining (NHEJ)	16
2.2.4 Homologous recombination (HR)	16
2.2.5 Cellular senescence	17
2.3 Chromatin architecture and gene expression	19
2.3.1 Nucleosome dynamics and chromatin remodelling	20
2.3.2 Histone modifications	20
2.3.4 Histone variant H2A.J	22
2.4 Transmission electron microscope (TEM)	23
2.5 Assay for Transposase-Accessible Chromatin sequencing (ATAC-seq)	24
2.6 RNA sequencing (RNA-seq)	25
2.7 Goals and hypothesis	25
3. Publications	28
3.1 Role of Histone Variant H2A.J in Fine-Tuning Chromatin Organization for the Establishment of ionizing Radiation-Induced Senescence	28
3.1.1 Summary of publication 1	28
3.2 Nuclear Fragility in Radiation-Induced Senescence: Blebs and Tubes Visualized by 3D Electron Microscope	30
3.2.1 Summary of publication 2	30
3.3 Automated Image Analysis of Transmission Electron Micrographs: Nanoscale Evaluation of Radiation-Induced DNA Damage in the Context of Chromatin	33
3.3.1 Summary of the publication 3	33
3.4 Immunomodulatory Effects of Histone Variant H2A.J in Ionizing Radiation Dermatitis	36
3.4.1 Summary of publication 4	36
4. Discussion	39
4.1 H2A.J overexpression affects chromatin architecture	40
4.2 Cells lose nuclear integrity during radiation-induced senescence	42

4.3 Radiation-induced DNA damage patterns and chromatin alterations revealed by automated image software	45
4.3.1 TEM analysis of DNA damage patterns: insights in the labelling of repairing sites after high-LET IR exposure	47
4.4 Effects of histone variant H2A.J in IR dermatitis	48
5. Conclusion and outlooks	51
6. References	53
7. Appendix	63
7.1 Publication 1	63
7.2 Publication 2	86
7.3 Publication 3	104
7.4 Publication 4	118
8. Acknowledgement	136
9. List of Tables	139
10. List of Figures	139

1. List of abbreviations:

AI	artificial intelligence
ATAC-seq	assay for transposase-accessible chromatin sequencing
ATM	ataxia-telangiectasia mutated
ATP	adenosine triphosphate
ATR	ataxia-telangiectasia and rad3-related
CCF	cytoplasmic chromatin fragments
CT	computed tomography
DAPI	4',6-diamidino-2-phenylindole -
DDR	DNA damage response
DNA	deoxyribonucleic acid
DNA-SCARS	DNA segments with chromatin alterations reinforcing senescence
DSB	double-strand break
ECM	extracellular matrix
ELISA	enzyme-linked immunosorbent assay
FACS	fluorescence-activated cell sorting
GDP	guanosine-5'-diphosphate
GM-CSF	granulocyte macrophage - colony stimulating factor
GTP	guanosine-5'-triphosphate
Gy	Gray
H2A.J_KI.H2A.J / OE	H2A.J_KI. H2A.J-knock-in/H2A.J overexpressing
HFSC	hair follicle stem cells
HR	homologous recombination
IFM	immunofluorescence microscopy
IHC	immunohistochemistry
IL-6	interleukin-6
IR	ionizing radiation
ISG	interferon stimulated genes
KO	knock-out
LET	linear energy transfer
MCP-1	monocyte chemoattractant protein-1
MMEJ	microhomology-mediated end-joining
MPO	myeloperoxidase
NHEJ	non-homologous end-joining
non-IR	non-irradiated
NT	no target
Ran-GTP	Ras-related nuclear protein-GTP
RBE	relative biological effectiveness
SAHF	senescence-associated heterochromatin foci
SASP	senescence-associated secretory phenotype
SA- β -GAL	senescence-associated beta-galactosidase
SBF-SEM	serial block-face scanning electron microscopy
SEM	standard error of mean
SSB	single-strand break

TEM
TF
WT

transmission electron microscopy
transcription factor
wild-type

1. Summary / Zusammenfassung

This thesis provides molecular insight into the H2A.J histone variant and its involvement in some biological processes as a reaction to ionizing radiation. The *in-vitro* study was conducted using WI-38 (no target (NT), knockdown (KD) and overexpressing (OE) H2A.J) cell line irradiated with 20Gy and labelled with several markers for investigating DNA damage and cell senescence. RNA-seq and enzyme-linked immunosorbent assay (ELISA) were used to examine the effect of H2A.J on the inflammatory response in cells. In addition, the study used assays for transposase-accessible chromatin sequencing (ATAC-seq) to investigate the role of H2A.J in the global chromatin conformation changes after IR. It was found that those cells, which have H2A.J involvement after radiation, show more resistance against senescence and apoptosis. Moreover, the conformational structure of the chromatin changes the global status of the transcription in the cells, especially for the senescence-associated secretory phenotype (SASP) genes in case of overexpressing H2A.J.

Many changes occur in the cells during senescence, including disruptions in the nucleus and cytoplasmic organelles. Disruption in the nuclear morphology was noticed in the radiation-induced senescent cells. Mass spectrometry-based proteomics and high-resolution tools were used to look into the relation between the disrupted nuclear membrane and the characteristic markers of senescence. Our study found that the cells lost their laminB1 during senescence, which may disrupt the nuclear envelope, leading to the ejection of chromatin fragments in the cytoplasm, and activating the cGAS-STING-dependent interferon signalling. Moreover, serial block-face scanning electron microscopy (SBF-SEM) revealed the establishment of nanotubes as a result of the nucleus envelope disruption. These nanotubes may have role in the cytoplasmic chromatin fragments (CCF) ejection into the cytoplasm.

After high-LET IR, the fibroblasts showed low electron density domains (LEDDs) in the nucleus caused by the centralized energy emitted next to the particle trajectories. Automated image analysis software with transmission electron microscopy (TEM) micrographs was used to detect the dynamics of DNA repair chromatin conformation. Fibroblasts were irradiated with low- and high-LET

photons, and then they were labelled nanoparticles-tagged with DNA repair markers. The automated software tools were used to analyze the TEM micrographs to determine the pattern of the DNA damage post-low-LET versus high-LET IR. Most DNA double-strand breaks (DSBs) were repaired totally and no changes in chromatin condensation were visible after low-LET irradiation, but compound DNA damages were detected along the particle trajectories induced by high-LET IR causing clear-bordered LEDDs. The chromatin densities and the distribution of nanoparticles (related to LEDDs and based on size and shape) in the nucleus were determined using an AI tool. These results showed the ability of the automated precise analysis for the nanoparticles and LEDDs in micrographs to describe the DNA damage patterns in the nucleus after radiation.

Additionally, an *in-vivo* study of H2A.J's role in senescence was conducted using H2A.J-knock-out (KO) mice. Skinfold of wildtype (WT) and KO mice were irradiated with 20Gy, and then for two weeks, the skin reactions were noticed macroscopically. Skin samples were collected, embedded, and labelled with several senescence and DNA damage markers. Transcriptome profile was examined using RNA-seq and RT-PCR, moreover, flow cytometry was used to explore the immune cell infiltration. An intensive reaction was observed on the skin of KO mice compared to WT, accompanied by enlargement of the epidermal thickness. More loss of hair follicles and their stem cells after radiation was found in KO skin which led to follicle vanishing. Also, increasing senescence gene expression was found in KO mice, which was associated with increased releasing of SASP factors. High numbers of infiltrated immune cells were found in both KO and WT; however, KO skin showed more induction of neutrophil numbers, irregular differentiation of and cornification of keratinocytes with increasing transcription of JunB after radiation in comparison to WT. In conclusion, the absence of H2A.J in irradiated keratinocytes is related to increasing senescence, SASP secretion, and immune response, combined with higher proliferation as an inflammatory reaction during radiation dermatitis.

In dieser Arbeit wurden die Histonvariante H2A.J, deren molekularbiologische Prozessierung und Beteiligung als Reaktion auf ionisierende Strahlung analysiert. Hierzu wurden in einer in-vitro-Studie WI-38-Zellen (Fibroblasten) verwendet, die unterschiedliche genetisch Modifikationen für die Histonvariante H2AJ aufwiesen (Non-Target, Knock-down, Over-expressing). Die Bestrahlung der Zellen erfolgte hochpräzise mit 20 Gy (6 MV Photonen) am Linearbeschleuniger der Klinik für Strahlentherapie und Radioonkologie um anschließend in unterschiedlichen Zeitabständen die Auswirkungen der strahleninduzierten DNA-Schäden und Prozesse der Zellalterung mikroskopisch zu untersuchen. RNA-Seq und ELISA wurden darüber hinaus verwendet, um eine mögliche Beteiligung von H2A.J auf die Entzündungsreaktion in den Zellen zu analysieren. Ebenfalls wurde ATAC-Seq angewendet, um die Rolle von H2A.J an den strahleninduzierten Modifikationen der Chromatinstruktur zu erforschen. Hierbei wurde festgestellt, dass die Zellen, in welchen eine Beteiligung von H2A.J auf molekularer Ebene nachweisbar ist, resistenter gegenüber Alterungsprozessen und Apoptoseinduktion aufweisen. Darüber hinaus konnte beobachtet werden, dass die Modifikationen des Chromatins auch die Transkription der zellulären DNA beeinflussen, insbesondere die SASP-Gene bei einer H2A.J-Überexpression. Alterungsbedingt teilungsunfähige seneszente Zellen weisen eine Vielzahl an Veränderungen in den zytoplasmatischen Organellen und den intra-nukleären Vorgängen auf. Bei strahleninduzierter Seneszenz wird insbesondere die Kernmorphologie beeinflusst, was mit Hilfe von massenspektrometrischer Proteomanalyse und hochauflösender Mikroskopie untersucht wurde, um die Verbindung zwischengeschädigter Kernmembran und den charakteristischen Seneszenz-Markern besser zu verstehen. Hierbei wurde nachgewiesen, dass die Veränderungen in der Kernlamina durch Lamin-B1-Verlust hervorgerufen werden, was in Folge zu einem Verlust von Chromatinfragmenten (CCFs) in das Zytoplasma führen und die cGAS-STING-abhängige Interferonsignalisierung aktivieren kann. Darüber hinaus konnten mittels Serial-Blockface-Rasterelektronenmikroskopie (SBF-SEM) Nanoröhren visualisiert werden, die bei dem Transport von CCFs aus dem Zellkern in das Zytoplasma beteiligt sind.

Nach der Bestrahlung von Fibroblasten mit Schwerionen, die einen hohen linearen Energietransfer (high-LET) aufweisen, wurden mittels elektronenmikroskopischer

Analyse in der homogenen Chromatinstruktur Bereiche mit niedriger Elektronendichte (LEDDs) sichtbar, welche durch die Ionisationsereignisse entlang der Partikelbahn verursacht wurden. Um diese zu untersuchen, wurde eine automatisierte Bildanalysesoftware (HALO) verwendet, um in den elektronenmikroskopischen Aufnahmen die Dynamik in der Veränderung der Chromatinstruktur zu beobachten. Hierzu wurden DNA-Reparaturproteinen antikörperbasiert mit kolloidalen Goldpartikeln markiert, um hochaufgelöst die Induktion und Reparatur von DNA-Schäden, insbesondere Doppelstrangbrüche (DSBs), zu untersuchen und die hierdurch gewonnenen Erkenntnisse mit denen nach low-LET-Bestrahlung zu vergleichen. Nach low-LET-Bestrahlung (Photonen) wurden fast alle DSBs repariert und es verblieben keine sichtbaren Chromatinveränderungen zurück. Hingegen waren nach high-LET-Bestrahlung (Schwerionen) entlang der Partikelbahn eine Vielzahl an Schäden nachweisbar, die zur Bildung der LEDDs führten. Innerhalb von diesen wurde die Chromatindichte sowie die Verteilung der mit kolloidalem Gold markierten Reparaturfaktoren mit Hilfe eines KI-basierten Softwaretools ausgewertet.

Der Einfluss von H2A.J auf die vielfältigen intrazellulären Prozesse bei Seneszenz wurde darüber hinaus in einer in-vivo-Studie an genetisch modifizierten H2A.J-knock-out-Mäusen (KO) durchgeführt und die Ergebnisse mit Wildtyp-Mäusen (WT) verglichen. Die Haut von WT- und KO-Mäusen wurden mit 20 Gy lokal bestrahlt, makroskopisch wurde über einen Zeitraum von 14 Tagen die Hautreaktion beobachtet, um anschließend entnommene Haut mittels RNA-Sequenzierung und RT-PCR auf Seneszenz und DANN-Reparatur zu untersuchen, ein Transkriptomprofil zu erstellen und die Infiltration von Immunzellen mit Hilfe von Durchflouzytometrie zu analysieren. Die Haut der KO-Mäuse zeigte hierbei eine intensivere Reaktion auf die Strahlung und eine Veränderung in der Epidermisdicke, einhergehend mit einem Verlust der Haarfollikelstammzellen und Haarfollikeln, im Vergleich zu den WT-Mäusen. Ebenso konnte eine erhöhte Genexpression von Seneszenz Faktoren und die Freisetzung von SASP-Faktoren festgestellt werden. Sowohl in den KO- wie auch bei den WT-Mäusen wurde eine vermehrte Infiltration der Haut durch Immunzellen nachgewiesen, jedoch zeigte die Haut der KO-Mäuse eine Vermehrung der Neutrophilen, eine unregelmäßige Differenzierung und Verhornung von Keratinozyten sowie eine Zunahme der JunB-

Transkription im Vergleich zur Haut der WT-Mäuse. Zusammenfassend wurde die Erkenntnis gewonnen, dass das Fehlen von H2A.J in bestrahlten murinen Keratinozyten, die zunehmende Seneszenz, SASP-Sekretion und Immunreaktionen sowie die erhöhte Proliferation mit der Entzündungsreaktion während der Strahlendermatitis zusammenhängt.

2. Introduction

2.1 Ionizing radiation and its physical properties

Radiation is defined as the transfer of energy without an intermediate medium. Sometimes, this radiation has enough energy to excite the surrounding neutral atoms by transferring this energy and changing their status to ions. This phenomenon is called ionizing radiation (IR). IR can be classified based on its components, sources, and effects.

When the energy of radiation penetrates materials, the kinetic energy (in the case of particle radiation) or the quantum energy (for electromagnetic waves) is transferred to electrons, which can cause disruption of the atomic stability, destroy chemical bonds, and induce extensive damage in the irradiated material. The relationship between the physical properties of IR and its effects on biological systems is remarkably diverse. That is why insight into the mechanisms of action is essential to understanding these effects at the cellular and molecular levels.

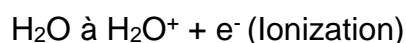
2.1.1 Linear energy transfer

A clear distinction is made between loosely and densely IR. The dose rate of IR diminishes during transfer through materials because energy is absorbed with each interaction through the material. Several factors can affect this, such as the distance and distribution of these ionization events. X-rays, γ -rays (photons) and electrons are considered loosely-IR because they create uniformly distributed ionization events along their path, which are relatively far apart from each other. On the other hand, protons, α -particles, fast neutrons, and heavy ions (nuclear particles), which produce many ionizations events within a small distance along their tracks, are considered as densely-IR.

Linear energy transfer (LET) refers to the volume of energy emitted per path length along the path of a particle; it depends on the atomic number of the irradiated matter (Kollias et al., 1998).

Direct and indirect radiation effects can influence cells and their components, including proteins, RNA and DNA (Munro, 1969). The direct radiation effect can be caused by high-energy particles. In the context of DNA, the energy transfers to the shell electrons of DNA molecules, which can then release secondary electrons. These events lead to direct chemical changes in DNA, such as single-strand breaks (SSB) and double-strand breaks (DSBs) caused by the breaking of covalent bonds in the DNA backbone.

Low-LET and loosely-IR are mainly responsible for producing the indirect effects. Due to the lack of electric charge, no interactions take place within the electromagnetic fields of the DNA molecule shell electrons. Instead, the energy of the photons is transferred to electrons of neighbouring water molecules through collisions. These electrons are then released, and, through the resulting ionization of water (radiolysis), free radicals are formed.



Due to their high reactivity, hydroxyl radicals have a short range and diffuse at most over a maximum length of two molecular diameters (Marnett LJ, 2000). However, OH-radicals generated by ionization in the DNA hydrate shell still reach DNA located a few nanometres away and thereby are responsible for a large part of the biologically severe damage (Goodhead DT, 1994).

2.2 Radiation induced DNA damage

Despite the fact that DNA is chemically stable, an estimated 10^4 – 10^5 instances of DNA damage occur within human cells each day (Lindahl & Barnes, 2000). Normally, these damages are caused through metabolism and other biological processes in the cell (Friedberg et al., 2005). Alternatively, they can be caused by external factors such as IR exposure. Usually, cells can cope with these damages and repair sufficiently to maintain a normal life cycle. However, sometimes these damages are irreparable and can cause cell arrest, which may lead to senescence or cell death (Jackson, 2009).

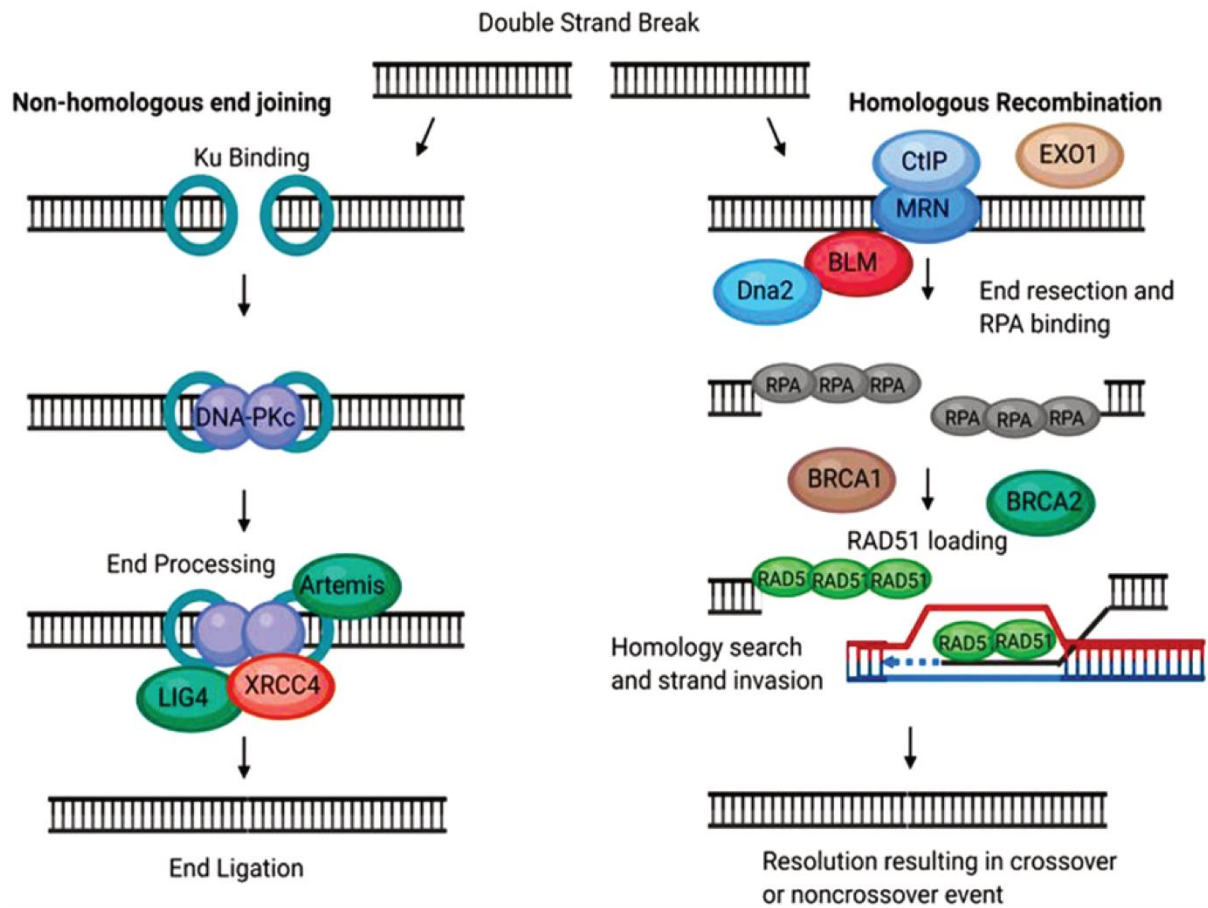
IR can induce numerous types of DNA damage such as protein-DNA crosslinks, intramolecular crosslinks, loss of nucleotides, SSBs and DSBs (Henner et al., 1982, 1983). It is estimated that 1 Gy of IR can induce 40 DSBs, 1000 SSBs and 1300 base damages within the DNA structure (Murray et al., 2019). In order to eliminate this damage, cells have developed several DNA repair mechanisms can interact directly with the lesions to restore the DNA sequence (Geacintov & Broyde, 2017).

2.2.1 Cellular responses to DNA damage

The aforementioned cellular mechanisms are designed to repair DNA thus preventing any damage that causes cancer, senescence, or cell death. These mechanisms include base excision repair, alternative excision repair, mismatch repair, nucleotide excision repair, transcription-coupled nucleotide excision repair, SSB repair, DSB repair, cell cycle arrest (senescence) and apoptosis (Friedberg et al., 2005). In this study, we focus on the DNA damage response (DDR) related to DNA DSBs, which, if left unrepaired, are the most harmful damages to the cell. Two major repair mechanisms in response to DSBs are a) homologous recombination (HR), which can be activated exclusively in the G2 and late S phase of the cell cycle, and b) non-homologous end-joining, which can work in all cell cycle phases (Lieber, 2008).

2.2.2 Strategies of DNA double-strand break repair

All living organisms have strategies to repair DNA DSBs (Lieber, 2008), and the two major systems are NHEJ and HR (Sonoda et al., 2006). In general, both the type of DNA damage and the cell cycle phase determine, which pathway (NHEJ or HR) is initiated to repair the damage (Lieber, 2008). Both pathways of DSBs repairing systems are accomplished in several reactions steps as shown in figure 1.



(Ruth F. Ketley; Monika Gullerova, 2020)

Figure 1: DNA DSB repair pathways: non-homologous end joining (left), and homologous recombination (right). Reprinted from 'Jack of all trades? The versatility of RNA in DNA double-strand break repair' by Ketley RF, Gullerova M. *Essays Biochem.* 2020 Oct 26;64(5):721-735. License: CC BY 4.0

2.2.3 Non-homologous end joining (NHEJ)

NHEJ is the most common DSB repair mechanism. NHEJ does not require a homologous chromosome to complete the repair process and so it can occur in any cell cycle phase (Moore & Haber, 1996). However, for the same reason, NHEJ is also one of the most error-prone DNA repair mechanisms. Simply, NHEJ just requires some random nucleotides to be added to or to be removed from the damage site and then ligates the two ends together; this can sometimes lead to serious mutations. On the other hand, it has the advantage of protecting DNA from losing many genes by restoring the backbone of the DNA structure (Rodgers & Mcvey, 2016).

Numerous proteins contribute to NHEJ including three types of enzymes: nucleases to eliminate the damaged DNA nucleotides, polymerases to help in the restructuring, and ligases to reinstall the phosphodiester backbone (Lieber et al., 2014).

2.2.4 Homologous recombination (HR)

Contrary to NHEJ, HR is restricted to S and G2 cell cycle phases. This restriction is due to the fact that HR uses the sister chromatid sequence as a copy to reproduce the damaged section of DNA. HR is one of the most precise DNA repair mechanisms and use of the sister chromatids prevents loss of genetic information (Giglia-Mari et al., 2011). HR has several sub-pathways, but it is always initiated in the same way.

HR not only plays a key role in DNA damage repair, but it is also pivotal in several biological processes such as telomere maintenance, chromosome separation and the DNA replication fork (Sung & Klein, 2006). In addition, any defect or mutation in HR genes can cause cell cycle arrest or cancer development (Sung & Klein, 2006).

2.2.5 Cellular senescence

One particular type of cell cycle arrest is senescence, which is a biological phenomenon that leads to the termination of the cell cycle during mitosis resulting in a functional decline of the cell (Kumari & Jat, 2021). Senescence is usually an irreversible process, which is characterized by augmented cellular size, changes in gene expression and high metabolic activity (Huang et al., 2022). Senescence can be triggered by different cellular stresses including DNA damage, telomere shortening, oncogene activation, tumor suppressor inactivation, and oxidative stress (figure 2). As a response to these stresses, cells initiate a complex signaling pathway that ends with an irreversible arrest of the cell cycle. This is usually initiated by activating cell cycle inhibitors such as p16^{INK4a} and p21^{Cip1} (Kumari & Jat, 2021). These inhibitors hold back the function of cyclin-dependent kinases thereby preventing the progression of the cell cycle.

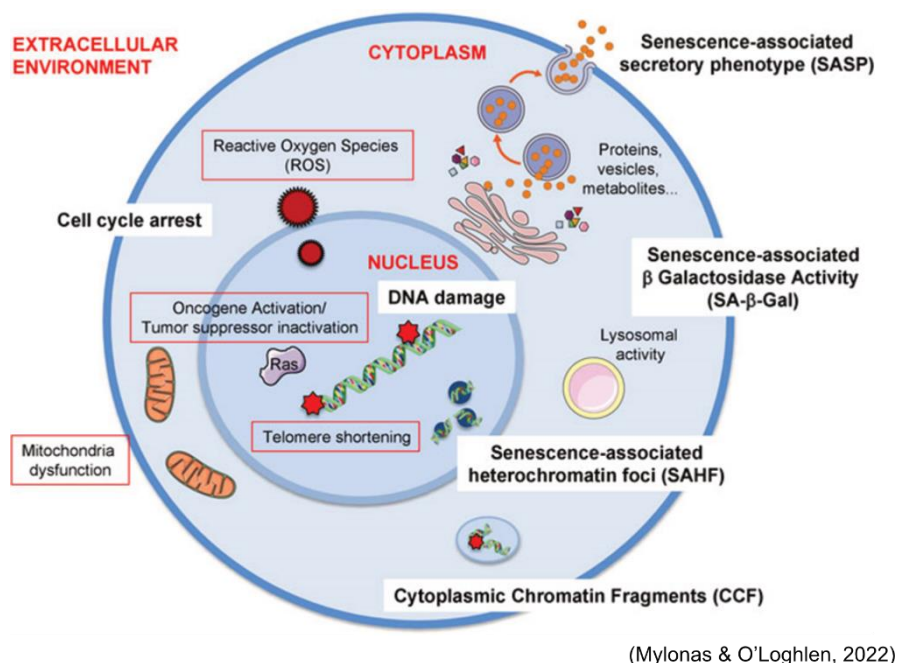


Figure 2: Senescence triggers and characteristics: diagrammatic representation of various stimulators and biomarkers of senescent cells. Reprinted from 'Cellular Senescence and Ageing: Mechanisms and Interventions.' by Mylonas A, O'Loughlen A. *Front Aging*. 2022 Mar 29; 3:866718. LicenseCC: BY 3.0

Besides cell cycle arrest, senescent cells show significant alterations in their secretory profile called the senescence-associated secretory phenotype (SASP) (Saleh et al., 2018). The SASP includes the production of pro-inflammatory cytokines, chemokines, and proteases (Lopes-Paciencia et al., 2019). SASP serves to notify the immune system of the presence of senescent cells, which can lead to their identification and subsequent elimination by immune cells.

Moreover, senescence is characterized by chromatin alterations such as the development of heterochromatin foci, known as senescence-associated heterochromatin foci (SAHF) (Narita et al., 2003), and the presence of chromatin fragments in the cytoplasm, referred to as cytoplasmic chromatin fragments (CCF) (Adams et al., 2013a). The most used marker to detect senescence is senescence-associated β -galactosidase activity (SA- β -Gal), which is related to high lysosomal activity. This characteristic, however, is not present in all senescent cells (Valieva et al., 2022).

Senescence plays a dual role in organisms. On the one hand, it is beneficial during embryonic development and wound healing by aiding tissue remodeling and the removal of potentially harmful cells (Jun & Lau, 2010). On the other hand, accumulation of senescent cells in tissues can contribute to ageing and the activation of age-related diseases such as cancer, cardiovascular disease, and neurodegenerative disorders (McHugh & Gil, 2018).

2.3 Chromatin architecture and gene expression

Recently, studies related to chromatin architecture focused on the hierarchical system of chromatin and found that chromatin structure had a huge impact on molecular biological processes such as DNA replication, gene expression, and DNA damage repair (Woodcock, 2006). The hierarchy of chromatin structure can be divided into the following: the primary structure, which refers to the features in linear DNA, the secondary structure, which is made up of interactions of nucleosomes like the '30 nm' chromatin fibre, and the tertiary structure, which is formed through interactions between secondary chromatin structures (Woodcock & Dimitrov, 2001). Moreover, the quaternary structure, which is related to the compaction during the mitotic phase of the cell cycle.

Recent studies found chromatin architecture and the 3D structure to be particularly important to recognize and diagnose the biological process and the health of cells. High-throughput chromosome conformation capture (Hi-C) techniques can give more information about the in-progress interactions inside the nucleus and these interactions partition into different topologically associated domains (TADs) (Khoury et al., 2020). These TADs are strongly related to senescence and quiescence by causing a shift from euchromatin to heterochromatin (Hi-C partition A to partition B) and vice versa. This DNA remodelling affects the expression of cell cycle genes (Criscione et al., 2016), which lead to more heterochromatinization or euchromatinization in the nucleus.

2.3.1 Nucleosome dynamics and chromatin remodelling

Eukaryotes' DNA is structured and wrapped twice around the core histones octamer (nucleosomes) repeatedly, and the linker histones link these nucleosomes (Li & Widom, 2004). This octamer structure is surrounded by 147 base pairs of genomic DNA wrapped around in 1.65 circles (Luger & Richmond, 1998). A nucleosome is a global protein unit with a molecular weight of 210 kDa containing a double copy of the four core histones H2A, H2B, H3, and H4. These core histones can be exchanged with histone variants (Suto et al., 2000, Muthurajan et al., 2003).

The DNA interacts with the histone proteins of the nucleosomes at 14 sites called superhelix locations (SHLs) and more than 120 direct atomic sites. In the SHLs, DNA is five times more compact than normal DNA (Pennings et al., 1991). However, the nucleosomes are still capable of easily moving and sliding along the DNA double strand. Some modifications to the nucleosome can open the tightly packed DNA in the interphase of the cell cycle, thereby making it more accessible for transcription (Gasser, 2002). Other reversible modifications can close the DNA and compact it very tightly, as seen in mitosis for example (Berger, 2002).

2.3.2 Histone modifications

As previously mentioned, a nucleosome contains an octamer of four histones (H2A, H2B, H3 and H4), and for a long time it was believed that these histones have just one function related to the packaging of DNA (Grunstein, 1992). However, recent studies showed that the histone has a bigger role to play in controlling many biological processes such as DNA transcription, replication, and repair (Lennartsson & Ekwall, 2009).

Histones can be modified in several ways, such as phosphorylation, ubiquitination, acetylation, methylation and SUMOylation (Strahl & Allis, 2000a). Each modification has a different function, for example, acetylation and methylation of the lysine in the histone tail play a role in chromatin structure, and hyperactive methylation is related to silencing and imprinting the gene, mainly in the X chromosome (Esteller, 2007).

The status of histone modifications in specific regions of DNA can lead to specific downstream events known as the 'Histone code' theory (Strahl & Allis, 2000b). This histone code directly affects multiple processes such as gene expression (Sanders et al., 2004), and organization of nuclear architecture, which is linked to a histone's modification, especially methylation (Espada et al., 2004). In general, any change in the histone code can affect the integrity of the genome and may lead to development of cancer (Seligson et al., 2005).

2.3.3 Histone variants

Almost all eukaryotes use histones for packaging their DNA, making it highly conserved across all of them. These histones, encoded by several repetitive genes, are usually transcribed side by side with DNA replication. It was found that other genes have the same order of repetition in the genome and encode another type of histones called histone variants. Histone variants only differ slightly in amino acid sequence compared to their core histone counterparts. Unlike core histones, variants are replication-independent and can be transcribed throughout the cell cycle (Kamakaka & Biggins, 2005). Histone variants have different functions from their canonical histones and are involved in several biological processes, such as DNA repair, chromosome segregation, transcription initiation, and spermatogenesis (Talbert & Henikoff, 2010). In addition, there are some differences related to structural changes that happen to the core octamer after replacement by the variant, which in turn affects the wrap of the

DNA around the histone core (Talbert & Henikoff, 2010). Histones variants just localized to the specific regions in the genome (Kamakaka & Biggins, 2005).

Up to now, many histone variants have been discovered and thus a need to classify them has arisen. Histones can be categorized according to their structure with regard to homomorphous and heteromorphous, and with regard to the differences in the amino acid sequence between the variant and the canonical histones (Grove & Zweidler, 1984). Histone variants with a small deviation in number/sequence of amino acids are called homomorphous and includes H2A.1 and H2A.2. Heteromorphous variants include variants with a large deviation in the body compared to canonical histones, such as H2A.X, H2A.Z, and macro H2A.

The swapping of histones with their variants can have a massive impact on the structure and the distribution of the nucleosome along the chromosome (Talbert & Henikoff, 2016). Some changes affect interactions between the chromatin and its remodelers, such as the replacement of H3 by CENPA in the centre of chromatin (Steiner & Henikoff, 2015).

Replacement of another canonical histone, such as H2A, has an effect on transcription, as is the case when H2A is replaced by H2A.Z, or H2A.B can start gene transcription in some sites (Adam et al., 2001). Replacing the same canonical histone with macroH2A can lead to gene silencing and nucleosome solidity (Ratnakumar et al., 2012, Yelagandula et al., 2014).

2.3.4 Histone variant H2A.J

H2A histone variants are the biggest group of variants (Maze et al., 2014), all of which are replication-independent, and each variant has a different function related to DNA structure and accessibility (Redon et al., 2021). A recently discovered H2A variant is

H2A.J, which is found specifically in mammalian cells. H2A.J differs from H2A in two main ways: the amino acid alanine is replaced by valine at position 10; the last seven amino acids of the histone tail contain an SQ motif (phosphorylation site) in H2A.J (Redon et al., 2021).

Unlike canonical histones, which are encoded by clusters of genes located on chromosomes 1-6, H2A.J is encoded by the unique H2A.J gene located on chromosome 12 in humans (Contrepois et al., 2017) and on chromosome 6 in mice. Examination of the H2A.J-H2B complex in comparison to H2A-H2B, showed a higher thermal stability, which may indicate a role of H2A.J in DNA regulation (Tanaka et al., 2020). H2A.J was found to play a role in inflammatory gene expression during senescence (Contrepois et al., 2017). A high level of H2A.J has been suggested to be involved in developing breast cancer (Cornen et al., 2014). In addition, H2A.J overexpression showed a link to chemotherapy sensitivity for hepatic and colorectal cancer (Wang et al., 2019; Yao et al., 2006). The recent work of Mangelinck et al., 2020, showed that replacing H2A with H2A.J affects the connection to the histone H1 and is related to the elevated expression of the interferon-stimulated gene (ISG) pathway. On the other hand, H2A.J was found at very low levels in the stem cells of the hair follicles and inter-follicular epithelial cells of young mice (Contrepois et al., 2017), but elevated in the same cells upon IR-induced aging. However, until now the precise mechanism and the functional role of H2A.J are still unknown.

2.4 Transmission electron microscope (TEM)

The TEM is a powerful instrument in scientific research, offering clear insight into the intricacies of the microscopic world. The principle of TEM depends on the movement of the electrons, which takes place when a stream of electrons passes through an ultra-thin sample, and some of these electrons interact with the sample and others go

through. The resulting virtual image is then amplified and focused onto a fluorescent screen or a sensor, enabling visualization and analysis (Kohl, 2016).

One of the major advantages of TEM is the high resolution that it provides due to the short wavelength of the electrons compared to light microscopy. The normal microscope utilizes visible light, limiting its resolution capability to around 200 nanometres (de Souza, 2009). In contrast, electron microscopes use electron beams, which enable electron microscopes to achieve atomic-level resolution. This capability allowed us to examine intricate details of specimens, such as cellular molecules, DNA and its interaction, or atomic arrangement within a crystal lattice.

2.5 Assay for Transposase-Accessible Chromatin sequencing (ATAC-seq)

ATAC-seq is one of the most exciting recent high-resolution techniques used in genomic research (Buenrostro et al., 2015). ATAC-seq uses the advantage of the hyperactive transposase Tn5 to bind to the open chromatin regions, unlike the closed chromatin, which is connected to DNA-bound factors such as nucleosomes (Goryshin & Reznikoff, 1998). After the integration of the Tn5 transposase into the open chromatin sites, a cut-paste process is done by the Tn5 transposase to chop off the accessible chromatin region of the DNA. The resulting DNA fragments are amplified for next-generation sequencing and the open chromatin areas can be detected.

In comparison to other techniques used for nucleosome mapping, ATAC-seq offers significant advantages such as generating maps with only a few cells and also using single-cell level (scATAC-seq) allowing the investigation of nucleosome variations between individual cells (Grandi et al., 2022). On the other hand, this method is a very rapid technique because of the simplicity of its two-steps protocol. In general, the

ATAC-seq technique gives insights into gene regulation and is considered a powerful tool for understanding chromatin dynamics and regulatory mechanisms.

2.6 RNA sequencing (RNA-seq)

RNA sequencing (RNA-seq) is one of the genomic methods used for detecting and quantifying the messenger RNA, which helps to study the cellular response and construct sequencing libraries (Haque et al., 2017). Although direct sequencing of RNA is possible, most RNA-seq approaches typically use DNA sequencing instruments. Consequently, converting RNA into a cDNA library is essential to perform RNA-Seq. Preparing this library depends on the RNA species being studied. Several applications use the RNA-seq method such as gene expression profiling, identifying allele-specific expression, and disease-related single nucleotide polymorphisms (SNPs) (Stark et al., 2019). Moreover, RNA-seq provides several advantages through hybridization-based approaches such as the high sensitivity of gene detection, genome independence that make it performed without sequenced genomes, and unlike the microarrays approach reduction of bias, unlike the microarrays approach (Haque et al., 2017). In general, RNA-seq has changed our understanding of gene expression and functional genomics.

2.7 Goals and hypothesis

The goals of the first study were to investigate the role of H2A.J in radiation-induced senescence and to understand how H2A.J influences the formation of SAHF and DNA-SCARS. ATAC-seq and RNA-seq was used to comprehensively analyze the epigenetic mechanisms of H2A.J, the influence of H2A.J on the dynamic changes in chromatin organization with differential binding of specific transcription factors as well as the resulting changes in the transcriptome. Current research suggests that H2A.J plays a

key role in radiation-induced senescence, affecting both chromatin organization, accessibility of TFs, and pro-inflammatory gene expression of senescent cells.

The second part of the study investigated the impact of high-dose of IR exposure on human WI-38 fibroblasts, particularly changes in protein expression and nuclear morphology during senescence progression. TEM and serial block-face scanning electron microscopy (SBF-SEM) were used to visualize the cellular ultrastructure and 3D morphological changes in senescent fibroblasts. Secretion of vesicles was detected to investigate the involvement of the cGAS-STING pathway in radiation-induced senescence and triggering inflammation.

In the third part of the study, the spatiotemporal dynamics of DNA repair and chromatin remodelling following exposure to high-LET and low-LET photons were analyzed in fibroblasts. For that, an established software (HALO™, IndicaLabs) with artificial intelligence (AI) was used to distinguish DNA damage patterns following low-LET versus high-LET IR. To precisely determine and quantify nanoparticles, their size, shape, and density were taken into account. In addition, we used AI to determine and segment the low electron density domains (LEDDs) induced by high-LET IR and to specify the spatial distribution of nanoparticles relative to the segmented LEDDs. Using this software our research revealed that different types of radiation cause unique DNA damage patterns in fibroblasts. The software made it possible to efficiently classify the complex DNA damage pattern by evaluating the differently sized nanoparticles within the respective chromatin ultrastructure.

In the fourth part of the study, the influence of H2A.J was analyzed in a preclinical model with H2A.J *knock-out* mice, by investigating the macroscopic and microscopic changes in irradiated skin. To study protein-coding transcriptome changes following

high-dose IR, RNA sequencing was used. The study aimed at analyzing the functional role of H2A.J in radiation dermatitis. The absence of H2A.J led to significantly stronger radiation reactions in the skin of H2A.J *knock-out* mice. This increased radiation reaction in H2A.J *knock-out* skin was due to increased senescence induction of epidermal keratinocytes, with augmented SASP secretion and subsequently more pronounced inflammatory reactions due to reactive immune cell infiltration.

3. Publications

3.1 Role of Histone Variant H2A.J in Fine-Tuning Chromatin Organization for the Establishment of ionizing Radiation-Induced Senescence

3.1.1 Summary of publication 1

Radiation-induced senescence can occur when cells experience irreversible DSBs due to IR. The histone variant H2A.J was previously defined as an indicator of persistent DNA damage in senescent cells and accumulates in DNA-SCARS.

This study investigated the role of the histone variant H2A.J in radiation-induced senescence and its impact on chromatin organization, gene expression, and establishment of the SASP. Techniques used included immunofluorescence microscopy (IFM), IHC-staining, ATAC-seq, ELISA, SA- β -Gal activity and RNA-seq analysis.

It was found that H2A.J incorporation into chromatin significantly affects the higher-order chromatin organization (figure 3), which may cause changes in chromatin accessibility. These, in turn, will be influencing the enrolment of transcription factors and the expression of inflammatory genes, contributing to the establishment of the SASP. The study also investigated H2A.J expression in irradiation-exposed lung tissue and observed dose-related H2A.J expression in pneumocytes - lung cells involved in pro-inflammatory tissue reactions.

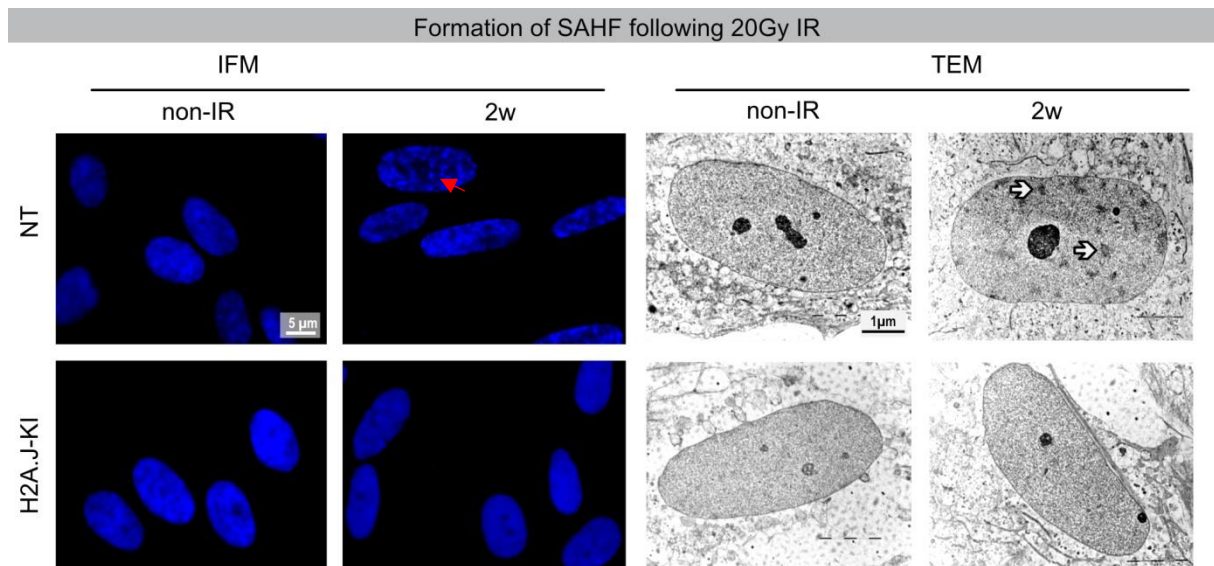


Figure 3: SAHFs formation in NT and H2A.J-KI fibroblasts before and after IR using IFM (left, red arrow) and TEM (right; white arrows). Reprinted after modification from 'Role of Histone Variant H2A.J in Fine-Tuning Chromatin Organization for the Establishment of Ionizing Radiation-Induced Senescence'. by Abd Al-razaq et al., 2023; *Cells*.12(6):916. LicenseCC: BY 4.0

In conclusion, H2A.J plays a role in radiation-induced senescence and is involved in chromatin reorganization, transcriptional regulation and SASP establishment. Understanding these epigenetic mechanisms may provide insights into regulating radiation-induced senescence and associated biological processes.

In this research paper, I was responsible for the cell culture processes, maintaining the fibroblasts under optimal conditions. Moreover, I utilized different staining techniques to visualize all described markers in the fibroblasts and took detailed images for the published figures. In addition, I performed the ELISA tests and RT-PCR for the quantification of proteins and genes specified in the study. Beyond the lab work, I analysed some images with the HALO™ software (IndicaLabs) for advanced image analysis. Additionally, I conducted the comprehensive statistical analysis of the data and prepared the figures for their informative visual presentation in the published paper. Moreover, I have written the material and method part and contributed in editing the other parts of the research paper under Prof Rube's supervision.

3.2 Nuclear Fragility in Radiation-Induced Senescence: Blebs and Tubes Visualized by 3D Electron Microscope

3.2.1 Summary of publication 2

Cellular senescence is a complex process associated with permanent cell cycle arrest, chromatin reorganization, distorted nuclear morphology, and development of a pro-inflammatory phenotype. DNA damage, particularly DSBs, is crucial in triggering senescence, and persistent DDR signalling is necessary for maintaining the SASP. The formation of nuclear blebs and discharge of chromatin fragments towards the cytosol may link DDR and SASP in senescent cells. This study focused on premature senescence, which can be induced by exposure to high-dose IR. The study was designed to explore the effects of radiation on cellular senescence in human WI-38 fibroblasts, observing changes in protein expression, chromatin remodelling, and nuclear morphology using various techniques.

The fibroblasts were exposed to 20Gy of 6 MV photons using an Artiste™ linear accelerator. After irradiation, the fibroblasts were cultured for two weeks and compared to non-irradiated controls. After two weeks of radiation, irradiated fibroblasts were compared to the non-irradiated control.

The cellular alteration caused by radiation-induction senescence was investigated by SA- β -Gal detection using the X-Gal staining solution. To study the expression of various proteins related to senescence and DDR, IFM was conducted for p21, Ki67, BrdU, Lamin B1, H3K27me3, H3K9me3, 53BP1, and γ H2AX using specific antibodies.

To identify and characterize the proteins that contribute to the cellular response in radiation-induced senescence, we performed protein extraction and examined the samples by mass spectrometry.

TEM and serial block-face scanning electron microscopy (SBF-SEM) techniques were used to visualize the cellular ultrastructure and morphological changes. TEM provided high-resolution images of fixed and sectioned samples (figure 4), while SBF-SEM allowed 3D reconstruction of senescent fibroblasts.

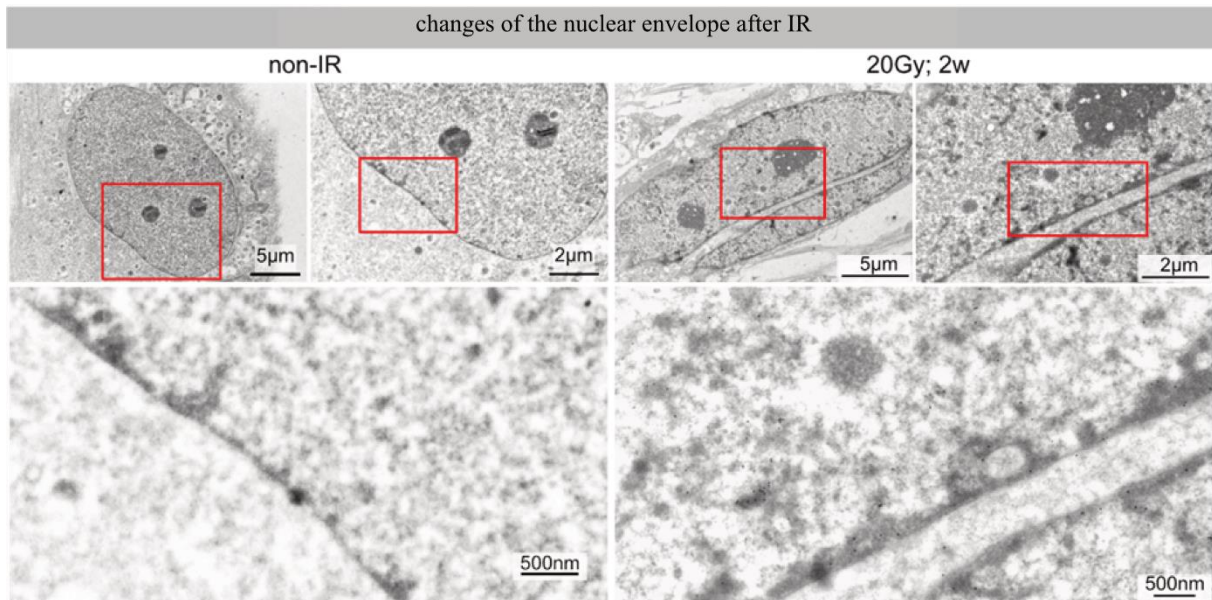


Figure 4: TEM micrograph showing the cellular ultrastructure and morphological changes of the nuclear envelope before (left) and after (right) IR. Reprinted after modification from 'Nuclear Fragility in Radiation-Induced Senescence: Blebs and Tubes Visualized by 3D Electron Microscopy' by Freyter et al., 2022. *Cells*. 11(2):273. LicenseCC: BY 4.0

An ELISA assay was used to estimate the concentration of 2'3'-cGAMP, involved in the cGAS-STING pathway and the induction of SASP.

Overall, this study showed that high-dose radiation exposure induces premature senescence in human fibroblasts, causing alteration in protein expression, chromatin remodelling, nuclear envelope destabilization, and alterations in nuclear morphology (figure 4). The findings give an insight of the mechanisms underlying radiation-induced senescence and its associated cellular changes.

In this research paper, my contributions were all cell culture procedures, including the irradiation at the linear accelerator. Moreover, I prepared the samples for IFM and TEM analysis and utilized different labelling techniques to study the expression of various proteins related to senescence and DDR. TEM and serial block-face scanning electron microscopy (SBF-SEM) techniques were used to visualize the cellular ultrastructure and morphological changes. TEM provided high-resolution images of sectioned samples, while SBF-SEM allowed 3D reconstruction of senescent fibroblasts. Beyond the lab work, I conducted the statistical analysis of the data and prepared the figures for publication. Furthermore, I have written the material and method part and contributed to editing the other parts of the research paper under Prof Rube's supervision.

3.3 Automated Image Analysis of Transmission Electron Micrographs: Nanoscale Evaluation of Radiation-Induced DNA Damage in the Context of Chromatin

3.3.1 Summary of the publication 3

Radiation therapy with heavy ion and high high-LET exhibits a distinct dose depth distribution and high biological effectiveness against the targeted cancer cells. Following the high-LET irradiation, the energy deposit is concentrated along particle paths, which cause multiple DNA lesions creating regions of LEDDs.

Automated analysis of transmission electron micrographs was performed to explore the spatiotemporal dynamics of DNA repair and chromatin remodelling.

At different time points (0.1 h, 0.5 h, 5 h, and 24 h) post-IR, irradiated fibroblast exposed to high-LET carbon ions or low-LET photons were fixated and then labelled with nanoparticles to mark DNA damage proteins (53BP1, pKu70, pKu80, DNA-PKcs). The labelled sections were observed via TEM focusing on the nuclei and tracking the creation and repair of DNA damage within the chromatin ultrastructure. AI-tools helped in innovative image analysis by distinguishing DNA damage patterns post-low-LET compared to high-LET IR.

Low-LET irradiated cells showed scattered single DNA damages through the nucleus and systematic repair for the majority of DNA DSBs with no signs of chromatin condensation.

High-LET IR induced clustered DNA damages centralized along particle paths, leading to LEDDs. The HALO software precisely determined and quantified variously sized nanoparticles, their distances from each other, and locations within micrographs (based on size, shape, and density).

Chromatin densities were defined through the variation in grayscale and the nanoparticle-localisation was automatically classified and categorized into euchromatin or heterochromatin.

The LEDDs induced by high-LET IR were determined and segmented using the AI algorithm of the HALO software, and the spatial allocation of nanoparticles relative to segmented LEDDs was determined (figure 5).

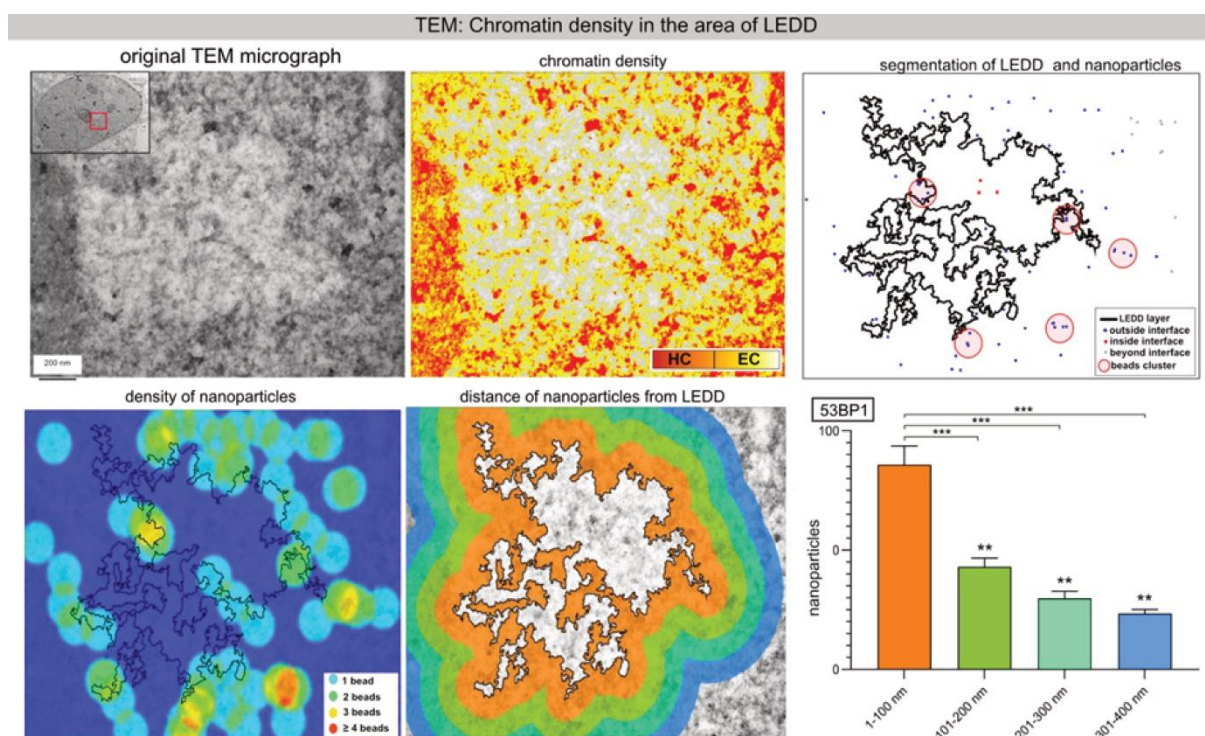


Figure 5: Automatic classification and segmentation of DNA density and the nanoparticles around LEDDs using HALO software. Reprinted after modification from Automated Image Analysis of Transmission Electron Micrographs: Nanoscale Evaluation of Radiation-Induced DNA Damage in the Context of Chromatin.' By Abd Al-razaq, Isermann, et al., 2023. , *Cells*. 12(20):2427. LicenseCC: BY 4.0

The automated analysis of the nanoparticles related to the DNA repair factors in chromatin ultrastructure permit to classification of specific DNA damage patterns after exposure to different radiation qualities.

In this research paper, I sectioned the samples (fibroblasts exposed to high-LET carbon ions or low-LET photons) for TEM experiments and used the nanoparticle

labelling technique to visualize the specific DDR proteins (53BP1, pKu70, pKu80, DNA-PKcs). The labelled sections were analysed via TEM focusing on the nuclei and investigated for radiation-induced DNA damage within the chromatin ultrastructure. Subsequently, I performed automated analysis of transmission electron micrographs (HALO™ software, IndicaLabs) to explore the spatiotemporal dynamics of DNA repair and chromatin remodelling. Chromatin densities were defined by grayscale levels and the localisation of nanoparticles was automatically classified and categorized into euchromatin or heterochromatin. Automated analysis of nanoparticles related to DNA repair factors in the chromatin ultrastructure permits the characterization of specific DNA damage patterns after exposure to different radiation qualities. Moreover, I conducted the statistical analysis of the data and prepared the figures for the publication. Additionally, I have written the material and method part and contributed to editing the other parts of the research paper.

3.4 Immunomodulatory Effects of Histone Variant H2A.J in Ionizing Radiation Dermatitis

3.4.1 Summary of publication 4

This study focuses on the role of H2A.J in radiation dermatitis, further exploring its role in radiation-induced premature senescence and SASP.

For this study, two groups of mice (C57bl/6N) Wild type (WT) and H2A.J^{-/-} were exposed to moderate (1x 2Gy, 5x 2Gy, full body IR) and high doses (\leq 20Gy, dorsal skinfold IR).

Following high-dose radiation exposure, the irradiated skin was examined macroscopically for skin lesions daily for two weeks. After 2 weeks, dorsal skin samples were collected for microscopic analysis. The skin samples were analysed for various parameters including DDR, senescence induction and proliferative capacity along with H2A.J expression in WT mice. Fluorescence techniques like immunohistochemistry and immunofluorescence was used as well as electron microscopy.

RNA sequencing was performed on dorsal skin samples to study transcriptome changes following high-dose IR, FACS was performed to investigate immune cell infiltration, and RT-PCR was performed to examine gene expression in non-irradiated WT versus KO skin samples.

Epidermal keratinocytes in WT skin samples showed time and dose dependent H2A.J accumulation following IR exposure. The irradiated KO skin displayed more inflammatory reactions, higher epidermal thickness, and progressive hair follicle loss compared to WT skin (figure 6a).

More pronounced radiation-induced senescence was observed following moderate and high doses in keratinocyte populations in KO skin, with severe damage observed in hair follicle stem cells (HFSCs) leading to follicular atrophy.

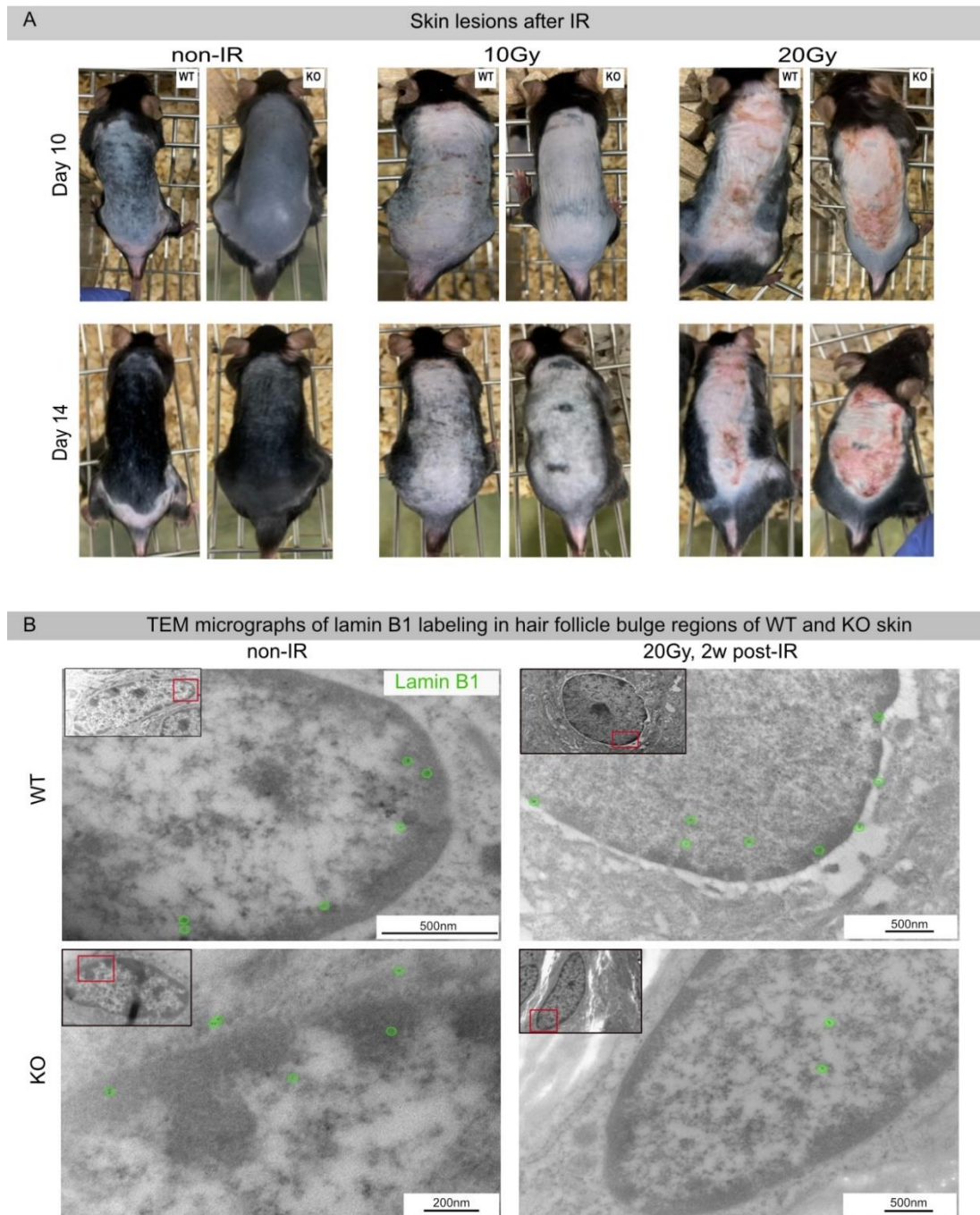


Figure 6 (a) Photographic representation of WT and KO post 20 Gy radiation exposure, (b) TEM micrographic representation of lamin B1 in WT and KO dorsal skin samples post 20 Gy radiation exposure. Reprinted after modification from 'Immunomodulatory Effects of Histone Variant H2A.J in Ionizing Radiation Dermatitis.' By Tewary et al., 2024. *IJROBP*, Volume 118, Issue 3, Pages 801-816, ISSN 0360-3016. LicenseCC:

The transcriptomic analysis showed increased radiation-induced senescence in irradiated KO skin following high-dose IR (figure 6b), along with an increased expression of SASP factors.

While flow cytometry analysis showed increased immune cell infiltration in both WT and KO irradiated skin samples, specific chemokine-mediated recruitment of neutrophils signalling was observed only in irradiated KO skin. Microscopic analysis showed hyper-proliferation, disturbed differentiation, and cornification of keratinocytes due to increased skin damage in irradiated H2A.J-KO mice skin, along with dysregulation of the transcription factor JunB.

In conclusion, the absence of H2A.J was linked with higher senescence induction, alteration of SASP expression, and heightened inflammatory skin reflection. Therefore, the H2A.J gene expression may play an essential role in keratinocyte immune behaviour as well as an important part in induction of the inflammatory response during radiation dermatitis.

My contribution to this research paper includes preparing skin tissue for TEM experiments and analyzing these skin samples by nanoparticle labelling techniques to visualize lamin B1. Moreover, I assisted in preparing the skin irradiation, in establishing the skin lesion scoring system and in the RT-PCR experiments. Beyond the lab work, I conducted the statistical analysis of the data and prepared the figures for publication. Also, I have contributed to writing the material and method part and in editing the other parts of the research.

4. Discussion

This study provides a comprehensive epigenetic insight into the role of the H2A.J histone variant in response to ionizing radiation, using WI-38 cells and H2A.J knockout mice. The *in-vitro* investigations showed that the involvement of H2A.J enhances resistance to irradiation-induced senescence and apoptosis by significant chromatin remodelling and transcriptional changes, particularly affecting SASP genes. Moreover, the *in-vivo* studies showed that the H2A.J absence magnifies the radiation-induced damage and inflammatory responses in the mice, which was reflected in severe skin reactions, increased epidermal thickness, hair follicle loss, and elevated senescence gene expression, coupled with heightened immune cell infiltration and irregular keratinocyte differentiation. On the other hand, advanced imaging tools and techniques such as TEM and AI provided insights into DNA damage patterns, caused by high-LET IR and about the disturbance in nuclear morphology and cytoplasmic organelles during the process of irradiation-induced senescence including chromatin fragment ejection and cGAS-STING activation.

The first study was conducted *in-vitro*, using WI-38 cells with different levels of H2A.J (NT, KD, and OE) expression. The results revealed that H2A.J enhanced the resistance to radiation-induced senescence, and global changes in chromatin conformation especially affecting the SASP genes when H2A.J is overexpressed. In another study, the radiation-induced cells showed disruptions in both nuclear and cytoplasmic organelles, especially in the nuclear morphology. Loss of laminB1 in the progression of senescence disrupted the nuclear envelope, which led to ejecting chromatin fragments into the cytoplasm.

On the other hand, it was found that the high-LET IR induces LEDDs in the nucleus of fibroblast. In this study, automated methodology was developed using TEM micrographs to analyse precisely these LEDDs boundaries and understand their dynamics. In addition, the *in-vivo* study used knockout (KO) and wild type (WT) mice to examine the role of H2A.J in radiation-induced senescence and dermatitis. Following radiation, KO mice exhibited more skin reactions, hair follicle loss, more immune cell infiltration, and higher senescence gene expression (as JunB and SASP genes) than WT mice. The absence of H2A.J showed higher senescence and higher proliferation in irradiated keratinocytes in the progression of radiation dermatitis.

4.1 H2A.J overexpression affects chromatin architecture

Histone variants significantly influence nucleosome functions, offering varied DNA packaging, stability, post-translational modifications, and interactions with chromatin components (Borg et al., 2021). Incorporation of H2A.J, distinct from canonical H2A, directly influences nucleosome structure and stability (Mangelinck et al., 2020). Unlike canonical histones, which are allocated uniformly during replication, variant-containing nucleosomes are inserted generally at specific sites. H2A.J replaces canonical H2A during radiation-induced senescence, throughout the entire nucleus (Isermann et al., 2020). Accurate H2A.J integration at DDR-related chromatin sites is essential for specific chromatin organization and for keeping heterochromatin-euchromatin borders. Overexpression of H2A.J in irradiated fibroblasts disrupts chromatin structure, impairing SAHF and DNA-SCARS formation, and changes the epigenetic state of senescence. In senescent cells, H2A.J integration into chromatin is related to global loss of canonical histones, especially linker histone H1, which plays an essential function in nucleosome arrangement and heterochromatin formation (Funayama et al., 2006).

The arrangement of nucleosomes throughout the genome plays a pivotal role in regulating chromatin accessibility via various mechanisms, including alteration of transcription factor (TF) binding by adjusting steric hindrance (Giles & Taberlay, 2019). Open and closed chromatin structure, as measured by ATAC-seq, reflects different functional situations of chromatin organization (Yan et al., 2020). Our studies indicate that modifications in senescence-associated chromatin organisations (SAHF and DNA-SCARS) influence the physical binding of transcription factors to chromatin. In addition, the ATAC-seq analysis revealed the involvement of AP-1 transcription factors, particularly JUN, FOS, and ATF families, in controlling the epigenomic pathway of radiation-induced senescence. The structured arrangement of TF networks confirms the role of AP-1 as the prime coordinator in arranging transcriptional programs, which takes place via communication with local vs. migrating TFs during the progress of senescence (Martínez-Zamudio et al., 2020). Fibroblasts with normal H2A.J expression showed modifications in open chromatin, which create accessibility for TFs in radiation-induced senescence, emphasizing their role in timely senescence accomplishment. Conversely, H2A.J suppression and overexpression influenced the formation of these chromatin accessibility sites, potentially affecting transcription profiles, flexibility, and fate of senescent cells.

In anticancer interventions like radiotherapy, senescence is induced in both healthy and cancer cells due to genotoxic stress (Jo et al., 2023). This results in a stable cell cycle arrest and activation of SASP, which contributes to pausing cell proliferation and preventing additional genomic instability. Recent work of our lab suggests that H2A.J gradually becomes integrated into chromatin following exposure to IR.

The genome-wide assessment of chromatin accessibility through techniques like ATAC-seq highlights the pivotal role of the histone variant H2A.J in senescence. After

combining ATAC-seq with RNA-seq datasets, it became evident that changes associated with H2A.J in chromatin accessibility are closely linked to alterations in the expression profiles of inflammatory genes.

Using WI-38 fibroblasts, where the H2A.J gene is either knocked down or overexpressed, we gained insights into how H2A.J influences chromatin conformation, the binding of transcription factors, and the expression of pro-inflammatory factors following exposure to IR. However, it is worth noting that fibroblasts are relatively radio-resistant. Therefore, these observations do not fully represent the radiation responses observed in diverse cell populations within complex normal tissues. For this reason, we continued experiments using an *in-vivo* model of H2A.J knockout mice to investigate the functional significance of H2A.J in the radiation response within the context of tissue homeostasis.

4.2 Cells lose nuclear integrity during radiation-induced senescence

Our studies gained valuable insights into the consequences of exposure to high doses of radiation on cellular processes and nuclear organization. It is known that the 3D organization of the genome into chromatin within the nucleus is particularly important for regulation of gene expression and cellular functions (Eriksson & Stigbrand, 2010). This 3D organization controls connections between the nuclear lamina and heterochromatin, which maintains the chromatin structure and the solidity of the nuclear envelope (Jiao et al., 2022). Interactions of genome organization with cellular biological processes are complex and have implications for various biological phenomena involving aging and cancer (Jiao et al., 2022).

High doses of radiation can cause severe DNA damage in cells. These damages can lead to several scenarios such as senescence, apoptosis, and necrosis (Eriksson &

Stigbrand, 2010; Jiao et al., 2022). Lamin B1 degrades throughout cellular senescence causing chromatin restructuring and nucleus blebbing in cytoplasm (Eriksson & Stigbrand, 2010).

Some mitotic problems can occur in the cells after IR exposure when cells prematurely or incorrectly enter mitosis, usually because of malfunctional cell cycle checkpoints (Matellán & Monje-Casas, 2020). Such mitotic problems cause abnormal separation of the chromosomes and sister chromatids, which leads to a generation of huge cells with irregular nuclear characteristics, multiple nuclei, and micronuclei (Potapova & Gorbsky, 2017). The generation of this type of giant nuclei may start a disturbance in the peripheral position of envelope-connected heterochromatin domains, which influences the long-term chromatin organization.

Recent research highlighted the critical role of lamina related to heterochromatin domains in preserving the structural and functional integrity of nuclear construction (Erenpreisa et al., 2021). Increased nuclear fragility can cause nuclear blebbing and chromatin organization, which leads to various pathologies, including cancer and age-related diseases (Gauthier & Comaills, 2021). Our investigations proved the complicated connection between chromatin restructuring in nuclei affected by lamin disruption and the deterioration of the nuclear envelope, which is responsible for releasing small chromatin fragments into the cytoplasm (Adams et al., 2013b). These results confirm the theory that CCFs initiate and maintain the immune signalling pathway. This leads to the production of SASP factors by stimulating the cGAS-STING-dependent pathway, which takes place during IR-induced senescence (Dou et al., 2017; Glück et al., 2017).

We investigated the characteristics of premature senescence induced by IR in human WI-38 fibroblasts, the most widely used cell culture model for studying cellular

senescence. Our studies have previously investigated human WI-38 fibroblasts and showed the production of SASP factors, like pro-inflammatory cytokines such as interleukin-6 (IL6), interleukin-8 (IL8), granulocyte-macrophage colony-stimulating factor (GM-CSF), and monocyte chemoattractant protein-1 (MCP1), due to IR-induced senescence (Isermann et al., 2020). These results were confirmed by estimating the expression of these genes using reverse-transcriptase quantitative polymerase-chain-reaction (RT-qPCR) which showed a significant increase following IR exposure. Using high-magnification tools and methods such as TEM and serial block-face scanning electron microscopy (SBF-SEM), we were able to restructure the 3D architecture of the nucleus. Furthermore, these methods gave us visual details about the formation, separation, and movement as well as the ejection of nuclear blebs into the cytoplasm of the senescent cells, something that cannot be achieved using light microscopy.

The decline of lamin B1 expression during senescence affects the entire structure- and mechanical properties of the cell's nucleus, triggering the separation of A-type and B-type lamins. This leads to an irregular mesh layer in the nuclear envelope (Shah et al., 2013). The lamin fibres start to separate in some regions causing bulges or transient breaks in the nuclear envelope. The mechanical forces are called 'pushing' forces produced by cytoskeletal filamentous proteins and 'pulling' forces generated by chromatin-lamin interactions, which can be responsible for the nanoscale invaginations of the nuclear envelope and large-scale chromatin rearrangements (Funkhouser et al., 2013). In addition, problems in the nucleo-cytoplasmic movements play an important role in senescence. Such as diminished response to external stress due to disrupted transmission of nuclear signals, which is one of the characteristics of senescence. (Koufi et al., 2023; Park et al., 2021). Such problems suggest that nuclear nanotubes are participating in intracellular transport to help defeat the nucleo-cytoplasmic barrier.

Studies on lamin-related diseases, such as lamin A mutations that trigger a premature ageing syndrome (Hutchinson–Gilford progeria), confirm the crucial role of nuclear integrity in chromatin construction (Gonzalo et al., 2017). Disorganization of lamin-interacting structures profoundly affects genome organization, playing a vital role in gene regulation.

Recent molecular research showed that these nuclear invaginations contain cytoskeletal filaments connected to the nuclear membrane proposing a direct link between the “nuclei interior and cell-cell or cell-extracellular matrix (ECM) adhesion sites” (Jorgens et al., 2017). Therefore, the ECM may control cell or tissue functions by transmitting signals between receptors, cytoskeleton, and nuclear matrix. Similarly, nanotubes may also be essential for 3D architectural components that connect the nucleus, cytoskeleton, and ECM in cellular communication. Moreover, nanotubes may be important for the construction and composition of the nuclear envelope in response to micro-environmental stimuli. Nevertheless, further investigation is required to analyze the exact pathophysiological role of nucleo-cytoplasmic nanotubes in lamin-disturbed nuclei.

4.3 Radiation-induced DNA damage patterns and chromatin alterations revealed by automated image software

The biological effect of IR exposure depends on how ionization and excitation events are distributed in space and time, which can cause diverse forms of complex DNA damage. Radiation-induced DNA damage is not solely based on physical characteristics of DNA or of the IR but also on several factors including the interaction between 3D chromatin arrangement, radiation trace structure, and dynamic reactions of chromatin (Baiocco et al., 2022). These interactions seriously influence some important biological processes related to DNA repair mechanisms.

Our study used the HALO™ software for automated image analysis of different TEM micrographs, which helped in investigating the radiation-induced DNA damage patterns in the nucleus at the nanometre level. Furthermore, the HALO™ software permitted the reliable detection of nanoparticles within the micrographs. This provided exact details of the DNA damage distribution in relation to chromatin architecture.

Robust analysis and very fast processing facilitated the comprehensive evaluation of radiation damage, which, in turn, enabled qualitative and quantitative evaluation of diverse DNA damage patterns induced by different radiation qualities. This methodology provides a deeper and very detailed level of understanding of the effects of radiation on the DNA structure and architecture. The use of specialized image analysis software allowed us to precisely quantify nanoparticles of varying sizes, shapes, densities, and their distances from one another as well as their exact positions within micrographs. To characterise the density of chromatin, it was classified according to its greyscale features using a cutting-edge machine-learning algorithm integrated within the tissue classifier module. The different levels of density were categorized into euchromatic or heterochromatic regions, thereby enhancing the objectivity of our analysis. In addition, these algorithms helped identification of nuclear segmentation across entire sections, thereby eliminating the need to manually outline the areas of interest. This not only streamlined the process, but also increased the reliability of the analysis. The use of the HALO™ spatial tool allowed us to determine the distribution patterns of the nanoparticles, their proximity, and their relative spatial distribution within nuclear domains. The spatial density heatmap analysis was used to estimate the average nanoparticle density within a specified distance of segmented LEDDs, and proximity histograms were automatically produced. In general, this AI-based image analysis approach offers numerous advantages. Most significantly, it

provides a much more accurate analysis of radiation-induced DNA damage patterns and accelerates data generation.

4.3.1 TEM analysis of DNA damage patterns: insights in the labelling of repairing sites after high-LET IR exposure

When creating samples for TEM analysis, cells go through different treatment stages i.e. fixation, dehydration, resin embedding, and sectioning for analysis (Petralia & Wang, 2021). Due to low atomic numbers in living organisms, the samples of biological origin are usually stained using heavy metal salts (such as osmium, lead citrate or uranyl acetate) to enhance contrast (Jones, 2016). Each salt has a specific binding site in biological samples. All samples must be prepared in the same way to enable meaningful comparisons. The sections undergo an immuno-labelling method of antigen detection on section surfaces, which uses gold nanoparticle-antibody conjugates for detecting the DNA damage sites on the sections. The high-level of electron density of gold in comparison to the proteins provides electron distraction and more contrast. However, the quantity of nanoparticles cannot refer in direct way to the number of antigens due to various influencing (physical, chemical, and biological) factors; usually they exert influence during the sample preparation (Petralia & Wang, 2021). In this research, gold nanoparticles with singular binding sites for the primary antibody were used for labelling, which allowed us to make a direct comparison of concentrations across various subcellular locations; however, despite the relative immune-gold labelling, it may not provide exact antigen concentrations.

TEM analysis revealed clear variations in DNA damage patterns and repair capabilities following exposure to low-LET versus high-LET IR. Automated image analysis of human fibroblasts at different time points following exposure to these different IR types allowed the effective assessment of nanoparticle-labelled DNA repair proteins within

the context of chromatin ultrastructure. The results from these studies give direct evidence that high-LET IR creates clustered DNA damage along particle paths during highly focused ionization events, resulting in wide chromatin remodelling characterized by LEDDs. DSBs become increasingly detectable along these particle paths during chromatin remodelling, particularly at the margin between euchromatin and heterochromatin. These findings propose that high-LET IR, unlike low-LET IR, leads to more pronounced chromatin unfolding in the form of LEDDs, which is crucial for repairing clustered DNA damage. The elevation of the number of DSBs in the heterochromatin areas and the sustained chromatin de-condensation in form of LEDDs in the nucleus refers to the struggle of the cells in the DNA damage repairing process and retrieving the original chromatin structure after high-LET IR.

4.4 Effects of histone variant H2A.J in IR dermatitis

Previous research showed the accumulation of the histone variant H2A.J in epidermal keratinocytes with persistent DNA damage in *ex-vivo* irradiated human skin samples (Contrepolis et al., 2017; Rube et al., 2021). Our *in-vivo* research used two groups of mice to explore the role of H2A.J in radiation dermatitis: wild-type (WT) and H2A.J knockout (KO) mice.

Following IR exposure, the evaluation of 53BP1 foci in keratinocytes revealed no significant differences in the DSB repair capacity in KO versus WT skin. This suggests that H2A.J has no direct influence on the acute DDR, which is in line with previous *in vitro* studies. Immunobiological staining of WT skin confirmed previous findings, namely a time- and dose-dependent H2A.J accumulation in epidermal keratinocytes after IR exposure (Hippchen et al., 2022). Unexpectedly, H2A.J-KO skin showed significantly stronger radiation-induced responses than WT skin at both microscopic

and macroscopic levels, which was associated with increased skin irritation and hair follicle loss. Analysis of senescence markers demonstrated higher levels of radiation-induced senescence in epidermal keratinocytes of H2A.J KO compared to WT skin, especially following high IR doses. Differences in senescence induction were found among the various keratinocyte populations. In particular, HFSCs were severely impaired in the bulge regions of H2A.J-KO skin after high-dose IR. This led to almost complete degeneration of the hair follicles. Premature senescence may disturb the niche of stem/progenitor cells, which is crucial for controlling the regeneration of hair follicles through intricate communication with papilla-specific paracrine factors (Matsumura et al., 2016; Rahmani et al., 2020). Our research indicates that keratinocytes in the bulge zone gradually experience premature senescence after exposure to high-dose IR, interfering with and disrupting the intricate dynamics within the stem cell niche. As a result, the CD34+ HFSCs eventually undergo significant decline, clearly more pronounced in irradiated H2A.J KO skin compared to WT skin. Apart from the IR-induced immune-mediated shrinkage of hair follicles, our transcriptome analysis of both WT and H2A.J KO skin demonstrated a reduction of multiple hair keratins.

An increased secretion of multiple pro-inflammatory SASP factors in irradiated H2A.J KO skin in comparison to WT skin was shown by transcriptome sequencing. This is aligned with the heightened senescence levels in H2A.J KO keratinocytes. Complex IR-induced DNA damage resulted in elevated levels of the transcription factor JunB, leading to extreme proliferation and irregular differentiation of keratinocytes, which ultimately resulted in a noticeable epidermal hyperplasia.

According to our results, H2A.J does not influence the acute response to radiation-induced DSBs. However, augmented levels of DNA damage-induced senescence

were noticed in the case of H2A.J KO skin, accompanied by an increase in SASP signalling. This in turn leads to increased infiltration of neutrophils into the skin, thereby exacerbating the inflammatory stage of radiation-induced skin reactions. After exposure to IR, the skin reacts in a specific temporal pattern. In addition, the acute inflammatory phase depends on factors such as radiation quality, total dose, dose rate and fractionation (Singh et al., 2016). IR disrupts the efficient balance of cell renewal and differentiation in the epidermis, which then severely affects the various cellular components of the skin (Liao et al., 2017). IR also influences the differentiation of keratinocytes, thereby disturbing the interactions between keratinocytes and immune cells. The increased induction of senescence in keratinocytes and their impaired differentiation trigger their increased release of mediators that promote skin inflammation (Nguyen & Soulika, 2019). Previously, studies with mouse models have already demonstrated an increase in senescence induction within epidermal keratinocytes and HFSCs after exposure to high dose radiation (McCart et al., 2017). Collectively, our finding highlights the potentially significant role of H2A.J in initiating and promoting the inflammatory state of IR-induced responses by mediating cytokine/chemokine crosstalk.

Earlier research revealed that irradiated epidermal keratinocytes (damaged or senescent) prompt expression of acute phase proinflammatory cytokines and chemokines that attract cells. This orchestrates the time and place of recruitment of immune cells to inflamed skin regions (Nguyen & Soulika, 2019). The findings of our research aligned with earlier studies, representing the significant roles of IL-1 and IL-6 as the most important cytokines in the skin's response to IR exposure (Paldor et al., 2022). Neutrophils play a vital role in the primary defence mechanism of innate immunity and use different mechanisms to fight against invading microbes such as

phagocytosis, intracellular breakdown, granule release, and the creation of neutrophil extracellular traps upon pathogen detection (SuYingjun & RichmondAnn, 2015). On the other hand, they can be involved in tissue lesions by boosting the inflammatory response and by releasing toxic effectors such as myeloperoxidase (MPO), which exacerbates tissue toxicities in the skin (An et al., 2022). The FACS analysis detected various immune cell populations infiltrating the skin following irradiation. Nevertheless, the neutrophilic immune response observed notable distinctions between irradiated WT and H2A.J KO skin.

It was found that the pathogenesis of psoriasis is caused mainly by the involvement of IL-17-expressing $\gamma\delta$ T-cells and the transcription factor $\text{I}\kappa\text{B}\zeta$ (Müller et al., 2018). The hyperactivation of this pathway induces the upregulation of pro-inflammatory genes such as Cxcl2 and Cxcl5, associated with neutrophils transferring to sites of inflammation (Liao et al., 2017; Ulrich et al., 2010). Our research implies that paralleling with psoriasis, the overactivation of pro-inflammatory pathways in irradiated H2A.J KO skin leads to increased keratinocyte proliferation and infiltration of immune cells.

Previous research has shown that H2A.J plays a significant role in the progression of senescence, cellular ageing, and that it is also involved in the IR-induced DNA damage response (Isermann et al., 2020). Numerous studies have investigated the various effects of H2A.J, however, the precise molecular mechanism underlying its effect on the nuclear structure and gene expression in response to IR-induced DNA damage remains elusive.

5. Conclusion and outlooks

In summary, our studies present a set of data suggesting that the incorporation of histone variant H2A.J modulates the global chromatin structure, leading to changes in

the DNA accessibility to TFs, thereby altering gene expression of multiple SASP factors following IR exposure. Moreover, our results show that by overexpressing H2A.J, the cells can overcome radiation-induced senescence and thus become radioresistant. Further investigations are required to identify, which signalling pathways may promote potential oncogenic transformation.

A better understanding of cellular senescence may open new therapeutic perspectives regarding age-related diseases. Through volume electron microscopy with the 3D reconstruction of senescent cells, both structure and function, in connection with the pathological organization of senescent cells, can be better characterized.

DNA lesions caused by IR exposure with different LET can threaten cell survival and/or may affect both genomic and epigenomic integrity. Additional insights into this coordination between DNA repair and restoration of chromatin structure will lead to a better understanding of genomic and epigenomic maintenance in response to DNA damage distributed differently in the cell nucleus. Automated image analysis of TEM micrographs reduces the time required and enables comparative analysis of DSB distributions at the nanoscale after exposure to different IR qualities. The generation of this TEM data may help in the functional characterization of different radiation qualities in the field of radiation therapy.

6. References

- Abd Al-razaq, M. A., Freyter, B. M., Isermann, A., Tewary, G., Mangelinck, A., Mann, C., & Rube, C. E. (2023). Role of Histone Variant H2A.J in Fine-Tuning Chromatin Organization for the Establishment of Ionizing Radiation-Induced Senescence. *Cells*, *12*(6), 916. <https://doi.org/10.3390/CELLS12060916/S1>
- Abd Al-razaq, M. A., Isermann, A., Hecht, M., & Rube, C. E. (2023). Automated Image Analysis of Transmission Electron Micrographs: Nanoscale Evaluation of Radiation-Induced DNA Damage in the Context of Chromatin. *Cells* 2023, Vol. 12, Page 2427, *12*(20), 2427. <https://doi.org/10.3390/CELLS12202427>
- Adam, M., Robert, F., Larochele, M., & Gaudreau, L. (2001). H2A.Z is required for global chromatin integrity and for recruitment of RNA polymerase II under specific conditions. *Molecular and Cellular Biology*, *21*(18), 6270–6279. <https://doi.org/10.1128/MCB.21.18.6270-6279.2001>
- Adams, P. D., Ivanov, A., Pawlikowski, J., Manoharan, I., Tuyn, J. Van, Nelson, D. M., Singh Rai, T., Shah, P. P., Hewitt, G., Korolchuk, V. I., Passos, J. F., Wu, H., & Berger, S. L. (2013a). Lysosome-mediated processing of chromatin in senescence. *Journal of Cell Biology*, *202*(1), 129–143. <https://doi.org/10.1083/JCB.201212110/VIDEO-1>
- Adams, P. D., Ivanov, A., Pawlikowski, J., Manoharan, I., Tuyn, J. Van, Nelson, D. M., Singh Rai, T., Shah, P. P., Hewitt, G., Korolchuk, V. I., Passos, J. F., Wu, H., & Berger, S. L. (2013b). Lysosome-mediated processing of chromatin in senescence. *Journal of Cell Biology*, *202*(1), 129–143. <https://doi.org/10.1083/JCB.201212110/VIDEO-1>
- Ahnesorg, P., Smith, P., & Jackson, S. P. (2006). XLF interacts with the XRCC4-DNA Ligase IV complex to promote DNA nonhomologous end-joining. *Cell*, *124*(2), 301–313. <https://doi.org/10.1016/J.CELL.2005.12.031/ATTACHMENT/6F09BA19-7550-465F-AADB-9E4CF52723CA/MMC1.PDF>
- An, S. Y., Kim, H. S., Kim, S. Y., Van, S. Y., Kim, H. J., Lee, J. H., Han, S. W., Kwon, I. K., Lee, C. K., Do, S. H., & Hwang, Y. S. (2022). Keratin-mediated hair growth and its underlying biological mechanism. *Communications Biology* 2022 5:1, *5*(1), 1–17. <https://doi.org/10.1038/s42003-022-04232-9>
- Baiocco, G., Bartzsch, S., Conte, V., Friedrich, T., Jakob, B., Tartas, A., Villagrasa, C., & Prise, K. M. (2022). A matter of space: how the spatial heterogeneity in energy deposition determines the biological outcome of radiation exposure. *Radiation and Environmental Biophysics* 2022 61:4, *61*(4), 545–559. <https://doi.org/10.1007/S00411-022-00989-Z>
- Berger, S. L. (2002). Histone modifications in transcriptional regulation. *Current Opinion in Genetics & Development*, *12*(2), 142–148. [https://doi.org/10.1016/S0959-437X\(02\)00279-4](https://doi.org/10.1016/S0959-437X(02)00279-4)
- Borg, M., Jiang, D., & Berger, F. (2021). Histone variants take center stage in shaping the epigenome. *Current Opinion in Plant Biology*, *61*, 101991. <https://doi.org/10.1016/J.PBI.2020.101991>
- Buenrostro, J. D., Wu, B., Chang, H. Y., & Greenleaf, W. J. (2015). ATAC-seq: A Method for Assaying Chromatin Accessibility Genome-Wide. *Current Protocols in Molecular Biology / Edited by Frederick M. Ausubel ... [et Al.]*, *109*, 21.29.1. <https://doi.org/10.1002/0471142727.MB2129S109>

- Contrepois, K., Coudereau, C., Benayoun, B. A., Schuler, N., Roux, P. F., Bischof, O., Courbeyrette, R., Carvalho, C., Thuret, J. Y., Ma, Z., Derbois, C., Nevers, M. C., Volland, H., Redon, C. E., Bonner, W. M., Deleuze, J. F., Wiel, C., Bernard, D., Snyder, M. P., ... Mann, C. (2017). Histone variant H2A.J accumulates in senescent cells and promotes inflammatory gene expression. *Nature Communications*, 8. <https://doi.org/10.1038/NCOMMS14995>
- Cornen, S., Guille, A., Adélaïde, J., Addou-Klouche, L., Finetti, P., Saade, M. R., Manai, M., Carbuccia, N., Bekhouche, I., Letessier, A., Raynaud, S., Charafe-Jauffret, E., Jacquemier, J., Spicuglia, S., De The, H., Viens, P., Bertucci, F., Birnbaum, D., & Chaffanet, M. (2014). Candidate Luminal B Breast Cancer Genes Identified by Genome, Gene Expression and DNA Methylation Profiling. *PLoS ONE*, 9(1). <https://doi.org/10.1371/JOURNAL.PONE.0081843>
- Criscione, S. W., Teo, Y. V., & Neretti, N. (2016). The chromatin landscape of cellular senescence. *Trends in Genetics : TIG*, 32(11), 751. <https://doi.org/10.1016/J.TIG.2016.09.005>
- de Souza, N. (2009). Light microscopy at the limit. *Nature Cell Biology* 2009 11:1, 11(1), S22–S22. <https://doi.org/10.1038/ncb1954>
- Dou, Z., Ghosh, K., Vizioli, M. G., Zhu, J., Sen, P., Wangensteen, K. J., Simithy, J., Lan, Y., Lin, Y., Zhou, Z., Capell, B. C., Xu, C., Xu, M., Kieckhafer, J. E., Jiang, T., Shoshkes-Carmel, M., Al Tanim, K. M. A., Barber, G. N., Seykora, J. T., Berger, S. L. (2017). Cytoplasmic chromatin triggers inflammation in senescence and cancer. *Nature* 2017 550:7676, 550(7676), 402–406. <https://doi.org/10.1038/nature24050>
- Erenpreisa, J., Krigerts, J., Salmina, K., Gerashchenko, B. I., Freivalds, T., Kurg, R., Winter, R., Krufczik, M., Zayakin, P., Hausmann, M., & Giuliani, A. (2021). Heterochromatin Networks: Topology, Dynamics, and Function (a Working Hypothesis). *Cells*, 10(7). <https://doi.org/10.3390/CELLS10071582>
- Eriksson, D., & Stigbrand, T. (2010). Radiation-induced cell death mechanisms. *Tumor Biology*, 31(4), 363–372. <https://doi.org/10.1007/S13277-010-0042-8/FIGURES/4>
- Espada, J., Ballestar, E., Fraga, M. F., Villar-Garea, A., Juarranz, A., Stockert, J. C., Robertson, K. D., Fuks, F., & Esteller, M. (2004). Human DNA methyltransferase 1 is required for maintenance of the histone H3 modification pattern. *The Journal of Biological Chemistry*, 279(35), 37175–37184. <https://doi.org/10.1074/JBC.M404842200>
- Esteller, M. (2007). Cancer epigenomics: DNA methylomes and histone-modification maps. *Nature Reviews Genetics* 2007 8:4, 8(4), 286–298. <https://doi.org/10.1038/nrg2005>
- Freyter, B. M., Abd Al-Razaq, M. A., Isermann, A., Dietz, A., Azimzadeh, O., Hekking, L., Gomolka, M., & Rube, C. E. (2022). Nuclear Fragility in Radiation-Induced Senescence: Blebs and Tubes Visualized by 3D Electron Microscopy. *Cells*, 11(2), 273. <https://doi.org/10.3390/CELLS11020273/S1>
- Friedberg, E. C., Walker, G. C., Siede, W., Wood, R. D., Schultz, R. A., & Ellenberger, T. (2005). DNA Repair and Mutagenesis. *DNA Repair and Mutagenesis*. <https://doi.org/10.1128/9781555816704>
- Friedberg, E., Walker, G., Siede, W., & Wood, R. (2005). *DNA repair and mutagenesis*. <https://books.google.com/books?hl=en&lr=&id=VAKsBAAAQBAJ&oi=fnd&pg=PT41&ots=2vFmUUKZWWh&sig=4SQ-AgtKSHq1QnT5qOUcgp5DkwU>

- Funayama, R., Saito, M., Tanobe, H., & Ishikawa, F. (2006). Loss of linker histone H1 in cellular senescence. *The Journal of Cell Biology*, 175(6), 869–880. <https://doi.org/10.1083/JCB.200604005>
- Funkhouser, C. M., Sknepnek, R., Shimi, T., Goldman, A. E., Goldman, R. D., & De La Cruz, M. O. (2013). Mechanical model of blebbing in nuclear lamin meshworks. *Proceedings of the National Academy of Sciences of the United States of America*, 110(9), 3248–3253. https://doi.org/10.1073/PNAS.1300215110/SUPPL_FILE/PNAS.201300215SI.PDF
- Gasser, S. M. (2002). Visualizing Chromatin Dynamics in Interphase Nuclei. *Science*, 296(5572), 1412–1416. <https://doi.org/10.1126/SCIENCE.1067703>
- Gauthier, B. R., & Comaills, V. (2021). Nuclear Envelope Integrity in Health and Disease: Consequences on Genome Instability and Inflammation. *International Journal of Molecular Sciences* 2021, Vol. 22, Page 7281, 22(14), 7281. <https://doi.org/10.3390/IJMS22147281>
- Geacintov, N. E., & Broyde, S. (2017). Repair-Resistant DNA Lesions. *Chemical Research in Toxicology*, 30(8), 1517. <https://doi.org/10.1021/ACS.CHEMRESTOX.7B00128>
- Giglia-Mari, G., Zotter, A., & Vermeulen, W. (2011). DNA Damage Response. *Cold Spring Harbor Perspectives in Biology*, 3(1), a000745. <https://doi.org/10.1101/CSHPERSPECT.A000745>
- Giles, K. A., & Taberlay, P. C. (2019). The Role of Nucleosomes in Epigenetic Gene Regulation. *Clinical Epigenetics*, 87–117. https://doi.org/10.1007/978-981-13-8958-0_4
- Glück, S., Guey, B., Gulen, M. F., Wolter, K., Kang, T. W., Schmacke, N. A., Bridgeman, A., Rehwinkel, J., Zender, L., & Ablasser, A. (2017). Innate immune sensing of cytosolic chromatin fragments through cGAS promotes senescence. *Nature Cell Biology*, 19(9), 1061–1070. <https://doi.org/10.1038/NCB3586>
- Gonzalo, S., Kreienkamp, R., & Askjaer, P. (2017). Hutchinson-Gilford Progeria Syndrome: A premature aging disease caused by LMNA gene mutations. *Ageing Research Reviews*, 33, 18–29. <https://doi.org/10.1016/J.ARR.2016.06.007>
- Goryshin, I. Y., & Reznikoff, W. S. (1998). Tn5 in vitro transposition. *The Journal of Biological Chemistry*, 273(13), 7367–7374. <https://doi.org/10.1074/JBC.273.13.7367>
- Grandi, F. C., Modi, H., Kampman, L., & Corces, M. R. (2022). Chromatin accessibility profiling by ATAC-seq. *Nature Protocols* 2022 17:6, 17(6), 1518–1552. <https://doi.org/10.1038/s41596-022-00692-9>
- Grove, G. W., & Zweidler, A. (1984). Regulation of nucleosomal core histone variant levels in differentiating murine erythroleukemia cells. *Biochemistry*, 23(19), 4436–4443. <https://doi.org/10.1021/BI00314A030>
- Grunstein, M. (1992). Histones as regulators of genes. *Scientific American*, 267(4). <https://doi.org/10.1038/scientificamerican1092-68>
- Haque, A., Engel, J., Teichmann, S. A., & Lönnberg, T. (2017). A practical guide to single-cell RNA-sequencing for biomedical research and clinical applications. *Genome Medicine*, 9(1), 1–12. <https://doi.org/10.1186/S13073-017-0467-4/TABLES/1>

- Henner, W. D., Grunberg, S. M., & Haseltine, W. A. (1982). Sites and structure of gamma radiation-induced DNA strand breaks. *Journal of Biological Chemistry*, 257(19), 11750–11754. [https://doi.org/10.1016/S0021-9258\(18\)33827-4](https://doi.org/10.1016/S0021-9258(18)33827-4)
- Henner, W. D., Rodriguez, L. O., Hecht, S. M., & Haseltine, W. A. (1983). gamma Ray induced deoxyribonucleic acid strand breaks. 3' Glycolate termini. *Journal of Biological Chemistry*, 258(2), 711–713. [https://doi.org/10.1016/S0021-9258\(18\)33104-1](https://doi.org/10.1016/S0021-9258(18)33104-1)
- Hippchen, Y., Tewary, G., Jung, D., Schmal, Z., Meessen, S., Palm, J., & Rube, C. E. (2022). Cultured Human Foreskin as a Model System for Evaluating Ionizing Radiation-Induced Skin Injury. *International Journal of Molecular Sciences*, 23(17), 9830. <https://doi.org/10.3390/IJMS23179830/S1>
- Huang, W., Hickson, L. T. J., Eirin, A., Kirkland, J. L., & Lerman, L. O. (2022). Cellular senescence: the good, the bad and the unknown. *Nature Reviews. Nephrology*, 18(10), 611. <https://doi.org/10.1038/S41581-022-00601-Z>
- Isermann, A., Mann, C., & Rube, C. E. (2020). Histone variant H2A.J marks persistent DNA damage and triggers the secretory phenotype in radiation-induced senescence. *International Journal of Molecular Sciences*, 21(23), 1–20. <https://doi.org/10.3390/ijms21239130>
- Jackson, S. P. (2009). The DNA-damage response: new molecular insights and new approaches to cancer therapy. *Biochemical Society Transactions*, 37(3), 483–494. <https://doi.org/10.1042/BST0370483>
- Jackson, S. P., & Bartek, J. (n.d.). *The DNA-damage response in human biology and disease*. <https://doi.org/10.1038/nature08467>
- Jiao, Y., Cao, F., & Liu, H. (2022). Radiation-induced Cell Death and Its Mechanisms. *Health Physics*, 123(5), 376. <https://doi.org/10.1097/HP.0000000000001601>
- Jo, H., Shim, K., & Jeoung, D. (2023). The Potential of Senescence as a Target for Developing Anticancer Therapy. *International Journal of Molecular Sciences 2023, Vol. 24, Page 3436*, 24(4), 3436. <https://doi.org/10.3390/IJMS24043436>
- Jones, J. C. R. (2016). Pre- and post-embedding immunogold labeling of tissue sections. *Methods in Molecular Biology*, 1474, 291–307. https://doi.org/10.1007/978-1-4939-6352-2_19
- Jorgens, D. M., Inman, J. L., Wojcik, M., Robertson, C., Palsdottir, H., Tsai, W. T., Huang, H., Bruni-Cardoso, A., López, C. S., Bissell, M. J., Xu, K., & Auer, M. (2017). Deep nuclear invaginations are linked to cytoskeletal filaments - integrated bioimaging of epithelial cells in 3D culture. *Journal of Cell Science*, 130(1), 177–189. <https://doi.org/10.1242/JCS.190967/259025/AM/DEEP-NUCLEAR-INVAGINATIONS-LINKED-TO-CYTOSKELETAL>
- Jun, J. II, & Lau, L. F. (2010). The matricellular protein CCN1 induces fibroblast senescence and restricts fibrosis in cutaneous wound healing. *Nature Cell Biology 2010 12:7*, 12(7), 676–685. <https://doi.org/10.1038/ncb2070>
- Kamakaka, R. T., & Biggins, S. (2005). Histone variants: deviants? *Genes & Development*, 19(3), 295–316. <https://doi.org/10.1101/GAD.1272805>
- Kastan, M. B., & Bartek, J. (2004). Cell-cycle checkpoints and cancer. *Nature 2004 432:7015*, 432(7015), 316–323. <https://doi.org/10.1038/nature03097>

- Khoury, A., Achinger-Kawecka, J., Bert, S. A., Smith, G. C., French, H. J., Luu, P. L., Peters, T. J., Du, Q., Parry, A. J., Valdes-Mora, F., Taberlay, P. C., Stirzaker, C., Statham, A. L., & Clark, S. J. (2020). Constitutively bound CTCF sites maintain 3D chromatin architecture and long-range epigenetically regulated domains. *Nature Communications* 2020 11:1, 11(1), 1–13. <https://doi.org/10.1038/s41467-019-13753-7>
- Kohl, H. (2016). Transmission Electron Microscopy. *Encyclopedia of Nanotechnology*, 4218–4233. https://doi.org/10.1007/978-94-017-9780-1_383
- Koufi, F. D., Neri, I., Ramazzotti, G., Rusciano, I., Mongiorgi, S., Marvi, M. V., Fazio, A., Shin, M., Kosodo, Y., Cani, I., Giorgio, E., Cortelli, P., Manzoli, L., & Ratti, S. (2023). Lamin B1 as a key modulator of the developing and aging brain. *Frontiers in Cellular Neuroscience*, 17, 1263310. <https://doi.org/10.3389/FNCEL.2023.1263310/BIBTEX>
- Kumari, R., & Jat, P. (2021). Mechanisms of Cellular Senescence: Cell Cycle Arrest and Senescence Associated Secretory Phenotype. *Frontiers in Cell and Developmental Biology*, 9, 645593. <https://doi.org/10.3389/FCELL.2021.645593/BIBTEX>
- Lennartsson, A., & Ekwall, K. (2009). Histone modification patterns and epigenetic codes. *Biochimica et Biophysica Acta (BBA) - General Subjects*, 1790(9), 863–868. <https://doi.org/10.1016/J.BBAGEN.2008.12.006>
- Liao, W., Hei, T. K., & Cheng, S. K. (2017). Radiation-induced dermatitis is mediated by IL17-expressing $\gamma\delta$ T cells. *Radiation Research*, 187(4), 454–464. <https://doi.org/10.1667/RR007CC.1>
- Lieber, M. R. (2008). The mechanism of human nonhomologous DNA End joining. *Journal of Biological Chemistry*, 283(1), 1–5. <https://doi.org/10.1074/JBC.R700039200/ATTACHMENT/BA22986F-3920-4A82-908E-F5E4916DE51D/MMC1.PDF>
- Lieber, M. R., Gu, J., Lu, H., Shimazaki, N., & Tsai, A. G. (2014). Nonhomologous DNA end joining (NHEJ) and chromosomal translocations in humans. *Subcellular Biochemistry*, 50, 279–296. https://doi.org/10.1007/978-90-481-3471-7_14/COVER
- Li, G., & Widom, J. (2004). Nucleosomes facilitate their own invasion. *Nature Structural & Molecular Biology* 2004 11:8, 11(8), 763–769. <https://doi.org/10.1038/nsmb801>
- Lindahl, T., & Barnes, D. E. (2000). Repair of Endogenous DNA Damage. *Cold Spring Harbor Symposia on Quantitative Biology*, 65, 127–134. <https://doi.org/10.1101/SQB.2000.65.127>
- Liu, Y., Masson, J. Y., Shah, R., O'Regan, P., & West, S. C. (2004). RAD51C is required for Holliday junction processing in mammalian cells. *Science (New York, N.Y.)*, 303(5655), 243–246. <https://doi.org/10.1126/SCIENCE.1093037>
- Lopes-Paciencia, S., Saint-Germain, E., Rowell, M. C., Ruiz, A. F., Kalegari, P., & Ferbeyre, G. (2019). The senescence-associated secretory phenotype and its regulation. *Cytokine*, 117, 15–22. <https://doi.org/10.1016/J.CYTO.2019.01.013>
- Luger, K., & Richmond, T. J. (1998). DNA binding within the nucleosome core. *Current Opinion in Structural Biology*, 8(1), 33–40. [https://doi.org/10.1016/S0959-440X\(98\)80007-9](https://doi.org/10.1016/S0959-440X(98)80007-9)
- Mangelinck, A., Coudereau, C., Courbeyrette, R., Ourarhni, K., Hamiche, A., Redon, C., Bonner, W. M., Dijk, E. van, Derbois, C., Olasso, R., Deleuze, J.-F., Fenaille, F., Rube, C. E., Thuret, J.-Y., & Mann, C. (2020). The H2A.J histone variant contributes to Interferon-Stimulated Gene expression in

- senescence by its weak interaction with H1 and the derepression of repeated DNA sequences. *BioRxiv*, 2020.10.29.361204. <https://doi.org/10.1101/2020.10.29.361204>
- Martínez-Zamudio, R. I., Roux, P. F., de Freitas, J. A. N. L. F., Robinson, L., Doré, G., Sun, B., Belenki, D., Milanovic, M., Herbig, U., Schmitt, C. A., Gil, J., & Bischof, O. (2020). AP-1 imprints a reversible transcriptional programme of senescent cells. *Nature Cell Biology* 2020 22:7, 22(7), 842–855. <https://doi.org/10.1038/s41556-020-0529-5>
- Matellán, L., & Monje-Casas, F. (2020). Regulation of Mitotic Exit by Cell Cycle Checkpoints: Lessons From *Saccharomyces cerevisiae*. *Genes* 2020, Vol. 11, Page 195, 11(2), 195. <https://doi.org/10.3390/GENES11020195>
- Matsuoka, S., Ballif, B. A., Smogorzewska, A., McDonald, E. R., Hurov, K. E., Luo, J., Bakalarski, C. E., Zhao, Z., Solimini, N., Lerenthal, Y., Shiloh, Y., Gygi, S. P., & Elledge, S. J. (2007). ATM and ATR substrate analysis reveals extensive protein networks responsive to DNA damage. *Science (New York, N.Y.)*, 316(5828), 1160–1166. <https://doi.org/10.1126/SCIENCE.1140321>
- Ma, Y., Lu, H., Tippin, B., Goodman, M. F., Shimazaki, N., Koiwai, O., Hsieh, C. L., Schwarz, K., & Lieber, M. R. (2004). A biochemically defined system for mammalian nonhomologous DNA end joining. *Molecular Cell*, 16(5), 701–713. <https://doi.org/10.1016/J.MOLCEL.2004.11.017/ATTACHMENT/1F113981-363C-4101-905D-ED6CEE0CF645/MMC1.PDF>
- Ma, Y., Pannicke, U., Lu, H., Niewolik, D., Schwarz, K., & Lieber, M. R. (2005). The DNA-dependent protein kinase catalytic subunit phosphorylation sites in human artemis. *Journal of Biological Chemistry*, 280(40), 33839–33846. <https://doi.org/10.1074/JBC.M507113200/ATTACHMENT/D6CF3D0A-41D2-4430-BD3F-B1FD0149EE79/MMC1.PDF>
- Maze, I., Noh, K. M., Soshnev, A. A., & Allis, C. D. (2014). Every amino acid matters: essential contributions of histone variants to mammalian development and disease. *Nature Reviews. Genetics*, 15(4), 259. <https://doi.org/10.1038/NRG3673>
- McHugh, D., & Gil, J. (2018). Senescence and aging: Causes, consequences, and therapeutic avenues. *The Journal of Cell Biology*, 217(1), 65. <https://doi.org/10.1083/JCB.201708092>
- Moore, J. K., & Haber, J. E. (1996). Cell cycle and genetic requirements of two pathways of nonhomologous end-joining repair of double-strand breaks in *Saccharomyces cerevisiae*. *Molecular and Cellular Biology*, 16(5), 2164–2173. <https://doi.org/10.1128/MCB.16.5.2164>
- Müller, A., Hennig, A., Lorscheid, S., Grondona, P., Schulze-Osthoff, K., Hailfinger, S., & Kramer, D. (2018). IκBζ is a key transcriptional regulator of IL-36–driven psoriasis-related gene expression in Keratinocytes. *Proceedings of the National Academy of Sciences of the United States of America*, 115(40), 10088–10093. https://doi.org/10.1073/PNAS.1801377115/SUPPL_FILE/PNAS.1801377115.SAPP.PDF
- Murray, V., Hardie, M. E., & Gautam, S. D. (2019). Comparison of Different Methods to Determine the DNA Sequence Preference of Ionising Radiation-Induced DNA Damage. *Genes* 2020, Vol. 11, Page 8, 11(1), 8. <https://doi.org/10.3390/GENES11010008>
- Muthurajan, U. M., Park, Y. J., Edayathumangalam, R. S., Suto, R. K., Chakravarthy, S., Dyer, P. N., & Luger, K. (2003). Structure and dynamics of nucleosomal DNA. *Biopolymers*, 68(4), 547–556. <https://doi.org/10.1002/BIP.10317>

- Narita, M., Núñez, S., Heard, E., Narita, M., Lin, A. W., Hearn, S. A., Spector, D. L., Hannon, G. J., & Lowe, S. W. (2003). Rb-mediated heterochromatin formation and silencing of E2F target genes during cellular senescence. *Cell*, *113*(6), 703–716. [https://doi.org/10.1016/S0092-8674\(03\)00401-X](https://doi.org/10.1016/S0092-8674(03)00401-X)
- Nguyen, A. V., & Soulika, A. M. (2019). The Dynamics of the Skin's Immune System. *International Journal of Molecular Sciences* 2019, Vol. 20, Page 1811, *20*(8), 1811. <https://doi.org/10.3390/IJMS20081811>
- Paldor, M., Levkovitch-Siany, O., Eidelstein, D., Adar, R., Enk, C. D., Marmary, Y., Elgavish, S., Nevo, Y., Benyamini, H., Plaschkes, I., Klein, S., Mali, A., Rose-John, S., Peled, A., Galun, E., & Axelrod, J. H. (2022). Single-cell transcriptomics reveals a senescence-associated IL -6/ CCR6 axis driving radiodermatitis. *EMBO Molecular Medicine*, *14*(8), 15653. https://doi.org/10.15252/EMMM.202115653/SUPPL_FILE/EMMM202115653-SUP-0005-SDATAEV2FIG.XLSX
- Park, J. H., Ryu, S. J., Kim, B. J., Cho, H. J., Park, C. H., Choi, H. J. C., Jang, E. J., Yang, E. J., Hwang, J. A., Woo, S. H., Lee, J. H., Park, J. H., Choi, K. M., Kwon, Y. Y., Lee, C. K., Park, J. T., Cho, S. C., Lee, Y. I., Lee, S. B., ... Park, S. C. (2021). Disruption of nucleocytoplasmic trafficking as a cellular senescence driver. *Experimental & Molecular Medicine* 2021 *53*:6, *53*(6), 1092–1108. <https://doi.org/10.1038/s12276-021-00643-6>
- Pennings, S., Meersseman, G., & Bradbury, E. M. (1991). Mobility of positioned nucleosomes on 5 S rDNA. *Journal of Molecular Biology*, *220*(1), 101–110. [https://doi.org/10.1016/0022-2836\(91\)90384-I](https://doi.org/10.1016/0022-2836(91)90384-I)
- Petralia, R. S., & Wang, Y. X. (2021). Review of Post-embedding Immunogold Methods for the Study of Neuronal Structures. *Frontiers in Neuroanatomy*, *15*, 763427. <https://doi.org/10.3389/FNANA.2021.763427/BIBTEX>
- Potapova, T., & Gorbsky, G. J. (2017). The Consequences of Chromosome Segregation Errors in Mitosis and Meiosis. *Biology* 2017, Vol. 6, Page 12, *6*(1), 12. <https://doi.org/10.3390/BIOLOGY6010012>
- Ratnakumar, K., Duarte, L. F., LeRoy, G., Hasson, D., Smeets, D., Vardabasso, C., Bönisch, C., Zeng, T., Xiang, B., Zhang, D. Y., Li, H., Wang, X., Hake, S. B., Schermelleh, L., Garcia, B. A., & Bernstein, E. (2012). ATRX-mediated chromatin association of histone variant macroH2A1 regulates α -globin expression. *Genes & Development*, *26*(5), 433. <https://doi.org/10.1101/GAD.179416.111>
- Redon, C. E., Schmal, Z., Tewary, G., Mangelinck, A., Courbeyrette, R., Thuret, J. Y., Aladjem, M. I., Bonner, W. M., Rube, C. E., & Mann, C. (2021). Histone Variant H2A.J Is Enriched in Luminal Epithelial Gland Cells. *Genes*, *12*(11). <https://doi.org/10.3390/GENES12111665>
- Rodgers, K., & Mcvey, M. (2016). Error-Prone Repair of DNA Double-Strand Breaks. *Journal of Cellular Physiology*, *231*(1), 15–24. <https://doi.org/10.1002/JCP.25053>
- Rube, C. E., Bäumer, C., Schuler, N., Isermann, A., Schmal, Z., Glanemann, M., Mann, C., & Scherthan, H. (2021). Human skin aging is associated with increased expression of the histone variant H2A.J in the epidermis. *Npj Aging and Mechanisms of Disease*, *7*(1). <https://doi.org/10.1038/S41514-021-00060-Z>
- Saleh, T., Tyutynuk-Massey, L., Cudjoe, E. K., Idowu, M. O., Landry, J. W., & Gewirtz, D. A. (2018). Non-cell autonomous effects of the senescence-associated secretory phenotype in cancer

- therapy. *Frontiers in Oncology*, 8(MAY), 319340.
<https://doi.org/10.3389/FONC.2018.00164/BIBTEX>
- Sanders, S. L., Portoso, M., Mata, J., Bähler, J., Allshire, R. C., & Kouzarides, T. (2004). Methylation of histone H4 lysine 20 controls recruitment of Crb2 to sites of DNA damage. *Cell*, 119(5), 603–614.
<https://doi.org/10.1016/J.CELL.2004.11.009>
- Seligson, D. B., Horvath, S., Shi, T., Yu, H., Tze, S., Grunstein, M., & Kurdistani, S. K. (2005). Global histone modification patterns predict risk of prostate cancer recurrence. *Nature*, 435(7046), 1262–1266. <https://doi.org/10.1038/NATURE03672>
- Shah, P. P., Donahue, G., Otte, G. L., Capell, B. C., Nelson, D. M., Cao, K., Aggarwala, V., Cruickshanks, H. A., Rai, T. S., McBryan, T., Gregory, B. D., Adams, P. D., & Berger, S. L. (2013). Lamin B1 depletion in senescent cells triggers large-scale changes in gene expression and the chromatin landscape. *Genes & Development*, 27(16), 1787–1799.
<https://doi.org/10.1101/GAD.223834.113>
- Shah, P. P., Zheng, X., Epshtein, A., Carey, J. N., Bishop, D. K., & Klein, H. L. (2010). Swi2/Snf2-Related Translocases Prevent Accumulation of Toxic Rad51 Complexes during Mitotic Growth. *Molecular Cell*, 39(6), 862–872. <https://doi.org/10.1016/J.MOLCEL.2010.08.028>
- Singh, M., Alavi, A., Wong, R., & Akita, S. (2016). Radiodermatitis: A Review of Our Current Understanding. *American Journal of Clinical Dermatology*, 17(3), 277–292.
<https://doi.org/10.1007/S40257-016-0186-4/TABLES/4>
- Smith, J., Mun Tho, L., Xu, N., & A. Gillespie, D. (2010). The ATM-Chk2 and ATR-Chk1 pathways in DNA damage signaling and cancer. *Advances in Cancer Research*, 108(C), 73–112.
<https://doi.org/10.1016/B978-0-12-380888-2.00003-0>
- Sonoda, E., Hohegger, H., Saberi, A., Taniguchi, Y., & Takeda, S. (2006). Differential usage of non-homologous end-joining and homologous recombination in double strand break repair. *DNA Repair*, 5(9–10), 1021–1029. <https://doi.org/10.1016/J.DNAREP.2006.05.022>
- Stark, R., Grzelak, M., & Hadfield, J. (2019). RNA sequencing: the teenage years. *Nature Reviews Genetics* 20:11, 20(11), 631–656. <https://doi.org/10.1038/s41576-019-0150-2>
- Steiner, F. A., & Henikoff, S. (2015). Diversity in the organization of centromeric chromatin. *Current Opinion in Genetics & Development*, 31, 28–35. <https://doi.org/10.1016/J.GDE.2015.03.010>
- Strahl, B. D., & Allis, C. D. (2000a). The language of covalent histone modifications. *Nature*, 403(6765), 41–45. <https://doi.org/10.1038/47412>
- Strahl, B. D., & Allis, C. D. (2000b). The language of covalent histone modifications. *Nature*, 403(6765), 41–45. <https://doi.org/10.1038/47412>
- Sung, P., & Klein, H. (2006). Mechanism of homologous recombination: mediators and helicases take on regulatory functions. *Nature Reviews Molecular Cell Biology* 2006 7:10, 7(10), 739–750.
<https://doi.org/10.1038/nrm2008>
- Suto, R. K., Clarkson, M. J., Tremethick, D. J., & Luger, K. (2000). Crystal structure of a nucleosome core particle containing the variant histone H2A.Z. *Nature Structural Biology* 2000 7:12, 7(12), 1121–1124. <https://doi.org/10.1038/81971>

- SuYingjun, & RichmondAnn. (2015). Chemokine Regulation of Neutrophil Infiltration of Skin Wounds. *Https://Home.Liebertpub.Com/Wound*, 4(11), 631–640. <https://doi.org/10.1089/WOUND.2014.0559>
- Talbert, P. B., & Henikoff, S. (2010). Histone variants — ancient wrap artists of the epigenome. *Nature Reviews Molecular Cell Biology* 2010 11:4, 11(4), 264–275. <https://doi.org/10.1038/nrm2861>
- Talbert, P. B., & Henikoff, S. (2016). Histone variants on the move: substrates for chromatin dynamics. *Nature Reviews Molecular Cell Biology* 2016 18:2, 18(2), 115–126. <https://doi.org/10.1038/nrm.2016.148>
- Tanaka, H., Sato, S., Koyama, M., Kujirai, T., & Kurumizaka, H. (2020). Biochemical and structural analyses of the nucleosome containing human histone H2A.J. *Journal of Biochemistry*, 167(4), 419–427. <https://doi.org/10.1093/JB/MVZ109>
- Tewary, G., Freyter, B., Al-razaq, M. A., Auerbach, H., Laschke, M. W., Kübelbeck, T., Kolb, A., Mangelinck, A., Mann, C., Kramer, D., & Rube, C. E. (2024). Immunomodulatory Effects of Histone Variant H2A.J in Ionizing Radiation Dermatitis. *International Journal of Radiation Oncology*Biological*Physics*, 118(3), 801–816. <https://doi.org/10.1016/J.IJROBP.2023.09.022>
- Ulrich, D., Ulrich, F., Unglaub, F., Piatkowski, A., & Pallua, N. (2010). Matrix metalloproteinases and tissue inhibitors of metalloproteinases in patients with different types of scars and keloids. *Journal of Plastic, Reconstructive & Aesthetic Surgery*, 63(6), 1015–1021. <https://doi.org/10.1016/J.BJPS.2009.04.021>
- Valieva, Y., Ivanova, E., Fayzullin, A., Kurkov, A., & Igrunkova, A. (2022). Senescence-Associated β -Galactosidase Detection in Pathology. *Diagnostics*, 12(10). <https://doi.org/10.3390/DIAGNOSTICS12102309>
- Wang, X., Ghareeb, W. M., Lu, X., Huang, Y., Huang, S., & Chi, P. (2019). Coexpression network analysis linked H2AFJ to chemoradiation resistance in colorectal cancer. *Journal of Cellular Biochemistry*, 120(6), 10351–10362. <https://doi.org/10.1002/JCB.28319>
- Woodcock, C. L. (2006). Chromatin architecture. *Current Opinion in Structural Biology*, 16(2), 213–220. <https://doi.org/10.1016/J.SBI.2006.02.005>
- Woodcock, C. L., & Dimitrov, S. (2001). Higher-order structure of chromatin and chromosomes. *Current Opinion in Genetics & Development*, 11(2), 130–135. [https://doi.org/10.1016/S0959-437X\(00\)00169-6](https://doi.org/10.1016/S0959-437X(00)00169-6)
- Yan, F., Powell, D. R., Curtis, D. J., & Wong, N. C. (2020). From reads to insight: a hitchhiker’s guide to ATAC-seq data analysis. *Genome Biology* 2020 21:1, 21(1), 1–16. <https://doi.org/10.1186/S13059-020-1929-3>
- Yao, J., Weremowicz, S., Feng, B., Gentleman, R. C., Marks, J. R., Gelman, R., Brennan, C., & Polyak, K. (2006). Combined cDNA Array Comparative Genomic Hybridization and Serial Analysis of Gene Expression Analysis of Breast Tumor Progression. *Cancer Research*, 66(8), 4065–4078. <https://doi.org/10.1158/0008-5472.CAN-05-4083>
- Yelagandula, R., Stroud, H., Holec, S., Zhou, K., Feng, S., Zhong, X., Muthurajan, U. M., Nie, X., Kawashima, T., Groth, M., Luger, K., Jacobsen, S. E., & Berger, F. (2014). The histone variant H2A.W defines heterochromatin and promotes chromatin condensation in Arabidopsis. *Cell*, 158(1), 98–109. <https://doi.org/10.1016/J.CELL.2014.06.006>

7. Appendix

7.1 Publication 1

Table 1 Literature information of publication I

Title	Role of Histone Variant H2A.J in Fine-Tuning Chromatin Organization for the Establishment of Ionizing Radiation-Induced Senescence
Authors and Affiliations	Mutaz A. Abd Al-razaq ^{1†} , Benjamin M. Freyter ^{1†} , Anna Isermann ¹ , Gargi Tewary ¹ , Adèle Mangelinck ² , Carl Mann ² and Claudia E. Rube ^{1*} ¹ Department of Radiation Oncology, Saarland University Medical Center, 66421 Homburg/Saar, Germany ² Institute for Integrative Biology of the Cell (I2BC), CEA, CNRS, Université Paris-Saclay, 91198 Gif-sur-Yvette, France * Author to whom correspondence should be addressed. † These authors contributed equally to this work.
Journal	Cells
Impact factor	7.666
Publication status	Published
Year of publication	2023
Type of article	Research article
Volume	12
Pages	916-935
DOI:	https://doi.org/10.3390/cells12060916

Article

Role of Histone Variant H2A.J in Fine-Tuning Chromatin Organization for the Establishment of Ionizing Radiation-Induced Senescence

Mutaz A. Abd Al-razaq ^{1,†} , Benjamin M. Freyter ^{1,†}, Anna Isermann ¹, Gargi Tewary ¹ , Adèle Mangelinck ², Carl Mann ²  and Claudia E. Rübe ^{1,*} 

¹ Department of Radiation Oncology, Saarland University Medical Center, 66421 Homburg/Saar, Germany

² Institute for Integrative Biology of the Cell (I2BC), CEA, CNRS, Université Paris-Saclay, 91198 Gif-sur-Yvette, France

* Correspondence: claudia.ruebe@uks.eu

† These authors contributed equally to this work.

Abstract: Purpose: Radiation-induced senescence is characterized by profound changes in chromatin organization with the formation of *Senescence-Associated-Heterochromatin-Foci* (SAHF) and *DNA-Segments-with-Chromatin-Alterations-Reinforcing-Senescence* (DNA-SCARS). Importantly, senescent cells also secrete complex combinations of pro-inflammatory factors, referred as *Senescence-Associated-Secretory-Phenotype* (SASP). Here, we analyzed the epigenetic mechanism of histone variant H2A.J in establishing radiation-induced senescence. Experimental Design: Primary and genetically-modified lung fibroblasts with down- or up-regulated H2A.J expression were exposed to ionizing radiation and were analyzed for the formation of SAHF and DNA-SCARS by immunofluorescence microscopy. Dynamic changes in chromatin organization and accessibility, transcription factor recruitment, and transcriptome signatures were mapped by ATAC-seq and RNA-seq analysis. The secretion of SASP factors and potential bystander effects were analyzed by ELISA and RT-PCR. Lung tissue of mice exposed to different doses were analyzed by the digital image analysis of H2A.J-immunohistochemistry. Results: Differential incorporation of H2A.J has profound effects on higher-order chromatin organization and on establishing the epigenetic state of senescence. Integrative analyses of ATAC-seq and RNA-seq datasets indicate that H2A.J-associated changes in chromatin accessibility of regulatory regions decisively modulates transcription factor recruitment and inflammatory gene expression, resulting in an altered SASP secretome. In lung parenchyma, pneumocytes show dose-dependent H2A.J expression in response to radiation-induced DNA damage, therefore contributing to pro-inflammatory tissue reactions. Conclusions: The fine-tuned incorporation of H2A.J defines the epigenetic landscape for driving the senescence programme in response to radiation-induced DNA damage. Deregulated H2A.J deposition affects chromatin remodeling, transcription factor recruitment, and the pro-inflammatory secretome. Our findings provide new mechanistic insights into DNA-damage triggered epigenetic mechanisms governing the biological processes of radiation-induced injury.

Keywords: histone variant H2A.J; ionizing radiation; radiation-induced senescence; Senescence-Associated Heterochromatin Foci (SAHF); DNA-Segments with Chromatin Alterations Reinforcing Senescence (DNA-SCARS); Senescence-Associated Secretory Phenotype (SASP)



Citation: Abd Al-razaq, M.A.; Freyter, B.M.; Isermann, A.; Tewary, G.; Mangelinck, A.; Mann, C.; Rübe, C.E. Role of Histone Variant H2A.J in Fine-Tuning Chromatin Organization for the Establishment of Ionizing Radiation-Induced Senescence. *Cells* **2023**, *12*, 916. <https://doi.org/10.3390/cells12060916>

Academic Editor: Isabella Saggio

Received: 16 February 2023

Revised: 7 March 2023

Accepted: 13 March 2023

Published: 16 March 2023



Copyright: © 2023 by the authors. Licensee MDPI, Basel, Switzerland. This article is an open access article distributed under the terms and conditions of the Creative Commons Attribution (CC BY) license (<https://creativecommons.org/licenses/by/4.0/>).

1. Introduction

Senescence is a stress response that limits the replication of damaged or aged cells by implementing permanent cell cycle arrest [1]. Senescent cells display profound changes in nuclear and chromatin organization with the formation of Senescence-Associated Heterochromatin Foci (SAHF). Importantly, senescent cells also secrete complex combinations of predominantly pro-inflammatory factors, collectively referred to as Senescence-Associated

Secretory Phenotype (SASP) [2]. Replicative senescence was first discovered in cultured fibroblasts, where prolonged passaging and replicative exhaustion led to growth arrest due to critically short telomeres [3]. Premature senescence can also be triggered in response to intrinsic and extrinsic stressors, such as acute DNA damage after exposure to ionizing radiation (IR). Double-strand breaks (DSBs) represent the most deleterious type of radiation-induced DNA lesions [4]. Subsequent DNA damage response (DDR) mechanisms coordinate cellular DSB repair activities by recruiting multiple repair proteins such as 53BP1 to break sites, forming radiation-induced DNA repair foci [5]. Severe or irreparable DNA damage can cause persistent 53BP1-foci, detectable for days and weeks after their formation, suggesting that DSB repair mechanisms are incapable of resolving these lesions [6]. In senescent cells, persistent DNA damage with accumulated DDR proteins, such as promyelocytic leukaemia (PML) nuclear bodies [7], form nuclear substructures called DNA-Segments with Chromatin Alterations Reinforcing Senescence (DNA-SCARS) [8,9]. Together with SAHF, DNA-SCARS are one of the most prevalent nuclear markers of cellular senescence.

Senescent cells undergo dramatic alterations to their chromatin landscape that affect genome accessibility and transcriptional programs [10]. Nucleosomes, the basic units of chromatin, are composed of 147 base pairs of DNA wrapped around the histone octamer core. The octamer contains four heterodimers of the canonical histone proteins H2A, H2B, H3, and H4. Linker histone H1 binds to internucleosomal DNA to stabilize higher-order chromatin structures and participate together with non-histone proteins in the dynamic regulation of chromatin compaction. Canonical histones are the most abundant in nucleosomes and are synthesized and incorporated in a replication-dependent manner. Additional diversity is provided by the incorporation of histone variants into chromatin [11]. Histone variants can profoundly change chromatin properties by modulating nucleosome stability and function, which may affect their interaction with chromatin remodelers and modifiers [12]. The deposition of canonical histones is coupled to DNA synthesis, whereby canonical histones assemble into nucleosomes behind replication forks. The incorporation of histone variants, in contrast, occurs throughout the cell-cycle and is independent of DNA synthesis. In non-cycling senescent cells, canonical histone production declines and variant histones tend to accumulate. The incorporation of histone variants can have direct effects on the structure and stability of nucleosomes, thereby modifying the accessibility of DNA and regulating the whole transcriptome by the dynamic binding of transcription factors (TF). Deciphering the underlying regulatory networks that balance the open/active and closed/repressed chromatin states and thereby modulating gene expression programmes may help to identify key regulators of radiation-induced senescence.

Previous studies have shown that histone variant H2A.J accumulates in human fibroblasts *in vitro* as well as in murine and human skin tissue *in vivo* during replicative, oncogene- and radiation-induced senescence, and affects the inflammatory gene expression of senescent cells [13–15]. In this study, we focused on the epigenetic mechanisms of H2A.J modifying transcription programmes during radiation-induced senescence progression and describe how these deregulations eventually contribute to radiosensitivity or radioresistance.

2. Materials and Methods

2.1. Cultured Lung Fibroblasts

Primary WI-38 human lung fibroblasts were obtained from ATCC. Immortalized WI-38 hTERT-fibroblasts were genetically modified to prepare H2A.J knock-down (H2A.J-KD) or knock-in (H2A.J-KI), canonical H2A knock-in (H2A-KI) and non-targeted controls (NT) as described previously [13]. Stable fibroblast populations were cultured at 5% O₂ and 5% CO₂ in MEM (Invitrogen, Karlsruhe, Germany) with 10% fetal bovine serum, 1 mM sodium pyruvate, 2 mM L-glutamine, 0.1 mM non-essential amino acids, and 1% penicillin/streptomycin. A total of 1 µg/mL doxycycline was added to medium for 1 week prior to IR to express shRNA sequences or to overexpress H2A or H2A.J. The cells

were homogeneously grown on coverslips and used for experiments once 90% confluency was achieved.

2.2. Radiation Exposure of Cultured Lung Fibroblasts

Cells were exposed to IR using the linear accelerator Artiste™ (Siemens, Munich, Germany) (6-MV photons; dose-rate 2 Gy/min). Cells were analyzed at different time-points (5 h, 24 h, 1 w and 2 w post-IR) following IR (20 Gy) and compared to non-irradiated controls (non-IR).

2.3. Immunofluorescence Microscopy (IFM) Analysis

Cells were fixed with 4% paraformaldehyde and permeabilised with 0.5% Triton X-100, washed with 0.1% Tween®-20, and incubated overnight with a primary antibody (anti-H2A.J, ActiveMotif, Waterloo, Belgium; anti-53BP1, Bethyl, Montgomery, TX, USA; anti-p21, Abcam, Berlin, Germany; anti-PML, Santa Cruz, CA, USA) followed by Alexa-Fluor®488 or Alexa-Fluor®568 secondary antibody (Invitrogen, Karlsruhe, Germany). Subsequently, cells were mounted in a VECTASHIELD™ mounting medium with 4', 6-diamidino-2-phenylindole (DAPI, Vector Laboratories, Burlingame, CA, USA). Fluorescence images were captured with a Nikon-Eclipse Ni fluorescence-microscope equipped with a Nikon DS-Qi2 camera (Nikon, Düsseldorf, Germany). For evaluating H2A.J-, 53BP1-, SAHF-, and p21-positivity, at least 200 cells were captured for each sample (positive cells in %). For quantifying 53BP1-foci per cell, at least 50 foci and/or 50 cells were analyzed per sample. For the identification of DNA-SCARS, 53BP1/PML co-localization was analyzed in 50 nuclei, and numbers of 53BP1/PML co-localizing foci relative to total 53BP1-foci were expressed in percentages.

2.4. Immunohistochemistry (IHC) Analysis (SA-β-Gal)

Following 5 min fixation with 2% paraformaldehyde and 0.2% glutaraldehyde, cells were incubated with X-Gal staining solution (AppliChem GmbH, Darmstadt, Germany) at 37 °C overnight. After 30 s of methanol incubation, the dried samples were permeabilised with 0.2% Triton X-100 and washed with 1% BSA. Samples were blocked with 4% BSA for 1 h, followed by an overnight incubation with H2A.J primary antibody. Incubation with Dako immunoglobulin/biotinylated secondary antibody (Agilent, Waldbronn, Germany) was followed by Vectastain ABC Peroxidase standard (Vector, Burlingame, CA, USA) and SIGMAFAST™ 3,3'-Diaminobenzidine (Merck, Darmstadt, Germany) incubations, respectively. Samples were finally mounted in Dako Faramount Mounting Medium (Agilent, Waldbronn, Germany).

2.5. RNA-Sequencing (RNA-Seq)

RNA extraction, library preparation, and paired-end (2 × 150 bp, 30 M reads per sample) sequencing using NovaSeq (Illumina, San Diego, CA, USA) were performed by GENEWIZ Germany GmbH (Leipzig, Germany). Subsequently, raw reads were trimmed with Cutadapt (v3.5) to clip low-quality ends from reads that were below a Phred quality score of 20. Additionally, a minimum read length of 50 was set. Data quality was inspected before and after trimming using FastQC (v0.11.3) [16]. Sequences were aligned to the human genome sequence GRC38.p13 [17] using the Burrows-Wheeler Alignment Tool (v0.7.17) [18] and counted with HTSeq (v0.13.5) [19]. Subsequently, a differential expression analysis was performed using DESeq2 (v1.34.0) [20].

2.6. Assay for Transposase-Accessible Chromatin (ATAC-Seq)

WI-38 hTERT-fibroblasts were washed and incubated with 1xDNase (Worthington Biochemical Corp., Lakewood, NJ, USA). Tagmentation, library preparation, and paired-end (2 × 42 bp, 10 M reads per sample) sequencing using NovaSeq500 (Illumina, San Diego, CA, USA) were performed by ActiveMotif (Carlsbad, CA, USA). The obtained sequences were aligned to the human genome sequence GRC38.p13 [17] using BWA (v0.7.12) [18], and PCR duplicates were removed. Next, peaks were called using MACS2 (v2.1.0) [21]

and normalized by random sampling and tag number reduction to the tag number of the smallest sample. Subsequently, overlapping intervals were grouped into merged regions, and differentially accessible sites were identified with DESeq2 (v1.34.0) [20]. Finally, motif analysis for the 2500 regions with the highest accessibility differences was performed using HOMER (v4.11) [22].

2.7. Integrative Analysis of ATAC-Seq and mRNA-Seq Data

Fragments per million mapped fragments were obtained with the `fpm` function of DESeq2 [20] and visualised as bar graphs using GraphPad Prism 9 (GraphPad Software, San Diego, CA, USA). Dot plots visualizing HOMER [22] differential chromatin accessibility analysis for each relevant condition were prepared using the `ggplot2` (v3.3.5) R package. BAM files of appropriate samples were merged using `Bedtools` (v2.23.2) [23] and sorted with `Samtools` (v1.14) [24]. Subsequently, `bedgraph` files were obtained and normalized to RPKM using `bamCoverage` from `deepTools` (v3.4.3) [25] and converted to `BigWig` format with `Bedgraphtobigwig` (v357). Subsequently, tracks were visualized using `Gviz` (v1.38.3) with the support of `biomaRt` (v2.50.3) for gene locations, and `tidyverse` (v1.3.1) R packages, combining expression data, chromatin accessibility, differentially accessible regions obtained with `MACS2` and `DESeq2` (differential accessibility adjusted p value ≤ 0.1), and motif locations from HOMER analysis.

2.8. Enzyme-Linked Immunosorbent Analysis (ELISA)

Conditioned media (CM) were collected from three independent cultures of NT, H2A.J-KD and H2A.J-KI fibroblasts. CM from cultured fibroblasts was collected at 2 weeks after 20 Gy IR compared to non-irradiated fibroblasts. Cell numbers in flasks were determined at the timepoint of the CM collection. CM samples were frozen at -80 °C until analysis. A Multi-Analyte ELISArray™ Kit (Qiagen, Hilden, Germany) was used to screen SASP factors with a standard ELISA plate reader, according to the supplier's protocol.

2.9. Reverse-Transcriptase Quantitative Polymerase-Chain-Reaction (RT-qPCR) analysis

RNA extraction was completed using `TRIzol™` (ThermoFisher Scientific, Darmstadt, Germany) and phenol/chloroform phase separation. A `QuantiTect®` Reverse Transcription Kit (Qiagen, Hilden, Germany) was used for cDNA synthesis and `Advanced Universal SYBR Green Supermix` (Bio-Rad Laboratories GmbH, Feldkirchen, Germany) was used for subsequent quantitative PCR in a `CFX96 Touch Real-Time PCR Detection System` (Bio-Rad Laboratories GmbH), as previously described [14].

2.10. Radiation Schedule and Lung Tissue Sampling in Mice

C57BL/6-N mice (2-month-old) were purchased from Charles River Laboratories (Sulzfeld, Germany) and housed in pathogen-free rooms to minimize infection risks, and supplied with a standard laboratory diet and water ad libitum. For whole-body irradiation (6-MV photons; dose-rate, 2 Gy/min) using an `Artiste™` linear accelerator (Siemens, Munich, Germany), the animals were placed in an 18 cm-diameter Plexiglass cylinder covered by 1.5 cm thick plastic to improve dose homogeneity. Computed-tomography-based three-dimensional dose calculations were made with the `Pinnacle planning system` (Philips Radiation Oncology Systems, Fitchburg, WI, USA). Animals were irradiated with single-doses (10 Gy or 2 Gy) or with fractionated IR (once daily from Monday to Friday: 5×2 Gy, 20×0.1 Gy). At defined time-points after the last IR exposure, mice were anesthetized, perfused, and the lungs were removed, fixed overnight in 4% paraformaldehyde (Sigma-Aldrich Chemie GmbH, Munich, Germany), and processed for further analysis. At least three biological (experimental animals) and three technical (whole lung slices) replicates were examined for each irradiation regimen. The experimental protocol was approved by Medical Sciences Animal Care and Use Committee of Saarland University.

2.11. IFM and IHC Analysis of Lung Tissue Sections

Formalin-fixed tissues were embedded in paraffin and sectioned at 4- μ m thickness. After deparaffinization in xylene and rehydration in decreasing alcohol concentrations, sections were boiled in a citrate buffer (Dako Agilent pathology solutions, Santa Clara, CA, USA) and incubated with Roti-Immunoblock (Carl Roth, Karlsruhe, Germany). For IFM analysis, sections were incubated with primary antibodies (anti-H2A.J, Active Motif, Carlsbad, CA, USA) followed by AlexaFluor-488 secondary antibody (Invitrogen, Karlsruhe, Germany) and mounted in VECTAshield with 4',6-diamidino-2-phenylindole (DAPI; Vector Laboratories, Burlingame, CA, USA). For IHC analysis, sections were incubated with anti-H2A.J antibody followed by biotin-labeled antibodies (Dako, Glostrup, Denmark) and staining was completed by incubation with 3,3'-diaminobenzidine and substrate chromogen. Finally, sections were counterstained with haematoxylin and mounted with Aqueous-Mounting-Medium (Dako, Glostrup, Denmark). For qualitative analysis, H2A.J-positive cells were visualized under the Nikon E600 epifluorescent microscope (Nikon, Düsseldorf, Germany).

2.12. Digital Image Analysis of H2A.J-Immunohistochemistry

Whole digital slide images were obtained from H2A.J-stained lung sections of irradiated (5 \times 2 Gy; 24 h post-IR) and non-irradiated mice using Axioscan 7 (ZEISS, Oberkochen, Germany). In lung parenchyma, 10 representative regions were annotated manually (excluding bronchiolar ducts and blood vessels) using the multiplex IHC module of HALO[®] image analysis software (version 3.4.2986; IndicaLabs, Albuquerque, NM, USA). In these regions of interest (ROI), the brown DAB staining signal for H2A.J was compared to the haematoxylin counterstain for each nucleus, and cells were categorised into no (blue), weak (yellow), moderate (orange) and strong (red) H2A.J-stained nuclei. The percentage of cells was calculated for each staining category in relation to the total cell numbers in ROIs.

2.13. Statistical Analysis

GraphPad Prism (version 9.4.1, GraphPad Software, San Diego, CA, USA) was used to collect and analyse data. Data are presented as the mean of three experiments \pm SEM. One-way analysis of variance (ANOVA) with Dunnett's multiple comparisons test was used for comparison among different groups. A *p* value of <0.05 was considered statistically significant, <0.01 as statistically highly significant, and <0.001 as extremely statistically significant. Significant statistical differences compared to non-irradiated controls (marked by asterisks alone) or between cell lines (asterisks with square brackets) are presented in the figures as * (*p* < 0.05), ** (*p* < 0.01), and *** (*p* < 0.001).

3. Results

3.1. H2A.J Accumulation and Radiation-Induced Senescence

Immortalized fibroblasts with H2A.J knock-down (H2A.J-KD) or knock-in (H2A.J-KI) and canonical H2A knock-in (H2A-KI) were analyzed compared to non-targeted controls (NT). Confluent H2A.J-KD, H2A.J-KI, H2A-KI and NT fibroblasts were irradiated with 20Gy, and H2A.J expression was analyzed at 24 h, 1 w and 2 w post-IR by IFM. For NT fibroblasts, we observed time-dependent increases of pan-nuclear H2A.J staining intensities (Figure 1A, left panel). The quantification of H2A.J+ cells revealed steady increases from \approx 10% in non-irradiated (non-IR) to \approx 80% in irradiated NT (2 w post-IR) (Figure 1A, right panel). While H2A.J-KD fibroblasts showed nearly no staining (\leq 6% H2A.J+ cells), H2A.J-KI fibroblasts revealed an intense pan-nuclear H2A.J staining for all analyzed time-points (90–100% H2A.J+ cells). Non-irradiated H2A-KI fibroblasts displayed slightly higher H2A.J expression levels (\approx 18%) than non-irradiated NT fibroblasts (\approx 10%); however, after IR exposure, the proportion of H2A.J+ cells increased to nearly 80%. Collectively, these findings indicate an effective and functioning cell system to study the pathophysiological role of H2A.J in radiation-induced senescence. The most widely used biomarker for aging cells is senescence-associated β -galactosidase (SA- β -Gal). Double-staining for H2A.J

(nuclear brown signal) and SA- β -Gal (cytoplasmic blue signal) was established to analyze these senescence markers simultaneously (Figure 1B, left panel). SA- β -Gal activity measured in non-irradiated NT, H2A.J-KD, H2A.J-KI and H2A-KI fibroblasts showed generally low numbers of SA- β -Gal+ cells ($\approx 10\%$). After IR exposure, NT, H2A.J-KD and H2A-KI fibroblasts revealed an increased expression of lysosomal β -galactosidase protein, and proportions of SA- β -Gal+ cells clearly increased to $\approx 95\%$ at 2 w post-IR, suggesting that these fibroblast populations properly enter the senescence state (Figure 1B; right panel). In H2A.J-KI fibroblasts, by contrast, SA- β -Gal induction was observed in only $\approx 50\%$ of fibroblasts at 1 w and 2 w post-IR, suggesting that high proportions of these cells failed to enter senescence (Figure 1B; right panel). Stringent cell growth arrest associated with cellular senescence can be determined by augmented levels of cyclin-dependent kinase inhibitor proteins, such as p21^{Cip1/Waf1}. Accordingly, p21 staining was established to verify our finding of reduced senescence induction in H2A.J-KI fibroblasts after IR exposure. While all non-irradiated fibroblast populations revealed very low p21 levels ($\leq 7\%$), the proportion of p21+ cells increased to 75–90% for NT, H2A.J-KD and H2A-KI after IR, reflecting their strong senescence response. Significantly, for H2A.J-KI fibroblasts, the p21 expression level remained very low even after IR exposure ($\approx 14\%$), suggesting that H2A.J-KI fibroblasts are largely resistant to radiation-induced senescence.

3.2. Formation of SAHF and DNA-SCARS following IR

The dynamic reorganization of the higher-order chromatin structure during senescence progression leads to the formation of dense, repressive heterochromatin foci, so-called SAHFs, visible via DAPI staining. To investigate the input of H2A.J expression to global chromatin organization, we quantified the number of SAHF+ cells at 2 w post-IR compared to their non-irradiated counterparts (Figure 2A). In NT and H2A.J-KD fibroblasts, SAHFs emerged in $\approx 70\%$ of the cells after IR exposure. For H2A-KI fibroblasts, the proportion of SAHF+ cells was significantly lower ($\approx 40\%$), and in H2A.J-KI fibroblasts the number of SAHF+ cells was reduced to only $\approx 10\%$, despite serious genotoxic insults induced by IR (Figure 2A). Previous studies have shown that, in contrast to the even genome-wide distribution of canonical H2A, the histone variant H2A.J predominantly localizes in distinct chromatin regions with persistent DNA damage and activated DDR mediators [14]. To test whether this specific deposition pattern of H2A.J is correlated with the formation of DNA-SCARS, double-staining for 53BP1 and PML was performed in NT, H2A.J-KD, H2A.J-KI and H2A-KI fibroblasts, before and 5 h, 24 h and 2 w post-IR (Figure 2B). For all analyzed cell lines, very low 53BP1-foci levels were observed in non-irradiated fibroblasts (0.1–1.8 foci/cell), but clearly higher 53BP1-foci levels were observed after IR exposure, with 42–50 foci/cell at 5 h post-IR, 12–15 foci/cell at 24 h post-IR, and 5–7 foci/cell at 2 w post-IR (Figure 2B). This similar decline of 53BP1-foci in H2A.J-gene depleted and overexpressed fibroblasts suggests, that the DSB repair capacity is not affected by differential H2A.J expression. Enumerating PML-foci per cell, we observed low foci levels (6–12 foci/cell) in all non-irradiated controls, slightly higher levels at 5 h and 24 h post-IR (10–17 foci/cell), but clearly higher values at 2 w post-IR, particularly in the H2A.J-KI and H2A-KI lines of fibroblasts (40–46 foci/cell) (Figure 2B). PML nuclear bodies are involved in genome maintenance pathways including DDR and DNA repair and p53-associated apoptosis. H2A.J knock-down did not affect the formation of PML-foci; H2A.J knock-in, however, led to an increased formation of PML-foci after IR compared to their NT counterpart. Quantitative scoring of 53BP1/PML-double-positive foci revealed clearly lower co-localization events in H2A.J-KI cells, and thus reduced the numbers of DNA-SCARS (Figure 2B). Collectively, these findings suggest that differential H2A.J deposition in chromatin may have profound effects on higher-order chromatin organization and on establishing the epigenetic state of senescence in response to DNA-damaging IR.

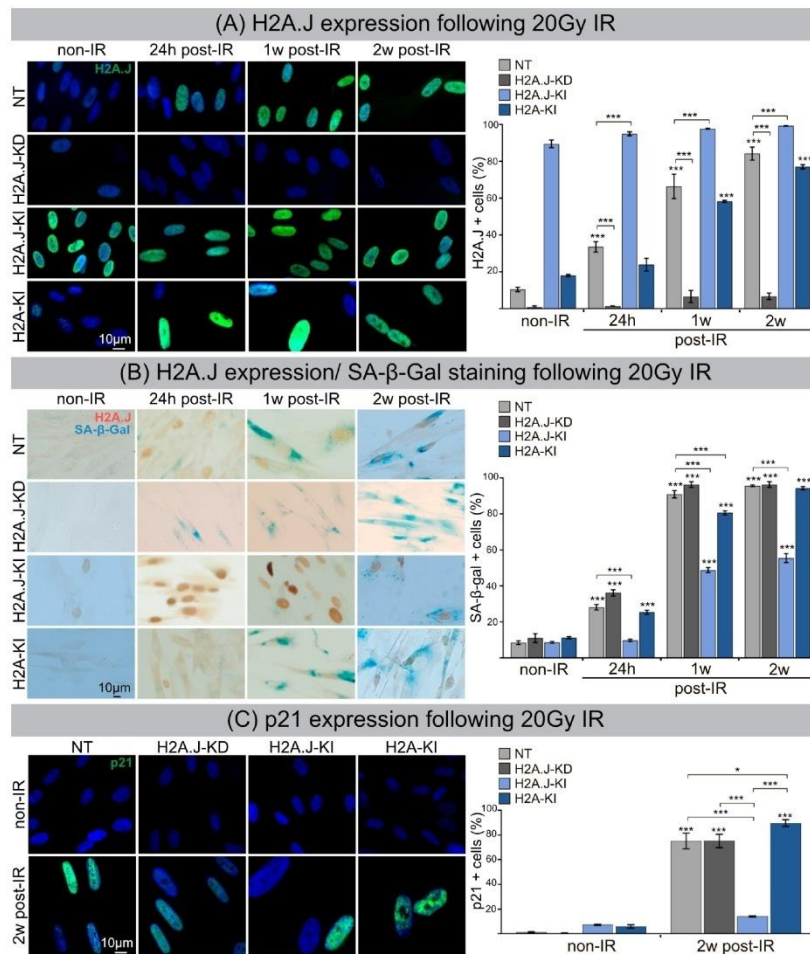


Figure 1. (A) H2A.J expression following 20 Gy IR. IFM micrographs of NT, H2A.J-KD, H2A.J-KI and H2A-KI fibroblasts show H2A.J+ cells at 24 h, 1 w and 2 w post-IR compared to non-irradiated fibroblasts. The adjacent graph shows the quantification of H2A.J+ cells. Data are presented as the mean of three experiments \pm SE. Significant statistical difference compared to non-irradiated controls (marked by asterisks alone) or between cell lines (asterisks with square brackets): * $p < 0.05$; *** $p < 0.001$. (B) H2A.J expression and SA- β -Gal staining following 20 Gy IR. IHC micrographs show H2A.J and SA- β -Gal staining of NT, H2A.J-KD, H2A.J-KI and H2A-KI fibroblasts following 20 Gy at 24 h, 1 w and 2 w post-IR compared to non-irradiated controls (non-IR). The adjacent graph shows the quantification of H2A.J+ and SA- β -Gal+ cells at 24 h, 1 w and 2 w post-IR, compared to non-irradiated controls. (C) p21 expression following 20 Gy IR. An IFM micrograph shows the p21 staining of NT, H2A.J-KD, H2A.J-KI and H2A-KI fibroblasts at 2 w post-IR compared to non-irradiated controls. The quantification of p21+ cells at 2 w post-IR compared to non-irradiated controls. Data are presented as the mean of three experiments \pm SE. Significant statistical difference compared to non-irradiated controls (marked by asterisks alone) or between cell lines (asterisks with square brackets): * $p < 0.05$; *** $p < 0.001$.

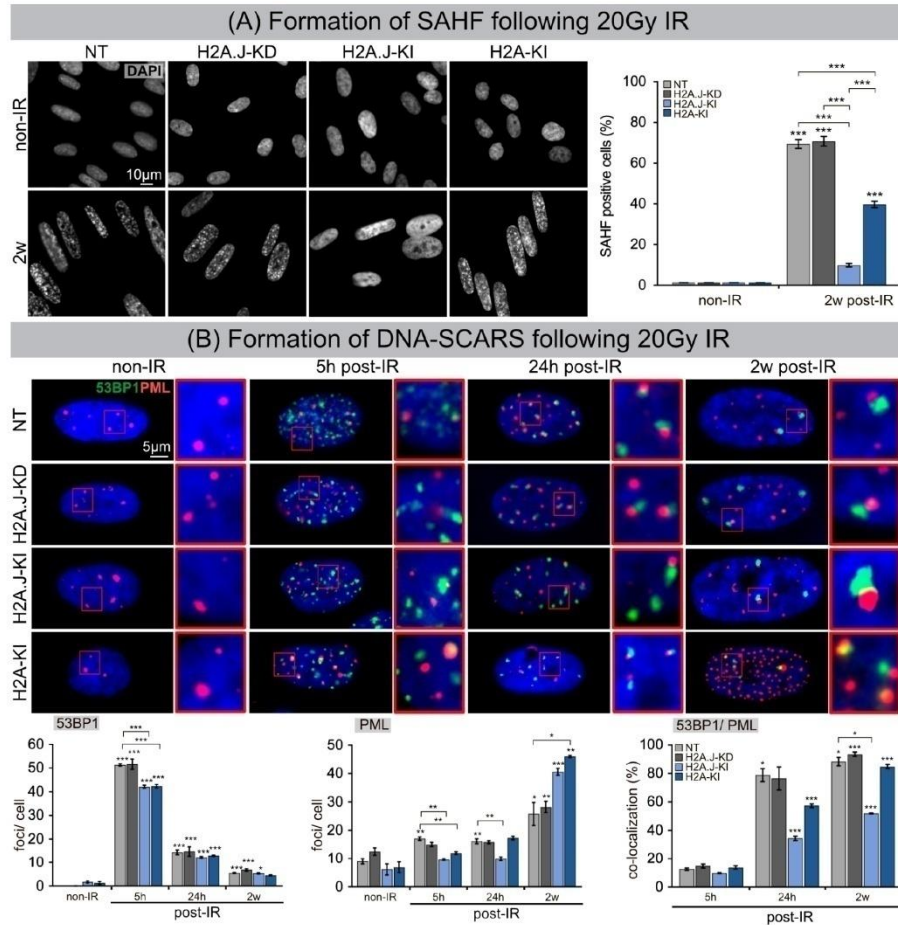


Figure 2. (A) Formation of SAHF following 20 Gy IR. IFM micrographs show the DAPI staining of NT, H2A.J-KD, H2A.J-KI and H2A-KI fibroblasts at 2 w post-IR, compared to non-IR controls. The adjacent graph shows the quantification of SAHF+ cells at 2 w post-IR compared to non-irradiated controls. Data are presented as the mean of three experiments \pm SE. Significant statistical difference compared to non-irradiated controls (marked by asterisks alone) or between cell lines (asterisks with square brackets): *** $p < 0.001$. (B) Formation of DNA-SCARS following 20 Gy IR. IFM micrographs show double-staining for 53BP1 and PML in NT, H2A.J-KD, H2A.J-KI and H2A-KI fibroblasts at 5 h, 24 h and 2 w post-IR, compared to non-irradiated controls. The adjacent graph shows the quantification of 53BP1 foci/cell, PML-foci/cell and 53BP1/PML co-localization in NT, H2A.J-KD, H2A.J-KI and H2A-KI fibroblasts at 24 h, 1 w and 2 w post-IR. Significant statistical difference compared to non-irradiated controls (marked by asterisks alone) or between cell lines (asterisks with square brackets): * $p < 0.05$; ** $p < 0.01$; *** $p < 0.001$.

3.3. ATAC-Seq for Chromatin Accessibility Analysis

Open and closed chromatin configurations regulate gene expression through regulatory networks of transcription factors (TF), which modulate transcription by recognizing and binding to specific DNA sequences. Changes in chromatin accessibility for TF binding

sites were studied by ATAC-seq, permitting the genome-wide analysis of transcriptionally open/active and closed/repressed regulatory elements. Using the motif discovery tool HOMER, the sequence-based prediction for TF motif frequency or activity was mapped and compared for different conditions: for each line of fibroblasts in their post-IR versus non-IR status (Figure 3A) and between different fibroblast lines for their non-IR (Figure 3B) and post-IR (Figure 3C) status. ATAC-seq data analysis identified numerous members of the Activator Protein-1 (AP-1) superfamily (ATF3, B ATF, FOSL2, JUNB) as the most affected motifs in differentially accessible chromatin regions of NT fibroblasts after IR exposure (Figure 3A). The dimeric AP-1 complex is composed of different members of ATF, FOS and JUN families, thereby providing multiplicity for regulatory control. Our findings correlate with previous studies in WI-38 lung fibroblasts, showing that these predominant transcription factors act as pioneers for imprinting the transcriptional programme of senescent cells [26]. H2A.J-KD and H2A.J-KI cells, in contrast, revealed less open chromatin configurations for these TF motifs after IR exposure (Figure 3A, left panel). Significantly, for H2A.J-KI fibroblasts, these chromatin regions are even less accessible after IR exposure, which may correlate with their increased resistance to radiation-induced senescence (Figure 3A, right panel). To address the functional importance of H2A.J in chromatin accessibility, these enriched TF motifs were profiled in NT, H2A.J-KD and H2A.J-KI fibroblasts, compared in each case for their non-IR and post-IR conditions. For these motifs, H2A.J-KI versus NT and, even more pronounced, H2A.J-KI versus H2A.J-KD fibroblasts revealed increasingly open chromatin in both, their non-IR (Figure 3B, left panel) and post-IR status (Figure 3C, left panel). Compared to this, H2A.J-KD fibroblasts clearly exhibit more closed chromatin configurations for these TF binding sites (Figure 3C, right panel). Collectively, our findings suggest that deregulated H2A.J expression compromised the dynamic response capacity for TF recruitment.

3.4. Integrative Analysis of ATAC-Seq and RNA-Seq Datasets

Transcriptionally active genes are characterized by accessible chromatin at their promoters, nearby enhancers, and some internal regions within the gene body itself. To determine whether differentially accessible chromatin configurations were correlated with their corresponding gene expression levels, ATAC-seq and mRNA-seq datasets were integrated for NT, H2A.J-KD and H2A.J-KI fibroblasts in their irradiated versus non-irradiated state. Figure 4 shows the integrated results from ATAC-seq and RNA-seq analysis for the previously identified signature genes interleukin-6 (IL6), colony-stimulating factor 2 (CSF2), CC-chemokine ligand 2 (CCL2), and C-X-C motif ligand 8 (CXCL8) (Figure 4). Strikingly, we observed clear differences between these genetically-modified fibroblast populations regarding their inflammatory gene regulation after IR exposure. By comparing ATAC-seq with RNA-seq data for NT fibroblasts, increased chromatin accessibility (green marks) after IR was correlated with increased IL6 mRNA signals. In contrast with H2A.J-KD fibroblasts, reduced chromatin accessibility (red marks) after IR was associated with the down-regulation of IL6 mRNA expression. In contrast with H2A.J-KI fibroblasts, different chromatin regions showed reduced or increased accessibility, ultimately leading to the overall down-regulation of IL6 mRNA expression. Similar correlations between ATAC-seq and RNA-seq data can be observed for the other immune-modulatory cytokines. Collectively, the integration of ATAC-seq and RNA-seq results indicate that changes in chromatin accessibility were clearly associated with inflammatory gene expression.

RNA-seq analysis was performed in NT, H2A.J-KD and H2A.J-KI fibroblasts for measuring gene expression changes in response to IR exposure. Volcano plots show unchanged, up- and down-regulated genes in NT, H2A.J-KD, and H2A.J-KI fibroblasts at 2 w post-IR, compared to their non-irradiated controls (Figure S1). During the progression of radiation-induced senescence, the chromatin structure changes fundamentally, and the proportion of canonical histones and histone variants changes significantly (Figures S2 and S3). The precise distribution of histones and histone variants is crucial for chromatin organization and its epigenetic states.

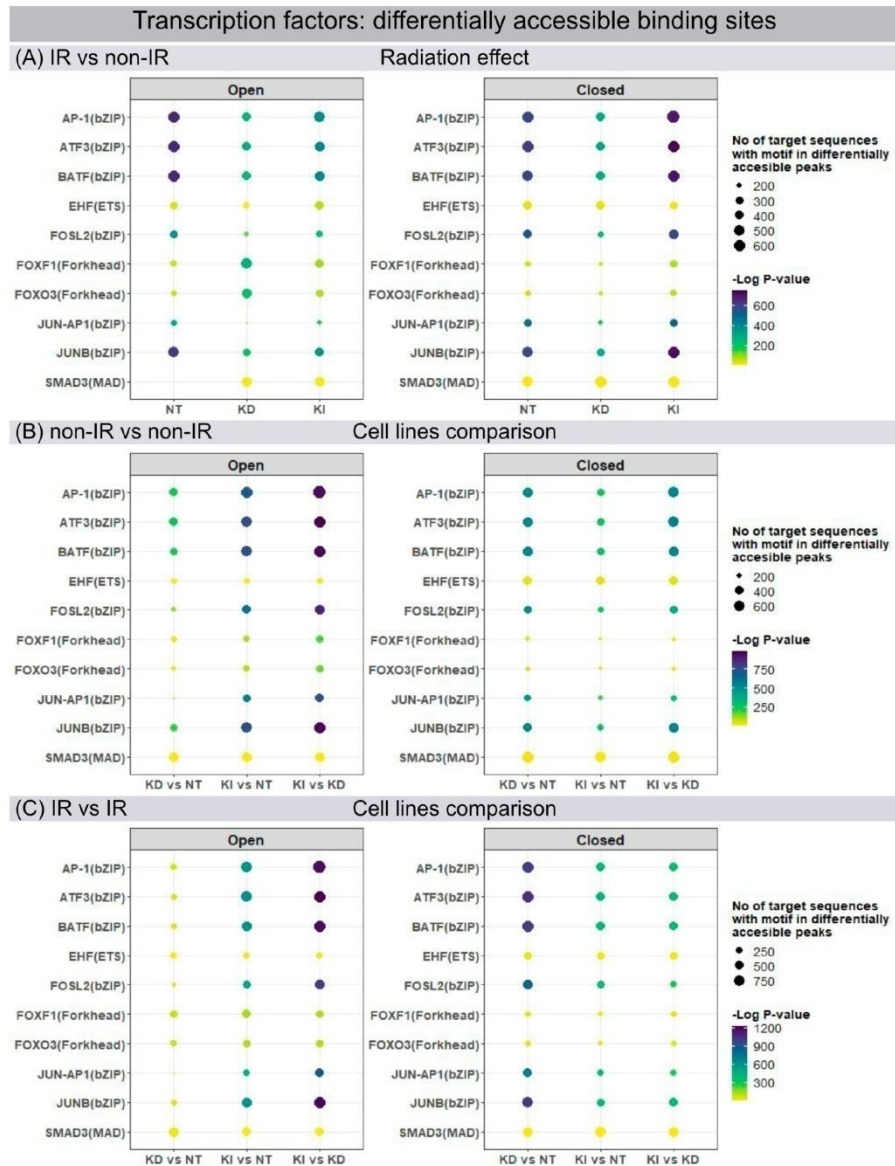


Figure 3. Genome-wide mapping of transcription factor binding sites. Changes in chromatin accessibility for transcription factor binding motifs in NT, H2A.J-KD and H2A.J-KI fibroblasts at 2 w post-IR, compared to their non-irradiated controls (A), and between NT, H2A.J-KD and H2A.J-KI fibroblasts in their non-irradiated (B) and their irradiated state (C).

3.5. Senescence-Associated Secretory Phenotype (SASP)

After high-dose IR exposure fibroblasts become senescent, but remain viable for long intervals and develop SASP with the secretion of inflammatory cytokines. For all lines

of fibroblasts (most pronounced for NT fibroblasts) transcribed SASP genes (IL6, CSF2, CCL2, CXCL8) were generally upregulated following IR compared to their non-irradiated counterparts. Subsequently, transcribed SASP genes were correlated with corresponding SASP proteins by investigating the secretion of interleukin-6 (IL6), granulocyte-macrophage colony-stimulating factor (GM-CSF), monocyte chemoattractant protein-1 (MCP1), and interleukin-8 (IL8) in culture media by ELISA, as readout for the inflammatory secretome. Non-irradiated NT, H2A.J-KD and H2A.J-KI fibroblasts expressed only low levels of these common SASP factors, and hence no senescence-messaging secretome (Figure 5B). NT fibroblasts in radiation-induced senescence, by contrast, secreted high levels of IL6, GM-CSF, MCP1 and IL8, demonstrating that SASP components were significantly increased between non-senescent and senescent states in NT fibroblasts (Figure 5B). Strikingly, H2A.J-KD and also H2A.J-KI fibroblasts revealed distinctly lower protein expression levels for most of these SASP factors in radiation-induced senescence (Figure 5B). The only exception was IL8 in H2A.J-KI fibroblasts, with clearly increased expression levels in non-irradiated H2A.J-KI compared to NT fibroblasts, and with further significant increases after IR exposure. In summary, our findings indicate that the genetically-modified H2A.J expression in H2A.J-KD and H2A.J-KI fibroblasts differentially modulates the various soluble signaling factors of SASP with similar expression patterns to those in RNA-seq experiments. Next, we explored whether SASP components enriched in culture media (CM) of senescent cells may affect paracrine functions in non-irradiated cells (Figure 5C). Naive NT fibroblasts were treated with CM from non-senescent or senescent cells (CM from NT fibroblasts: non-IR versus post-IR) for periods of 24 h or 72 h, respectively, and the relative gene expression of these SASP factors (IL6, CSF2, CCL2, CXCL8) was monitored by RT-qPCR (Figure 5C). A gene expression analysis of NT fibroblasts revealed the significantly increased mRNA expression of IL6 and CXCL8 (with up to ~5-fold increases; Figure 5C) after treatment with CM from senescent cells. Our results show that treatment with senescent CM induced paracrine effects on naive cells and resulted in secondary SASP induction with significantly elevated transcription levels of proinflammatory cytokines. These findings suggest that senescent lung fibroblasts affect their local environment and induce so-called 'bystander' effects through the secretion of bioactive SASP components.

3.6. H2A.J Expression in Lung Tissue after IR Exposure

Previous studies noted organ-specific differences in H2A.J protein expression in normal tissues generally, with strong labeling of luminal epithelial cells, even without IR exposure [27]. Here, we used IFM to visualize H2A.J expression within different cell types in lung tissue of mice exposed to different doses of IR. Lung parenchyma are comprised of greatly varying cell populations with bronchiolar and alveolar epithelium (comprising type I and II pneumocytes), alveolar macrophages, and endothelial and interstitial cells. In non-irradiated lung tissue, the bronchial epithelium and some type II pneumocytes, characterized by more spherical shapes and known to release pulmonary surfactant to lower surface tension, stained positive for H2A.J. After IR with moderate doses (single-dose or fractionated IR with 2 Gy), we observed clear increases in the number of H2A.J-positive pneumocytes, most pronounced at 24 h post-IR (Figure 6A). After high-dose exposure with 10 Gy (24 h post-IR), we observed striking increases of H2A.J expression in the alveolar epithelium and in multiple other cell types, including interstitial fibroblasts, scattered throughout the lung parenchyma. Moreover, we observed cytosolic H2A.J staining after high-dose IR, which was most pronounced in the bronchiolar epithelium. The meaning of this finding is currently unclear, but recent studies suggest that histones are released into the extracellular space after significant cellular damage, thereby triggering thrombus formation and innate immunity during acute tissue injury [28]. Previous studies have shown that acute exposure to high-dose IR disrupts the alveolo-capillary barrier and increases cytokine release, resulting in pulmonary edema and promoting the recruitment of inflammatory cells [29,30]. As a proof-of-concept, we applied automated whole-slide imaging and high-resolution image analysis of chromogenic H2A.J-staining to show that

clinically relevant fractionation schemes result in increased H2A.J expression in lung tissue. In representative regions of irradiated (5×2 Gy, 24 h post-IR) versus non-irradiated lung parenchyma, cells were classified into no (blue), weak (yellow), and moderate.

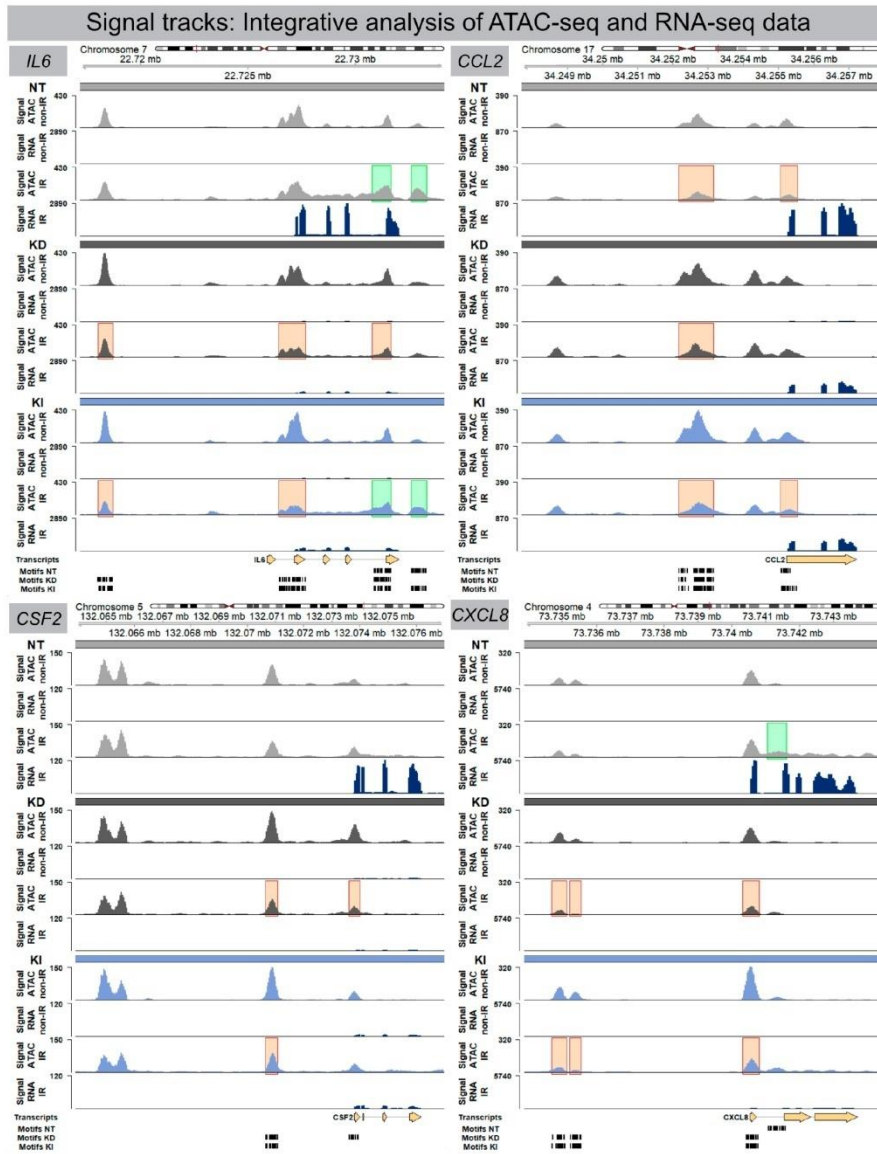


Figure 4. Signal track integration for SASP gene expression. Region-specific analysis of chromatin accessibility (ATAC-seq) and RNA expression (RNA-seq) for SASP factors IL6, CSF2, CCL2 and CXCL8 in NT, H2A.J-KD, and H2A.J-KI fibroblasts at 2 w post-IR, compared to non-irradiated controls. Colour-coded boxes covering ATAC-seq signal tracks in irradiated conditions indicate more

(green) or less (red) accessible chromatin regions (compared to non-irradiated controls) and depicts a strong correlation with RNA-seq signals (blue), (orange), and *strong* (red) H2A.J-stained nuclei (Figure 6B). After automatic classification, the percentage of cells with different nuclear H2A.J-staining intensities was quantified in relation to total cell numbers. Our quantitative results show an overall increase of H2A.J+ cells from ≈ 20 to $\approx 40\%$ after IR exposure; in addition, we observed an increase of H2A.J+ cells within each category, reflecting that H2A.J expression is significantly enhanced after IR exposure (Figure 6B). Collectively, our findings suggest that dose-dependent H2A.J expression triggered by the initial exposure to IR may contribute to the initiation and progression of radiation-induced lung injury.

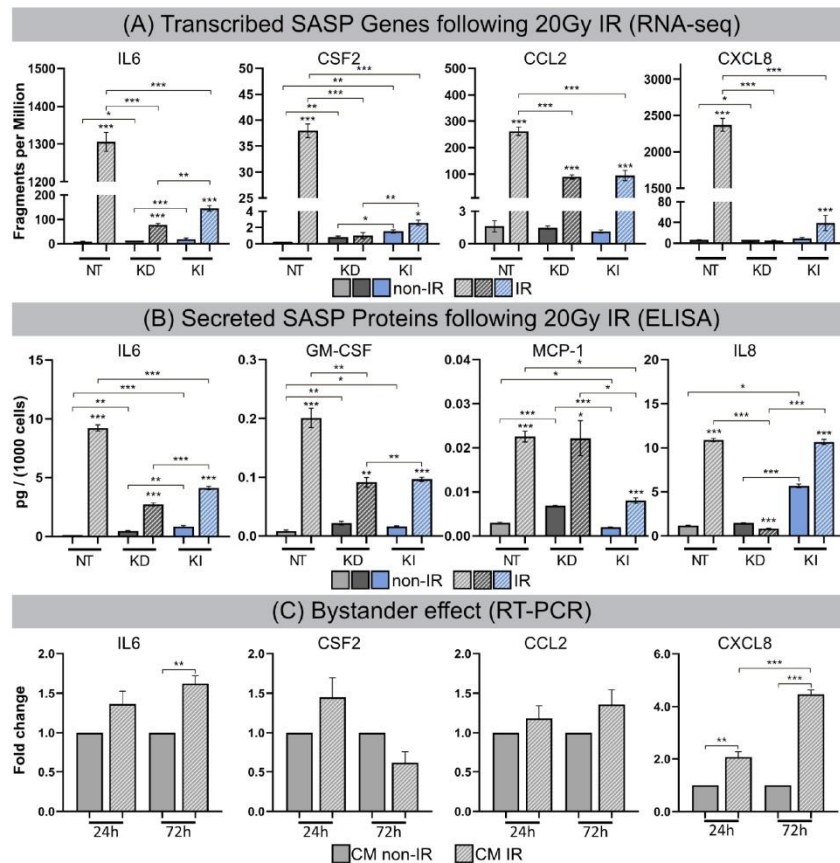


Figure 5. (A) Transcribed SASP genes following 20 Gy IR. Quantification of mRNA expression (mRNA-seq) for IL6, CSF2, CCL2 and CXCL8 in NT, H2A.J-KD, and H2A.J-KI fibroblasts at 2 w post-IR, compared to non-irradiated controls. (B) Secreted SASP proteins following 20 Gy IR. Quantification of protein expression (ELISA) for IL6, GM-CSF, MCP-1, IL8 in conditioned medium of NT, H2A.J-KD, and H2A.J-KI fibroblasts at 2 w post-IR, compared to non-irradiated controls. (C) Bystander effect. Quantification of mRNA expression (RT-PCR) for IL6, CSF2, CCL2 and CXCL8 in NT fibroblasts after 24 h- or 72 h-exposure to conditioned medium of irradiated (CM IR) or non-irradiated (CM non-IR) NT fibroblasts. Significant statistical difference compared to non-irradiated controls (marked by asterisks alone) or between cell lines (asterisks with square brackets): * $p < 0.05$; ** $p < 0.01$; *** $p < 0.001$.

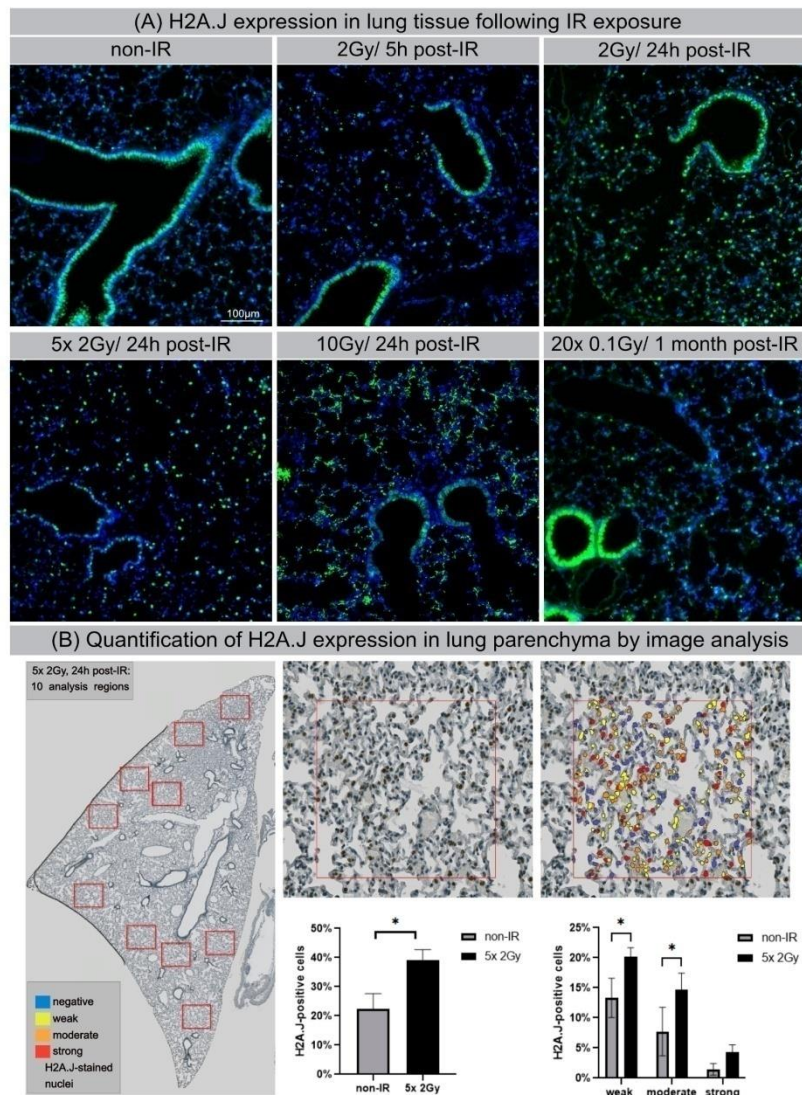


Figure 6. H2A.J expression in lung tissue after IR exposure (A) IFM micrographs of H2A.J expression in lung tissue after single-dose exposure with 2 Gy (5 h and 24 h post-IR) or 10 Gy (24 h post-IR) and after fractionated IR with 5×2 Gy or 20×0.1 Gy, compared to non-irradiated control tissue. (B) Quantitative whole-slide digital image analysis of nuclear H2A.J immunohistochemistry in lung parenchyma after fractionated IR (5×2 Gy; 24 h post-IR). Significant statistical difference compared to non-irradiated controls (marked by asterisk with square brackets): * $p < 0.05$.

4. Discussion

Chromatin organization and transcriptional profiles undergo tremendous rearrangements during senescence progression. To explore the potential epigenetic mechanisms of

histone variant H2A.J in the regulatory networks of radiation-induced senescence, lung fibroblasts with down- and upregulated H2A.J expression levels were analyzed for their dynamic changes in chromatin organization, epigenetic and transcriptional landscape, and their cellular function following IR exposure. Through integrative ATAC-seq and RNA-seq analysis and functional validation of the senescence state, we identified and analyzed mechanistic interrelations between H2A.J incorporation and altered chromatin architecture with modified genome accessibility and transcription factor recruitment, changed SASP expression, and senescence competence. Our findings demonstrate that the fine-tuned incorporation of histone variant H2A.J defines the epigenetic landscape for driving the senescence programme in response to DNA-damaging stress. H2A.J overexpression, in contrast, was associated with reduced senescence-associated chromatin alterations, significant changes in the SASP secretome, and the potential to overcome senescence-associated growth arrest. Analyzing lung tissues following IR exposure, we observed increased H2A.J expression in specific cell populations (particularly in pneumocytes), most pronounced after high doses, but even after moderate and low doses. These findings suggest that H2A.J-associated epigenetic mechanisms play decisive roles even at therapeutic doses used during fractionated radiotherapy. It is increasingly recognized that DNA-damage triggered events stimulate inflammation and modulate cellular functions in injured normal tissues over months to years [31]. Future studies have to elucidate the precise role of H2A.J in triggering cytokine production during the temporal progression of lung injury, which manifests as acute pneumonitis and later as pulmonary fibrosis.

Collectively, our discoveries about the H2A.J-associated epigenetic mechanisms that drive radiation-induced damage development complement the traditional radiobiological conception of normal tissue injury. Understanding the precise molecular events responsible for the perpetuation of normal tissue injury is critical for developing therapeutic strategies to prevent, mitigate, and treat radiation toxicities.

Histone variants greatly expand the roles and dynamics of nucleosomes by wrapping more or less DNA, by having greater or lesser stability, through unique post-translational modifications, or by interacting with specific chromatin components [32]. Previous studies have shown that the incorporation of H2A.J, with its distinct sequence and properties compared to canonical H2A histone have direct effects on the structure and stability of nucleosomes [33]. Unlike canonical histones, which are distributed equally along the chromatin during replication, nucleosomes containing histone variants are deposited throughout the cell cycle at specific locations. Previous electron microscopic studies with H2A.J immunogold-labeling have shown that during radiation-induced senescence, H2A.J replaces canonical H2A preferentially at persisting DNA damage sites, and is enriched at the border of heterochromatic domains of DNA-SCARS arranged at the periphery of SAHF [14]. Our present findings suggest that fine-tuned H2A.J incorporation at chromatin sites involved in DDR processes is crucially important for establishing specific chromatin configurations and maintaining heterochromatin-euchromatin boundaries. Accordingly, deregulated H2A.J histone deposition in irradiated fibroblasts modifies local and global chromatin organization, and these structural changes impair the formation of SAHF and DNA-SCARS, thereby altering the epigenetic state of senescence. Increased H2A.J incorporation into senescent chromatin was also associated with the global loss of canonical histones, particularly for the different forms of the linker histone H1, which is known to play crucial roles in nucleosome positioning and heterochromatin formation [34].

The topological organization of nucleosomes across the genome regulate chromatin accessibility through a variety of chromatin mechanisms, such as altering TF binding by modulating steric hindrance. ATAC-seq measurements of open and closed chromatin accessibility reflect regulatory capacities and distinct functional states of chromatin organization [35]. Our findings indicate that the remodeling of senescence-related chromatin structures (SAHF and DNA-SCARS) modulates the physical access of transcription factors to chromatinized DNA. Our ATAC-seq analysis showed that AP-1 transcription factors, including members of the ATF, FOS, and JUN families, participate in the regulatory

epigenome network of radiation-induced senescence. These findings confirm the previously described hierarchical structure of TF networks with AP-1 as the master regulator to choreograph transcriptional programmes via dynamic interactions with settler and migrant TFs during senescence progression [26]. In lung fibroblasts with properly regulated H2A.J expression, accessible chromatin sites for these senescence TFs were modified to the strongest degree following IR exposure, presumably to effectively regulate transcriptional activities for the timely execution of the senescence programme. H2A.J depletion in H2A.J-KD fibroblasts, by contrast, revealed notably reduced modulation capabilities for these chromatin accessibility sites following IR exposure, potentially implying their less flexible senescence regulation. H2A.J overexpression in H2A.J-KI fibroblasts revealed a lower open but a more closed TF interactome, potentially reflecting the disruption of TF senescence networks, with important implications for their senescent cell fate.

A substantial number of anticancer interventions, such as radiotherapy, induce senescence in normal but also in cancer cells by triggering genotoxic stress, leading to stable cell cycle arrest and SASP induction. Therefore, therapy-induced senescence serves as an initial antitumour mechanism to halt proliferation and prevent further genomic instability. However, we here present the first experimental evidence that H2A.J is progressively incorporated into the chromatin following IR exposure, and that H2A.J overexpression can reverse this radiation-induced cell cycle arrest. Therefore, H2A.J overexpression may promote tumorigenesis or even improve resistance to cancer treatments. Within the scope of our current studies on irradiated skin tissue, we observed that mitochondria-associated genes are also strongly modulated by H2A.J. Increasing evidence suggests that an altered mitochondrial metabolism is associated with the onset of resistance to radiotherapy [36]. However, the precise role of H2A.J in the context of mitochondrial metabolism and tumor response to radiotherapy has to be investigated in appropriate experimental studies.

Genome-wide chromatin accessibility profiling for TF-binding motifs using ATAC-seq emphasize the functional role of the histone variant H2A.J for regulatory senescence networks. Collectively, integrative analysis of ATAC-seq and RNA-seq datasets indicate that H2A.J-associated changes in chromatin accessibility in regulatory regions were clearly associated with modified inflammatory gene expression profiles. Our *in vitro* model with knock-down or knock-in of the H2A.J gene in a defined cell type makes it possible to study very precisely the functional effects of H2A.J on chromatin organization, the recruitment of transcription factors, and the pro-inflammatory secretome after IR exposure. However, fibroblasts are a rather radioresistant cell population that does not reflect the radiation reactions of diverse cell populations found in complex tissues. In future research work, knock-out mice will be examined before and after IR exposure in order to investigate the importance of H2A.J for the radiation response in the context of complex tissue homeostasis.

5. Conclusions

Cellular senescence is a stable cell growth arrest that is characterized by the silencing of proliferation-promoting genes through the compaction of chromosomes into SAHF [37,38]. Our findings suggest the differential incorporation of non-canonical histone variant H2A.J alter global chromatin architecture and as a consequence the epigenetic landscape. Different H2A.J deposition levels differentially modify the chromatin accessibility to transcription factors and selectively regulate the expression of inflammatory genes during radiation-induced senescence. Previous studies have shown that the depletion of H2A.J downregulates and the overexpression of H2A.J upregulates the expression of SASP components, but neither condition had any obvious effect on senescence-associated cell cycle arrest [13,14]. Here, we observed that the overexpression of H2A.J, in contrast, altered the senescence-associated proliferation arrest after IR exposure. These inconsistencies regarding the phenotypic effects of H2A.J overexpression can be explained by different analytical methods and by the different intensity and nature of senescence-inducing stressors. Our current findings suggest that the overexpression of H2A.J may impede heterochromatin formation following IR exposure and therefore inhibit the SAHF-mediated gene silencing of proliferation-promoting genes.

DNA damage-induced senescence act as a potent anti-tumor mechanism by preventing the proliferation of potentially cancerous cells. Bypassing senescence and acquiring limitless replicative potential is a key event required for malignant transformation and for the development of radioresistance [39].

Supplementary Materials: The following supporting information can be downloaded at: <https://www.mdpi.com/article/10.3390/cells12060916/s1>, Figure S1: RNA-seq for gene expression analysis: RNA-seq analysis was performed in NT, H2A.J-KD and H2A.J-KI fibroblasts for measuring gene expression changes in response to IR exposure. Volcano plots show unchanged, up- and down-regulated genes in NT, H2A.J-KD, and H2A.J-KI fibroblasts at 2 w post-IR, compared to their non-irradiated controls (A) and between NT, H2A.J-KD and H2A.J-KI fibroblasts in their non-irradiated (B) and their irradiated state (C). The precise distribution of histones and histone variants is crucial for chromatin organization and its epigenetic states. Figure S2: RNA-seq for gene expression analysis: histone expression, part 1: Increased substitutions of canonical histones by non-canonical variants are dynamic processes that change the composition of chromatin during senescence progression. Suppl. 2 shows RNA-seq analysis in NT, H2A.J-KD and H2A.J-KI fibroblasts for measuring gene expression changes in response to IR exposure. While non-irradiated NT fibroblasts revealed very low H2A.J expression, these H2A.J transcript levels were significantly increased after IR exposure, as was anticipated. H2A.J-KD fibroblasts, in contrast, showed significantly lower transcript levels, which were not affected by IR exposure. H2A.J-KI fibroblasts already displayed significantly elevated transcript levels without IR exposure, and this level even increased significantly after IR exposure. Collectively, these findings confirm that our cell-based system with down- or up-regulated H2A.J expression works as expected and fulfils specified requirements. Contrary to the H2A.J expression, transcript levels of histone variants H2A.X and H2AZ1 decreased significantly in NT fibroblasts, and were even more pronounced in H2A.J-KD and H2A.J-KI fibroblasts after IR exposure. The phosphorylation of the H2A.X variant at sites of DNA double-stranded breaks is an early event in DSB repair to concentrate components of the repair machinery, whereas H2A.Z is a negative regulator of p21 transcription and the p53→p21 senescence pathway. The depletion of H2A.Z in human fibroblasts leads to p21 activation and premature senescence [40]. Taken together, our findings suggest that the composition of these histone variants within nucleosomes is dynamic, and varies significantly after IR exposure, with elevated H2A.J incorporation but progressive H2AX and H2AZ ejection. The histone H2A family contains many sequence variants that confer structural and functional variability to nucleosomes. Our transcriptome analysis showed that many canonical H2A histones (H2AC 4/8/11/13/20/21) are strongly down-regulated in NT, H2A.J-KD and H2A.J-KI fibroblasts in response to IR, probably because their synthesis is coupled to DNA replication during the S-phase. Figure S3: RNA-seq for gene expression analysis: histone expression, part 2: Linker histone H1 has been demonstrated to be essential for the structural and functional integrity of chromatin by driving the compaction of chromatin fibres. Our results in Suppl. 3 showed that multiple H1 isoforms (H1-1/2/3/4/5) are depleted during radiation-induced senescence, and are even more pronounced in H2A.J-KD and H2A.J-KI fibroblasts (Suppl. 3). Modified chromatin architectures with the transition from highly condensed to loosely packed chromatin structures may lead to the de-repression of silenced genes, and as a consequence to global changes in gene expression. Collectively, these findings correlate with the reduced SAHF formation and senescence induction in H2A.J-KI fibroblasts after IR exposure. Histone variants are synthesized throughout the cell cycle, and specific H2A variants may preferentially associate with each other resulting in different combinations and leading to the increased combinatorial complexity of nucleosomes in post-mitotic chromatin. MacroH2A isoforms are unique H2A histone variants due to their 30 kDa macrodomains at their C-termini. MacroH2A1 and macroH2A2 isoforms are encoded by two distinct genes (H2AFY and H2AFY2, respectively), and are generally considered transcriptionally repressive in nature, due to their association with condensed chromatin such as in SAHFs in senescent cells [37]. While macroH2A1 decreased significantly in NT and H2A.J-KD fibroblasts after IR, the transcription levels of macroH2A2 were already significantly elevated in non-irradiated H2A.J-KI compared to NT and H2A.J-KD fibroblasts, and even increased after IR exposure, (Suppl. 3), possibly reflecting compensatory effects caused by H2A.J overexpression. Collectively, our findings support the general observation of the global loss of canonical histones and the increasing incorporation of histone variants in post-mitotic senescent chromatin.

Author Contributions: Conceptualization: C.E.R. and C.M.; investigations (IFM, IHC, ELISA, RT-PCR, digital image analysis): M.A.A.A.-r. and A.I.; ATAC-seq and RNA-seq data analysis: BMF; irradiation experiments in mice, IFM/IHC analysis of lung tissue: G.T.; validation of in-vitro fibroblast model: A.M.; writing—original draft preparation: C.E.R.; writing—review and editing, C.E.R. and C.M.; visualization: M.A.A.A.-r. and B.M.F.; supervision and project administration: C.E.R.; funding acquisition: C.E.R. and C.M. All authors have read and agreed to the published version of the manuscript.

Funding: C.E.R. received funding from the German Research Foundation (Deutsche Forschungsgemeinschaft; grant number RU821/8-1), the German Cancer Aid (Deutsche Krebshilfe; grant number 70113135), and the Federal Ministry of Education and Research (BMBF; 02NUK035A; 02NUK058B). C.M. was supported by grants from the ANR (ANR-17-CE12-0008) and the CEA radiobiology program.

Institutional Review Board Statement: The experimental protocol was approved by the Medical Sciences Animal Care and Use Committee of Saarland University (approval number 29/2020).

Informed Consent Statement: Not applicable.

Data Availability Statement: Research data are stored in an institutional repository and will be shared upon request to the corresponding author.

Acknowledgments: The authors thank our medical physicists for their technical support in radiation planning.

Conflicts of Interest: The authors declare that they have no conflict of interest. The funders had no role in the design of the study; in the collection, analyses, or interpretation of data; in the writing of the manuscript; or in the decision to publish the results.

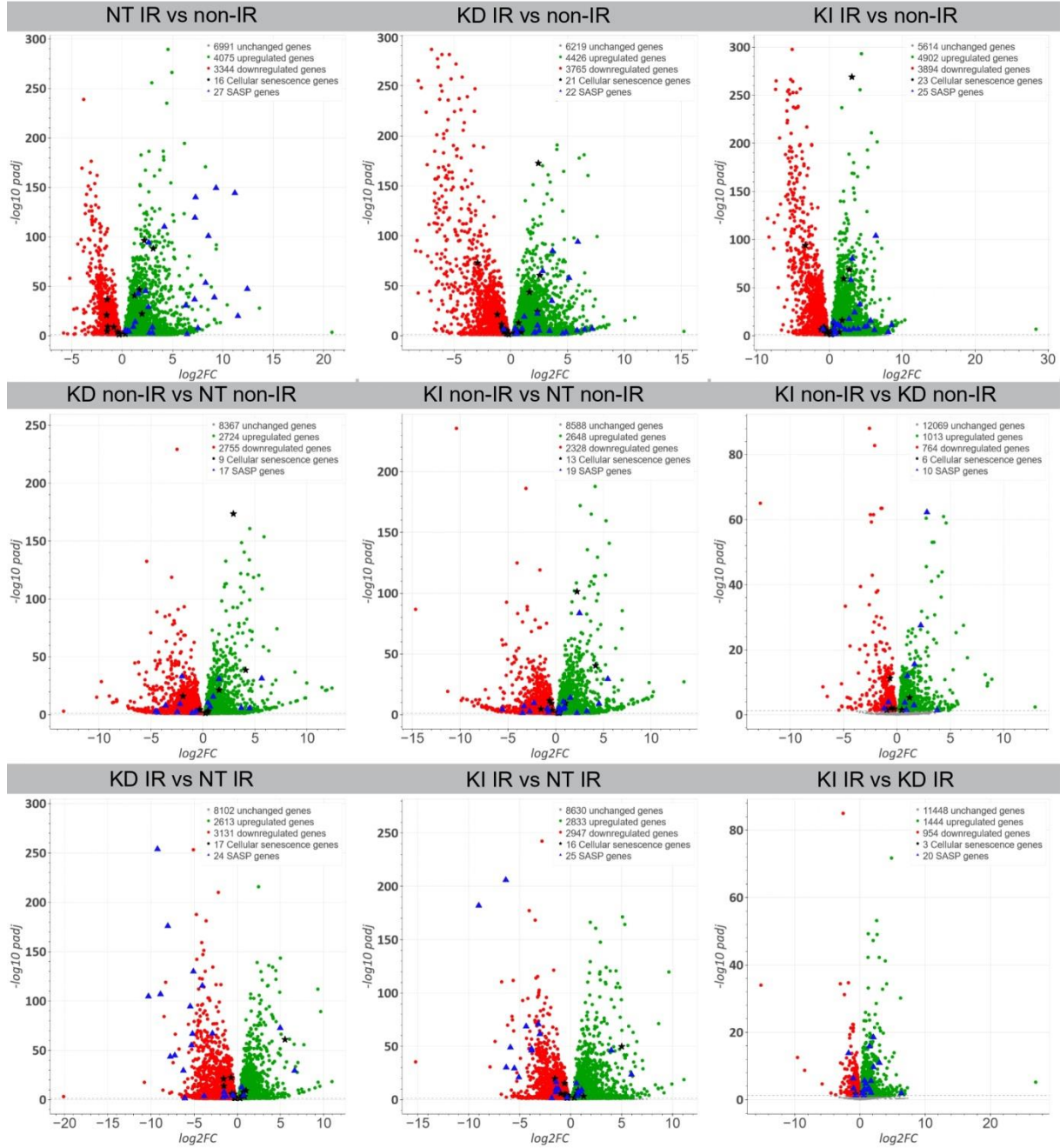
References

- Di Micco, R.; Krizhanovsky, V.; Baker, D.; d'Adda di Fagagna, F. Cellular senescence in ageing: From mechanisms to therapeutic opportunities. *Nat. Rev. Mol. Cell. Biol.* **2021**, *22*, 75–95. [[CrossRef](#)] [[PubMed](#)]
- Nacarelli, T.; Liu, P.; Zhang, R. Epigenetic Basis of Cellular Senescence and Its Implications in Aging. *Genes* **2017**, *8*, 343. [[CrossRef](#)] [[PubMed](#)]
- Campisi, J.; Robert, L. Cell senescence: Role in aging and age-related diseases. *Interdiscip. Top. Gerontol.* **2014**, *39*, 45–61. [[CrossRef](#)] [[PubMed](#)]
- Price, B.D.; D'Andrea, A.D. Chromatin remodeling at DNA double-strand breaks. *Cell* **2013**, *152*, 1344–1354. [[CrossRef](#)] [[PubMed](#)]
- Panier, S.; Boulton, S.J. Double-strand break repair: 53BP1 comes into focus. *Nat. Rev. Mol. Cell. Biol.* **2014**, *15*, 7–18. [[CrossRef](#)]
- Lorat, Y.; Schanz, S.; Rube, C.E. Ultrastructural Insights into the Biological Significance of Persisting DNA Damage Foci after Low Doses of Ionizing Radiation. *Clin. Cancer Res.* **2016**, *22*, 5300–5311. [[CrossRef](#)] [[PubMed](#)]
- Vancurova, M.; Hanzlikova, H.; Knoblochova, L.; Kosla, J.; Majera, D.; Mistrik, M.; Burdova, K.; Hodny, Z.; Bartek, J. PML nuclear bodies are recruited to persistent DNA damage lesions in an RNF168-53BP1 dependent manner and contribute to DNA repair. *DNA Repair* **2019**, *78*, 114–127. [[CrossRef](#)]
- Rodier, F.; Coppe, J.P.; Patil, C.K.; Hoeijmakers, W.A.; Munoz, D.P.; Raza, S.R.; Freund, A.; Campeau, E.; Davalos, A.R.; Campisi, J. Persistent DNA damage signalling triggers senescence-associated inflammatory cytokine secretion. *Nat. Cell Biol.* **2009**, *11*, 973–979. [[CrossRef](#)]
- Rodier, F.; Munoz, D.P.; Teachenor, R.; Chu, V.; Le, O.; Bhaumik, D.; Coppe, J.P.; Campeau, E.; Beausejour, C.M.; Kim, S.H.; et al. DNA-SCARS: Distinct nuclear structures that sustain damage-induced senescence growth arrest and inflammatory cytokine secretion. *J. Cell Sci.* **2011**, *124*, 68–81. [[CrossRef](#)]
- Klemm, S.L.; Shipony, Z.; Greenleaf, W.J. Chromatin accessibility and the regulatory epigenome. *Nat. Rev. Genet.* **2019**, *20*, 207–220. [[CrossRef](#)]
- Talbert, P.B.; Henikoff, S. Histone variants at a glance. *J. Cell Sci.* **2021**, *134*, jcs.244749. [[CrossRef](#)] [[PubMed](#)]
- Talbert, P.B.; Henikoff, S. Histone variants on the move: Substrates for chromatin dynamics. *Nat. Rev. Mol. Cell Biol.* **2017**, *18*, 115–126. [[CrossRef](#)] [[PubMed](#)]
- Contrepois, K.; Coudereau, C.; Benayoun, B.A.; Schuler, N.; Roux, P.F.; Bischof, O.; Courbeyrette, R.; Carvalho, C.; Thuret, J.Y.; Ma, Z.; et al. Histone variant H2A.J accumulates in senescent cells and promotes inflammatory gene expression. *Nat. Commun.* **2017**, *8*, 14995. [[CrossRef](#)] [[PubMed](#)]
- Isermann, A.; Mann, C.; Rube, C.E. Histone Variant H2A.J Marks Persistent DNA Damage and Triggers the Secretory Phenotype in Radiation-Induced Senescence. *Int. J. Mol. Sci.* **2020**, *21*, 9130. [[CrossRef](#)]
- Rube, C.E.; Baumert, C.; Schuler, N.; Isermann, A.; Schmal, Z.; Glanemann, M.; Mann, C.; Scherthan, H. Human skin aging is associated with increased expression of the histone variant H2A.J in the epidermis. *NPJ Aging Mech. Dis.* **2021**, *7*, 7. [[CrossRef](#)]
- Wingett, S.W.; Andrews, S. FastQ Screen: A tool for multi-genome mapping and quality control. *F1000Res* **2018**, *7*, 1338. [[CrossRef](#)]

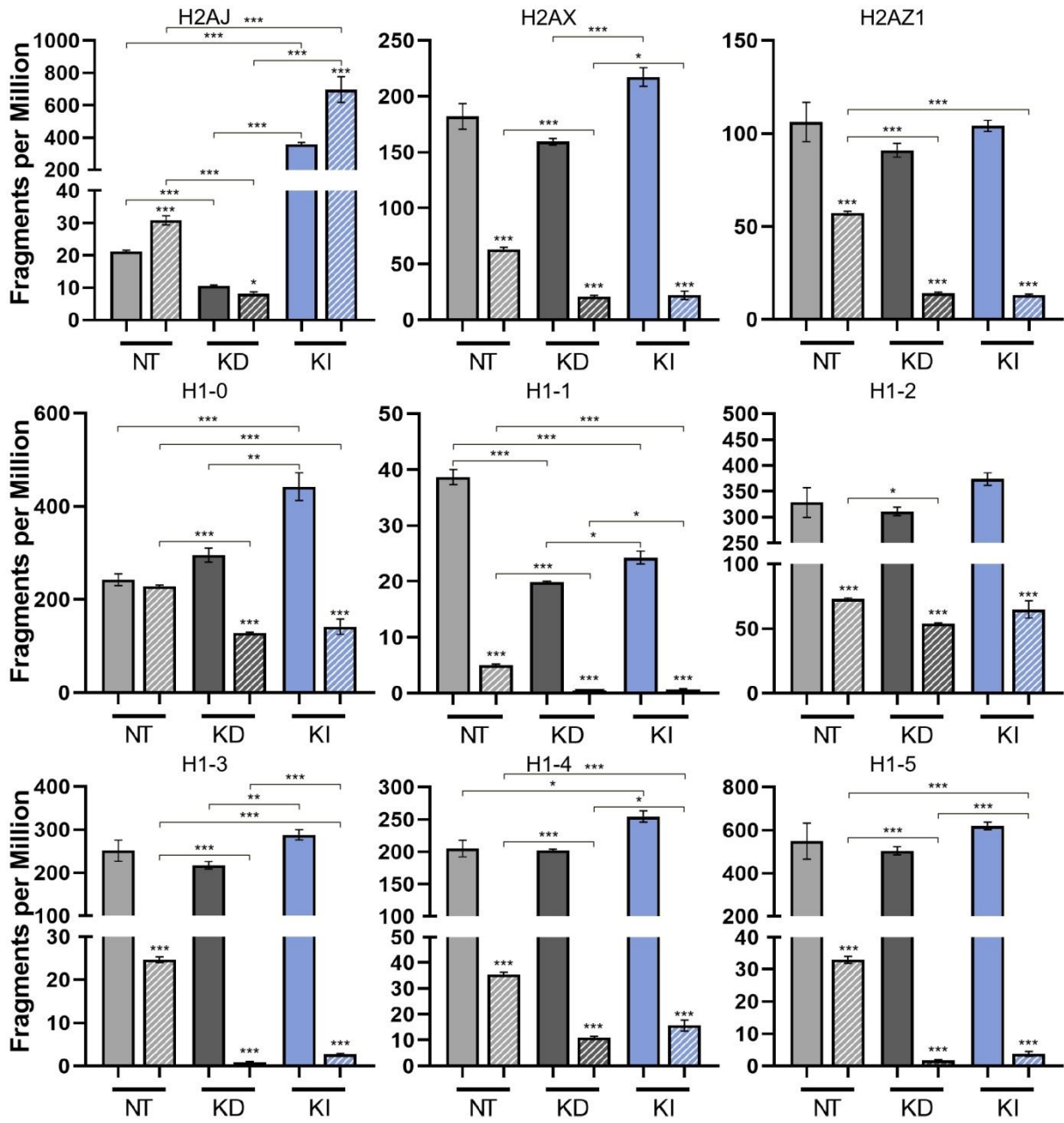
17. Frankish, A.; Diekhans, M.; Jungreis, I.; Lagarde, J.; Loveland, J.E.; Mudge, J.M.; Sisu, C.; Wright, J.C.; Armstrong, J.; Barnes, I.; et al. Gencode 2021. *Nucleic Acids Res.* **2021**, *49*, D916–D923. [[CrossRef](#)]
18. Li, H.; Durbin, R. Fast and accurate short read alignment with Burrows-Wheeler transform. *Bioinformatics* **2009**, *25*, 1754–1760. [[CrossRef](#)]
19. Anders, S.; Pyl, P.T.; Huber, W. HTSeq—A Python framework to work with high-throughput sequencing data. *Bioinformatics* **2015**, *31*, 166–169. [[CrossRef](#)]
20. Love, M.I.; Huber, W.; Anders, S. Moderated estimation of fold change and dispersion for RNA-seq data with DESeq2. *Genome Biol.* **2014**, *15*, 550. [[CrossRef](#)]
21. Zhang, Y.; Liu, T.; Meyer, C.A.; Eeckhoutte, J.; Johnson, D.S.; Bernstein, B.E.; Nusbaum, C.; Myers, R.M.; Brown, M.; Li, W.; et al. Model-based analysis of ChIP-Seq (MACS). *Genome Biol.* **2008**, *9*, R137. [[CrossRef](#)] [[PubMed](#)]
22. Heinz, S.; Benner, C.; Spann, N.; Bertolino, E.; Lin, Y.C.; Laslo, P.; Cheng, J.X.; Murre, C.; Singh, H.; Glass, C.K. Simple combinations of lineage-determining transcription factors prime cis-regulatory elements required for macrophage and B cell identities. *Mol. Cell* **2010**, *38*, 576–589. [[CrossRef](#)] [[PubMed](#)]
23. Hahne, F.; Ivanek, R. Visualizing Genomic Data Using Gviz and Bioconductor. *Methods Mol. Biol.* **2016**, *1418*, 335–351. [[CrossRef](#)] [[PubMed](#)]
24. Durinck, S.; Spellman, P.T.; Birney, E.; Huber, W. Mapping identifiers for the integration of genomic datasets with the R/Bioconductor package biomaRt. *Nat. Protoc.* **2009**, *4*, 1184–1191. [[CrossRef](#)] [[PubMed](#)]
25. Lawrence, M.; Huber, W.; Pages, H.; Aboyoun, P.; Carlson, M.; Gentleman, R.; Morgan, M.T.; Carey, V.J. Software for computing and annotating genomic ranges. *PLoS Comput. Biol.* **2013**, *9*, e1003118. [[CrossRef](#)]
26. Martinez-Zamudio, R.I.; Roux, P.F.; de Freitas, J.; Robinson, L.; Dore, G.; Sun, B.; Belenki, D.; Milanovic, M.; Herbig, U.; Schmitt, C.A.; et al. AP-1 imprints a reversible transcriptional programme of senescent cells. *Nat. Cell Biol.* **2020**, *22*, 842–855. [[CrossRef](#)]
27. Redon, C.E.; Schmal, Z.; Tewary, G.; Mangelinck, A.; Courbeyrette, R.; Thuret, J.Y.; Aladjem, M.I.; Bonner, W.M.; Rube, C.E.; Mann, C. Histone Variant H2A.J Is Enriched in Luminal Epithelial Gland Cells. *Genes* **2021**, *12*, 1665. [[CrossRef](#)]
28. Silk, E.; Zhao, H.; Weng, H.; Ma, D. The role of extracellular histone in organ injury. *Cell Death Dis.* **2017**, *8*, e2812. [[CrossRef](#)]
29. Rube, C.E.; Uthe, D.; Schmid, K.W.; Richter, K.D.; Wessel, J.; Schuck, A.; Willich, N.; Rube, C. Dose-dependent induction of transforming growth factor beta (TGF-beta) in the lung tissue of fibrosis-prone mice after thoracic irradiation. *Int. J. Radiat. Oncol. Biol. Phys.* **2000**, *47*, 1033–1042. [[CrossRef](#)]
30. Rube, C.E.; Uthe, D.; Wilfert, F.; Ludwig, D.; Yang, K.; Konig, J.; Palm, J.; Schuck, A.; Willich, N.; Remberger, K.; et al. The bronchiolar epithelium as a prominent source of pro-inflammatory cytokines after lung irradiation. *Int. J. Radiat. Oncol. Biol. Phys.* **2005**, *61*, 1482–1492. [[CrossRef](#)]
31. Beach, T.A.; Groves, A.M.; Johnston, C.J.; Williams, J.P.; Finkelstein, J.N. Recurrent DNA damage is associated with persistent injury in progressive radiation-induced pulmonary fibrosis. *Int. J. Radiat. Biol.* **2018**, *94*, 1104–1115. [[CrossRef](#)] [[PubMed](#)]
32. Borg, M.; Jiang, D.; Berger, F. Histone variants take center stage in shaping the epigenome. *Curr. Opin. Plant. Biol.* **2021**, *61*, 101991. [[CrossRef](#)]
33. Mangelinck, A.; Coudereau, C.; Courbeyrette, R.; Ourarhni, K.; Hamiche, A.; Redon, C.; Bonner, W.M.; van Dijk, E.; Derbois, C.; Olasso, R.; et al. The H2A.J histone variant contributes to Interferon-Stimulated Gene expression in senescence by its weak interaction with H1 and the derepression of repeated DNA sequences. *bioRxiv* **2020**. [[CrossRef](#)]
34. Funayama, R.; Saito, M.; Tanobe, H.; Ishikawa, F. Loss of linker histone H1 in cellular senescence. *J. Cell Biol.* **2006**, *175*, 869–880. [[CrossRef](#)] [[PubMed](#)]
35. Yan, F.; Powell, D.R.; Curtis, D.J.; Wong, N.C. From reads to insight: A hitchhiker’s guide to ATAC-seq data analysis. *Genome Biol.* **2020**, *21*, 22. [[CrossRef](#)]
36. Taghizadeh-Hesary, F.; Houshyari, M.; Farhadi, M. Mitochondrial metabolism: A predictive biomarker of radiotherapy efficacy and toxicity. *J. Cancer Res. Clin. Oncol.* **2023**, 1–23. [[CrossRef](#)] [[PubMed](#)]
37. Zhang, R.; Poustovoitov, M.V.; Ye, X.; Santos, H.A.; Chen, W.; Daganzo, S.M.; Erzberger, J.P.; Serebriiskii, I.G.; Canutescu, A.A.; Dunbrack, R.L.; et al. Formation of MacroH2A-containing senescence-associated heterochromatin foci and senescence driven by ASF1a and HIRA. *Dev. Cell* **2005**, *8*, 19–30. [[CrossRef](#)]
38. Aird, K.M.; Iwasaki, O.; Kossenkov, A.V.; Tanizawa, H.; Fatkhutdinov, N.; Bitler, B.G.; Le, L.; Alicea, G.; Yang, T.L.; Johnson, F.B.; et al. HMG2 orchestrates the chromatin landscape of senescence-associated secretory phenotype gene loci. *J. Cell Biol.* **2016**, *215*, 325–334. [[CrossRef](#)]
39. Gonzalez, L.C.; Ghadaouia, S.; Martinez, A.; Rodier, F. Premature aging/senescence in cancer cells facing therapy: Good or bad? *Biogerontology* **2016**, *17*, 71–87. [[CrossRef](#)]
40. Gevry, N.; Chan, H.M.; Laflamme, L.; Livingston, D.M.; Gaudreau, L. p21 transcription is regulated by differential localization of histone H2A.Z. *Genes Dev.* **2007**, *21*, 1869–1881. [[CrossRef](#)]

Disclaimer/Publisher’s Note: The statements, opinions and data contained in all publications are solely those of the individual author(s) and contributor(s) and not of MDPI and/or the editor(s). MDPI and/or the editor(s) disclaim responsibility for any injury to people or property resulting from any ideas, methods, instructions or products referred to in the content.

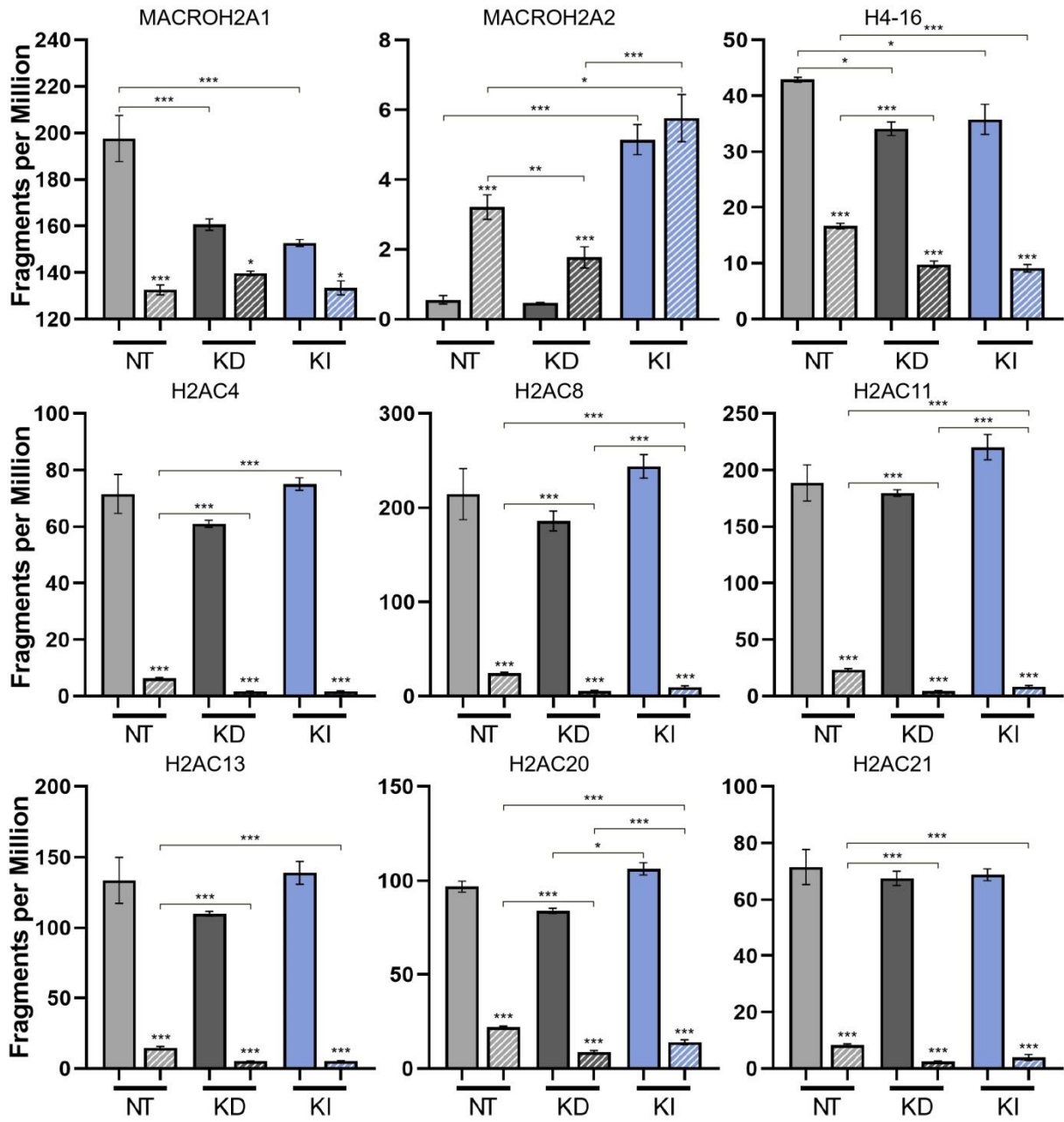
RNA Seq volcano plots



Histone expression (RNA-seq)



Histone expression (RNA-seq)



7.2 Publication 2

Table 2 Literature information of publication II

Title	Nuclear Fragility in Radiation-Induced Senescence: Blebs and Tubes Visualized by 3D Electron Microscopy
Authors and Affiliations	Benjamin M. Freyter ^{1,†} , Mutaz A. Abd Al-razaq ^{1,†} , Anna Isermann ¹ , Anne Dietz ² , Omid Azimzadeh ² , Liesbeth Hekking ³ , Maria Gomolka ² and Claudia E. Rube ^{1,*}
	¹ Department of Radiation Oncology, Saarland University Medical Center, Kirrbergerstrasse Building 6.5, 66421 Homburg, Germany; benjamin.freyter@uks.eu (B.M.F.); mutaz.abd-al-razaq@uks.eu (M.A.A.A.-r.); anna.isermann@uks.eu (A.I.)
	² Department of Effects and Risks of Ionising & Non-Ionising Radiation, Federal Office for Radiation Protection, 85764 Oberschleißheim, Germany; adietz@bfs.de (A.D.); oazimzadeh@bfs.de (O.A.); MGomolka@bfs.de (M.G.)
	³ Thermo Fisher Scientific, 5651 Eindhoven, The Netherlands; liesbeth.hekking@thermofisher.com
	* Correspondence: claudia.ruebe@uks.eu ; Tel.: +49-6841-1634614; Fax: +49-6841-1624699
	† These authors contributed equally to this work.
Journal	Cells
Impact factor	7.666

Publication status	Published
Year of publication	2022
Type of article	Research article
Volume	11
Pages	273-289
DOI:	https://doi.org/10.3390/cells11020273

Article

Nuclear Fragility in Radiation-Induced Senescence: Blebs and Tubes Visualized by 3D Electron Microscopy

Benjamin M. Freyter^{1,†}, Mutaz A. Abd Al-razaq^{1,†}, Anna Isermann¹ , Anne Dietz², Omid Azimzadeh² , Liesbeth Hekking³, Maria Gomolka² and Claudia E. Rube^{1,*} 

¹ Department of Radiation Oncology, Saarland University Medical Center, Kirrbergerstrasse Building 6.5, 66421 Homburg, Germany; benjamin.freyter@uks.eu (B.M.F.); mutaz.abd-al-razaq@uks.eu (M.A.A.A.-r.); anna.isermann@uks.eu (A.I.)

² Department of Effects and Risks of Ionising & Non-Ionising Radiation, Federal Office for Radiation Protection, 85764 Oberschleißheim, Germany; adietz@bfs.de (A.D.); oazimzadeh@bfs.de (O.A.); MGomolka@bfs.de (M.G.)

³ Thermo Fisher Scientific, 5651 Eindhoven, The Netherlands; liesbeth.hekking@thermofisher.com

* Correspondence: claudia.ruebe@uks.eu; Tel.: +49-6841-1634614; Fax: +49-6841-1624699

† These authors contributed equally to this work.



Citation: Freyter, B.M.; Abd Al-razaq, M.A.; Isermann, A.; Dietz, A.; Azimzadeh, O.; Hekking, L.; Gomolka, M.; Rube, C.E. Nuclear Fragility in Radiation-Induced Senescence: Blebs and Tubes Visualized by 3D Electron Microscopy. *Cells* **2022**, *11*, 273. <https://doi.org/10.3390/cells11020273>

Academic Editors: Alessandro Attanzio, Erica Buoso, Fabrizio Biundo and Christoph Englert

Received: 22 October 2021

Accepted: 12 January 2022

Published: 13 January 2022

Publisher's Note: MDPI stays neutral with regard to jurisdictional claims in published maps and institutional affiliations.



Copyright: © 2022 by the authors. Licensee MDPI, Basel, Switzerland. This article is an open access article distributed under the terms and conditions of the Creative Commons Attribution (CC BY) license (<https://creativecommons.org/licenses/by/4.0/>).

Abstract: Irreparable DNA damage following ionizing radiation (IR) triggers prolonged DNA damage response and induces premature senescence. Cellular senescence is a permanent state of cell-cycle arrest characterized by chromatin restructuring, altered nuclear morphology and acquisition of secretory phenotype, which contributes to senescence-related inflammation. However, the mechanistic connections for radiation-induced DNA damage that trigger these senescence-associated hallmarks are poorly understood. In our in vitro model of radiation-induced senescence, mass spectrometry-based proteomics was combined with high-resolution imaging techniques to investigate the interrelations between altered chromatin compaction, nuclear envelope destabilization and nucleo-cytoplasmic chromatin blebbing. Our findings confirm the general pathophysiology of the senescence-response, with disruption of nuclear lamin organization leading to extensive chromatin restructuring and destabilization of the nuclear membrane with release of chromatin fragments into the cytosol, thereby activating cGAS-STING-dependent interferon signaling. By serial block-face scanning electron microscopy (SBF-SEM) whole-cell datasets were acquired to investigate the morphological organization of senescent fibroblasts. High-resolution 3-dimensional (3D) reconstruction of the complex nuclear shape allows us to precisely visualize the segregation of nuclear blebs from the main nucleus and their fusion with lysosomes. By multi-view 3D electron microscopy, we identified nanotubular channels formed in lamin-perturbed nuclei of senescent fibroblasts; the potential role of these nucleo-cytoplasmic nanotubes for expulsion of damaged chromatin has to be examined.

Keywords: cellular senescence; ionizing radiation; radiation-induced senescence; chromatin reorganization; nuclear blebbing; transmission electron microscopy (TEM); serial block-face scanning electron microscopy (SBF-SEM); cytosolic chromatin fragments (CCF); cGAS-STING signaling

1. Introduction

Cellular senescence is a complex stress response leading to permanent cell cycle arrest with resistance to mitogenic or apoptotic signals [1]. Senescent cells are characterized by extensive chromatin restructuring with formation of senescence-associated heterochromatic foci (SAHF) and altered nuclear morphology. Senescent cells acquire the senescence-associated secretory phenotype (SASP), with increased production of pro-inflammatory cytokines [2,3]. Accumulation of senescent cells during aging has been implicated in promoting various age-related diseases [4,5]. As cellular senescence is characterized as the basis for aging in organisms, culturing of normal human fibroblasts to mimic the in vivo

aging processes has been developed as major methods to investigate cellular and molecular events involved in aging [6].

Normal cells undergo premature senescence in response to severe or irreparable DNA damage, induced, e.g., by ionizing radiation (IR) [3]. Radiation-induced DNA damage, such as double-strand breaks (DSBs), triggers DNA damage response (DDR) mechanisms to coordinate DSB repair activities within the chromatin context [7,8]. During this DDR, multiple repair proteins are recruited to DSB sites, forming radiation-induced foci (e.g., γ H2AX- and 53BP1-foci) [9,10]. Focal accumulation of DSB repair factors around persisting DNA lesions is a characteristic feature of cellular senescence [11].

Senescent cells undergo striking morphological changes with irregular-shaped nuclei characterized by protrusions and invaginations. Recent work highlighted the important role of the nuclear envelope in regulating chromatin organization and maintaining nuclear stability [12]. The nuclear envelope consists of an outer nuclear membrane continuous with the endoplasmic reticulum, and an inner nuclear membrane facing the nucleoplasm and nuclear pore complexes. The inner surface of the nuclear envelope is lined by lamina, which contributes to the size, shape, and stability of the nucleus [13]. Major structural components of this filament meshwork are the nuclear lamins, categorized as A-type and B-type lamins. Opening of these separate but interacting lamin meshworks is responsible for nuclear bleb formation [14]. Lamins have also been found to interact with chromatin by forming physical connections at the nuclear periphery [15]. These structural associations of the nuclear lamina with peripheral chromatin called lamina-associated domains (LADs) mediate functional organization of the genome [16,17]. Previous studies in oncogene-induced senescence have shown that the dissociation of the lamina from peripheral heterochromatin is associated with the formation of SAHFs [18].

Persistent DDR signaling is essential to establish and maintain the SASP in senescent cells [3,19]. However, the mechanisms linking DDR and SASP in radiation-induced senescence are incompletely explored. Recent studies suggest that nucleus-to-cytoplasm blebbing of chromatin with the formation of cytoplasmic chromatin fragments (CCFs) may connect these central concepts in cellular senescence [20,21]. Chromatin fragments released into the cytosol by nuclear envelope ruptures can be recognized by cyclic GMP-AMP synthase (cGAS) protein, and may thereby activate stimulator of interferon genes (STING). This cGAS-STING signaling pathway is a first line defence component of the innate immune system that mediates type I interferon inflammatory responses to repel viral and bacterial infections [22]. Only recently has it been shown that the cGAS-STING signaling is also activated by endogenous DNA aberrantly localized in the cytosol, such as extranuclear chromatin resulting from genotoxic stress [23]. Accordingly, recognition of CCFs by the cGAS-STING pathway could be essential for the induction of SASP in senescent cells [22].

During senescence progression, the precise mechanisms governing the assembly and expulsion of damaged chromatin through the nuclear membrane are still unclear. Combining proteome analysis with different high-resolution imaging techniques, we comprehensively investigate the interrelations between altered chromatin compaction, nuclear envelope destabilization, and nucleus-to-cytoplasm blebbing during radiation-induced senescence.

2. Materials and Methods

Cell culture: Human WI-38 fibroblasts were obtained from the American Type Culture Collection (ATCC NPO, Manassas, VA, USA). Fibroblasts were cultured at 5% O₂ and 5% CO₂ in Minimum Essential Media (MEM; Invitrogen, Karlsruhe, Germany) with 10% fetal bovine serum, 1 mM sodium pyruvate, 2 mM L-glutamine, 0.1 mM non-essential amino acids, and 1% penicillin/streptomycin. For monolayer experiments, cells were grown on coverslips to 90% confluence before starting experiments; for protein analysis cells were grown in T75 flasks.

Radiation exposure: Fibroblasts were irradiated with 20 Gy using Artiste™ linear accelerator (Siemens, Munich, Germany) (6 MV photons; dose-rate 2 Gy/min). After IR exposure fibroblasts were cultured for 2 weeks and compared to non-irradiated controls.

Cytochemical detection of SA- β -Gal: Following 5 min fixation with 2% paraformaldehyde and 0.2% glutaraldehyde, cells were incubated with X-Gal staining solution (AppliChem GmbH, Darmstadt, Germany) at 37 °C overnight. After 30 s methanol incubation, dried samples were permeabilized with 0.2% TritonX-100 and washed with 1% BSA. Samples were blocked with 4% BSA for 1 h, followed by an overnight incubation with anti-H2A.J primary antibody. Incubation with Dako biotinylated secondary antibody (Agilent, Waldbronn, Germany) was followed by Vectastain ABC Peroxidase (Vector, Burlingame, CA, USA) and SIGMAFAST™ 3,3'-diaminobenzidine (Merck, Darmstadt, Germany) incubations, respectively. Samples were mounted in Dako Faramount Mounting Medium (Agilent, Waldbronn, Germany).

2'3'-cGAMP ELISA: 2 weeks after (sham-) IR exposure, medium of 20 Gy-irradiated and non-irradiated fibroblasts was aspirated and cells were gently washed with phosphate-buffered solution (PBS; ThermoFisher Scientific) and lysed using M-PER™ Mammalian Protein Extraction Reagent. Lysates were centrifuged at 13,000 \times g for 10 min at 4 °C. 2'3'-cGAMP concentration was measured in supernatants using 2'3'-cGAMP ELISA assay (Cayman Chemical, Ann Arbor, MI, USA), and data were analyzed using four-parameter log fit according to manufacturer's manual.

Immunofluorescence microscopy (IFM): Cells were fixed with 4% paraformaldehyde and permeabilized with 0.5% TritonX-100, washed with 0.1% Tween®20 and incubated overnight with primary antibody (anti-p21, Abcam, Berlin, Germany; anti-Ki67 ThermoFisher, Waltham, MA, USA; anti-BrdU, Bio-Rad Laboratories, Munich, Germany; anti-Lamin B1, Proteintech, Manchester, UK; anti-H3K27me3 and anti-H3K9me3, Abcam, Berlin, Germany; anti-53BP1, Bethyl, Montgomery, TX, USA; anti- γ H2AX, MilliporeSigma, Sigma-Aldrich Chemie GmbH, Germany) followed by Alexa-Fluor®488 or Alexa-Fluor®568 secondary antibody (Invitrogen, Karlsruhe, Germany). Subsequently, cells were mounted in VECTAshield™ mounting medium with 4',6-diamidino-2-phenylindole (DAPI, Vector Laboratories, Burlingame, CA, USA). Fluorescence images were captured with Nikon-Eclipse Ni fluorescence microscope equipped with Nikon DS-Qi2 camera (Nikon, Düsseldorf, Germany). For evaluating SA- β -Gal, p21, Ki67 and BrdU positivity, at least 200 cells were captured for each sample (positive cells in %). For the measurement of lamin B1 fluorescence intensity the FITC signal was normalized to DAPI signal in 200 cells using Nikon NIS-Elements Basic Research acquisition software (Nikon, Düsseldorf, Germany).

BrdU labeling: To test the stability of senescence-associated growth arrest, 20 Gy-irradiated and non-irradiated cells were pulsed with 10 μ mol/L 5-bromo-2'-deoxyuridine (BrdU) in culture medium for 24 h. After medium removal and PBS washing steps, cells were fixed and permeabilized as described for standard IFM. DNA denaturation was completed through 1 h incubation in 2 M HCl. Following, the cells were washed with PBS and incubated for 2 h in primary anti-BrdU antibody (Bio-Rad Laboratories, Munich, Germany) in 0.1% Tween, 1% bovine serum albumin (BSA) in PBS. After washes of Tween/BSA/PBS, samples were incubated with fluorescence-coupled anti-rat secondary antibody in Tween/BSA/PBS for 2 h. After PBS washes, coverslips were mounted with hard-set mounting medium containing DAPI.

Protein extraction and determination of protein concentration: Cell pellets (1×10^6) were thawed on ice before lysed in radio-immunoprecipitation assay (RIPA) buffer containing 25 mM Tris.HCl (pH 7.6), 150 mM NaCl, 1% NP-40, 1% sodium deoxycholate, 0.1% SDS + 1 \times Halt™ Protease and Phosphatase Inhibitor Cocktail (Thermo Fisher Scientific, USA). The reaction was suspended and incubated on ice for 15 min followed by 5 min incubation at 95 °C. To achieve efficient cell disruption, reaction was subjected to Bioruptor® Pico sonication device (Diagenode, Belgium) with 5 sonication cycles (30 s ON/30 s OFF) at 4 °C followed by centrifugation (10 min, 22,000 \times g, 4 °C). Supernatants containing protein lysate were transferred to LoBind tubes. Protein concentrations were determined

in duplicate by RC DC™ kit as recommended by the manufacturer (Bio-Rad Laboratories, Inc., Hercules, CA, USA) using bovine serum albumin (BSA) as standard on Infinite M200 Spectrophotometer (Tecan GmbH, Germany). For mass spectrometry analyses, 5 µg of each protein lysate was used.

High-performance liquid chromatography online coupled to tandem mass spectrometry (HPLC-MS/MS): Protein lysates were digested using modified filter-aided sample preparation (FASP) protocol, as described [24,25]. MS data were acquired on Q-Exactive HF-X mass spectrometer (Thermo Fisher Scientific, Waltham, MA, USA) coupled to nano-RSLC (Ultimate 3000 RSLC; Dionex, Thermo Fisher Scientific, Waltham, MA, USA) [26]. Proteome Discoverer (PD) 2.4 software (Thermo Fisher Scientific; version 2.4.1.15) was used for peptide and protein identification via database search (Sequest HT search engine) against the Swiss-Prot human database (Release 2020_02, 20349 sequences in PD). Peptide spectrum matches and peptides were performed by accepting only top-scoring hit for each spectrum, and satisfying cut-off values for FDR < 1%, and posterior error probability < 0.01. The final protein ratio was calculated using the median abundance values of 4 replicates for each of the experimental groups. Statistical significance of the ratio change was ascertained employing the *t*-test approach. For final quantifications, proteins identified with more than one unique peptide in at least 2 of 3 replicates and having ratios greater than 1.5-fold or less than 0.66-fold (adj. *p*-value < 0.05) were defined as being significantly differentially expressed. Pathway analysis was performed using ReactomePA.

Transmission electron microscopy (TEM): Cells were fixed overnight using 2% paraformaldehyde and 0.05% glutaraldehyde in PBS. Samples were dehydrated in increasing ethanol concentrations and infiltrated overnight with LR White resin (EMS, Hatfield, PA, USA) followed by overnight embedding at 65 °C with fresh LR White resin containing LR White Accelerator (EMS, Hatfield, PA, USA). Microtome Ultracut UCT (Leica, Wetzlar, Germany) and diamond knife (Diatome, Biel, Switzerland) were used to acquire ultrathin sections (70 nm) picked up on pioloform-coated nickel grids and prepared for immunogold-labelling. Non-specific labeling was blocked using Aurion blocking solution (Aurion, Wageningen, The Netherlands), sections were rinsed and incubated overnight with primary antibodies (anti-Lamin B1, Proteintech, Manchester, UK) at 4 °C, followed by incubation with 10 nm gold particle-conjugated secondary antibodies (Aurion, Wageningen, The Netherlands) for 1.5 h. Finally, sections were contrasted with uranyl acetate. Tecnai Biotwin™ transmission electron microscope (FEI, Eindhoven, The Netherlands) was employed for visual analysis.

Serial block-face scanning electron microscopy (SBF-SEM): Cells were fixed using 1.25% glutaraldehyde, 2.5% paraformaldehyde, and 2 mM CaCl₂ in 0.15 M cacodylate buffer (pH 7.4; EMS, Hatfield, PA, USA) at 4 °C, followed by 2% OsO₄, 1% uranyl acetate and en-block lead aspartate contrasting steps and ethanol/acetone step-wise dehydration. Samples were infiltrated overnight using increasing proportions of Durcupan (EMS, Hatfield, PA, USA) in acetone solutions. Embedding steps were performed at 65 °C with fresh Durcupan resin. Finally, samples were detached from coverslips by shrinking Durcupan resin by rapid temperature reduction and attached to sample holders for SEM imaging. For high-resolution imaging of the ultrastructure of senescent fibroblasts, serial block-face imaging was performed in VolumeScope™ SEM (Thermo Fisher Scientific, Waltham, MA, USA). Serial block-face imaging combines mechanical sectioning using a chamber microtome with automated image acquisition to obtain large sample volumes. Slice thickness was 50 nm and images were acquired in low vacuum (30 Pa) with 2 kV, current of 100 pA and dwelltime of 2 µs. For 3D reconstruction, the entire volume of whole cells was captured through stacking of sequential images and micrographs were manually segmented using analytical software Amira 6.7.0 (Thermo Fisher Scientific, Waltham, MA, USA).

Statistical Analysis: Data were presented as mean ± SEM, where normally distributed data were analyzed by Student's *t*-test to evaluate differences between 20 Gy-irradiated and non-irradiated cells. Statistical analyses were performed by Graphpad Prism 9.2.0

(Graphpad Software, San Diego, CA, USA). Statistical significance was presented as * $p < 0.05$, ** $p < 0.01$, *** $p < 0.001$.

3. Results

3.1. Premature Senescence after High-Dose IR Exposure

Previous studies in our lab showed that irreparable DSBs in response to IR trigger prolonged DDR and induce premature senescence in human WI-38 fibroblasts [3].

After IR exposure (20 Gy, 2 w post-IR), $\approx 90\%$ of WI-38 fibroblasts showed increasing staining intensities for the senescence marker SA- β -Gal and p21, suggesting progressive entry of these cells into radiation-induced senescence (Figure 1A). Reduced proliferation rates of 20 Gy-irradiated fibroblasts were verified by clearly diminished Ki67 expression and reduced BrdU incorporation (Figure 1B). Moreover, the expression of lamin B1 was explored by IFM and TEM. In non-irradiated fibroblasts lamin B1 was evenly expressed at the inner surface of the nuclear membrane, but in 20 Gy-irradiated fibroblasts lamin B1 was strongly down-regulated (Figure 1C). For lamin B1 the relative fluorescence intensity (IFM: FITC signal normalized to DAPI by Nikon NIS-Elements™) and relative protein abundance (proteome analysis by HPLC-MS/MS; LMNB1 in Supplementary Table S1) was measured in non-irradiated versus irradiated fibroblasts. Both measurement methods for lamin B1 quantification confirmed the senescence-associated lamina decline, potentially affecting the integrity and stability of the nuclear membrane (Figure 1C). Our data indicate that radiation exposure to 20 Gy induces reliably premature senescence in human fibroblasts and thus represents an excellent model to study the nuclear fragility during radiation-induced senescence.

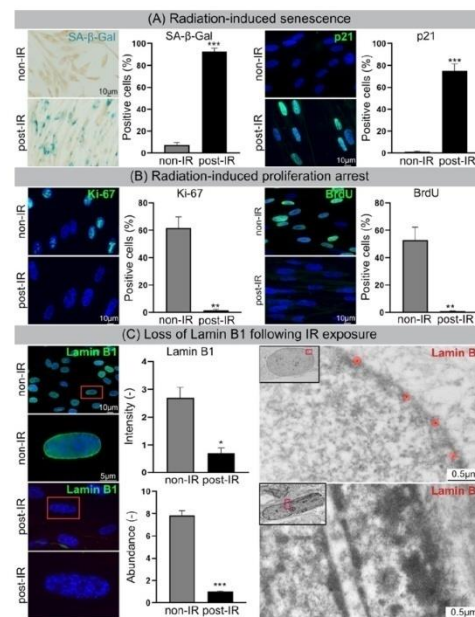


Figure 1. Cellular senescence following IR. (A) Increased numbers of SA- β -Gal-positive and p21-positive cells following IR. (B) Decrease in Ki-67-positive and BrdU-positive cells. (C) Lamin B1 loss in nuclear envelope following IR exposure visualized by IFM (left) and TEM (right). Quantification of lamin B1 in WI-38 fibroblasts by IFM (top middle), and MS (bottom middle). Data are presented as mean \pm SEM, * $p < 0.05$, ** $p < 0.01$, *** $p < 0.001$.

3.2. Proteome Analysis

Label-free proteome analysis was performed to generate comprehensive protein profiles in 20 Gy-irradiated versus non-irradiated WI-38 fibroblasts. Principal component analysis (PCA) (based on normalized intensity of all identified proteins) indicates that 20 Gy- and non-irradiated samples clustered into two separate groups (PC1 49.7% and PC2 24.7%) (Supplementary Figure S1). Among 4142 quantified proteins with at least two unique peptides (Supplementary Table S1), the expression of 96 proteins was significantly different (+1.5-fold; adj. p -value < 0.05) after IR. Out of those, 58 proteins were down- and 38 up-regulated (Figure 2A and Supplementary Table S2). Detailed analysis of functional interactions was performed using R package ReactomePA to screen for different pathways involved in radiation-induced senescence. Most affected pathways in 20 Gy-irradiated versus non-irradiated fibroblasts were related to DNA damage/telomere stress induced senescence, chromatin organization and SAHF formation (Figure 2B and Supplementary Table S3). Accordingly, our proteome data are in line with previous studies, showing that cellular senescence is characterized by extensive chromatin restructuring with global histone H1 loss and SAHF formation, as well as with nuclear degradation of lamin B1 (Supplementary Table S4). Moreover, our proteome data suggest that interferon signaling may drive the production of inflammatory SASP components (Figure 2C).

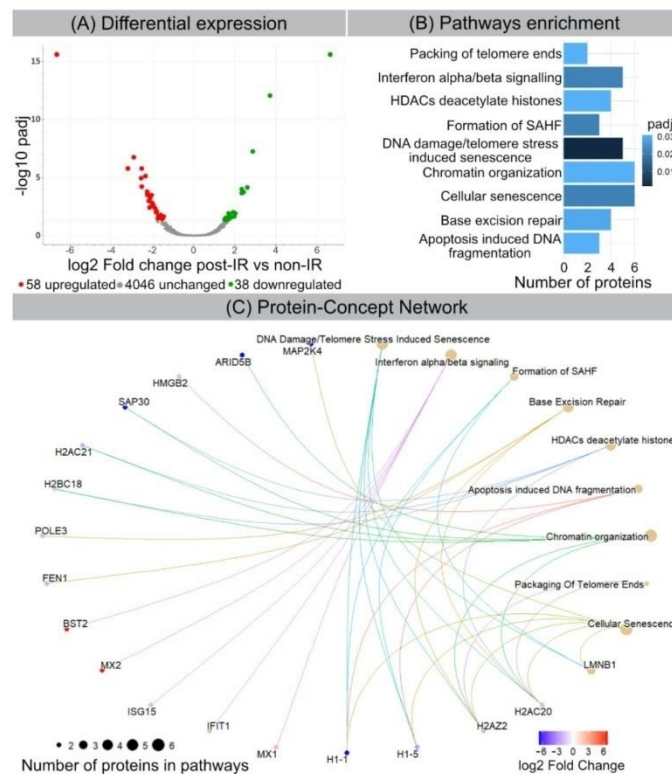


Figure 2. Radiation-induced changes in protein expression. (A) Volcano plot showing differential protein expression following IR. (B) Senescence-related pathway enrichment results were generated using ReactomePA R package. (C) Visualization of enriched pathways components by enrichplot R package.

3.3. Chromatin Remodeling and Nuclear Blebbing during Radiation-Induced Senescence Visualized by IFM

Following IR exposure, human WI-38 fibroblasts undergo striking morphological changes during senescence progression, which can be visualized by IFM. While non-irradiated fibroblasts harbor more or less elongated, but smoothly ovoidal nuclei, senescent fibroblasts following IR exposure reveal enlarged nuclei with distorted morphologies and SAHFs visible as distinct DAPI-dense foci (Figure 3A). At their core, these SAHFs are enriched for heterochromatin marks, such as tri-methylation of histone H3 on lysine 9 (H3K9me3) and lysine 27 (H3K27me3), but generally exclude euchromatic markers (Figure 3A). Accordingly, chromatin layering in SAHF is associated with spatial segregation of different chromatin types and therefore demarcate active and repressed chromatin domains. Degradation of the nuclear envelope component lamin B1 and herniation of nuclear chromatin into the cytosol are well-described features of senescent cells. In accordance with this, cytosolic chromatin fragments (CCF) were visualized and quantified in 20 Gy-irradiated versus non-irradiated fibroblasts by IFM, based on their intense γ H2AX staining (Figure 3B). The percentage of CCF-positive cells was significantly increased in 20 Gy-irradiated compared to non-irradiated fibroblasts (Figure 3B, Supplementary Figure S2). These data suggest that radiation-induced senescence promotes the release of nuclear chromatin and the formation of CCFs.

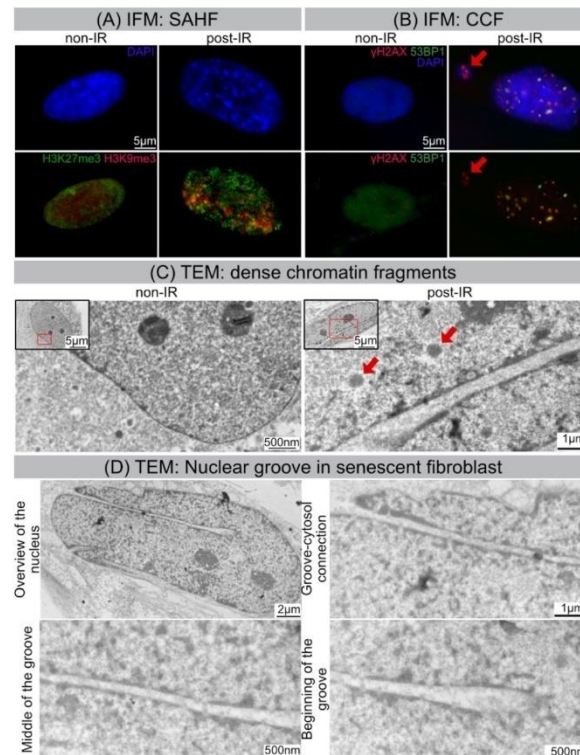


Figure 3. IR-induced morphological changes in WI-38 fibroblasts. **(A)** Visualization of SAHF formation by IFM. **(B)** Visualization of CCF formation by IFM. **(C)** Visualization of dense chromatin fragments (marked by red arrows) by TEM. **(D)** Visualization of nuclear groove in senescent fibroblast by TEM.

Cyclic GMP-AMP synthase (cGAS) protein acts as cytosolic DNA sensor that binds DNA and activates the cGAS-STING interferon signaling, a critical component of the innate immune response. In the presence of nucleic acids in the cytosol cGAS catalyzes the synthesis of cGAMP, that activates the adaptor protein STING (stimulator of interferon genes), thereby triggering an innate immune type I interferon response. In order to investigate potential activation of the cGAS-STING pathway in response to cytoplasmic DNA, we measured cGAMP concentrations by a colorimetric assay (cGAMP ELISA). The concentration of cGAMP was clearly increased in 20 Gy-irradiated, but not in non-irradiated fibroblasts, suggesting that cGAS-STING signaling contributes to the production of inflammatory cytokines in senescent cells (Supplementary Figure S2). The induction of the interferon immune response could be proven by our proteome analysis (Figure 2).

TEM allows us to study the internal ultrastructure of nuclei and to analyze specific features of chromatin compaction with much higher spatial resolutions. Our TEM studies show that interphase chromatin of non-irradiated fibroblasts revealed homogeneous ultrastructural appearance with more electron-dense roundish structures representing the nucleoli with more compacted ribosomal DNA (Figure 3C, left panel). These nucleoli have the highest RNA synthesis rate in cell nuclei and as site of ribosome biogenesis hold a pivotal role in cell metabolism [27]. Following IR exposure, nuclei of senescent fibroblasts exhibit dramatic alterations to their higher-order chromatin structure. Chromatin compaction in spatially defined domains leads to the assembly of dense chromatin fragments (circular electron-dense bodies of 500–600 nm in diameter). These heterochromatinized fragments, sometimes closely arranged in rows, are surrounded by more decondensed areas (Figure 3C, right panel).

3.4. Nuclear Grooves in Senescent Fibroblasts Visualized by TEM

High-resolution TEM was used for direct imaging the nuclear ultrastructure of senescent nuclei at nanometer resolution. While non-irradiated fibroblasts have regular nuclei without any nuclear blebs and grooves, $\approx 70\%$ of irradiated fibroblasts revealed grooved nuclei with invaginations of various depths and sizes. These irregular invaginations (sometimes multiple fissures within one cell) were observed in different parts of senescent nuclei and seemed to be formed by nuclear membranes. TEM has an unparalleled resolution in X and Y dimensions, but due to limited field views and absence of Z dimensions, it can generate only fragmented 2D views of senescent cells. Therefore, we used volume electron microscopy to identify and localize deep irregular-formed invaginations in three-dimensional space.

3.5. High-Resolution Imaging of Senescent Fibroblasts by SBF-SEM

Serial block-face scanning electron microscopy (SBF-SEM) is a powerful method to analyze the cellular ultrastructure in three dimensions (3D). After optimising contrasting and embedding conditions for fibroblast monolayers, the sample block was sectioned and imaged in sequence every 50 nm within the scanning electron microscope. This automated acquisition of serial-section imaging data covered the volume of entire fibroblasts (Figure 4A). The resulting EM image stacks were segmented manually for different organelles and reconstructed using AMIRA software. Figure 4 shows the 3D reconstruction of whole senescent fibroblast with accurate segmentation of the nucleus (light-blue), nucleoli (red), CCF (light-red) and lysosomes (blue) to study their characteristic morphologies (Figure 4B).

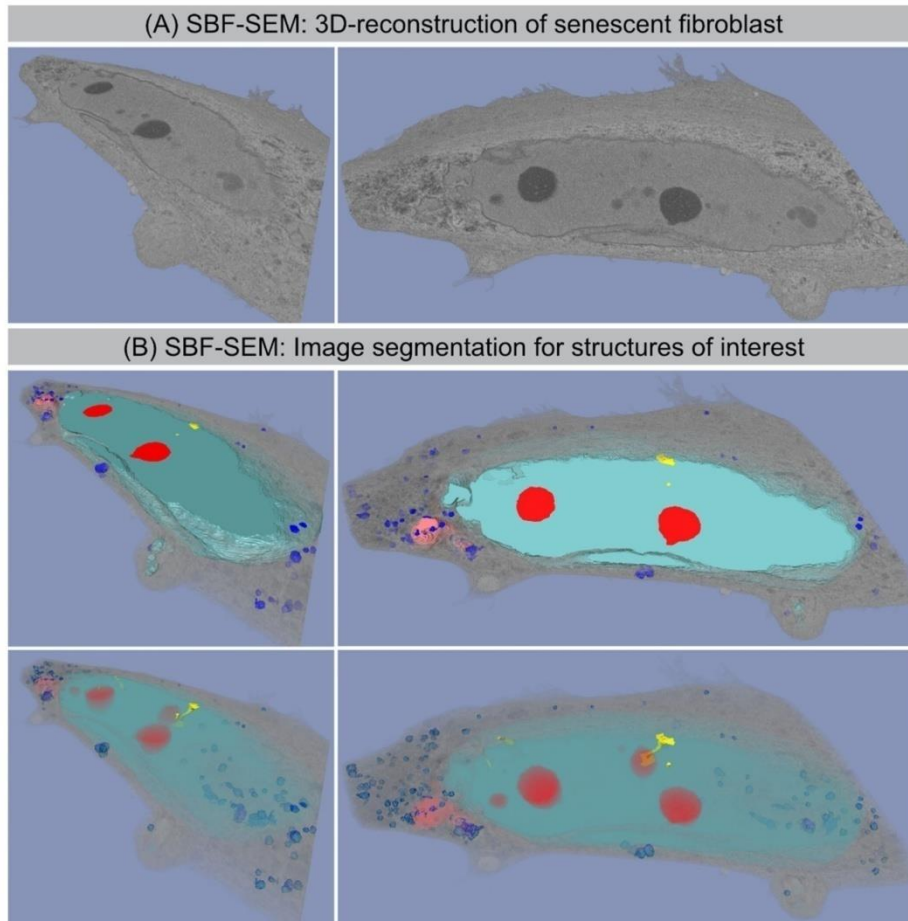


Figure 4. SBF-SEM: 3D reconstruction of senescent fibroblast. (A) Original SBF-SEM sections were used for 3D reconstruction. (B) Serial SBF-SEM sections were segmented for structures of interest: nucleus (light-blue), nucleoli (red), lysosomes (blue), and CCF (light-red), nanotubes (yellow), cytosol (gray) and used for 3D visualization (bottom row: transparent view).

3.6. SBF-SEM: Visualization of CCF Segregation

Computer-assisted segmentation and 3D reconstruction of sequential SEM images provide detailed views of the separation process of CCFs (light red) from the nucleus and their spatial relationship to lysosomes (blue) (Figure 5). Some CCFs are already spatially isolated from the main nucleus. In the cytoplasm, CCFs are targeted to the autophagy machinery, thereby initiating their lysosomal-mediated proteolytic degradation. Supplementary Figure S3 shows lysosomes (size $\sim 0.5\text{--}1\ \mu\text{m}$ in diameter) fusing with the outer membrane of detached CCFs (size $\sim 1\text{--}1.2\ \mu\text{m}$ in diameter), thereby initiating their autophagic degradation.

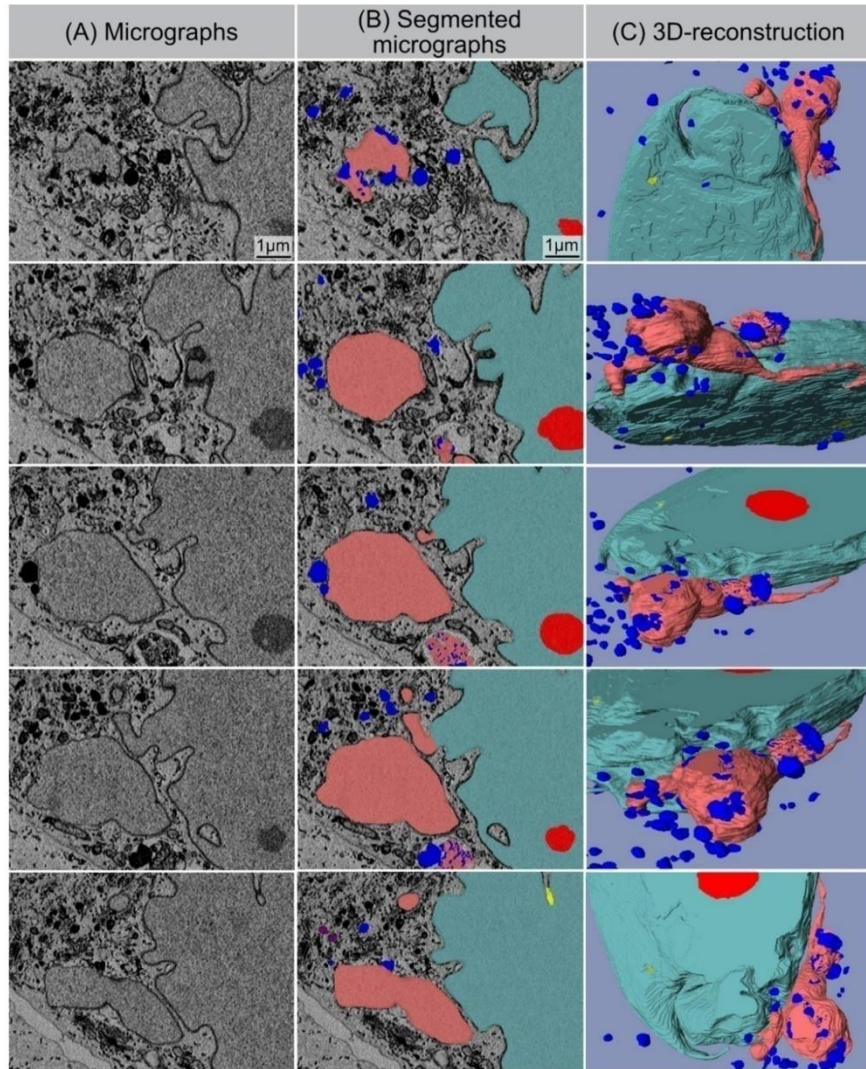


Figure 5. SBF-SEM: Separation process of CCF. (A) Original micrographs presenting detaching CCF. (B) Segmented micrographs of the same regions. (C) 3D reconstruction of detaching CCF: nucleus (light-blue), nucleoli (red), lysosomes (blue), and CCF (light-red), nanotubes (yellow).

3.7. SBF-SEM: Visualization of Nucleo-Cytoplasmic Nanotubes

Our SBF-SEM datasets also allowed for the accurate segmentation of the deep invaginations towards the interior of the nucleus, which likely represent the nuclear grooves observed by 2D TEM. These tube-like structures emerge from the nuclear surface at different positions in a non-specific manner, and physically connects the cytoplasm with deeper areas of the nucleus. These tunnel-like invaginations contain inner and outer nuclear membranes. Higher-magnification micrographs clearly evidence that these invaginations

touch the nucleolus and/or even cross the whole nucleus (Figure 6). The diameters of these intrusions range from 200 to 600 nm. This is very similar to the spatial dimensions obtained by our 2D TEM technique, indicating agreement and accurate quantification. Moreover, numerous electron dense particles (identical density as the nucleolus) could be visualized within these nuclear channels, suggesting a functional role for nuclear transport.

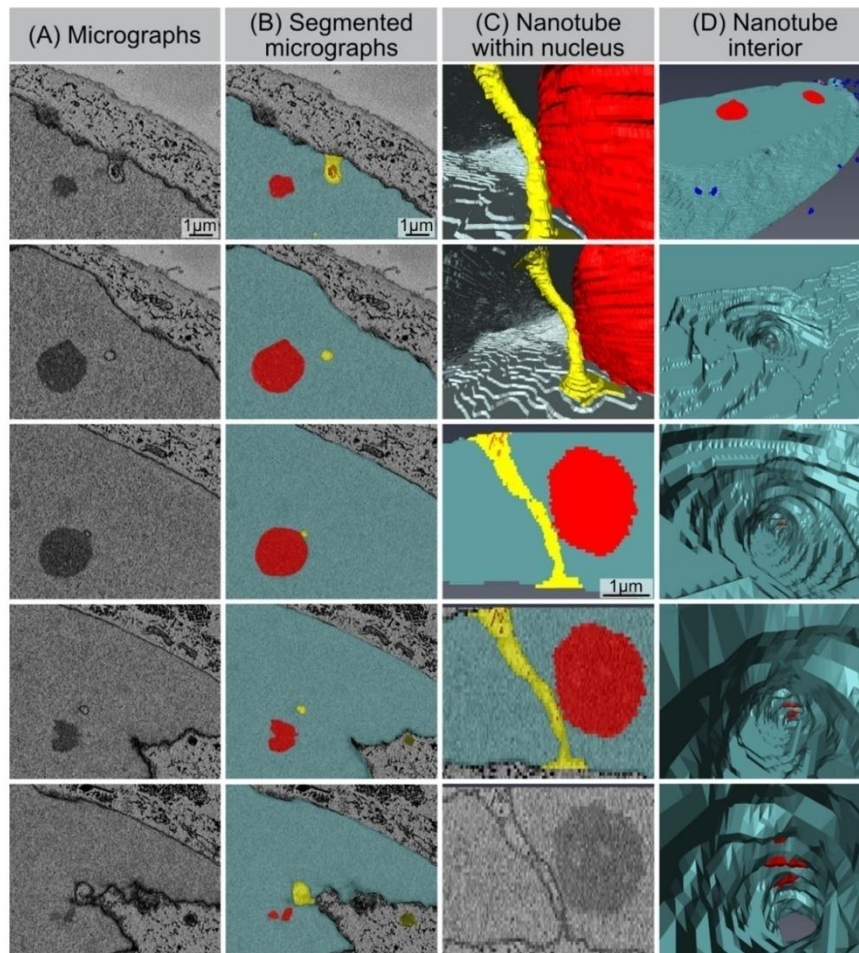


Figure 6. Nucleo-cytoplasmic nanotube. (A) Original micrographs showing cross-sections of the nanotube. (B) Segmented micrographs for the same area: nucleus (light-blue), nucleoli (red), nanotubes (yellow). (C) Models showing nanotube's appearance from within the nucleus (1st and 2nd image from top), segmented volume showing the nanotube from side (3rd and 4th image from top), and original micrograph of the same region. (D) Visualization of the nanotube's interior.

4. Discussion

In the 3D nuclear space, the hierarchical genome organization into chromatin serves to precisely orchestrate cellular functions by controlling gene expression [28]. Spatial genome conformation is modulated by interactions between heterochromatin and nuclear

lamina, providing peripheral tethering points to confer physiological chromatin organization. Accordingly, biophysical properties of the lamina are essential not only for the nuclear envelope stability, but also for maintaining the well-organized architecture of chromatin. Cellular senescence is characterized by the degradation of lamin B1, causing detachment of peripheral chromatin from the lamina, thereby leading to extensive chromatin restructuring. During senescence, the progressive destabilization of the nuclear envelope leads to the nucleus-to-cytoplasm blebbing of chromatin. For future studies, it will be an interesting point to study the role of CCFs in degrading nuclear components by autophagy. Previous work has shown that the autophagy protein LC3, which is involved in autophagy membrane trafficking and substrate delivery, is present in the nucleus and directly interacts with the nuclear lamina protein lamin B1, and binds to lamin-associated domains on chromatin [29]. Recent studies suggest that autophagy may be important in the regulation of cancer development and progression and in determining the response of tumor cells to anticancer therapy. The inhibition of lysosomal activities, thereby blocking the formation of autophagosomes that capture degraded components and then fuse with lysosomes to recycle these components, is a promising potential therapeutic target in cancer treatment [30].

Apart from radiation-induced senescence, cells exposed to high doses of IR can enter other modes of cell death mechanisms, such as apoptosis and necrosis [31]. Moreover, radiation-induced mitotic catastrophes may occur due to premature or improper entry of cells into mitosis in response to DNA damage and deficient cell cycle checkpoints. Disordered mitosis can produce atypical chromosome segregation and cell division and can lead to the formation of giant cells with aberrant nuclear morphology, multiple nuclei, and/or several micronuclei [31]. The generation of polyploid giant nuclei can disturb peripheral positioning of envelope-bound heterochromatin domains and can therefore disrupt the long-term balance of chromatin organization [32]. Recent work highlights the important role of lamina-associated heterochromatin domains of the structural and functional maintenance of nuclear architecture [33].

Here, we combined mass spectrometry-based proteomics and high-resolution microscopy techniques to study the hallmarks of radiation-induced senescence and to obtain insights into the pathophysiological role of nucleo-cytoplasmic chromatin blebbing. Our findings confirm the complex interrelations between chromatin restructuring in lamin-perturbed nuclei and nuclear envelope destabilization with the release of chromatin fragments into the cytosol [21]. Our results support the prevailing view that CCFs activate the cGAS-STING-dependent innate immune signaling, thereby triggering the production of SASP factors during radiation-induced senescence [20,23]. In our previous work, we showed that human WI-38 fibroblasts develop SASP with the secretion of numerous cytokines after IR exposure (analyzed at 2 weeks after 20 Gy). The pro-inflammatory cytokines interleukin-6 (IL6) and interleukin-8 (IL8), granulocyte-macrophage colony-stimulating factor (GM-CSF), and monocyte chemoattractant protein-1 (MCP1) were quantified in the supernatant of non-irradiated versus irradiated fibroblasts by enzyme-linked immunosorbent assay (ELISA). Our results showed that non-irradiated fibroblasts expressed low levels of these common SASP factors, and hence no senescence-messaging secretome. Human fibroblasts in radiation-induced senescence, by contrast, secreted high levels of IL6, IL8, GM-CSF, and MCP1, demonstrating that SASP components were significantly increased between non-senescent and senescent states in human fibroblasts [3]. Moreover, the relative gene expression of these SASP factors were quantified during radiation-induced senescence by reverse-transcriptase quantitative polymerase-chain-reaction (RT-qPCR). Gene expression analysis of WI-38 fibroblasts after senescence-inducing IR revealed significantly increased mRNA expression of IL6, CXCL8, CSF2, and CCL2 with 10–30-fold increases [3]. Collectively, these findings confirm the robust induction of SASP expression during radiation-induced senescence. Furthermore, automated image capturing and data processing of SBF-SEM provides unprecedented multi-view 3D reconstruction of the morphological organization of senescent fibroblasts. While imaging by standard diffraction

limited fluorescence light microscopy shows general nuclear information with resolution in the range of ≈ 200 nm, our SEM data sets allow us to reconstruct 3D structures of senescent cells to the 3–5 nm resolution. The accuracy of reconstruction allows us to illustrate the complex nuclear shape of senescent cells and the precise visualization of nuclear blebs with their segregation from the main nucleus and their fusion with lysosomes. Only by high-resolution 3D imaging were we able to identify and characterize the nanoscale invaginations formed regularly in the nuclei of senescent fibroblasts. High-resolution 3D whole-cell data sets of non-irradiated fibroblasts can be obtained from the open access volume electron microscopy atlas repository [34].

Depletion of lamin B1 during senescence progression leads to segregation of A-type and B-type lamins from one another, and results in an uneven mesh layer with altered mechanical properties [14]. In some regions, lamina's fibers begin to gap and separate, giving rise to bulges or even transient ruptures in the cell's nuclear envelope. Accordingly, these tubular membrane structures may arise as a consequence of different mechanical forces, 'pushing' forces exerted, e.g., by cytoskeletal filaments, or 'pulling' forces by chromatin-lamin interactions and large-scale rearrangements of chromatin [14,35,36]. Another explanation of these nanoscale invaginations of the nuclear envelope may be related to the disturbed nucleo-cytoplasmic trafficking in senescent cells [37]. Senescent cells exhibit reduced responses to intrinsic and extrinsic stimuli. This diminished reaction is explained by the disrupted transmission of nuclear signals. Disruption of the nucleo-cytoplasmic trafficking is an essential feature of cellular senescence, and thus may suggest that these selective nuclear channels are involved in intracellular transport to overcome the nucleo-cytoplasmic barrier. Recent work showed that nuclear invaginations often contain cytoskeletal filaments, linked to the nuclear envelope, suggesting a direct link between regions deep inside the nuclei and cell-cell and/or cell-ECM adhesion sites [38]. Accordingly, ECM may signal through receptors, via the cytoskeleton, through nuclear matrix to chromatin to control cell- or tissue-specific function and vice versa. Potentially, nanotubes are essential 3D architectural elements of the interconnected network of the nucleus, cytoskeleton and ECM in cell communication and the structure and composition of the nuclear envelope responds to microenvironmental stimuli with important consequences for gene regulation. However, the precise pathophysiological role of these nucleo-cytoplasmic nanotubes in lamin-perturbed nuclei has to be clarified in future studies.

In the present study, the hallmark features of premature senescence triggered by ionizing radiation were analyzed in human fibroblasts, the most common cell culture system for cellular senescence. Currently, it is unclear if all cell types (even terminally differentiated cells) or only replicative or mitotically competent cells can become senescent in normal tissues [39]. Changes in nuclear fragility leading to nuclear blebbing and altered chromatin organization are indicative of a wide range of pathologies, including cancer and other age-related diseases [40]. Exploration of laminopathies, such as Hutchinson–Gilford progeria, a premature aging syndrome caused by lamin A mutations, has demonstrated the critical importance of the nuclear integrity for chromatin architecture [41]. Disruption of lamin-interacting structures have profound effects on the high-order organization of genomes and is functionally important for gene regulation.

5. Conclusions

Understanding the precise pathomechanisms responsible for the formation of nuclear blebs and tubes may provide new insights into the aging process and age-related diseases. Volume electron microscopy allows for automated acquisition of serial-section imaging data that can be segmented and reconstructed, thereby providing detailed 3D views of senescent cells with precise morphologies. Unraveling complex 3D architectures is crucial for structure–function correlations to gain novel insights into the pathogenic organization of senescent cells. Our findings may help to improve the current understanding of nuclear fragility during radiation-induced senescence.

Supplementary Materials: The following supporting information can be downloaded at: <https://www.mdpi.com/article/10.3390/cells11020273/s1>, Figure S1: Principal component analysis (PCA): Pattern analysis of the investigated data sets for irradiated (20 Gy post-IR) and non-irradiated (non-IR) fibroblasts. Figure S2: CCF formation and cGAMP concentration: Quantification of CCF-positive cells by IFM for non-irradiated (non-IR) and irradiated (20 Gy, 2 weeks post-IR) fibroblasts (right panel). Quantification of cGAMP concentration: Quantification of cGAMP protein relative to total protein (g = gram) in non-irradiated (non-IR) and irradiated (20 Gy, 2 weeks post-IR) fibroblasts (left panel). Figure S3: SBF-SEM: fusion of CCF with lysosomes: High-resolution display of the fusion of CCF with lysosomes to become autolysosomes, in which the sequestered cargos are degraded and recycled for the maintenance of cellular homeostasis.

Author Contributions: M.A.A.A.-r. performed IFM and TEM experiments. B.M.F. prepared figures for the manuscript, and reconstructed senescent fibroblast from SFB-SEM micrographs, which were prepared by L.H. A.I. performed IFM experiments and prepared samples for proteome analysis. A.D., O.A. and M.G. performed proteome analysis. C.E.R. planned, managed, and coordinated the research activities. M.G. and C.E.R. acquired the funding for the project. C.E.R. wrote the manuscript. All authors have read and agreed to the published version of the manuscript.

Funding: This work was funded by the German Federal Ministry of Education and Research (Bundesministerium für Bildung und Forschung: 02NUK035A and 02NUK058B).

Institutional Review Board Statement: Not applicable.

Informed Consent Statement: Not applicable.

Data Availability Statement: The data that support the findings of this study are available from the Department of Radiation Oncology, Saarland University Hospital, Homburg/Saar, Germany.

Acknowledgments: We thank Yvonne Lorat, the staff of the Electron Microscopy Facility at the NanoPort Center (Eindhoven, The Netherlands) and the Research Unit Protein Science of the HMGU, Munich, for their excellent technical support.

Conflicts of Interest: The authors declare no conflict of interest. The funders had no role in the design of the study; in the collection, analyses, or interpretation of data; in the writing of the manuscript, or in the decision to publish the results.

References

1. Salama, R.; Sadaie, M.; Hoare, M.; Narita, M. Cellular senescence and its effector programs. *Genes Dev.* **2014**, *28*, 99–114. [[CrossRef](#)] [[PubMed](#)]
2. Kumari, R.; Jat, P. Mechanisms of Cellular Senescence: Cell Cycle Arrest and Senescence Associated Secretory Phenotype. *Front. Cell Dev. Biol.* **2021**, *9*, 645593. [[CrossRef](#)] [[PubMed](#)]
3. Isermann, A.; Mann, C.; Rube, C.E. Histone Variant H2A.J. Marks Persistent DNA Damage and Triggers the Secretory Phenotype in Radiation-Induced Senescence. *Int. J. Mol. Sci.* **2020**, *21*, 9130. [[CrossRef](#)] [[PubMed](#)]
4. Campisi, J.; Robert, L. Cell senescence: Role in aging and age-related diseases. *Interdiscip. Top. Gerontol.* **2014**, *39*, 45–61. [[CrossRef](#)]
5. Rube, C.E.; Baumert, C.; Schuler, N.; Isermann, A.; Schmal, Z.; Glanemann, M.; Mann, C.; Scherthan, H. Human skin aging is associated with increased expression of the histone variant H2A.J. in the epidermis. *NPJ Aging Mech. Dis.* **2021**, *7*, 7. [[CrossRef](#)] [[PubMed](#)]
6. Chen, H.; Li, Y.; Tollefsbol, T.O. Cell senescence culturing methods. *Methods Mol. Biol.* **2013**, *1048*, 1–10. [[CrossRef](#)] [[PubMed](#)]
7. Kim, J.J.; Lee, S.Y.; Miller, K.M. Preserving genome integrity and function: The DNA damage response and histone modifications. *Crit. Rev. Biochem. Mol. Biol.* **2019**, *54*, 208–241. [[CrossRef](#)]
8. Rube, C.E.; Lorat, Y.; Schuler, N.; Schanz, S.; Wennemuth, G.; Rube, C. DNA repair in the context of chromatin: New molecular insights by the nanoscale detection of DNA repair complexes using transmission electron microscopy. *DNA Repair.* **2011**, *10*, 427–437. [[CrossRef](#)]
9. Lorat, Y.; Brunner, C.U.; Schanz, S.; Jakob, B.; Taucher-Scholz, G.; Rube, C.E. Nanoscale analysis of clustered DNA damage after high-LET irradiation by quantitative electron microscopy—The heavy burden to repair. *DNA Repair.* **2015**, *28*, 93–106. [[CrossRef](#)]
10. Lorat, Y.; Schanz, S.; Schuler, N.; Wennemuth, G.; Rube, C.; Rube, C.E. Beyond repair foci: DNA double-strand break repair in euchromatic and heterochromatic compartments analyzed by transmission electron microscopy. *PLoS ONE* **2012**, *7*, e38165. [[CrossRef](#)]
11. Sedelnikova, O.A.; Horikawa, I.; Redon, C.; Nakamura, A.; Zimonjic, D.B.; Popescu, N.C.; Bonner, W.M. Delayed kinetics of DNA double-strand break processing in normal and pathological aging. *Aging Cell.* **2008**, *7*, 89–100. [[CrossRef](#)] [[PubMed](#)]

12. Corpet, A.; Stucki, M. Chromatin maintenance and dynamics in senescence: A spotlight on SAHF formation and the epigenome of senescent cells. *Chromosoma* **2014**, *123*, 423–436. [[CrossRef](#)]
13. Zuela, N.; Bar, D.Z.; Gruenbaum, Y. Lamins in development, tissue maintenance and stress. *EMBO Rep.* **2012**, *13*, 1070–1078. [[CrossRef](#)]
14. Funkhouser, C.M.; Sknepnek, R.; Shimi, T.; Goldman, A.E.; Goldman, R.D.; Olvera de la Cruz, M. Mechanical model of blebbing in nuclear lamin meshworks. *Proc. Natl. Acad. Sci. USA* **2013**, *110*, 3248–3253. [[CrossRef](#)] [[PubMed](#)]
15. Camps, J.; Erdos, M.R.; Ried, T. The role of lamin B1 for the maintenance of nuclear structure and function. *Nucleus* **2015**, *6*, 8–14. [[CrossRef](#)]
16. Briand, N.; Collas, P. Lamina-associated domains: Peripheral matters and internal affairs. *Genome Biol.* **2020**, *21*, 85. [[CrossRef](#)]
17. van Steensel, B.; Belmont, A.S. Lamina-Associated Domains: Links with Chromosome Architecture, Heterochromatin, and Gene Repression. *Cell* **2017**, *169*, 780–791. [[CrossRef](#)] [[PubMed](#)]
18. Lenain, C.; de Graaf, C.A.; Pagie, L.; Visser, N.L.; de Haas, M.; de Vries, S.S.; Peric-Hupkes, D.; Van Steensel, B.; Peeper, D.S. Massive reshaping of genome-nuclear lamina interactions during oncogene-induced senescence. *Genome Res.* **2017**, *27*, 1634–1644. [[CrossRef](#)]
19. Rodier, F.; Coppe, J.P.; Patil, C.K.; Hoeijmakers, W.A.; Munoz, D.P.; Raza, S.R.; Freund, A.; Campeau, E.; Davalos, A.R.; Campisi, J. Persistent DNA damage signalling triggers senescence-associated inflammatory cytokine secretion. *Nat. Cell Biol.* **2009**, *11*, 973–979. [[CrossRef](#)]
20. Dou, Z.; Ghosh, K.; Vizioli, M.G.; Zhu, J.; Sen, P.; Wangenstein, K.J.; Smithy, J.; Lan, Y.; Lin, Y.; Zhou, Z.; et al. Cytoplasmic chromatin triggers inflammation in senescence and cancer. *Nature* **2017**, *550*, 402–406. [[CrossRef](#)]
21. Ivanov, A.; Pawlikowski, J.; Manoharan, I.; van Tuyn, J.; Nelson, D.M.; Rai, T.S.; Shah, P.P.; Hewitt, G.; Korolchuk, V.; Passos, J.; et al. Lysosome-mediated processing of chromatin in senescence. *J. Cell Biol.* **2013**, *202*, 129–143. [[CrossRef](#)]
22. Hopfner, K.P.; Hornung, V. Molecular mechanisms and cellular functions of cGAS-STING signalling. *Nat. Rev. Mol. Cell Biol.* **2020**, *21*, 501–521. [[CrossRef](#)]
23. Gluck, S.; Guey, B.; Gulen, M.F.; Wolter, K.; Kang, T.W.; Schmacke, N.A.; Bridgeman, A.; Rehwinkel, J.; Zender, L.; Ablasser, A. Innate immune sensing of cytosolic chromatin fragments through cGAS promotes senescence. *Nat. Cell Biol.* **2017**, *19*, 1061–1070. [[CrossRef](#)] [[PubMed](#)]
24. Wisniewski, J.R.; Zougman, A.; Nagaraj, N.; Mann, M. Universal sample preparation method for proteome analysis. *Nat. Methods* **2009**, *6*, 359–362. [[CrossRef](#)] [[PubMed](#)]
25. Subramanian, V.; Seemann, I.; Merl-Pham, J.; Hauck, S.M.; Stewart, F.A.; Atkinson, M.J.; Tapio, S.; Azimzadeh, O. Role of TGF Beta and PPAR Alpha Signaling Pathways in Radiation Response of Locally Exposed Heart: Integrated Global Transcriptomics and Proteomics Analysis. *J. Proteome Res.* **2017**, *16*, 307–318. [[CrossRef](#)]
26. Azimzadeh, O.; Azizova, T.; Merl-Pham, J.; Blutke, A.; Moseeva, M.; Zubkova, O.; Anastasov, N.; Feuchtinger, A.; Hauck, S.M.; Atkinson, M.J.; et al. Chronic Occupational Exposure to Ionizing Radiation Induces Alterations in the Structure and Metabolism of the Heart: A Proteomic Analysis of Human Formalin-Fixed Paraffin-Embedded (FFPE) Cardiac Tissue. *Int. J. Mol. Sci.* **2020**, *21*, 6832. [[CrossRef](#)]
27. Bassler, J.; Hurt, E. Eukaryotic Ribosome Assembly. *Annu. Rev. Biochem.* **2019**, *88*, 281–306. [[CrossRef](#)]
28. Janssen, A.; Colmenares, S.U.; Karpen, G.H. Heterochromatin: Guardian of the Genome. *Annu. Rev. Cell Dev. Biol.* **2018**, *34*, 265–288. [[CrossRef](#)]
29. Dou, Z.; Xu, C.; Donahue, G.; Shimi, T.; Pan, J.A.; Zhu, J.; Ivanov, A.; Capell, B.C.; Drake, A.M.; Shah, P.P.; et al. Autophagy mediates degradation of nuclear lamina. *Nature* **2015**, *527*, 105–109. [[CrossRef](#)] [[PubMed](#)]
30. Yun, C.W.; Lee, S.H. The Roles of Autophagy in Cancer. *Int. J. Mol. Sci.* **2018**, *19*, 3466. [[CrossRef](#)]
31. Eriksson, D.; Stigbrand, T. Radiation-induced cell death mechanisms. *Tumor Biol.* **2010**, *31*, 363–372. [[CrossRef](#)]
32. Schwarz-Finsterle, J.; Scherthan, H.; Huna, A.; Gonzalez, P.; Mueller, P.; Schmitt, E.; Erenpreisa, J.; Hausmann, M. Volume increase and spatial shifts of chromosome territories in nuclei of radiation-induced polyploidizing tumour cells. *Mutat. Res.* **2013**, *756*, 56–65. [[CrossRef](#)] [[PubMed](#)]
33. Erenpreisa, J.; Krigerts, J.; Salmina, K.; Gerashchenko, B.I.; Freivalds, T.; Kurg, R.; Winter, R.; Krufczik, M.; Zayakin, P.; Hausmann, M.; et al. Heterochromatin Networks: Topology, Dynamics, and Function (a Working Hypothesis). *Cells* **2021**, *10*, 1582. [[CrossRef](#)] [[PubMed](#)]
34. Xu, C.S.; Pang, S.; Shtengel, G.; Muller, A.; Ritter, A.T.; Hoffman, H.K.; Takemura, S.-Y.; Lu, Z.; Pasolli, H.A.; Iyer, N.; et al. An open-access volume electron microscopy atlas of whole cells and tissues. *Nature* **2021**, *599*, 147–151. [[CrossRef](#)]
35. Srivastava, N.; Nader, G.P.F.; Williard, A.; Rollin, R.; Cuvelier, D.; Lomakin, A.; Piel, M. Nuclear fragility, blaming the blebs. *Curr. Opin. Cell Biol.* **2021**, *70*, 100–108. [[CrossRef](#)]
36. Schoen, I.; Aires, L.; Ries, J.; Vogel, V. Nanoscale invaginations of the nuclear envelope: Shedding new light on wormholes with elusive function. *Nucleus* **2017**, *8*, 506–514. [[CrossRef](#)]
37. Park, J.H.; Ryu, S.J.; Kim, B.J.; Cho, H.J.; Park, C.H.; Choi, H.J.C.; Jang, E.-J.; Yang, E.J.; Hwang, J.-A.; Woo, S.-H.; et al. Disruption of nucleocytoplasmic trafficking as a cellular senescence driver. *Exp. Mol. Med.* **2021**, *53*, 1092–1108. [[CrossRef](#)] [[PubMed](#)]
38. Jorgens, D.M.; Inman, J.L.; Wojcik, M.; Robertson, C.; Palsdottir, H.; Tsai, W.T.; Huang, H.; Bruni-Cardoso, A.; López, C.S.; Bissell, M.J.; et al. Deep nuclear invaginations are linked to cytoskeletal filaments-integrated bioimaging of epithelial cells in 3D culture. *J. Cell Sci.* **2017**, *130*, 177–189. [[CrossRef](#)]

39. von Zglinicki, T.; Wan, T.; Miwa, S. Senescence in Post-Mitotic Cells: A Driver of Aging? *Antioxid. Redox Signal.* **2021**, *34*, 308–323. [[CrossRef](#)]
40. Gauthier, B.R.; Comaills, V. Nuclear Envelope Integrity in Health and Disease: Consequences on Genome Instability and Inflammation. *Int. J. Mol. Sci.* **2021**, *22*, 7281. [[CrossRef](#)]
41. Gonzalo, S.; Kreienkamp, R.; Askjaer, P. Hutchinson-Gilford Progeria Syndrome: A premature aging disease caused by LMNA gene mutations. *Ageing Res. Rev.* **2017**, *33*, 18–29. [[CrossRef](#)] [[PubMed](#)]

7.3 Publication 3

Table 3 Literature information of publication III

Title	Automated Image Analysis of Transmission Electron Micrographs: Nanoscale Evaluation of Radiation-Induced DNA Damage in the Context of Chromatin
Authors and Affiliations	Mutaz A Abd Al-razaq , Anna Isermann, Markus Hecht, Claudia E Rube Department of Radiation Oncology, Saarland University Medical Center, 66421 Homburg/Saar, Germany *Author to whom correspondence should be addressed.
Journal	Cells
Impact factor	7.666
Publication status	Published
Year of publication	2023
Type of article	Research article
Volume	12
Pages	2427
DOI:	https://doi.org/10.3390/cells12202427

Article

Automated Image Analysis of Transmission Electron Micrographs: Nanoscale Evaluation of Radiation-Induced DNA Damage in the Context of Chromatin

Mutaz A. Abd Al-razaq , Anna Isermann, Markus Hecht  and Claudia E. Rübe *

Department of Radiation Oncology, Saarland University Medical Center, Kirrbergerstr, Building 6.5, 66421 Homburg, Saar, Germany; mutaz.abd-al-razaq@uks.eu (M.A.A.A.-r.)
* Correspondence: claudia.ruebe@uks.eu

Abstract: Background: Heavy ion irradiation (IR) with high-linear energy transfer (LET) is characterized by a unique depth dose distribution and increased biological effectiveness. Following high-LET IR, localized energy deposition along the particle trajectories induces clustered DNA lesions, leading to low electron density domains (LEDDs). To investigate the spatiotemporal dynamics of DNA repair and chromatin remodeling, we established the automated image analysis of transmission electron micrographs. Methods: Human fibroblasts were irradiated with high-LET carbon ions or low-LET photons. At 0.1 h, 0.5 h, 5 h, and 24 h post-IR, nanoparticle-labeled repair factors (53BP1, pKu70, pKu80, DNA-PKcs) were visualized using transmission electron microscopy in interphase nuclei to monitor the formation and repair of DNA damage in the chromatin ultrastructure. Using AI-based software tools, advanced image analysis techniques were established to assess the DNA damage pattern following low-LET versus high-LET IR. Results: Low-LET IR induced single DNA lesions throughout the nucleus, and most DNA double-strand breaks (DSBs) were efficiently rejoined with no visible chromatin decondensation. High-LET IR induced clustered DNA damage concentrated along the particle trajectories, resulting in circumscribed LEDDs. Automated image analysis was used to determine the exact number of differently sized nanoparticles, their distance from one another, and their precise location within the micrographs (based on size, shape, and density). Chromatin densities were determined from grayscale features, and nanoparticles were automatically assigned to euchromatin or heterochromatin. High-LET IR-induced LEDDs were delineated using automated segmentation, and the spatial distribution of nanoparticles in relation to segmented LEDDs was determined. Conclusions: The results of our image analysis suggest that high-LET IR induces chromatin relaxation along particle trajectories, enabling the critical repair of successive DNA damage. Following exposure to different radiation qualities, automated image analysis of nanoparticle-labeled DNA repair proteins in the chromatin ultrastructure enables precise characterization of specific DNA damage patterns.

Keywords: automated image analysis; transmission electron microscopy (TEM); heavy ion irradiation; linear energy transfer (LET); DNA damage; DNA double-strand breaks (DSBs); chromatin remodelling



Citation: Abd Al-razaq, M.A.; Isermann, A.; Hecht, M.; Rübe, C.E. Automated Image Analysis of Transmission Electron Micrographs: Nanoscale Evaluation of Radiation-Induced DNA Damage in the Context of Chromatin. *Cells* **2023**, *12*, 2427. <https://doi.org/10.3390/cells12202427>

Academic Editor: Alexandra Lusser

Received: 4 September 2023

Revised: 3 October 2023

Accepted: 9 October 2023

Published: 10 October 2023



Copyright: © 2023 by the authors. Licensee MDPI, Basel, Switzerland. This article is an open access article distributed under the terms and conditions of the Creative Commons Attribution (CC BY) license (<https://creativecommons.org/licenses/by/4.0/>).

1. Introduction

Heavy ion irradiation (IR) has a favorable dose distribution with higher linear energy transfer (LET) and relative biological effectiveness (RBE) compared with photon-based radiotherapy [1]. The enhanced RBE of high-LET versus low-LET IR is driven by unique DNA damage patterns characterized by clustered lesions along particle trajectories that overwhelm the DNA repair capacity of normal and malignant cells [2]. Due to these physical and radiobiological properties, heavy ion IR has strong tumor-killing effects and, at the same time, has the potential to maximally spare normal tissues [3]. Double-strand breaks (DSBs), the most deleterious type of radiation-induced DNA damage, are

primarily repaired by two pathways: homologous recombination and non-homologous end-joining (NHEJ). The choice of which is largely dependent on the cell cycle phase and local chromatin landscape [4]. In non-proliferating cells, circular Ku70/Ku80 heterodimer binds to both ends of individual DSBs and initiates NHEJ at damaged DNA sites, followed by loading of DNA-dependent protein kinase catalytic subunits (DNA-PKcs) onto the DNA-Ku complexes [5]. This DNA-PK holoenzyme then phosphorylates various components of the NHEJ machinery to facilitate final processing and rejoining [5].

The repair of radiation-induced DSBs occurs within a complex chromatin environment. In the undamaged state, chromatin exists in different topological and functional domains that can change dynamically. Based on the degree of compaction (originally defined by contrast staining with basic dyes), chromatin is classified as open, transcriptionally active, gene-rich euchromatin or as more condensed, transcriptionally inert heterochromatin. In response to radiation-induced DSBs, heterochromatic domains are converted to euchromatin, allowing the repair machinery access to areas of damaged DNA. After the DNA damage has been processed and repaired, the original chromatin organization must be restored to ensure cellular functionality. Thus, chromatin responds dynamically to radiation-induced DNA damage by decompacting and expanding, which in turn changes the mobility and accessibility of the damaged locus [6].

Currently, various experimental techniques exist to detect radiation-induced DNA damage, but most methods are not suitable for high-resolution imaging of complex DNA damage patterns in the context of chromatin. Presently, DNA repair markers such as phosphorylated H2AX (γ H2AX) and 53-binding protein 1 (53BP1) are visualized as DNA damage foci in DAPI-stained cell nuclei using immunofluorescence microscopy (IFM) [7]. However, because of the limited resolution of conventional IFM, the detailed structure of these DNA damage foci (especially in the case of clustered DSBs after high-LET IR) cannot be examined in detail or within the context of chromatin. To detect DNA-repair proteins within the chromatin ultrastructure, we established immunogold-labeling techniques using transmission electron microscopy (TEM) [8–10]. The nanometer resolution of TEM permits the visualization of repair proteins at the single-molecule level in different chromatin compartments [11]. In previous IFM and TEM analyses, we characterized DNA damage patterns in human fibroblasts following low-LET and high-LET IR, respectively [8,12]. After high-LET IR, densely clustered DNA damage in areas of low electron density domains (LEDDs) was detectable using TEM [13]. However, counting individual nanoparticles and determining clustered lesions using electron microscopy was extremely time-consuming, and unambiguous assignment to euchromatic or heterochromatic compartments with exact demarcation of LEDDs was not always possible. In addition, as quantitative evaluations become the standard in biological research, the need for higher data acquisition throughput in TEM imaging also grows. Therefore, we have established the automated analysis of TEM images using existing AI-based software tools to effectively enable the automatic detection of individual nanoparticles based on their specific characteristics (size, round shape, electron density) and their precise localization in different chromatin densities. Here, we used these advanced image analysis techniques to assess the DNA damage pattern in human fibroblasts following high-LET IR.

2. Materials and Methods

Cell Culture: Human dermal fibroblasts (PromoCell, Heidelberg, Germany) were grown on coverslips in Fibroblast Growth Medium (PromoCell) at 37 °C and 5% CO₂. Confluent interphase cells (with homogenous chromatin density) were used for experiments.

Low-LET and high-LET irradiation: Low-LET IR with 6-MV photons (10 Gy; dose-rate 2 Gy/min) was performed at the Department of Radiation Oncology, Saarland University (Homburg, Germany) using the linear accelerator Artiste™ (Siemens, München, Germany). High-LET IR with carbon ions (9.5 MeV/nucleon; LET 190 keV/μm; fluence 5 × 10⁶ particles/cm²; calculated mean dose: 1.52 Gy) was performed at GSI Center for Heavy Ion Research (Darmstadt, Germany) using the UNILAC accelerator as previously described [13]. Cells were

analyzed at different time points after low-LET or high-LET IR and compared with sham-irradiated cells.

Immunofluorescence microscopy analysis: Cells were fixed in 4% paraformaldehyde and permeabilized in 0.2% Triton X-100. After blocking with 1% BSA in PBS overnight, cells were incubated with primary antibodies (anti-53BP1, Novus Biologicals, Wiesbaden Nordenstadt, Germany; anti-pKu70, Abcam, Cambridge, UK, anti-pKu80, LifeSpan Biosciences, Seattle, WA, USA, anti-DNA-PKcs, Novus Biologicals, Wiesbaden Nordenstadt, Germany), followed by AlexaFluor-488 or AlexaFluor-568 secondary antibodies (Invitrogen, Karlsruhe, Germany). Finally, cells were mounted in VECTAshield™ mounting medium with 4',6-diamidino-2-phenylindole (DAPI, Vector Laboratories, Burlingame, CA, USA). Fluorescence images were captured using a Nikon-Eclipse Ni fluorescence microscope equipped with a charge-coupled device camera and acquisition software (Nikon, Düsseldorf, Germany). Foci numbers were quantified, and foci areas were measured at an objective magnification of 60× until at least 50 cells were registered per sample.

Transmission Electron Microscopy analysis: Cells were fixed with 2% paraformaldehyde and 0.05% glutaraldehyde in PBS. Fixed samples were dehydrated using increasing concentrations of ethanol and infiltrated with LR White resin overnight (Plano, Wetzlar, Germany). Subsequently, samples were embedded in fresh resin with an accelerator at 37 °C until the resin polymerized. Ultrathin sections (70 nm) were cut on a Microtome Ultracut UCT (Leica, Wetzlar, Germany) with diamond knives (Diatome, Biel, Switzerland), gathered on pioloform-coated nickel grids, and processed for nanoparticle-labelling. To block nonspecific staining, sections were placed on drops of blocking solution (Aurion, Wageningen, The Netherlands). Afterward, sections were rinsed and incubated with primary antibodies (anti-53BP1, Novus Biologicals, Wiesbaden Nordenstadt, Germany; anti-pKu70, Abcam, Cambridge, UK, anti-pKu80, LifeSpan Biosciences, Seattle, WA, USA, anti-DNA-PKcs, Novus Biologicals, Wiesbaden Nordenstadt, Germany), overnight at 4 °C. After washing, secondary antibodies conjugated with 6 nm or 10 nm gold particles (Aurion, Wageningen, The Netherlands) were applied to the sections for 1.5 h. Sections were then rinsed and fixed with 2% glutaraldehyde in PBS. All sections were stained with uranyl acetate and examined using Tecnai Biotwin™ transmission electron microscope (FEI, Eindhoven, The Netherlands). For each radiation quality (low-LET photons, high-LET carbons), single- and clustered nanoparticles were counted in ≥25 randomly chosen nuclear sections per examination time. The number and area of LEDDs were also measured in ≥25 cell nuclei.

Automated image analysis of transmission electron micrographs: Nuclear sections were systematically scanned at sufficient resolution to identify cells with LEDDs. Manual annotations were made for each micrograph to avoid artifacts and non-relevant areas. Acquired micrographs with LEDDs were edited by adjusting the contrast to enhance nanoparticle detection. For automatic annotation of gold nanoparticles, the brightness (50% increase) and contrast (80% increase) adjustments were uniformly applied to all original TEM images. Regions of interest were segmented and analyzed using a well-trained AI classifier using HALO® Image Analysis Platform version 3.4.2986 (Indica Labs, Albuquerque, NM, USA). The software was able to automatically identify and select LEDD areas using the Area Quantification module v2.4.2, and LEDD areas were further subdivided into different regions related to the LEDD border. All nanoparticles around the LEDDs were detected and counted automatically, followed by the calculation of the nanoparticle distribution and clusters per unit area using the spatial plot tool.

Statistical analysis: GraphPad Prism (version 9.4.1, GraphPad Software, San Diego, CA, USA) was used to analyze data. Data were presented as the mean of at least three experiments ± SE. Two-way ANOVA (multiple comparisons) and the Mann–Whitney Test were used for estimating the differences among groups, followed by multiple comparisons between data sets. A *p*-value of <0.05 was considered statistically significant, <0.01 as highly statistically significant, and <0.001 as exceptionally statistically significant. In the figures, statistically significant differences are indicated as asterisks directly above the

bar when comparing to the previous time point and as asterisks above brackets when comparing between two different study groups (* $p < 0.05$, ** $p < 0.01$, and *** $p < 0.001$).

3. Results

3.1. Clustered Foci and Decondensed Chromatin Regions following High-LET IR

In earlier work, fluorescence microscopy was used to show that exposure of cell nuclei to heavy carbon ions leads to spatially defined DNA damage along the particle trajectories [14,15]. To study the initial formation and subsequent repair of this clustered DNA damage, cell monolayers were irradiated with vertical beam direction (90° angle to the monolayer plane). Using IFM, DNA damage-induced foci appeared within the nuclei 0.5 h after high-LET IR, generating small co-localizing foci for pKu70 and pKu80 and larger clustered foci for 53BP1 and pKu80 (Figure 1A, left panel). Radiation-induced foci formed after high-LET IR are brighter and larger than those generated following low-LET IR, likely because many DSBs are induced within these particle trajectories. Using IFM, the number and area of 53BP1 and pKu80 foci per cell nucleus were quantified at different time points after high-LET IR (Figure 1A, right panel). The mean number of clustered foci per cell increased until 0.5 h post-IR (53BP1: 5.00 ± 0.13 foci/cell; pKu80: 4.62 ± 0.11 foci/cell) and subsequently decreased within 24 h post-IR (53BP1: 2.00 ± 0.26 foci/cell; Ku80: 2.34 ± 0.18). The maximal track number 0.5 h after irradiation with vertical beam direction correlates with the applied particle fluence of 5×10^6 particles/cm². Moreover, measuring the mean area of clustered foci after vertical beam direction, we observed an increase in the mean track area over time, with the maximum at 5 h post-IR (53BP1: 2.28 ± 0.14 μm^2 ; pKu80 1.33 ± 0.09 μm^2) and with slight reductions at 24 h post-IR.

Subsequently, TEM imaging was used to characterize the ultrastructural pattern of DNA damage caused in cells exposed to high-LET IR. For TEM analysis, irradiated cells were harvested as monolayers to preserve the structural organization of the nucleus, as well as the beam direction in the embedded cells. Cell samples were stained with uranyl acetate to enhance the contrast of chromatin, and defined levels of gray were assigned to euchromatin and heterochromatin. Detecting multiple repair factors within the chromatin ultrastructure using TEM requires the selective use of gold-conjugated antibodies with varying particle sizes (10-nm or 6-nm nanoparticles), which were subsequently colored in the micrograph for better visualization. Non-irradiated fibroblasts are characterized by a homogenous chromatin organization throughout the entire nucleus. Following low-LET IR, no distinct local or global changes in the nanostructural chromatin organization were detectable during the DNA repair process. Following high-LET IR with vertical beam direction, varying numbers of electron-lucent regions were observed, likely reflecting LEDDs following particle transversals. In an earlier study, we were able to show that these LEDDs in TEM reflect the clustered foci in IFM [13]. Subsequently, DNA repair proteins (pKu70, pKu80, and 53BP1) were labeled with immunogold beads, and these nanoparticles were visualized in the chromatin ultrastructure using TEM. Our results show that pKu70 (blue) and pKu80 (red) were predominantly located at the border of LEDDs, while 53BP1 (green) was also found in heterochromatic domains within LEDDs. A phosphorylated Ku70/80 heterodimer is required for efficient repair of radiation-induced DSBs via the NHEJ pathway, with a single Ku70/80 heterodimer binding each of the two broken ends of the DSB. Our findings show that compared with low-LET IR, where only isolated DNA damage was detectable in the entire nucleus, there is a high concentration of actively processed DSBs around the LEDDs of high-LET irradiated cells.

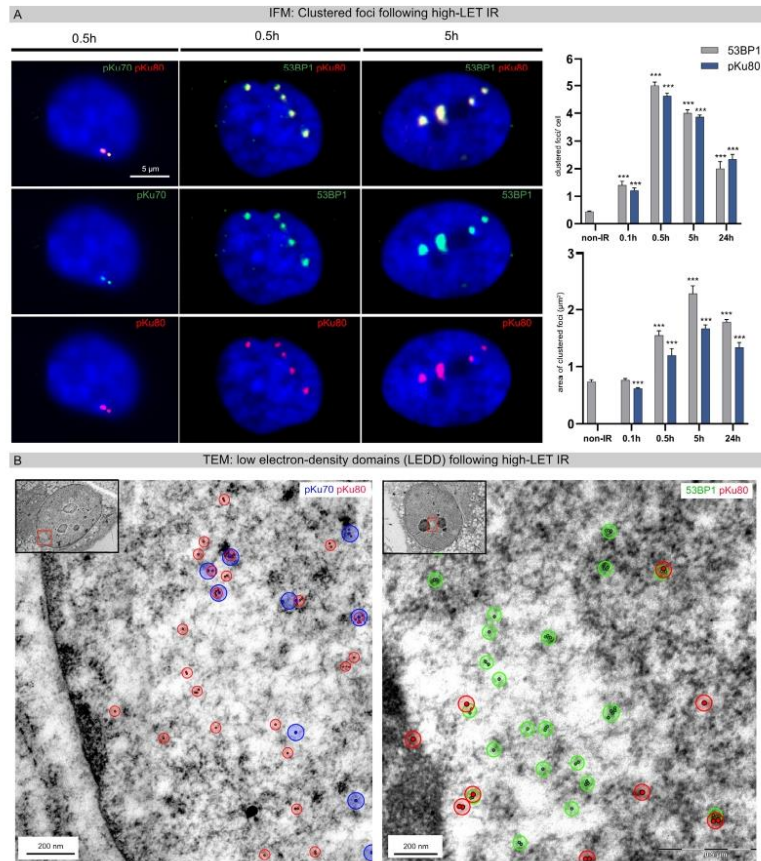


Figure 1. Clustered foci and decondensed chromatin regions (LEDDs) following high-LET IR. (A) IFM micrographs of DAPI-stained nuclei double-stained for pKu70 (green) with pKu80 (red) or 53BP1 (green) with pKu80 (red), analyzed at 0.5 h and 5 h after high-LET IR (vertical beam direction). For 53BP1 and pKu80, the number and area of clustered foci were quantified at 0.1 h, 0.5 h, 5 h, and 24 h after high-LET IR. (B) TEM micrographs of nanoparticle-labeled pKu70 (blue), pKu80 (red), and 53BP1 (green) in the chromatin ultrastructure. Within 5 h after high-LET IR, multiple pKu70 (blue), pKu80 (red), and 53BP1 nanoparticles occasionally formed clusters distributed inside and outside LEDDs. Insets: overview images of the nucleus; framed regions are shown at higher magnification. Statistically significant differences are indicated as asterisks directly above the bar when comparing to the previous point of investigation (***) $p < 0.001$.

3.2. Quantification of pKu80 and DNA-PKcs following Low-LET versus High-LET IR

In the early stage of the NHEJ process, DNA-PKcs is recruited to Ku70/Ku80 heterodimer-bound DNA ends. To monitor DSB repair within the chromatin ultrastructure of human fibroblasts following low-LET versus high-LET IR, nuclear sections were immunogold-labeled for pKu80 and pDNA-PKcs (6-nm versus 10-nm particle size), and these nanoparticles were counted in defined euchromatic and heterochromatic regions (Figure 2A).

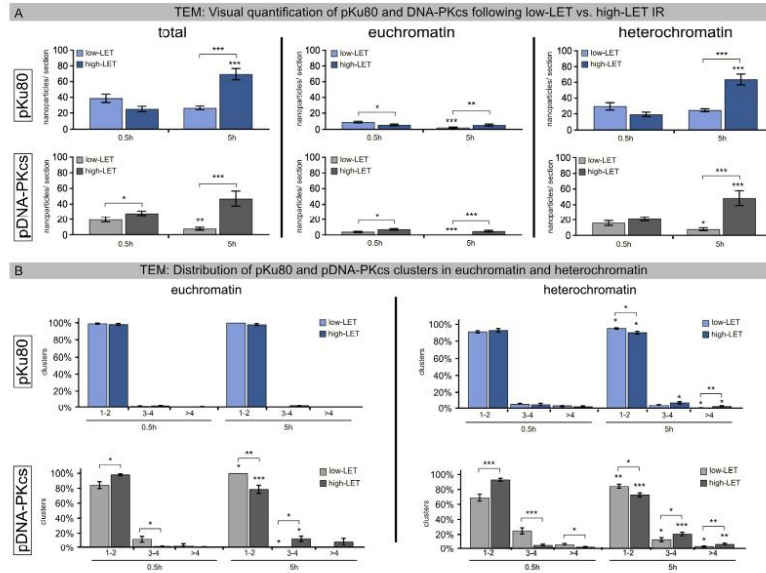


Figure 2. Quantification of pKu80 and DNA-PKcs following low-LET versus high-LET IR. (A) The mean number of nanoparticles labeling pKu80 and DNA-PKcs (per nuclear section) in euchromatin and heterochromatin. (B) Percentage of clusters (subdivided into 1–2, 3–4, and >4 categories) in euchromatin and heterochromatin quantified in nuclear sections using TEM at 0.5 h and 5 h after low-LET versus high-LET IR. Statistically significant differences are indicated as asterisks directly above the bar when comparing to the previous time point and as asterisks above brackets directly above the bar when comparing between two different study groups (* $p < 0.05$, ** $p < 0.01$, and *** $p < 0.001$).

Following low-LET IR, the mean number of radiation-induced pKu80 and DNA-PKcs nanoparticles decreased from 0.5 h post-IR to 5 h post-IR (pKu80: 38.7 ± 5.1 to 26.6 ± 2.3 nanoparticles; DNA-PKcs: 19.8 ± 3.3 to 7.7 ± 1.8 nanoparticles), indicating slower, but efficient, repair kinetics in heterochromatic compartments. By contrast, following high-LET IR, the mean number of pKu80 and DNA-PKcs nanoparticles increased from 0.5 h post-IR to 5 h post-IR (pKu80: 25.2 ± 3.4 to 69.5 ± 7.2 nanoparticles; DNA-PKcs: 28.3 ± 2.8 to 47.2 ± 9.6 nanoparticles) (Figure 2A). While euchromatic regions revealed a slight decrease in pKu80 and DNA-PKcs nanoparticles with time, the heterochromatin, however, showed a significant increase. Based on these data, we hypothesize that the delay in the detection of DSBs clustered in heterochromatic compartments induced by high-LET IR is due to essential chromatin remodeling.

To further characterize the DNA-damage patterns caused by low-LET versus high-LET IR, we quantified the clusters for pKu80 and DNA-PKcs (subdivided into size categories 1–2, 3–4, >4 beads per cluster) separately in euchromatic and heterochromatic regions (Figure 2B). Following low-LET and high-LET IR, most of the pKu80 clusters consisted of two beads separated by an almost constant distance, reflecting each pKu80 molecule bound to the free ends of single breaks (>90–100%). In heterochromatin, the number of complex DSBs (≤ 3 beads) already increased at 0.5 h (~5%) after high-LET IR and further increased at 5 h (10%). This trend was even more impressive for DNA-PKcs. 5 h after high-LET IR, almost 30% of heterochromatic lesions were clustered DSBs (≤ 3 nanoparticles) (Figure 2B). Together, these findings indicate that high-LET IR induces clustered DNA lesions in heterochromatic regions, and this damage level even increased over time, suggesting that DSB clustering in heterochromatin following high-LET IR perturbs efficient repair.

3.3. Detection of Nanoparticles in the Areas of LEDDs Using Automated Image Analysis

After loading the TEM images into the HALO® Image Analysis platform and adjusting the scale for the micrographs, LEDDs were automatically segmented based on electron density, and the area of the LEDDs was calculated (Figure 3A). With this automated segmentation, 63 LEDDs were delineated following high-LET IR, with an averaged area of 0.76 ± 0.22 at 0.5 h post-IR and 1.65 ± 0.44 at 5 h post-IR (Figure 3A, right lower panel), correlating with the areas measured for clustered foci using IFM (Figure 1A). To capture the distribution of DNA repair factors associated with chromatin remodeling, the areas inside, outside, and at the border of the LEDDs were defined (each at 300 nm intervals) and segmented accordingly (Figure 3A, left lower panel). After appropriate contrast adjustment, nanoparticles were automatically recognized and quantified for the various repair factors (pKu80 and DNA-PKcs). All nanoparticles were automatically assigned to the corresponding region so that the spatial distribution in relation to the LEDD could be determined for each repair factor (Figure 3A, right panel). Figure 3B shows the quantitative evaluation of heterochromatic pKu80 and DNA-PKcs clusters (≥ 3 nanoparticles) in relation to the LEDD region after 0.5 h and 5 h post-IR. A shift in cluster size as a function of time was observed for both repair factors. At the early time point (0.5 h post-IR), only a few clusters were detected inside the LEDDs (pKu80: $2.8\% \pm 0.78\%$; pDNA-PKcs: $4.9\% \pm 1.18\%$), a little more in the border region (pKu80: $15.8\% \pm 1.49\%$; DNA-PKcs: $16.0\% \pm 2.77\%$) and most outside the LEDDs (pKu80: $56.6\% \pm 2.75\%$; $53.9\% \pm 3.58\%$). By contrast, 5 h post-IR, most of the pKu80 and DNA-PKcs clusters were observed in the border areas of LEDDs (pKu80: $45.6\% \pm 1.44\%$; DNA-PKcs: $55.8\% \pm 2.55\%$) (Figure 3B). Along with the observed enlargement of LEDDs, our findings suggest that the chromatin within the particle trajectory area progressively opened to allow the repair of clustered DNA damage.

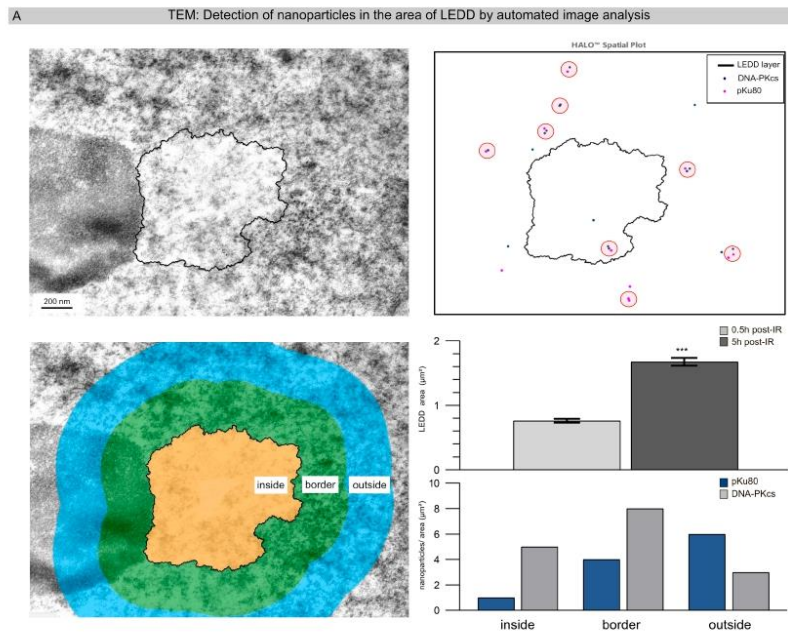


Figure 3. Cont.

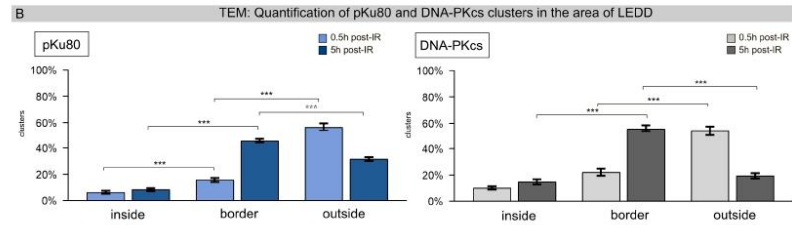


Figure 3. Detection of nanoparticles in the areas of LEDDs using automated image analysis. (A) TEM micrographs 5 h after high-LET IR show an LEDD next to the nucleolus. Using the spatial analysis tool of the HALO software, version 3.4.2986 (Indica Labs, Albuquerque, NM, USA), the LEDD was automatically segmented, and the differently-sized nanoparticles were detected. For further characterization of the repair factors in relation to the LEDD, the areas inside and outside the LEDD, as well as the border area, were defined, and the number of pKu80 and DNA-PKcs nanoparticles was automatically quantified. The area of each LEDD was quantified at 0.5 h and 5 h after high-LET IR. (B) Quantification of pKu80 and DNA-PKcs clusters inside and outside the LEDD, as well as in the border region, analyzed at 0.5 h and 5 h after high-LET IR. Statistically significant differences are indicated as asterisks directly above the bar when comparing to the previous time point and as asterisks above brackets when comparing between two different study groups (***) ($p < 0.001$).

3.4. Precise Analysis of the LEDD Boundaries Using Automated Image Analysis

To investigate the opening of chromatin in relation to the density of 53BP1 nanoparticles in more detail, we focused on the border areas of LEDDs. Based on the original TEM micrograph, the chromatin density was defined according to grayscale features and categorized into euchromatin versus heterochromatin (Figure 4A). Subsequently, high-LET-IR-induced LEDDs were delineated using automated segmentation. The nanoparticles within the LEDDs and the border regions, as well as beyond, were also segmented (Figure 4B, left panel). The spatial distribution of nanoparticles, especially regarding cluster formation, was visualized with the density heat map module. This density map clearly shows that most of the 53BP1 nanoparticles were located in the immediate border area of the LEDDs, and the formation of clustered lesions mainly occurs in heterochromatic areas (Figure 4B, right panel: ≥ 4 beads \rightarrow orange-red areas). Dividing the boundary regions around segmented LEDDs into four different distance ranges (1–100 nm, 101–200 nm, 201–300 nm, 301–400 nm), our results showed that the density of 53BP1 nanoparticles decreases significantly with increasing distance from the LEDD (Figure 4C). These results suggest that radiation-induced DSBs lead to an opening of the chromatin and, thus, to an increasing enlargement of the LEDDs following high-LET IR.

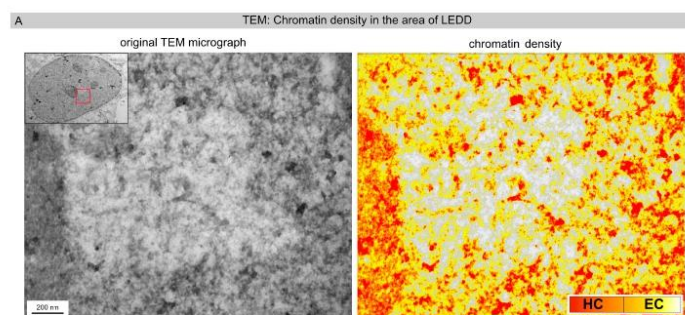


Figure 4. Cont.

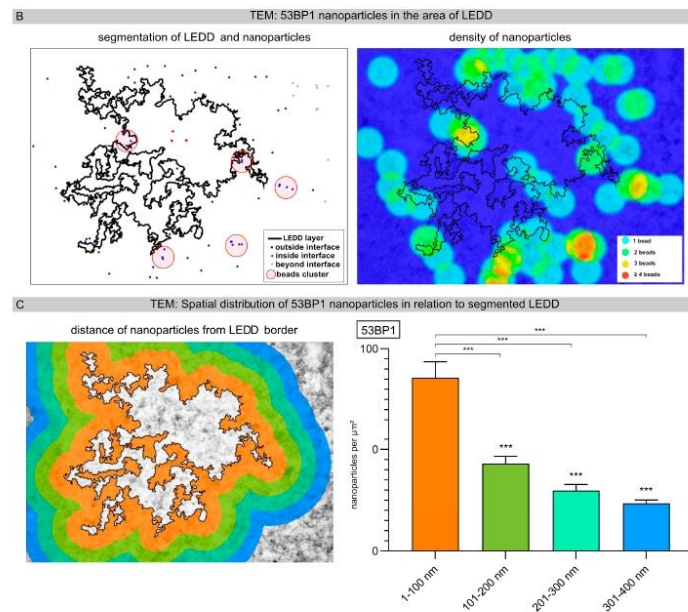


Figure 4. Precise analysis of LEDD boundaries using automated image analysis. (A) Based on the original TEM micrograph, chromatin density was defined according to grayscale features and categorized into euchromatin versus heterochromatin. (B) High-LET-IR-induced LEDDs and nanoparticles were delineated using automated segmentation. The spatial distribution of the nanoparticles, particularly regarding cluster formation, was visualized as a density heatmap. (C) Different boundary regions around the high-LET-IR-induced LEDDs were defined, and the spatial distribution of nanoparticles relative to segmented LEDDs was determined. In the inset, the red square shows the enlarged image section of the entire cell nucleus. Statistically significant differences are indicated as asterisks directly above the bar when comparing to the previous point of investigation (***) $p < 0.001$.

4. Discussion

In living organisms, the biological outcome of IR exposure is determined by the spatial and temporal distribution of ionization and excitation events, leading to the occurrence of different types of complex DNA damage. Approaches such as nanodosimetry/microdosimetry and Monte Carlo track-structure simulations have been successfully adopted to describe radiation quality effects. However, physical features alone are not sufficient to assess the extent and complexity of radiation-induced DNA damage. The latter is the result of an interplay between radiation trace structure and spatial chromatin and depends on the dynamic response of chromatin, affecting the activation and efficiency of the DNA repair machinery [16]. In future collaborative projects, our experimental TEM results will be compared with the biophysical simulation code PARTRAC for stochastic modeling of DSB repair after photon and ion IR. PARTRAC combines track structure calculations with DNA models on diverse genomic scales and, therefore, enables the prediction of DNA damage yields and patterns for various radiation qualities.

The aim of the present study was to establish the automated image analysis of transmission electron micrographs to investigate patterns of radiation-induced DNA damage within the cell nucleus on the nanometer scale. Here, we show that automated image analysis of nanoparticles in TEM micrographs enables precise characterization of complex DNA damage in combination with chromatin architecture and dynamics [17]. With powerful analysis functions and fast processing speeds, this automation strategy enables the in-depth

characterization of radiation damage with high sample throughput so that the specific DNA damage pattern following exposure to different radiation qualities can be recorded not only qualitatively but also quantitatively [18]. Based on their circumscribed size, shape, and density, the exact number of the different-sized nanoparticles, their distance to each other, as well as their exact localization in the micrographs can be determined with appropriate image analysis software. With the tissue classifier module, we used a state-of-the-art machine learning algorithm to identify chromatin densities based on grayscale features and categorized them into euchromatic or heterochromatic regions. Automating nuclear segmentation to delineate LEEDs across entire sections eliminated the need to manually draw outlines of areas of interest, increasing the objectivity of the analysis. In addition, we used different spatial analysis tools to identify the proximity and relative spatial distribution of nanoparticles throughout the nuclear domains. Using the spatial density heatmap analysis algorithm, we were able to measure and calculate the average density of nanoparticles within a certain distance of segmented LEEDs, and corresponding proximity histograms were automatically generated. Overall, our earlier TEM results were confirmed using this automation strategy. Moreover, this AI-based image analysis not only enables significantly faster data generation but also a far more precise analysis of the radiation-induced DNA damage pattern [19]. Visual TEM evaluation already highlighted clear differences in the DNA damage pattern and DNA repair capacity between low-LET and high-LET IR [20]. The automated image analysis of human fibroblasts at different times after low-LET versus high-LET IR enables the efficient evaluation of nanoparticle-labeled DNA repair proteins in the context of chromatin ultrastructure.

Radiation-induced DSBs have major effects on cell biology of transcription, replication, and interface with metabolic responses. Accurate recognition and timely repair of DSBs in complex chromatin environments requires a tightly coordinated DNA damage response (DDR). To detect DSBs in cell nuclei, IFM is generally used for visualization of γ H2AX or other radiation-induced foci. However, the resolution of standard fluorescence microscopy is too low to detect individual proteins at the single-molecule level, so DNA repair events cannot be linked to other DDR mechanisms. Our previous TEM studies with nanoscale-resolution imaging of accumulated DNA damage after high-LET IR revealed intriguing new insights into DSB processing within the chromatin environment. The basic idea of this TEM study was not only to go beyond the resolution of IFM but to systematically record and evaluate the various repair factors related to the chromatin status with a feasible time commitment. Automated image analysis of TEM micrographs offers an unbiased approach to investigating DDR by measuring protein localizations, interactions, and concentrations in the ultrastructure of the cell nucleus.

In this study, we used the computational pathology software HALO AI (version 3.4.2986; Indica Labs, Albuquerque, NM, USA) to evaluate TEM micrographs. HALO AI image analysis platform is specialized for quantitative analysis in digital pathology, enabling segmentation using artificial intelligence. User-friendly, intuitive HALO modules for different applications improve image processing speed and permit transparent workflows. Here, we used automatic segmentation of differently sized nanoparticles in combination with spatial analysis to analyze precisely immunogold-labeling patterns in nuclear sections, thereby characterizing the DNA damage pattern after exposure to different radiation qualities.

In traditional post-embedding TEM experiments, cells are chemically fixed, dehydrated, and embedded in resins. Resin blocks containing the specimen are then sectioned into thin slices to ensure the collection of the electron beam after passing through the sample. Since biological specimens (cells and tissue) are composed of elements with low atomic numbers, the difference in electron density is small, resulting in low-contrast images. To increase specimen contrast, biological samples are traditionally stained with heavy metal salts, such as osmium tetroxide, lead citrate, and uranyl acetate. Osmium interacts with lipids, uranium binds to phosphate and amino groups, and lead interacts with negatively charged groups. Overall, these metallic dyes enable differential staining of organelles and

compartments in mammalian cells. To ensure meaningful comparisons of the complex organization within cells at the ultrastructural level, all samples must be processed in exactly the same way. Moreover, threshold values for determining LEDDs must not be changed in original TEM images; otherwise, the shape and area of LEDDs would have been variable depending on the setting. Another important point is that uranyl acetate contrasting is not specific to DNA and, therefore, is not a reliable marker for DNA compactness in TEM imaging applications. In future projects, systematic investigations are planned to analyze the pathophysiological significance of these LEDDs using immunogold labeling for euchromatic and heterochromatic histone modifications.

Post-embedding immunoelectron microscopy is a powerful method for detecting antigens on the surface of sections. Nanoparticle-antibody conjugates with defined structure and stoichiometry are indispensable tools for subcellular mapping in high-resolution TEM. Electron microscopic imaging exploits the high electron density of gold (19.3 g/mL) compared with that of proteins (1.35 g/mL), providing electron opacity and high contrast to biological materials, and thus guarantees reliable detection during visual or automated evaluation. Due to its particulate and countable nature, colloidal gold is preferred as an antibody label as it offers the ability to quantify the concentration of antigens. However, the specificity and affinity of the antibody can influence nanoparticle quantification measurements. Accordingly, the number of nanoparticles cannot be directly derived from the number of antigens on the sample section because the labeling efficiency is influenced by various physical, chemical, and biological factors, mainly arising from sample preparation. However, constant and reproducible labeling efficiencies achieved by standardizing processing conditions are usually considered sufficient for quantification purposes. In our study, gold nanoparticles carried a single binding site for the primary antibody. Therefore, we hypothesize that although relative immunogold labeling does not provide the exact antigen concentration, it allows direct comparisons between subcellular site concentrations.

Our results provide direct evidence that high-LET IR induces clustered DNA damage along particle trajectories through highly focused ionization events, leading to extensive chromatin remodeling with the formation of LEDDs. In these particle trajectories, DSBs are increasingly detectable during this chromatin remodeling process, preferentially in the border areas between euchromatin and heterochromatin. Our results suggest that high-LET IR, in contrast to low-LET IR, is associated with pronounced chromatin relaxation in the form of LEDDs to enable the critical repair process of clustered DNA damage. The increase in heterochromatic DSBs and the sustained chromatin decondensation in the form of LEDDs indicates that cells are unable to repair the accumulated DNA damage and restore the original chromatin organization after high-LET IR.

5. Conclusions

Highly clustered DNA lesions, generated by extremely localized energy deposition of high-LET IR, pose a serious threat to cell viability by compromising both genomic and epigenomic integrity. A better understanding of this coordination between repairing DNA damage and restoring original chromatin structures will advance our view of genomic and epigenomic maintenance in response to DNA damage [13]. Overall, this automation strategy for quantifying nanoparticles in the chromatin context significantly reduces workload and enables comparative studies to evaluate dose distributions on micro- and nanometer scales following exposure to different radiation qualities. The increased throughput provided using automated acquisition schemes and the resulting generation of large amounts of data opens new possibilities for quantitative TEM studies in radiation research.

Author Contributions: M.A.A.-r. established automated image analysis of transmission electron micrographs and visualized the data; A.I. performed IFM and TEM data analysis and aided in data visualization; M.H. contributed analysis tools; C.E.R. planned, managed, and coordinated the research activities, acquired the funding for the project and wrote the manuscript. All authors have read and agreed to the published version of the manuscript.

Funding: The research leading to these results has received funding from the Federal Ministry of Education and Research (Bundesministerium für Bildung und Forschung; grant number 02NUK058B) and the German Cancer Aid (Deutsche Krebshilfe; grant number 70113135) to C.E.R.

Institutional Review Board Statement: Not applicable.

Informed Consent Statement: Not applicable.

Data Availability Statement: The data presented in this study are available on request from the corresponding author.

Acknowledgments: We would like to thank the medical physicists for their technical support during cell irradiation at the linear accelerators and Sara Timm for her excellent assistance with the TEM experiments.

Conflicts of Interest: The authors declare no conflict of interest. The funders had no role in the design of this study, in the collection, analyses, or interpretation of data, in the writing of the manuscript, or in the decision to publish the results.

References

- Mohamad, O.; Yamada, S.; Durante, M. Clinical Indications for Carbon Ion Radiotherapy. *Clin. Oncol.* **2018**, *30*, 317–329. [[CrossRef](#)] [[PubMed](#)]
- Mladenova, V.; Mladenov, E.; Stuschke, M.; Iliakis, G. DNA Damage Clustering after Ionizing Radiation and Consequences in the Processing of Chromatin Breaks. *Molecules* **2022**, *27*, 1540. [[CrossRef](#)] [[PubMed](#)]
- Hagiwara, Y.; Oike, T.; Niimi, A.; Yamauchi, M.; Sato, H.; Limsirichaikul, S.; Held, K.D.; Nakano, T.; Shibata, A. Clustered DNA double-strand break formation and the repair pathway following heavy-ion irradiation. *J. Radiat. Res.* **2019**, *60*, 69–79. [[CrossRef](#)] [[PubMed](#)]
- Chen, Z.; Tyler, J.K. The Chromatin Landscape Channels DNA Double-Strand Breaks to Distinct Repair Pathways. *Front. Cell Dev. Biol.* **2022**, *10*, 909696. [[CrossRef](#)] [[PubMed](#)]
- Chen, S.; Lees-Miller, J.P.; He, Y.; Lees-Miller, S.P. Structural insights into the role of DNA-PK as a master regulator in NHEJ. *Genome Instab. Dis.* **2021**, *2*, 195–210. [[CrossRef](#)] [[PubMed](#)]
- Garcia Fernandez, F.; Fabre, E. The Dynamic Behavior of Chromatin in Response to DNA Double-Strand Breaks. *Genes* **2022**, *13*, 215. [[CrossRef](#)] [[PubMed](#)]
- Rothkamm, K.; Barnard, S.; Moquet, J.; Ellender, M.; Rana, Z.; Burdak-Rothkamm, S. DNA damage foci: Meaning and significance. *Environ. Mol. Mutagen.* **2015**, *56*, 491–504. [[CrossRef](#)] [[PubMed](#)]
- Lorat, Y.; Brunner, C.U.; Schanz, S.; Jakob, B.; Taucher-Scholz, G.; Rube, C.E. Nanoscale analysis of clustered DNA damage after high-LET irradiation by quantitative electron microscopy—The heavy burden to repair. *DNA Repair.* **2015**, *28*, 93–106. [[CrossRef](#)] [[PubMed](#)]
- Lorat, Y.; Schanz, S.; Schuler, N.; Wennemuth, G.; Rube, C.; Rube, C.E. Beyond repair foci: DNA double-strand break repair in euchromatic and heterochromatic compartments analyzed by transmission electron microscopy. *PLoS ONE* **2012**, *7*, e38165. [[CrossRef](#)] [[PubMed](#)]
- Rube, C.E.; Lorat, Y.; Schuler, N.; Schanz, S.; Wennemuth, G.; Rube, C. DNA repair in the context of chromatin: New molecular insights by the nanoscale detection of DNA repair complexes using transmission electron microscopy. *DNA Repair.* **2011**, *10*, 427–437. [[CrossRef](#)] [[PubMed](#)]
- Lorat, Y.; Schanz, S.; Rube, C.E. Ultrastructural Insights into the Biological Significance of Persisting DNA Damage Foci after Low Doses of Ionizing Radiation. *Clin. Cancer Res.* **2016**, *22*, 5300–5311. [[CrossRef](#)] [[PubMed](#)]
- Lorat, Y.; Reindl, J.; Isermann, A.; Rube, C.; Friedl, A.A.; Rube, C.E. Focused Ion Microbeam Irradiation Induces Clustering of DNA Double-Strand Breaks in Heterochromatin Visualized by Nanoscale-Resolution Electron Microscopy. *Int. J. Mol. Sci.* **2021**, *22*, 7638. [[CrossRef](#)] [[PubMed](#)]
- Timm, S.; Lorat, Y.; Jakob, B.; Taucher-Scholz, G.; Rube, C.E. Clustered DNA damage concentrated in particle trajectories causes persistent large-scale rearrangements in chromatin architecture. *Radiother. Oncol.* **2018**, *129*, 600–610. [[CrossRef](#)] [[PubMed](#)]
- Jakob, B.; Scholz, M.; Taucher-Scholz, G. Biological imaging of heavy charged-particle tracks. *Radiat. Res.* **2003**, *159*, 676–684. [[CrossRef](#)] [[PubMed](#)]
- Jakob, B.; Splinter, J.; Taucher-Scholz, G. Positional stability of damaged chromatin domains along radiation tracks in mammalian cells. *Radiat. Res.* **2009**, *171*, 405–418. [[CrossRef](#)] [[PubMed](#)]
- Baiocco, G.; Bartsch, S.; Conte, V.; Friedrich, T.; Jakob, B.; Tartas, A.; Villagrana, C.; Prise, K.M. A matter of space: How the spatial heterogeneity in energy deposition determines the biological outcome of radiation exposure. *Radiat. Environ. Biophys.* **2022**, *61*, 545–559. [[CrossRef](#)] [[PubMed](#)]
- Gumbiowski, N.; Loza, K.; Heggen, M.; Epple, M. Automated analysis of transmission electron micrographs of metallic nanoparticles by machine learning. *Nanoscale Adv.* **2023**, *5*, 2318–2326. [[CrossRef](#)] [[PubMed](#)]

18. Jerez, D.; Stuart, E.; Schmitt, K.; Guerrero-Given, D.; Christie, J.M.; Hahn, W.E.; Kamasawa, N.; Smirnov, M.S. A deep learning approach to identifying immunogold particles in electron microscopy images. *Sci. Rep.* **2021**, *11*, 7771. [[CrossRef](#)] [[PubMed](#)]
19. Baxi, V.; Edwards, R.; Montalto, M.; Saha, S. Digital pathology and artificial intelligence in translational medicine and clinical practice. *Mod. Pathol.* **2022**, *35*, 23–32. [[CrossRef](#)] [[PubMed](#)]
20. Tonnemacher, S.; Eltsov, M.; Jakob, B. Correlative Light and Electron Microscopy (CLEM) Analysis of Nuclear Reorganization Induced by Clustered DNA Damage Upon Charged Particle Irradiation. *Int. J. Mol. Sci.* **2020**, *21*, 1911. [[CrossRef](#)] [[PubMed](#)]

Disclaimer/Publisher's Note: The statements, opinions and data contained in all publications are solely those of the individual author(s) and contributor(s) and not of MDPI and/or the editor(s). MDPI and/or the editor(s) disclaim responsibility for any injury to people or property resulting from any ideas, methods, instructions or products referred to in the content.

7.4 Publication 4

Table 4 Literature information of publication IV

Title	Immunomodulatory Effects of Histone Variant H2A.J in Ionizing Radiation Dermatitis
Authors and Affiliations	Gargi Tewary *, Benjamin Freyter PhD *, Mutaz Abd Al-razaq MS*, Hendrik Auerbach PhD *, Matthias W. Laschke MD,PhD †, Tanja Kübelbeck MS ‡, Antonia Kolb MS ‡, Adèle Mangelinck PhD §, Carl Mann PhD §, Daniela Kramer PhD ‡, Claudia E. Rube MD, PhD * *Department of Radiation Oncology, Saarland University Medical Center, Homburg/Saar, Germany †Institute for Clinical and Experimental Surgery, Saarland University, Homburg/Saar, Germany ‡Department of Dermatology, Medical Center of the Johannes Gutenberg University, Mainz, Germany §Institute for Integrative Biology of the Cell, Université Paris-Saclay, Gif-sur-Yvette Cedex, France
Journal	International Journal of Radiation Oncology* Biology* Physics
Impact factor	7.0
Publication status	Published
Year of publication	2023
Type of article	Research article
Volume	12

Pages	2427
DOI:	https://doi.org/10.3390/cells12202427

BIOLOGY CONTRIBUTION

Immunomodulatory Effects of Histone Variant H2A.J in Ionizing Radiation Dermatitis



Gargi Tewary,* Benjamin Freyter, PhD,* Mutaz Abd Al-razaq, MS,* Hendrik Auerbach, PhD,* Matthias W. Laschke, MD, PhD,[†] Tanja Kübelbeck, MS,[‡] Antonia Kolb, MS,[‡] Adèle Mangelinck, PhD,[§] Carl Mann, PhD,[§] Daniela Kramer, PhD,[‡] and Claudia E. Rube, MD, PhD*

*Department of Radiation Oncology, Saarland University Medical Center, Homburg/Saar, Germany; [†]Institute for Clinical and Experimental Surgery, Saarland University, Homburg/Saar, Germany; [‡]Department of Dermatology, Medical Center of the Johannes Gutenberg University, Mainz, Germany; and [§]Institute for Integrative Biology of the Cell, Université Paris-Saclay, Gif-sur-Yvette Cedex, France

Received Apr 20, 2023; Accepted for publication Sep 14, 2023

Purpose: Histone variant H2A.J is associated with premature senescence after ionizing radiation (IR) and modulates senescence-associated secretory phenotype (SASP). Using constitutive H2A.J knock-out mice, the role of H2A.J was investigated in radiation dermatitis.

Methods and Materials: H2A.J wild-type (WT) and knock-out (KO) mice were exposed to moderate or high IR doses (≤ 20 Gy, skinfold IR). Radiation-induced skin reactions were investigated up to 2 weeks post-IR at macroscopic and microscopic levels. H2A.J and other senescence markers, as well as DNA damage and proliferation markers, were studied by immunohistochemistry, immunofluorescence, and electron microscopy. After high-dose IR, protein-coding transcriptomes were analyzed by RNA sequencing, immune cell infiltration by flow cytometry, and gene expression by reverse transcription polymerase chain reaction in (non-) irradiated WT versus KO skin.

Results: In WT skin, epidermal keratinocytes showed time- and dose-dependent H2A.J accumulation after IR exposure. Unexpectedly, stronger inflammatory reactions with increased epidermal thickness and progressive hair follicle loss were observed in irradiated KO versus WT skin. Clearly more radiation-induced senescence was observed in keratinocyte populations of KO skin after moderate and high doses, with hair follicle stem cells being particularly badly damaged, leading to follicle atrophy. After high-dose IR, transcriptomic analysis revealed enhanced senescence-associated signatures in irradiated KO skin, with intensified release of SASP factors. Flow cytometric analysis indicated increased immune cell infiltration in both WT and KO skin; however, specific chemokine-mediated signaling in irradiated KO skin led to more neutrophil recruitment, thereby aggravating radiation toxicities. Increased skin damage in irradiated KO skin led to hyperproliferation, abnormal differentiation, and cornification of keratinocytes, accompanied by increased upregulation of transcription-factor JunB.

Conclusions: Lack of radiation-induced H2A.J expression in keratinocytes is associated with increased senescence induction, modulation of SASP expression, and exacerbated inflammatory skin reactions. Hence, epigenetic H2A.J-mediated gene

Corresponding author: Claudia E. Rube, MD, PhD; E-mail: claudia.ruebe@uks.eu

Gargi Tewary and Benjamin Freyter made equal contributions to this study.

Disclosures: C.E.R. reports funding from the German Research Foundation (Deutsche Forschungsgemeinschaft; grant no. RU821/8-1), German Cancer Aid (Deutsche Krebshilfe; grant no. 70113135) and from the Federal Ministry of Education and Research (Bundesministerium für Bildung

und Forschung; grant no. 02NUK058B); D.K. reports funding from Else-Kröner-Fresenius-Stiftung, TR/SFB156, TR/SFB355, and Peter-Hans-Hofschneider Foundation; and C.M. reports funding from the French Agence Nationale de la Recherche (grant no. ANR-17-CE12-008).

Data Sharing Statement: Research data are stored in an institutional repository and will be shared upon request to the corresponding author.

Supplementary material associated with this article can be found in the online version at [doi:10.1016/j.ijrobp.2023.09.022](https://doi.org/10.1016/j.ijrobp.2023.09.022).

expression in response to IR regulates keratinocyte immune functions and plays an essential role in balancing the inflammatory response during radiation dermatitis. © 2023 Elsevier Inc. All rights reserved.

Introduction

Histone variants contribute to the maintenance of genome integrity in response to radiation-induced DNA damage.¹ DNA damage response (DDR) after exposure to ionizing radiation (IR) is accompanied by significant alterations in chromatin structure, which are tightly controlled in time and space by histone variant dynamics.² A key player in DDR is histone variant H2A.X, required for DNA damage signaling at double-stranded DNA breaks (DSB). Phosphorylation of Ser-139 residues leading to γ H2AX-foci formation has emerged as a specific and sensitive molecular marker for monitoring DNA damage initiation and resolution.³ In addition to DNA damage signaling, histone variants also participate in restoration of chromatin structure upon DNA damage by fine-tuning local and large-scale chromatin reorganization.^{4,5}

Previous studies have shown that after IR exposure the H2A variant H2A.J is incorporated into nucleosomes at persisting DNA damage, so called “DNA segments with chromatin alterations reinforcing senescence,” and contributes to the chromatin organization even after DNA repair is complete.⁶ Importantly, H2A.J histones incorporated in radiation-damaged nucleosomes modulate structural chromatin organization and thereby determine gene regulation,⁷⁻⁹ raising the question of their possible effect on epigenetic states and cell fate transitions.

Acute radiation dermatitis remains a serious side effect of clinical radiation therapy, with symptoms ranging from mild erythema with skin dryness to more severe skin inflammation with moist desquamation and up to skin ulceration after high IR doses.¹⁰ High-energy radiation delivered during radiation therapy produces direct and indirect ionization events that lead to damage of cellular macromolecules, most importantly in the form of DSBs. Through this DNA damaging mechanism, radiation therapy affects all cell populations within epidermis/dermis and initiates inflammation-mediated processes of radiation-induced skin injury.¹⁰ Within the epidermis, radiation-induced DNA damage disrupts normal proliferation, differentiation, and cornification of keratinocytes, thereby affecting protective skin barrier functions.¹¹ Complex radiation reaction of the dermis includes damage to hair follicles (HFs) and sebaceous glands, leading to the acute effects of hair loss and skin dryness.¹² HFs extend into the deep dermis and comprise various segments characterized by differential expression of cell-associated markers and divergent proliferation patterns.¹³ Within the bulge region of murine skin, slow-cycling CD34+ HF stem cells (HFSCs) play an essential role in HF regeneration.¹⁴ Dependent on periodic HF growth, keratinocytes in the papilla proliferate to form the shaft of

growing hair. The uppermost segment, called “infundibulum,” extends from the epidermal surface to the opening of sebaceous ducts.¹³ Following IR exposure, the infiltration of immune cells, including T cells, monocytes/macrophages, and neutrophils, to irradiated skin, and the reactive hyperproliferation of epidermal keratinocytes constitute commonly recognized hallmarks of radiation dermatitis. Proinflammatory cytokines and chemokines play important roles in immune cell activation and contribute to clinical radiation dermatitis syndrome.¹⁵ However, because of the complexity of skin tissue, involving the crosstalk between numerous cell populations, much of the cellular and molecular interactions leading to radiation dermatitis remain unclear.

Previous studies have shown that the histone variant H2A.J accumulates in human fibroblasts during replicative and radiation-induced senescence and modulates the secretion of inflammatory cytokines.^{6,7} Senescent cells are characterized by their permanent cell cycle arrest, their resistance to apoptosis, and the secretion of a plethora of inflammatory mediators, termed “senescence-associated secretory phenotype” (SASP).^{16,17} Previous research showed that H2A.J is a sensitive marker of senescent keratinocytes in human epidermis in the context of skin aging and radiation response.¹⁸ Here, we analyzed the functional role of histone variant H2A.J during radiation dermatitis. Using H2A.J wild-type (WT) and knock-out (KO) mice we investigated the pathophysiological role of H2A.J in murine skin after moderate and high IR doses to elucidate molecular and cellular events that drive radiation-induced skin injury.

Methods and Materials

Mouse strains

For generation of H2A.J KO mice, a 7 bp deletion at the beginning of the *H2afj* gene was introduced by transcription activator-like effector nuclease-mediated DNA break in the C57BL/6-N genome (Cyagen). This *H2AFJ Δ 7* mutation created a frameshift with premature stop codon at the beginning of the H2AFJ coding sequence.¹⁹ The founder heterozygous mutation was then back-crossed 6 times to C57BL/6-N mice (WT; Janvier Laboratory). Homozygous *H2AFJ Δ 7* mice were viable and fertile. To prove the absence of H2A.J protein in homozygous *H2AFJ Δ 7* mice, we used immunofluorescence and mass spectrometry techniques. Immunofluorescence staining for H2A.J was performed on mouse embryonic fibroblasts (MEFs) prepared from WT and homozygous *H2AFJ Δ 7* mouse embryos. [Figure E1](#) shows that although H2A.J could be clearly detected in the

nuclei of WT MEFs, the H2A.J staining in *H2AFJΔ7* MEFs was completely negative. Likewise, we previously showed the absence of H2A.J expression by immunohistochemistry of multiple tissues of homozygous *H2AFJΔ7* mice compared with WT mice.¹⁹ Finally, we verified the absence of H2A.J through top-down mass spectrometry of acid-extracted histones from various organs of *H2AFJΔ7* mice, compared with the H2A.J peak that was present in the same tissues in WT mice. Figure E2 shows the results for liver tissue with the specific peak for H2A.J in WT mice but the absence of the H2A.J peak in KO mice. We previously described in detail this top-down mass spectrometry methodology to identify H2A.J in cells and mouse tissues.⁷ Given the nature of the *H2AFJΔ7* mutation and our inability to detect H2A.J protein in the cells and tissues of homozygous *H2AFJΔ7* mice, we consider this mouse to be an H2A.J KO (H2A.J-KO). All mice were housed in groups in individually ventilated cage cages with steady temperature ($22 \pm 1^\circ\text{C}$), humidity ($55\% \pm 10\%$), and 12-hour light-dark cycles with free access to standard pellet food and water.

Whole-body or dorsal skinfold IR

Whole-body IR with 1x or 5x fractions of 2 Gy (daily from Monday to Friday) was carried out as already described.²⁰ Fractionated IR with 5×2 Gy was carried out daily at the same time of the day from Monday to Friday, corresponding to clinical radiation therapy. For isolated high-dose irradiation of dorsal skinfolds (10 or 20 Gy, respectively), backs of anesthetized mice were shaved and completely depilated with hair removal cream. Dorsal skinfolds were lifted off the animals' backs and fixed with holding sutures, which temporarily creates a slight tension in the skin. Plexiglas panels were placed over the skinfolds without pinching the tissue to achieve dose build-up effects in this tissue-equivalent material. Computer tomography based 3-dimensional dose calculations were performed using the Eclipse treatment planning system (Varian Medical Systems) and showed homogeneous dose distributions with 100% isodoses completely enclosing the skinfolds (Fig. E2). Skinfolds of 6 anesthetized, video-monitored animals (3 WT and 3 KO mice) were irradiated simultaneously for each treatment group and timepoint at the linear accelerator (TrueBeam; Varian Medical Systems). The following set-up was used for the irradiation of skinfolds: radiation field: 0.10×0.31 m; collimator and gantry angle: 0° ; source-surface-distance: 0.987 m; beam energy: 6 MV photons; dose-rate: 3 Gy/min. After IR exposure, skinfold sutures were loosened immediately, so that the skin could reattach to subcutaneous tissue. During the post-IR period, all mice were monitored daily for potential radiation reactions. At defined timepoints after exposure, (non-) irradiated animals (3 WT and 3 KO mice per treatment group and per timepoint) were anesthetized intraperitoneally using ketamine ($120 \mu\text{g/g}$ body weight) and xylazine ($16 \mu\text{g/g}$) before tissue collection. For each treatment group and timepoint, 3 male mice were used

(biologic replicates), of which 3 technical replicates were analyzed. At the time of IR exposure, WT and KO mice were between 10 to 12 weeks old. For each treatment group (1×2 , 5×2 , 1×10 , and 1×20 Gy), nonirradiated control groups consisted of 3 male 12-week-old WT or KO animals, which were euthanized in parallel at the first timepoint after IR exposure. Experimental studies were approved by the Medical Sciences Animal Care and Use Committee of Saarland (trial nos.: 29/2020; 27/2021).

Immunofluorescence microscopy

Formalin-fixed skin tissues were embedded in paraffin and sectioned to $4\text{-}\mu\text{m}$ thickness. After dewaxing in xylene and rehydration in decreasing concentrations of alcohol, sections were boiled in citrate buffer and blocked with 10% immunoblock (Carl Roth). Sections were incubated with primary antibodies anti-53BP1 (DNA damage marker; cat. NB-100-304; Bio-Techne GmbH), anti-CD34 (marker for bulge HFSCs; cat. 553731; BD Pharmingen, BD Biosciences), anti-Ki67 (proliferation marker; cat. ab15580; Abcam), antilamin B1 (nuclear envelope marker whose downregulation is associated with senescence; cat. ab133741; Abcam), and anti-JunB (transcription factor for epidermal proliferation/differentiation; cat. C37F9; Cell Signaling Technology), followed by AlexaFluor-488 or AlexaFluor-568 secondary antibodies (Invitrogen). Finally, sections were mounted in VECTAshield with 4',6-diamidino-2-phenylindole (Vector Laboratories).

Immunohistochemistry

For SA- β -Gal staining (established senescence marker) dissected skin samples were prefixed and incubated in X-Gal staining solution (Merck Millipore) followed by end-fixation overnight. Formalin-fixed (and SA- β -Gal-stained) skin was embedded in paraffin and sectioned at $4\text{-}\mu\text{m}$ thickness. After dewaxing in xylene and rehydration in decreasing concentrations of alcohol, antigen retrieval was performed in citrate buffer and sections were incubated with the primary antibodies anti-H2A.J (cat. 61793; Active Motif) or anti-myeloperoxidase (MPO; indicator of neutrophil activation; cat. AF3667) followed by biotin-labeled antibodies (Dako). Staining was completed by incubation with 3,3'-diaminobenzidine and substrate chromogen. Finally, sections were counterstained with hematoxylin and mounted with Aqueous Mounting Medium (Dako).

Quantitative immunofluorescence microscopy and immunohistochemistry evaluation

For quantitative analysis, ≥ 200 cells in relevant areas of 10 different HFs and/or epidermal areas were registered for each tissue section (3 technical replicates each of 3 biologic replicates). Using a Nikon-Eclipse Ni fluorescence

microscope equipped with Nikon DS-Qi2 camera (Nikon), 53BP1-foci per cell, SA- β -Gal+ and H2A.J+ cells were counted separately in different HF regions (bulge, papilla, infundibulum). Lamin B1+ (HF and epidermis), CD34+ (bulge region), Ki67+, JunB+, and MPO+ cells in relevant areas (epidermis/ dermis) were enumerated and relative amounts of positive cells were depicted as percentage.

Scoring of skin injury

After high-dose IR exposure, the severity of radiation dermatitis was measured based on acute cutaneous reactions in irradiated skin areas. Under the same lighting conditions and camera settings, the extent of skin lesions was measured and photo-documented every other day. For each mouse, the severity of radiation dermatitis was graded on a scale of zero (none), 1 (slight erythema), 2 (intense erythema), 3 (dry desquamation), 4 (moist desquamation), 5 (<50% inflamed tissue with few spots of excoriations), or 6 (>50% inflamed tissue with extensive excoriations). For each treatment group (10 Gy/WT; 10 Gy/KO; 20 Gy/WT; 20 Gy/KO; compared with nonirradiated WT and KO mice, non-IR) the most severe skin lesion was recorded for each individual mouse every second day, and the mean score of 3 different mice was calculated on the relevant day after IR exposure (2, 4, 6, 8, 10, 12, and 14 days post-IR).

Measurement of epidermal thickness and HF density

Digital brightfield images (10x magnification) of hematoxylin and eosin stained skin sections were acquired by Nikon-Eclipse microscope (Nikon Instruments). Ten different images were obtained from each skin section at 10x magnification and saved as tagged image file format files. In these tagged image file format images, the perimeter of the epidermis was marked using the line tool in the image analysis program, outlining the epidermal borders in the form of closed polygons. From this, the NIS-Elements imaging software (Nikon Instruments) calculated the epidermis area in mm². For determining HF density, the number of follicular structures was recorded at various anatomic levels from epidermis to subcutis. HF densities were determined by counting follicle units (all stages of hair cycle from anagen to telogen) per epidermal area (mm²).

RNA-sequencing for analysis of differential gene expression

After high-dose IR (20 Gy, 1 week post-IR), skin tissue of (non-)irradiated WT and KO mice was collected in 1 mL TRIzol (Thermo Fisher Scientific) and stored at -80°C (3 biologic replicates per condition). RNA extraction, library preparation, and paired-end (2 × 150 bp, 30 M reads per sample) sequencing using NovaSeq (Illumina) were

performed by GENEWIZ Germany GmbH. Subsequently, raw reads were trimmed with Cutadapt (v3.5) to clip low-quality ends from reads that were below the Phred quality score of 20. Additionally, minimum read length of 50 was set. Data quality was inspected before and after trimming using FastQC (v0.11.3).²¹ Sequences were aligned to the murine genome sequence GRCm39²² using STAR Aligner (v. 2.7.10a)²³ and counted with HTSeq (v. 0.13.5).²⁴ Subsequently, differential expression analysis was performed using DESeq2 (v1.34.0).²⁵ For data visualization, R (v. 4.2.2) packages ggplot2 (v. 3.4.0) and pheatmap (v. 1.0.12) were used. Gene names were obtained with Bioconductor package biomaRt (v. 2.54.0).

Flow cytometry analysis of skin-infiltrating immune cell populations

After high-dose IR (20 Gy, 1 week post-IR), removed skin tissue of (non-)irradiated WT and KO mice was cut into small pieces and incubated with 300 μ g/mL liberase (Roche, Basel, Suisse) and 50 U/mL DNaseI (Thermo Fisher Scientific) in 10% false discovery rate in Roswell Park Memorial Institute medium for 1.5 hours at 37°C. Afterward, cells were passed through 100 μ m cell strainers (cat. 83.3945.100; Sarstedt) to obtain single-cell suspensions. After cell counting, 2 × 10⁶ cells were treated with Fc-Block (Bio-Rad,) for 10 minutes and surface stained with the following mouse-specific antibodies: anti-CD4-PE (cat. 100408), anti-CD8a-APC (cat. 100712), anti-CD11c-APC (cat. 117310), anti-CD25-APC (cat. 101910), anti-Ly6C-APC (cat. 128016), anti-F4/80-FITC (cat. 123107), anti-Ly6G-PE (cat. 127607; all from Biolegend), anti-TCR $\alpha\beta$ -PB (cat. HM 3628; Invitrogen), and anti-TCR $\gamma\delta$ -PE (cat. 553178; BD Biosciences). After washing, acquisition was performed with LSRII flow cytometer (BD Biosciences), and live single cells were gated using FlowJo (Tree Star, Inc) software.

RNA extraction and quantitative reverse transcription polymerase chain reaction

Total RNA was extracted from dorsal skin with QIAzol (QIAGEN) according to manufacturer's instructions. Contaminating genomic DNA was removed by treatment with DNaseI (Thermo Fisher Scientific) in the presence of Ribonuclease Inhibitor (Thermo Fisher Scientific). For reverse transcription, cDNA was synthesized from 4 μ g total RNA using oligo dT primer (Thermo Fisher Scientific) and Revert Aid reverse transcriptase. cDNA reaction was performed for 1 hour at 42°C. Relative gene expression was quantified by real-time polymerase chain reaction (PCR) using the Green master mix (Genaxxon) and self-designed primers. Real-time PCR analysis was performed on CFX384 (Bio-Rad) using the following PCR conditions: initial denaturation 15 minutes at 95°C, followed by 40 cycles of 95°C for 15 seconds and 60°C for 45 seconds. Relative mRNA levels were

calculated by normalization to reference gene *Actin* using the $2^{-\Delta\Delta Ct}$ method.

Transmission electron microscopy

Skin samples were fixed overnight with 2% paraformaldehyde and 0.05% glutaraldehyde in phosphate buffered saline. Fixed samples were dehydrated using increasing ethanol concentrations and permeated with LR White resin (EMS), followed by overnight embedding at 65°C with fresh LR White resin containing LR White Accelerator (EMS). Microtome Ultracut UCT (Leica) equipped with diamond knives (Diatome) were used for cutting ultrathin sections (70 nm), which were picked up on pioloform-coated nickel grids and prepared for immunogold-labeling. Nonspecific labeling was blocked using blocking solution (Aurion), sections were rinsed and incubated overnight with primary antibodies (anti-lamin B1; cat. 133741; Abcam) at 4°C, followed by incubation with 10-nm gold particle-conjugated secondary antibodies (Aurion) for 1.5 hours. Finally, sections were contrasted with uranylacetate. A Tecnai Biotwin transmission electron microscope (FEI) was employed for visual analysis.

Statistical analysis

GraphPad Prism (version 9.4.1; GraphPad Software) was used to collect and analyze data. Data are presented as the mean of 3 experiments with \pm standard deviation, which means 3 different animals per treatment group and timepoint (3 biologic replicates, $n = 3$) were examined, each with 3 technical replicates. Two-way analysis of variance (multiple comparisons) was used for estimating the differences among different groups followed by multiple comparisons between data sets. A *P* value of $<.05$ was considered statistically significant, $<.01$ as statistically highly significant, and $<.001$ as extremely statistically significant. Significant statistical differences compared with non-irradiated WT or KO controls (marked by asterisks alone) or between mouse lines (asterisks with square brackets) are presented in the figures as $*P < .05$, $**P < .01$, and $***P < .001$.

Results

DSB repair and senescence induction after whole-body IR exposure with moderate doses

To compare DSB repair capacity, WT and KO mice were exposed to whole-body IR with 2 Gy, and skin samples were analyzed for 53BP1-foci at 24 hours, 72 hours, and 1 week post-IR. 53BP1-foci were quantified in different HF regions to capture potential differences in DSB repair capacity of HFSCs in bulge regions and proliferating keratinocytes at dermal papillae (Fig. 1A). Analysis of these epidermal cell

populations revealed significantly increased 53BP1-foci levels at 24 hours, 72 hours, and even at 1 week post-IR compared with non-irradiated controls, likely reflecting un- or misrepaired DNA damage (Figs. 1A and E3A). However, no significant differences in DSB repair capacities were observed between these epidermal cell populations, nor between WT versus KO skin, suggesting that H2A.J is not involved in the acute process of DSB repair after moderate doses (Fig. 1A). To test histone variant H2A.J as a potential marker for radiation-induced senescence, WT and KO mice were irradiated with 1 or 5 daily fractions of 2 Gy (whole-body IR), and at different timepoints after IR exposure skin samples were stained simultaneously for H2A.J and SA- β -Gal (Fig. 1B). For WT mice time- and dose-dependent increases of H2A.J were observed with maximal values at 1 week post-IR after 2 Gy ($26.5\% \pm 5\%$) and even more clearly pronounced at 2 weeks post-IR after 5×2 Gy IR ($68.5\% \pm 4\%$) compared with non-irradiated skin tissue (2%-4%; Fig. 1B). These H2A.J and SA- β -Gal data for WT mice have already been published.²⁶ As expected, no H2A.J expression (independent of IR exposure) could be detected in the epidermis or dermis of KO mice (Figs. 1B and E3B). By counting SA- β -Gal+ cells, enhanced senescence induction was observed in WT and KO skin with increasing time after IR exposure. Although only minor differences in senescence induction were observed in the bulge region, highly significant differences in SA- β -Gal+ cells between WT and KO were observed in the proliferative papilla and infundibulum segment (Figs. 1C and E3B). Despite increased senescence induction, no clinical skin changes were observed at these moderate doses.

Analysis of skin lesions after high-dose IR exposure of dorsal skinfolds

To detect potential differences in skin reactions between WT and KO mice, dorsal skinfolds were irradiated with single doses of 10 and 20 Gy, respectively. After 10 Gy exposure, only slight external signs of skin injury with mild lesions (day 4-8) and delayed hair growth occurred, more noticeable in WT mice (Fig. 2A). After 20 Gy exposure, radiation-induced skin reactions were observed from day 10 to 14 in both WT and KO mice (Fig. 2A). Unexpectedly, radiation-induced skin lesions were more pronounced in KO mice, with more than 50% of irradiated skin being severely inflamed and showing extensive excoriations (Fig. 2A). Histologic analysis of hematoxylin and eosin stained skin sections from WT and KO mice irradiated with 20 Gy revealed striking morphologic changes in both epidermal and dermal layers. After IR exposure with 20 Gy, epidermal thickness increased in both WT and KO mice with increasing time, but epidermal hyperplasia was clearly more pronounced in KO versus WT skin (Figs. 2B and E4A). Quantification of epidermal areas revealed significant increases from ≈ 2.0 mm² in non-irradiated skin to 6.7 ± 1.6 mm² in WT and 22.5 ± 3.8 mm² in KO mice at 2

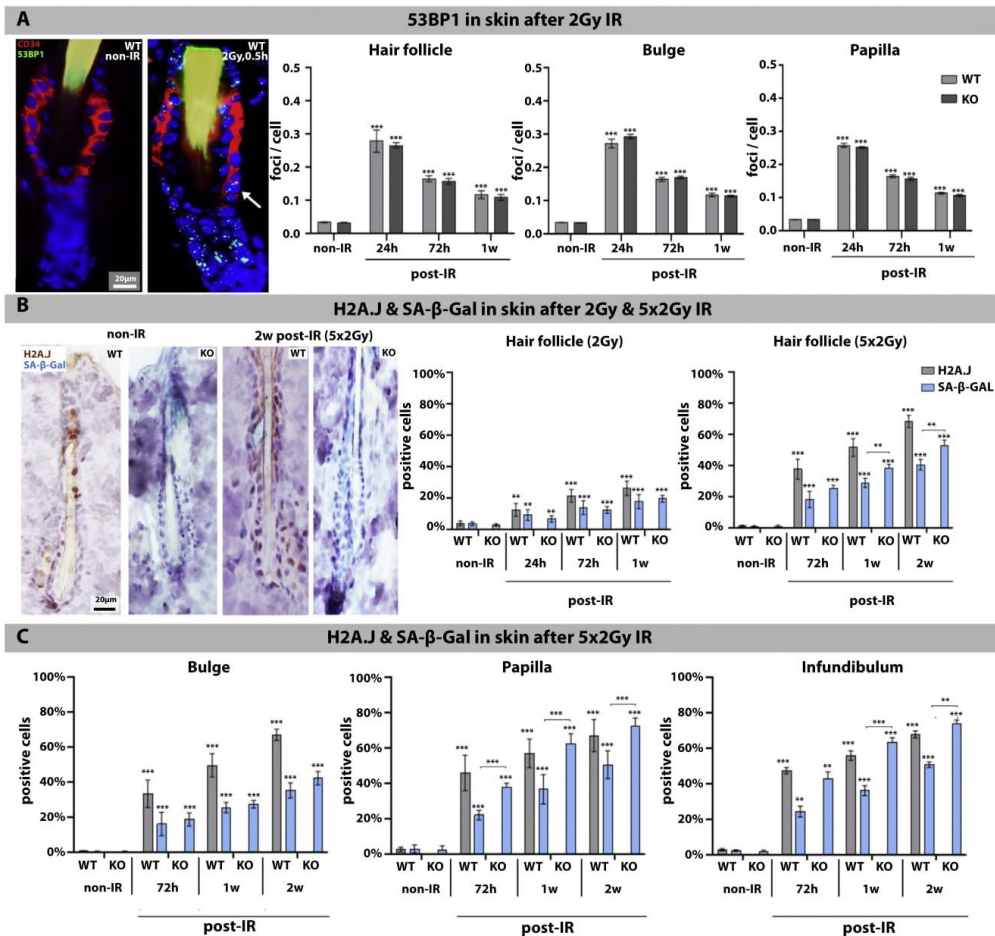


Fig. 1. Double-stranded DNA break repair and senescence induction after whole body IR with moderate doses. (A) IF micrographs of 53BP1 and CD34 double-staining in murine hair follicle after IR exposure (2 Gy; 0.5 hours post-IR) compared with non-irradiated control. The arrow shows a 53BP1 focus. Graphic presentation of 53BP1-foci quantification (foci/cell) in different hair follicle segments. (B) Immunohistochemistry micrographs of H2A.J and SA- β -Gal double-staining in murine hair follicle after IR exposure (5×2 Gy; 2 weeks post-IR) compared with non-irradiated control. Graphic presentation of quantification of H2A.J+ and SA- β -Gal+ cells at 24 hours, 72 hours, and 1 week post-IR after 2 Gy or at 72 hours, 1 week, and 2 weeks post-IR after 5×2 Gy. (C) Quantification of H2A.J+ and SA- β -Gal+ cells at 72 hours, 1 week, and 2 weeks post-IR after 5×2 Gy. Data are presented as mean \pm standard deviation ($n = 3$). For wild-type and knock-out mice the values at different timepoints after IR were compared with corresponding non-irradiated controls (significance asterisks directly above the corresponding bars). Moreover, values for wild-type with knock-out mice were compared with each other at the different timepoints after IR (presented by connecting brackets with significance asterisks). Statistical significances are presented as * $P < .05$, ** $P < .01$, *** $P < .001$. Abbreviations: IF = immunofluorescence; IR = ionizing radiation.

weeks post-IR, so that radiation-induced increase in epidermis thickness was significantly more pronounced in KO mice (Fig. 2C). According to reduced hair growth, there were significant differences in HF densities in WT versus KO skin after 20 Gy exposure. Quantification of HFs in epidermal and dermal compartments revealed

more pronounced reductions of HF densities in KO mice (3.7 ± 1.4 HF/mm² in WT and 1.2 ± 0.9 HF/mm² in KO skin at 2 weeks post-IR; Fig. 2C). Collectively, radiation-induced epidermal hyperplasia and HF atrophy were significantly more pronounced in irradiated KO versus WT skin.

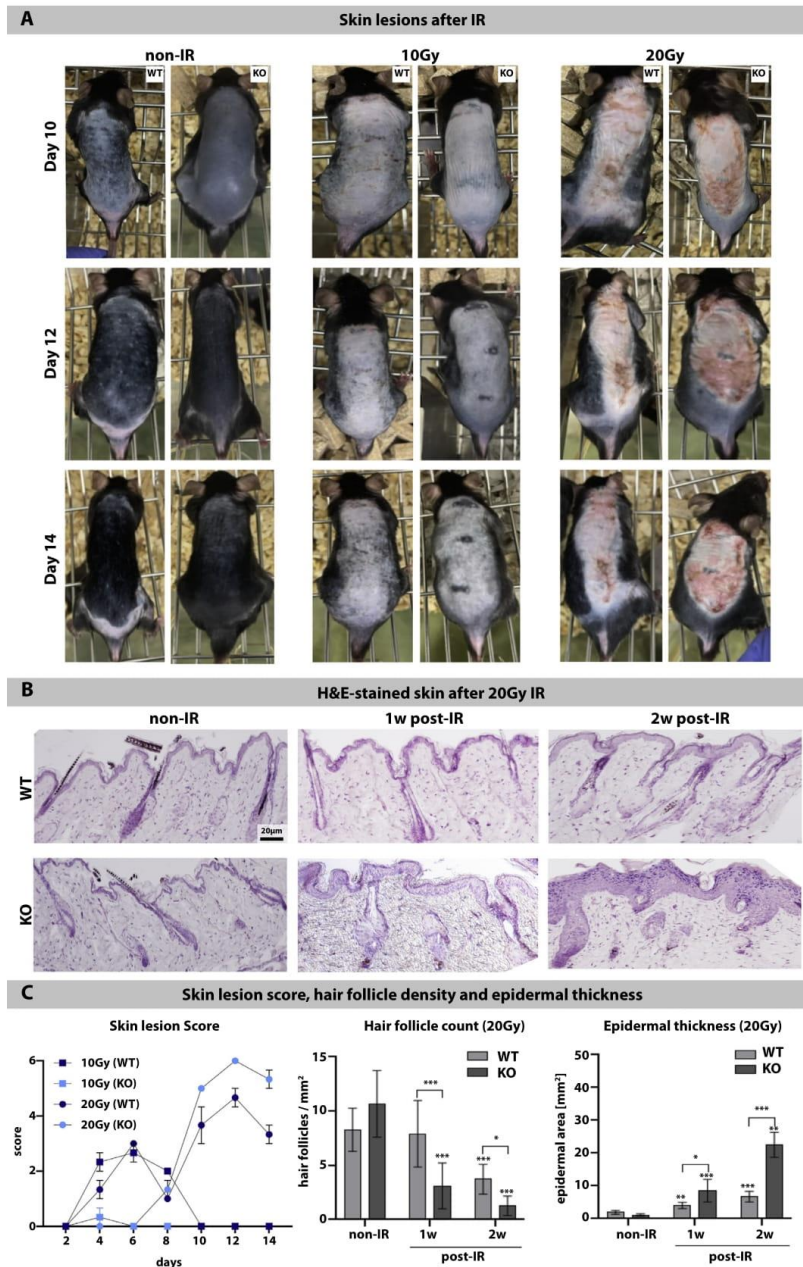


Fig. 2. Analysis of skin lesions after high-dose IR exposure of dorsal skinfolds. (A) Photo documentation of cutaneous reactions in irradiated skin areas of WT and KO mice after 10 or 20 Gy exposure compared with non-irradiated control. (B) Histologic micrographs of hematoxylin and eosin stained skin of WT and KO mice after 20 Gy exposure compared with non-irradiated control. (C) Graphic presentation of skin lesion scores, hair follicle densities, and epidermal thickness of WT and KO skin after 20 Gy exposure compared with non-irradiated control. Data are presented as mean \pm standard deviation (n = 3). For WT and KO mice the values at different timepoints after IR were compared with corresponding non-irradiated

Senescence induction and HFSC depletion after high-dose IR exposure of dorsal skinfolds

To elucidate the underlying causes of HF atrophy after IR exposure more precisely, induction of cellular senescence and stem cell loss after IR with 20 Gy were investigated. In different HF regions, proportions of H2A.J+ and SA- β -Gal+ keratinocytes were determined in skin samples stained simultaneously for SA- β -Gal and H2A.J. In irradiated WT skin, both the proportion of H2A.J+ (64% \pm 2.9%) and SA- β -Gal+ (36.0% \pm 5.0%) increased significantly to maximal values at 2 weeks post-IR (Fig. 3A). Strikingly, in irradiated KO skin, the increase of SA- β -Gal+ cells was even greater at 1 and 2 weeks post-IR, indicating that radiation-induced senescence was more pronounced in KO mice. Remarkably, in contrast to IR exposure with moderate doses (1 \times and 5 \times 2 Gy; Fig. 1), the bulge region was particularly affected by senescence induction after high-dose IR exposure (Figs. 3A and E3C). Previous studies have shown that lamin B1 declines during DNA damage-induced senescence.²⁷ Accordingly, immunofluorescence and electron microscopy analysis were performed to visualize lamin B1 levels in HF and epidermis in response to senescence-inducing IR doses (Fig. E5). In non-irradiated WT and KO skin nearly all keratinocytes in HF and epidermis revealed an intense lamin B1 signal in the nuclear envelope (Fig. 3B). After 20 Gy IR exposure, by contrast, numbers of lamin B1+ cells declined with increasing time in HF (WT: 75.6% \pm 4.1%; KO: 8.7% \pm 1.3%) and epidermis (WT: 28.8% \pm 9.6%; KO: 9.7% \pm 2.3% at 2 weeks post-IR) of both WT and KO mice (Fig. 3B). Remarkably, this pronounced senescence induction in stem cell niches correlated with marked reductions of CD34+ HFSCs in irradiated KO skin (WT: 13.0% \pm 2.4%; KO: 2.8% \pm 0.7%; Fig. 3C). Cyclic growth of HF depends on functional HFSCs in their physiological micro-environment. Increased senescence and SASP induction after IR exposure may attract immune cells to injured HFSC niches, leading to dysfunctional hair regeneration and long-term hair loss.

Transcriptome analysis after high-dose IR exposure of dorsal skinfolds

For deciphering regulatory networks underlying radiation-induced skin injury and accurately assessing the relative contribution of H2A.J depletion, protein-coding transcriptomes were determined by RNA sequencing (RNA-seq) of epidermal skin of (non-)irradiated WT and KO mice taken 1 week post-IR (20 Gy). In these transcriptomes of whole-skin tissues, we identified 4334 differentially expressed genes

(DEGs) between WT IR versus WT non-IR (of which 2087 were upregulated and 2247 were downregulated), 2475 DEGs between KO IR versus KO non-IR (1114 upregulated, 1361 downregulated), 138 DEGs between KO non-IR versus WT non-IR (93 upregulated, 45 downregulated), and 2455 DEGs between KO IR versus WT IR (1424 upregulated, 1031 downregulated; Fig. 4A). In these RNA-seq data sets only very small differences were observed between non-irradiated skin of WT and KO mice, corresponding to their indistinguishable phenotype under unstressed conditions. Greatest differences in transcriptomic signatures were observed between non-irradiated and irradiated skin tissue for both WT and KO mice, reflecting the major stress response caused by IR exposure (Fig. 4A). However, crucial differences in the transcriptome were also observed between irradiated skin tissues of KO versus WT mice. Upon examining the list of DEGs, we identified significant numbers of hits comprising the senescence program. Especially, genes encoding known SASP factors were upregulated in a more pronounced manner in irradiated KO versus WT skin. This differential expression of SASP components correlates with our finding that in irradiated KO skin \approx 50% (20 Gy, 1 week post-IR) or \approx 70% (20 Gy, 2 weeks post-IR) stained positive for SA- β -Gal, but in irradiated WT skin only \approx 20% (20 Gy, 1 weeks post-IR) or 40% (20 Gy, 2 weeks post-IR) of keratinocytes were positive. Thus, radiation-induced senescence appears to be the most important stimulus for altered transcription, with consequently more pronounced SASP expression in irradiated KO skin. Accordingly, our RNA-seq data sets showed strong upregulation of SASP-associated cytokines (*Il1a*, *Il1b* and *Il6*, *insulin-like growth factor binding protein [Igfbp] 4/5/6*, *tumor necrosis factor receptor superfamily Tnfrsf 10b/11b/ 18*), chemokines (*Ccl2*, *Ccl5*, *Ccl12*, *Ccl20*, *Ccr3*, *Cxcl1*, *Cxcl5*), adhesion molecules (such as *intercellular adhesion molecule-1*, *Icam1*), and matrix metalloproteinases and their inhibitors (*Mmp1b*, *Mmp3*, *Mmp10*, *Mmp12*, *Mmp13*, *Mmp14*, *Timp2*) in response to IR exposure, but clearly more pronounced in irradiated KO skin (Fig. 4B). The complex senescence phenotype is not mediated by senescence-specific events, but rather represents a collection of cellular functions that involves DNA damage repair and persistent DDR, cell-cycle arrest, chromatin reorganization, and tumor suppression, along with morphologic changes and metabolic reprogramming that are also associated with other cellular events. Accordingly, genes associated with these basic cellular functions were also screened for transcriptional activation in irradiated KO versus WT skin. Comparative analysis of gene expression in KO IR versus WT IR revealed many significant DEGs in these fundamental cellular programs that are either directly or indirectly involved in driving the complex senescence

controls (significance asterisks directly above the corresponding bars). Moreover, values for WT with KO mice were compared with each other at the different timepoints after IR (presented by connecting brackets with significance asterisks). Statistical significances are presented as * P < .05, ** P < .01, *** P < .001. Abbreviations: IR = ionizing radiation; KO = knock-out; WT = wild-type.

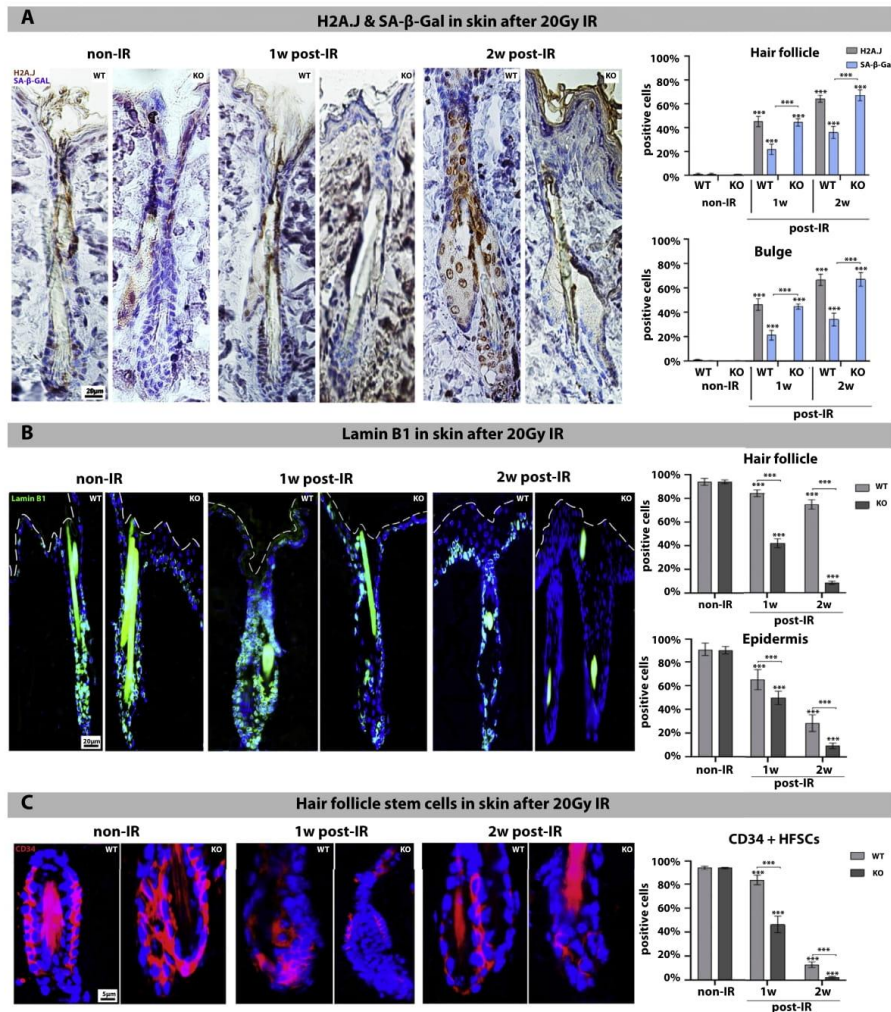


Fig. 3. Senescence induction and hair follicle stem cell depletion after high-dose IR of dorsal skinfolds. (A) Immunohistochemistry micrographs of H2A.J and SA-β-Gal double-staining in murine hair follicle after 20 Gy exposure compared with non-irradiated control. Graphic presentation of quantification of H2A.J+ and SA-β-Gal+ cells after 20 Gy exposure. (B) IF micrographs of lamin B1 staining in hair follicle after 20 Gy exposure compared with non-irradiated control. Graphic presentation of quantification of lamin B1+ cells in hair follicle and epidermis. (C) IF micrographs of CD34 staining in bulge regions of hair follicles. Graphic presentation of quantification of CD34+ hair follicle stem cells after 20 Gy exposure compared with non-irradiated control. Data are presented as mean ± standard deviation (n = 3). For wild-type and knock-out mice, the values at different timepoints after IR were compared with corresponding non-irradiated controls (significance asterisks directly above the corresponding bars). Moreover, values for wild-type with knock-out mice were compared with each other at the different timepoints after IR (presented by connecting brackets with significance asterisks). Statistical significances are presented as * $P < .05$, ** $P < .01$, *** $P < .001$. Abbreviations: IF = immunofluorescence; IR = ionizing radiation.

response. Accordingly, genes involved in cell cycle regulation are more suppressed in WT IR versus KO IR skin, possibly reflecting the lower proliferation of keratinocytes in irradiated WT versus KO epidermis (Fig. E6A). Chromatin

alterations in senescent cells are mediated by changes in the abundance of histone components. Our RNA-seq analysis showed that irradiated WT skin, characterized by moderate senescence induction and less reactive proliferation

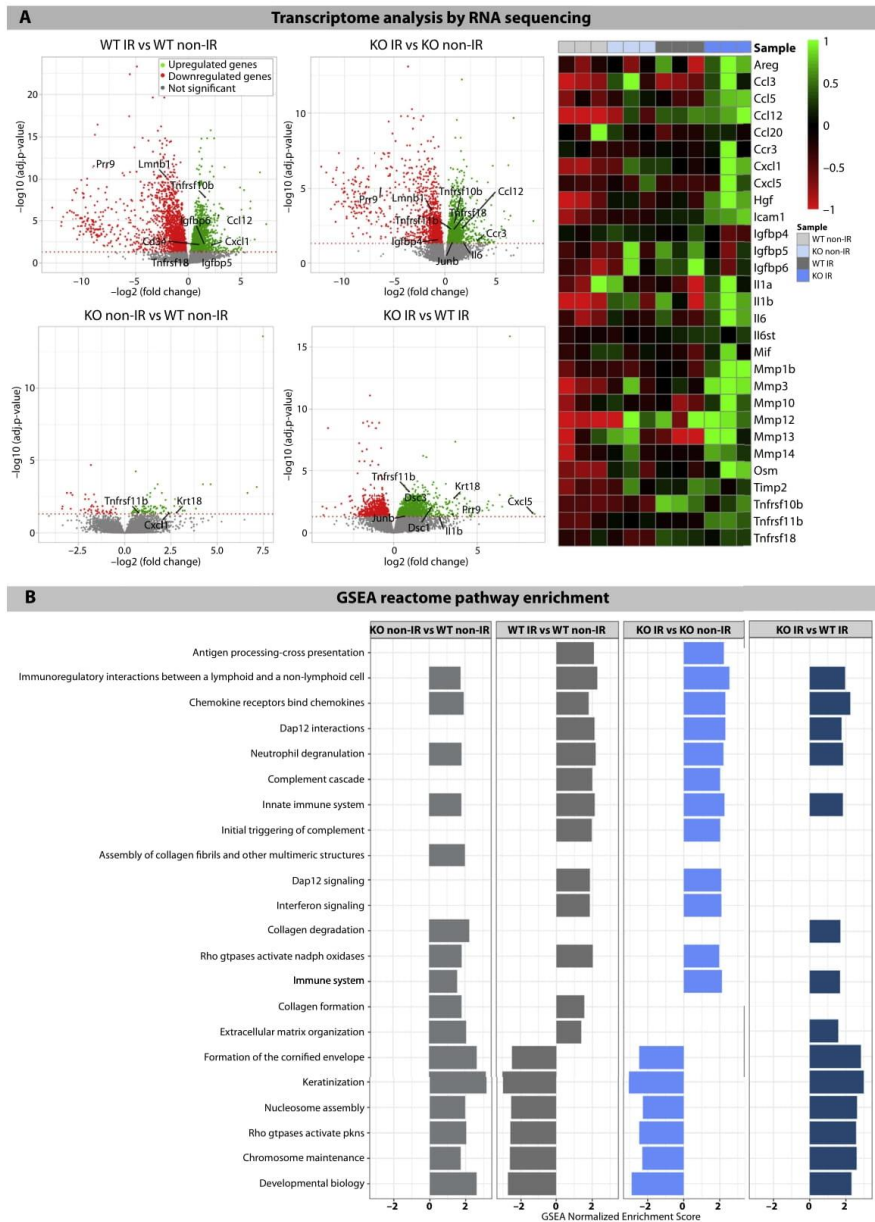


Fig. 4. RNA-seq transcriptome analysis after high-dose IR of dorsal skinfolds. (A) Volcano plots of differential expressed genes between WT irradiated (WT_IR) versus WT non-irradiated (WT_non-IR), KO irradiated (KO_IR) versus KO non-irradiated (KO_non-IR), KO non-irradiated (KO_non-IR) versus WT non-irradiated (WT_non-IR), and KO irradiated (KO_IR) versus WT irradiated (WT_IR). Scatterplot shows statistical significance ($-\log_{10} padj$) versus magnitude of change ($\log_2 FC$). Genes are colored if they pass the thresholds for $\log_{10} padj$ and $\log_2 FC$: Red/green dots denote down-/upregulated gene expression, blue dots denote SASP factors. Genes of interest were visualized (black) in comparison to the other genes. (B) Heat map of RNA-seq expression data showing senescence-associated secretory phenotype genes that were differentially regulated in

compared with irradiated KO skin, displayed clearly decreased mRNA expression levels of canonical histones (Fig. E6B). DNA repair and DDR genes were more downregulated in WT IR versus KO IR skin, possibly reflecting the reduced radiation damage in WT skin (Fig. E7A). Genes encoding cytokines and cytokine receptors are more strongly upregulated in KO IR versus WT IR, likely reflecting the increased inflammation in irradiated KO skin (Fig. E7B). In contrast, the DEG results between WT IR and KO IR for multiple oncogenes and tumor suppressor genes were not that uniform, suggesting that individual genes have to be analyzed specifically to investigate the potential role of H2A.J during tumor development and progression (complete list of DEG is available on request). For example, the *Acod1* gene was one of the most deregulated genes between WT and KO skin before and particularly after IR exposure (ratio ≈ 23 between KO non-IR vs WT non-IR; ratio ≈ 130 between KO IR vs WT IR). The mitochondria-associated *Acod1* gene plays a fundamental role in immunometabolism, modulating the interactions between immune and metabolic pathways during stress responses.²⁸⁻³⁰ Collectively, our findings show that –within the context of radiation dermatitis– H2A.J-associated effects are not limited to the interplay between SASP signalling and immune surveillance. Instead, H2A.J appears to affect the highly complex pathogenesis of radiation dermatitis by modulating diverse senescence-associated processes with beneficial and/or deleterious contributions to skin tissue homeostasis. Moreover, bioinformatic comparison using gene set enrichment analysis reactome pathway enrichment analysis was performed to explore pathophysiological pathways that characterize the molecular and cellular interactions in response to high-dose IR exposure (Fig. 4B). Most prominent ranked pathways were associated with inflammatory and immunoregulatory interactions but also with collagen and extracellular matrix organization, keratinization, and formation of the cornified envelope (Fig. 4B). Significantly, most of these critical networks were even stronger upregulated in H2A.J-depleted skin after IR exposure, suggesting that senescence-induced inflammatory processes exacerbate the detrimental radiation effects to skin homeostasis.

Immune cell infiltration after high-dose IR exposure of dorsal skinfolds

To investigate the effect of immune cell infiltration during radiation dermatitis, skin samples from (non-)irradiated WT and KO mice (20 Gy, 1 week post-IR) were analyzed using

flow cytometry (Fig. 5A). In non-irradiated skin of WT and KO mice, no differences were observed in the number of Langerhans and dendritic cells (CD45+, CD11c+), T-cell populations (CD4+, CD8+, CD25+, $\alpha\beta$ TCR+, $\gamma\delta$ TCR+), macrophages and monocyte-derived macrophages (F4/80+, Ly6C+), or neutrophils (Ly6G+; Fig. 5A). After IR exposure, the inflammatory phase in WT and KO skin was characterized by increased infiltration with $\alpha\beta$ and $\gamma\delta$ T-lymphocytes and monocyte-derived macrophages. Remarkably, neutrophil numbers (Ly6G+) were exclusively increased in inflamed skin of KO mice (Fig. 5A). Subsequently, real-time quantitative PCR analysis of whole-skin RNA was performed to evaluate the effect of high-dose IR on chemokine-mediated recruitment of inflammatory cells. In non-irradiated skin the chemokines *CC chemokine ligand 2* (*Ccl2*) and *C-X-C motif chemokine ligand 2 and 5* (*Cxcl2*, *Cxcl5*) were expressed at low levels, with no clear differences between non-irradiated WT and KO skin. After IR exposure *Ccl2* was significantly upregulated in both WT and KO skin, correlating with increased monocyte/macrophage trafficking during inflammatory skin reactions, regardless of H2A.J status. *Cxcl2* and *Cxcl5* are important chemoattractants for neutrophil granulocytes.³¹ After IR exposure, *Cxcl2* and *Cxcl5* mRNA expression was exclusively increased in irradiated KO skin; these findings correlate with our transcriptome results and increased neutrophil recruitment into the more inflamed skin of irradiated KO mice. We also analyzed the mRNA expression of *Nfkbiz*, the gene encoding transcription factor $\kappa B\zeta$, and interleukin *Il17a* and *Il36g*, which are involved in inflammatory skin diseases such as psoriasis.^{32,33} Remarkably, significant elevations were observed for the *Nfkbiz* and *Il17/ Il36* axis, known to establish cytokine networks responsible for the development and maintenance of the inflamed state and for keratinocyte hyperproliferation.

Neutrophil-driven inflammation is associated with increased proliferation of basal keratinocytes

Neutrophils are important effector cells of the innate immune system and destroy invading pathogens through phagocytosis with intracellular degradation or release of lysosomal enzymes, such as MPO, during their degranulation. To determine whether radiation-induced skin damage is associated with neutrophil-derived MPO release, percentages of MPO+ cells were quantified in (non-)irradiated WT and KO skin. Although no MPO+ cells could be detected in unexposed skin, the percentage of MPO+ cells was

(non-)irradiated WT and KO skin. Gene expression is shown in normalized log₂ counts per million. Differentially expressed genes were selected based on ± 1 -fold change and FDR < 0.05. (C) GSEA Reactome pathway enrichment analysis revealed 22 statistically significant pathways, listed separately for KO_non-IR versus WT_non-IR, WT_IR versus WT_non-IR, KO_IR versus KO_non-IR, and KO_IR versus WT_IR. GSEA Normalized Enrichment Score was used to compare analysis results across different gene sets. *Abbreviations:* FDR = false discovery rate; GSEA = gene set enrichment analysis; IR = ionizing radiation; KO = knock-out; WT = wild-type.

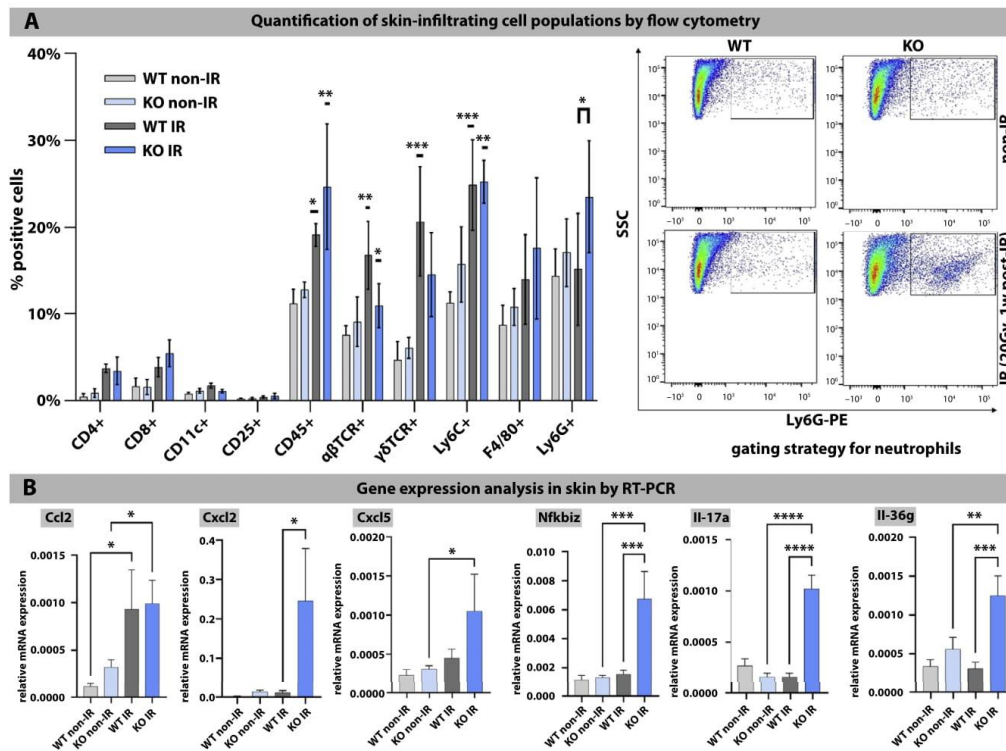


Fig. 5. Immune cell infiltration after high-dose IR exposure of dorsal skinfolds. (A) Quantification of flow cytometry analysis for CD4+, CD8+, CD11+, CD25+, CD45+, $\alpha\beta$ TCR+, $\gamma\delta$ TCR+, Ly6C+, F4/80+, and Ly6G+ cells in (non-)irradiated WT and KO skin. (B) Gene expression analysis in (non-)irradiated WT and KO skin by reverse transcription polymerase chain reaction. Data are presented as mean \pm standard deviation ($n = 3$). For WT and KO mice, the values at different timepoints after IR were compared with corresponding non-irradiated controls (significance asterisks directly above the corresponding bars). Moreover, values for WT with KO mice were compared with each other at the different timepoints after IR (presented by connecting brackets with significance asterisks). Statistical significances are presented as * $P < .05$, ** $P < .01$, *** $P < .001$. Abbreviations: IR = ionizing radiation; KO = knock-out; WT = wild-type.

significantly increased in KO versus WT skin at both 1 and 2 weeks post-IR (20 Gy), with KO skin showing higher numbers of MPO+ cells (Fig. 6A). Our findings regarding increased neutrophil recruitment (Fig. 5) and pronounced tissue damage in irradiated KO skin (Fig. 2) confirm the critical role for neutrophil-derived MPO in the elicitation phase of radiation-induced skin injury.

To analyze keratinocyte proliferation, Ki67+ cells were quantified in (non-)irradiated WT and KO epidermis at 1 and 2 weeks post-IR (20 Gy). Although non-irradiated WT and KO skin showed only low proliferation rates, significant hyperproliferation of basal keratinocytes was observed, especially in irradiated KO skin at 1 week post-IR but even stronger at 2 weeks post-IR (Fig. 6B). Transcription factor JunB regulates skin homeostasis through

balancing proliferation and differentiation of epidermal stem/progenitor cells.^{34,35} During normal physiology, JunB expression was very low in non-irradiated WT and KO skin, with low epidermal cell turnover (Fig. 6C). After radiation-induced skin injury, the interfollicular epidermis was characterized by excessive proliferation and abnormal differentiation of keratinocytes, with intense JunB expression in basal and differentiated keratinocytes. Of note, JunB expression was clearly more pronounced in KO versus WT epidermis at 1 week post-IR, likely reflecting intensified skin repair upon enhanced neutrophil activation (Fig. 6C). However, JunB staining decreased at 2 weeks post-IR in KO skin (but not in WT skin), although many Ki-67+ keratinocytes were still present. Perhaps there is a more rapid initiation and resolution of the JunB

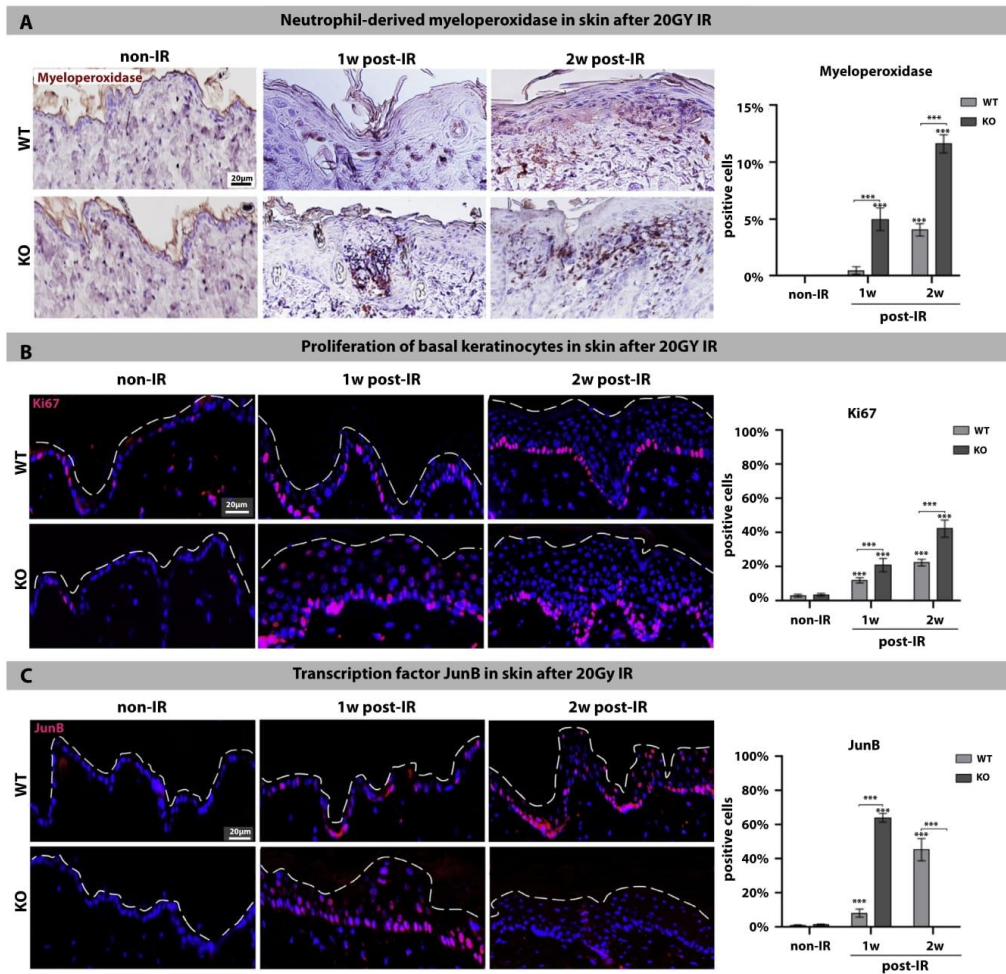


Fig. 6. Neutrophil-driven inflammation and increased proliferation of basal keratinocytes. (A) Immunohistochemistry micrographs of neutrophil-derived myeloperoxidase in the epidermis after 20 Gy exposure (1 and 2 weeks post-IR) compared with non-irradiated control. Graphic presentation of the quantification of myeloperoxidase + cells (in percentage). (B) IF micrographs of Ki67 in epidermis after 20 Gy exposure (1 and 2 weeks post-IR) compared with non-irradiated control. Graphic presentation of the quantification of Ki67+ cells (in percentage). (C) IF micrographs of transcription factor JunB in epidermis after 20 Gy exposure (1 and 2 weeks post-IR) compared with non-irradiated control. Graphic presentation of the quantification of JunB+ cells (in percentage). Data are presented as mean ± standard deviation (n = 3). For wild-type and knock-out mice, the values at different timepoints after IR were compared with corresponding non-irradiated controls (significance asterisks directly above the corresponding bars). Moreover, values for wild-type with knock-out mice were compared with each other at the different timepoints after IR (presented by connecting brackets with significance asterisks). Statistical significances are presented as * $P < .05$, ** $P < .01$, *** $P < .001$. Abbreviation: IF = immunofluorescence; IR = ionizing radiation.

activation, driving the amplified transcriptional stress response after IR exposure in KO skin. Collectively, these results suggest that JunB maintains the structural integrity

of the epidermis after transient stress, such as radiation-induced injury, by concomitant fine-tuning of proliferation and differentiation.

Dysfunction of the protective skin barrier due to disturbed keratinization and cornification

Normal epidermal differentiation and barrier formation require the carefully choreographed expression of cytoskeletal, cell adhesion, and cell envelope proteins specific for each cell layer.³⁶ IR exposure disrupts the epidermal permeability barrier by altering the arrangement of desmosomes, corneodesmosomes, tight junctions, cornified cell envelope, and keratin filaments (Fig. E8). In KO versus WT skin, the epidermal architecture was more damaged after IR exposure. Accordingly, RNA-seq analysis revealed an upregulation of desmosomal and specific keratin-encoding genes (desmocollin [*dsc*] 1/3, keratin [*krt*] 18) in irradiated KO skin, which may reflect increased structural repair during the epidermal recovery process. In contrast, reduced mRNA levels of hair-associated keratins (keratin [*krt*] 25/27/35/71/73) and structural proteins (peptidyl arginine deiminase 3 [*padi3*]; proline rich 9 [*prrr9*]) were observed in both irradiated WT and KO skin, likely reflecting suppressed HF formation and hair growth due to damaged or destroyed HFSCs. As keratinocytes progress toward the upper epidermis, they undergo the cornification process, involving cross-linking of keratinocyte proteins and breakdown of nuclei and other organelles by intracellular and secreted proteases. Following high-dose IR exposure these fine-tuned keratinization and cornification processes were disturbed (more pronounced in KO skin), thereby leading to skin barrier dysfunction and as a consequence to reactive epidermal hyperplasia.

Discussion

Previous studies of *ex vivo* irradiated human skin tissues have shown that histone variant H2A.J accumulates in epidermal keratinocytes with persistent DNA damage.^{7,18} Here, using an *in vivo* model with H2A.J WT and KO mice we investigated the role of H2A.J in radiation dermatitis, with special focus on radiation-induced senescence and subsequent immunomodulatory effects. Analyzing 53BP1-foci after IR exposure showed no differences in DSB repair capacity of KO versus WT keratinocytes, suggesting that H2A.J is not involved in the acute DSB repair process after moderate doses. Immunohistological studies of WT skin confirm previous results of time- and dose-dependent H2A.J accumulation in epidermal keratinocytes of mouse skin after IR exposure.²⁶ Unexpectedly, significantly stronger radiation reactions were observed in irradiated KO versus WT skin at both macroscopic and microscopic levels, with more skin inflammation and increased HF loss. Remarkably, analyzing established senescence markers clearly showed more radiation-induced senescence in epidermal keratinocytes of KO versus WT skin after both moderate and high IR doses. Moreover, significant differences in senescence induction were observed between various keratinocyte

populations in irradiated WT and KO skin, with HFSCs in bulge regions of KO skin being particularly badly damaged at high doses, leading to almost complete atrophy of HFs. Whole-transcriptome sequencing revealed an intensified release of multiple proinflammatory SASP factors in irradiated KO compared with WT skin, likely reflecting the increased IR-associated senescence induction in KO keratinocytes. Flow cytometry analysis indicated an increased skin infiltration with various immune cells in both irradiated WT and KO skin, but specific chemokine-mediated signaling in irradiated KO skin led to more efficient recruitment of neutrophils. Cxcl2- and Cxcl5-mediated neutrophil influx with enhanced MPO production aggravated tissue toxicities in KO skin. As a result of increased tissue damage in irradiated KO skin, reactive upregulation of transcription factor JunB led to excessive proliferation and abnormal differentiation of keratinocytes, leading to a more pronounced epidermal hyperplasia. Collectively, our findings show that H2A.J has no effect on the acute DSB repair process, but the absence of H2A.J leads to enhanced induction of DNA damage-induced senescence with intensified SASP signals. This enforced SASP activation of immune responses leads to enhanced recruitment of inflammatory cells, particularly neutrophils, and thereby aggravates the inflammatory phase of radiation-induced skin reactions.

Skin reactions after IR exposure occur in a characteristic temporal pattern, whereby duration and severity of acute and chronic phases mainly depend on radiation quality, total dose, dose rate, and fractionation.¹⁰ IR exposure has an effect on virtually every cellular component of the skin. In the epidermis, the well-regulated balance of cell renewal and differentiation processes is essential for skin homeostasis. This balance is impaired after exposure to high-dose IR, leading to abnormal proliferation and differentiation of keratinocytes, disturbed formation of the cornified envelope, and eventually to the disruption of the protective stratum corneum barrier.³⁷ However, IR exposure not only affects keratinocyte proliferation and differentiation but also modulates the communication between epidermal keratinocytes and immune cells by producing proinflammatory mediators.³⁸ Using the H2A.J KO mouse model, we can show that the absence of H2A.J is associated with increased radiation-induced senescence induction in epidermal keratinocytes and enhanced SASP signaling, which amplifies the acute cutaneous inflammation by the recruitment and activation of immune cell populations. Our results suggest that H2A.J-dependent cytokine/chemokine expression has a functional importance for the intercellular communication between keratinocytes and immune cells and that the lack of H2A.J leads to stronger inflammatory reactions within the framework of radiation-induced skin reactions. With the histone variant H2A.J, we were able to identify an epigenetic regulatory mechanism that, starting from radiation-induced DNA damage, leads to altered cell functions after IR exposure via chromatin remodeling and transcriptional gene regulation, as we were able to show in our previous *in vitro* studies with H2A.J knock-down and

knock-in fibroblasts.⁹ Our results to date suggest that H2A.J is likely to play an important role in mediating the radiation response in other normal tissues as well. In future work, the exact tissue-specific mechanisms need to be analyzed to determine how the histone variant H2A.J can epigenetically control the acute and chronic radiation responses at the cell and tissue levels.

Earlier studies on mouse models have already demonstrated increased senescence induction in epidermal keratinocytes and HFSCs after high doses of IR.³⁹ Premature senescence may contribute to radiation-induced HF loss by affecting particularly the stem/progenitor cell niche, known to modulate HF regeneration by complex interactions with papilla-specific paracrine factors.⁴⁰⁻⁴² Previous results show that keratinocytes in bulge regions went increasingly into premature senescence after high-dose IR, thereby affecting the complex functional interactions within the stem cell niche. Consequently, the stem cell reservoir of CD34+ HFSCs decreased to a few percent over time, clearly more pronounced in irradiated KO versus WT skin. In agreement with this radiation-induced, immune-mediated HF atrophy, our transcriptomic profiles of WT and KO skin revealed the downregulation of multiple hair keratins after high-dose IR.

Previous studies have shown that in response to IR exposure, damaged/senescent keratinocytes in the epidermis trigger the local expression of acute phase proinflammatory and chemoattractant chemokines to regulate temporal and spatial recruitment of immune cells to inflamed skin areas.³⁸ Our results correlate with previous studies indicating that IL-1 and IL-6 are major cytokines in the response of skin cells to IR exposure.⁴³ Our flow cytometry analysis revealed the radiation-induced skin infiltration with various immune cell populations; however, significant differences between irradiated WT and KO skin could only be observed in the neutrophilic immune response. Neutrophils are crucial for the first-line defense of the innate immune system. Mature neutrophils capture and destroy invading microorganisms through phagocytosis and intracellular degradation, release of granules, and formation of neutrophil extracellular traps after detecting pathogens.⁴⁴ However, neutrophils can contribute to tissue injury by amplifying the inflammatory response and direct release of toxic effectors, such as MPO.⁴⁵ Neutrophil-derived MPO increases the production of proinflammatory cytokines (such as IL-1 and IL-6) and thereby regulates matrix-metalloproteinases and their endogenous inhibitors tissue inhibitors of metalloproteinases (TIMPs), which are involved in extracellular matrix turnover and tissue remodeling. The matrix-metalloproteinases/TIMP counterbalancing system plays a major role for the pathogenesis of skin fibrosis.⁴⁶ Previous studies have demonstrated the essential role of IL-17 expressing $\gamma\delta$ T-cells in mediating the radiation-induced inflammatory response in radiation dermatitis.³⁷ IL-17 and transcription factor I κ B ζ encoded by the gene *Nfkbiz* are of particular importance for the pathogenesis of psoriasis, an autoinflammatory skin disease, characterized by cytokine-driven keratinocyte proliferation and infiltration of immune cells.³³ I κ B ζ , an atypical I κ B family member, leads to activation or repression of

selective subsets of NF- κ B target genes. In epidermal keratinocytes, IL-17A, alone or in combination with TNF- α or IL-36 cytokines, triggers NF- κ B- and STAT3-dependent transcriptional upregulation of I κ B ζ expression and thereby induces subsets of IL-36 and IL-17 responsive target genes, including *Cxcl2* and *Cxcl5*, which have already been implicated in neutrophil trafficking to sites of inflammation.³³ Our results suggest that, similar to psoriasis, hyperactivation of these proinflammatory pathways in irradiated KO skin leads to keratinocyte hyperproliferation and immune cell infiltration.

Cellular senescence but especially the SASP is a highly dynamic process over time and differs in response to different stress signals. Furthermore, the composition of SASP varies depending on the cell type undergoing senescence in different tissues. Accordingly, our findings suggest that also the effects of H2A.J inactivation on gene expression appear to be specific to cell type and context. So far, the exact molecular mechanism—by which incorporation of histone variant H2A.J into chromatin after radiation-induced DNA damage affects nuclear organization and gene expression—has not been elucidated. Previous *in vitro* studies on human fibroblasts have shown that H2A.J is widely distributed in the chromatin of human fibroblasts,⁷ but it is also incorporated at persisting DSBs induced by IR, leading to the reorganization of damaged chromatin during senescence progression.⁶ Depletion of H2A.J in human fibroblasts induced into senescence by DNA damage inhibited inflammatory gene expression rather than increasing it.^{6,7} Luminal epithelial cells also express H2A.J at high levels, and knock-out of the gene encoding H2A.J in a luminal epithelial breast cancer cell line led to decreased expression of subsets of genes regulated by the estrogen receptor.¹⁹ In previous *in vitro* studies on fibroblasts it could be shown that deregulated H2A.J deposition affects chromatin remodeling, transcription-factor recruitment, and the proinflammatory secretome during senescence progression.⁹ However, further work is required to understand how H2A.J regulates gene expression in a cell type-specific and context-specific manner.

Conclusion

In this *in vivo* model with high-dose IR of murine skin, we identified an epigenetic regulation in which radiation-induced H2A.J in epidermal keratinocytes is required to moderate the immune response to IR-damaged skin by limiting the expression of key inflammatory genes. Investigation into the precise mechanisms of keratinocyte-immune cell interaction networks may shed light on these complex inflammatory responses and ultimately has the aim of eliciting therapeutic options for restoring skin homeostasis in the context of radiation dermatitis.

References

1. Chen D, Jin C. Histone variants in environmental-stress-induced DNA damage repair. *Mutat Res Rev Mutat Res* 2019;780:55-60.

2. Ferrand J, Rondinelli B, Polo SE. Histone variants: Guardians of genome integrity. *Cells* 2020;9:2424.
3. Lukas J, Lukas C, Bartek J. More than just a focus: The chromatin response to DNA damage and its role in genome integrity maintenance. *Nat Cell Biol* 2011;13:1161-1169.
4. Polo SE, Almouzni G. Chromatin dynamics after DNA damage: The legacy of the access-repair-restore model. *DNA Repair (Amst)* 2015;36:114-121.
5. Talbert PB, Henikoff S. Histone variants at a glance. *J Cell Sci* 2021;134:jcs244749.
6. Isermann A, Mann C, Rube CE. Histone variant H2A.J marks persistent DNA damage and triggers the secretory phenotype in radiation-induced senescence. *Int J Mol Sci* 2020;21:9130.
7. Contrepois K, Coudereau C, Benayoun BA, et al. Histone variant H2A.J accumulates in senescent cells and promotes inflammatory gene expression. *Nat Commun* 2017;8:14995.
8. Mangelinck A, Coudereau C, Courbeyrette R, et al. The H2A.J histone variant contributes to interferon-stimulated gene expression in senescence by its weak interaction with H1 and the derepression of repeated DNA sequences. *bioRxiv* 2020. <https://doi.org/10.1101/2020.10.29.361204>
9. Abd Al-Razaq MA, Freyter BM, Isermann A, et al. Role of histone variant H2A.J in fine-tuning chromatin organization for the establishment of ionizing radiation-induced senescence. *Cells* 2023;12:916.
10. Singh M, Alavi A, Wong R, Akita S. Radiodermatitis: A review of our current understanding. *Am J Clin Dermatol* 2016;17:277-292.
11. Lippens S, Denecker G, Ovaere P, Vandenabeele P, Declercq W. Death penalty for keratinocytes: Apoptosis versus cornification. *Cell Death Differ* 2005;12(Suppl 2):1497-1508.
12. Bray FN, Simmons BJ, Wolfson AH, Nouri K. Acute and chronic cutaneous reactions to ionizing radiation therapy. *Dermatol Ther (Heidelb)* 2016;6:185-206.
13. Welle MM, Wiener DJ. The hair follicle: A comparative review of canine hair follicle anatomy and physiology. *Toxicol Pathol* 2016;44:564-574.
14. Schuler N, Timm S, Rube CE. Hair follicle stem cell faith is dependent on chromatin remodeling capacity following low-dose radiation. *Stem Cells* 2018;36:574-588.
15. Muller K, Meineke V. Radiation-induced alterations in cytokine production by skin cells. *Exp Hematol* 2007;35:96-104.
16. Sharpless NE, Sherr CJ. Forging a signature of in vivo senescence. *Nat Rev Cancer* 2015;15:397-408.
17. Tchkonja T, Zhu Y, van Deursen J, Campisi J, Kirkland JL. Cellular senescence and the senescent secretory phenotype: Therapeutic opportunities. *J Clin Invest* 2013;123:966-972.
18. Rube CE, Baumert C, Schuler N, et al. Human skin aging is associated with increased expression of the histone variant H2A.J in the epidermis. *NPJ Aging Mech Dis* 2021;7:7.
19. Redon CE, Schmal Z, Tewary G, et al. Histone variant H2A.J is enriched in luminal epithelial gland cells. *Genes (Basel)* 2021;12:1665.
20. Schmal Z, Hammer B, Muller A, Rube CE. Fractionated low-dose radiation induces long-lasting inflammatory responses in the hippocampal stem cell niche. *Int J Radiat Oncol Biol Phys* 2021;111:1262-1275.
21. Wingett SW, Andrews S. FastQ Screen: A tool for multi-genome mapping and quality control. *F1000Res* 2018;7:1338.
22. Frankish A, Diekhans M, Jungreis I, et al. Gencode 2021. *Nucleic Acids Res* 2021;49:D916-D923.
23. Li H, Durbin R. Fast and accurate short read alignment with Burrows-Wheeler transform. *Bioinformatics* 2009;25:1754-1760.
24. Anders S, Pyl PT, Huber W. HTSeq—a Python framework to work with high-throughput sequencing data. *Bioinformatics* 2015;31:166-169.
25. Love MI, Huber W, Anders S. Moderated estimation of fold change and dispersion for RNA-seq data with DESeq2. *Genome Biol* 2014;15:550.
26. Hippchen Y, Tewary G, Jung D, et al. Cultured human foreskin as a model system for evaluating ionizing radiation-induced skin injury. *Int J Mol Sci* 2022;23:9830.
27. Freund A, Laberge RM, Demaria M, Campisi J. Lamin B1 loss is a senescence-associated biomarker. *Mol Biol Cell* 2012;23:2066-2075.
28. Chen F, Elgaher WAM, Winterhoff M, et al. Citraconate inhibits ACOD1 (IRG1) catalysis, reduces interferon responses and oxidative stress, and modulates inflammation and cell metabolism. *Nat Metab* 2022;4:534-546.
29. Frieler RA, Vigil TM, Song J, et al. Aconitate decarboxylase 1 regulates glucose homeostasis and obesity in mice. *Obesity (Silver Spring)* 2022;30:1818-1830.
30. Wu R, Chen F, Wang N, Tang D, Kang R. ACOD1 in immunometabolism and disease. *Cell Mol Immunol* 2020;17:822-833.
31. Bonocchi R, Mantovani A, Jaillon S. Chemokines as regulators of neutrophils: Focus on tumors, therapeutic targeting, and immunotherapy. *Cancers (Basel)* 2022;14:680.
32. Lorscheid S, Muller A, Loffler J, et al. Keratinocyte-derived IkappaBzeta drives psoriasis and associated systemic inflammation. *JCI Insight* 2019;4:e130835.
33. Muller A, Hennig A, Lorscheid S, et al. IkappaBzeta is a key transcriptional regulator of IL-36-driven psoriasis-related gene expression in keratinocytes. *Proc Natl Acad Sci U S A* 2018;115:10088-10093.
34. Singh K, Camera E, Krug L, et al. JunB defines functional and structural integrity of the epidermo-pilosebaceous unit in the skin. *Nat Commun* 2018;9:3425.
35. Maity P, Singh K, Krug L, et al. Persistent JunB activation in fibroblasts disrupts stem cell niche interactions enforcing skin aging. *Cell Rep* 2021;36:109634.
36. Ishida-Yamamoto A, Igawa S, Kishibe M. Molecular basis of the skin barrier structures revealed by electron microscopy. *Exp Dermatol* 2018;27:841-846.
37. Liao W, Hei TK, Cheng SK. Radiation-induced dermatitis is mediated by IL17-expressing gammadelta T cells. *Radiat Res* 2017;187:454-464.
38. Nguyen AV, Soulika AM. The dynamics of the skin's immune system. *Int J Mol Sci* 2019;20:1811.
39. McCart EA, Thangapazham RL, Lombardini ED, et al. Accelerated senescence in skin in a murine model of radiation-induced multi-organ injury. *J Radiat Res* 2017;58:636-646.
40. Matsumura H, Mohri Y, Binh NT, et al. Hair follicle aging is driven by transepidermal elimination of stem cells via COL17A1 proteolysis. *Science* 2016;351:aad4395.
41. Rahmani W, Sinha S, Biernaskie J. Immune modulation of hair follicle regeneration. *NPJ Regen Med* 2020;5:9.
42. SY An, Kim HS, Kim SY, et al. Keratin-mediated hair growth and its underlying biological mechanism. *Commun Biol* 2022;5:1270.
43. Paldor M, Levkovitch-Siany O, Eidelstein D, et al. Single-cell transcriptomics reveals a senescence-associated IL-6/CCR6 axis driving radiodermatitis. *EMBO Mol Med* 2022;14:e15653.
44. Su Y, Richmond A. Chemokine regulation of neutrophil infiltration of skin wounds. *Adv Wound Care (New Rochelle)* 2015;4:631-640.
45. Dominguez-Diaz C, Varela-Trinidad GU, Munoz-Sanchez G, et al. To trap a pathogen: Neutrophil extracellular traps and their role in mucosal epithelial and skin diseases. *Cells* 2021;10:1469.
46. Ulrich D, Ulrich F, Unglaub F, Piatkowski A, Pallua N. Matrix metalloproteinases and tissue inhibitors of metalloproteinases in patients with different types of scars and keloids. *J Plast Reconstr Aesthet Surg* 2010;63:1015-1021.

8. Acknowledgement

First and foremost, I would like to thank God for granting me the strength, perseverance, and wisdom to navigate this challenging journey. Without His guidance and grace, this achievement would not have been possible.

I would also like to extend my deepest appreciation to my advisor, Prof. Rube. Her unwavering support and belief in my abilities have pushed me to constantly improve and reach new heights, for which I am incredibly grateful. Thank you for allowing me to work in your lab as a PhD candidate and for your expertise and thoughtful approach have significantly shaped the direction of this thesis, I am truly fortunate to have the privilege of working under your mentorship.

I am also deeply thankful to Prof. Meier, that her critical feedback and insightful suggestions have greatly enriched my work. Her expertise and a keen eye for detail helped refine my ideas and approach, pushing me to explore deeper and think more critically.

I would also like to extend special thanks to Prof. Dr med Christian Rube and Prof Dr med. Markus Hecht, directors of the Department for Radiation Therapy and Radiation Oncology, for providing all their support and for the use of the clinic accelerator. Additionally, I would also like to thank all the staff, from planners to technicians, in the clinic who have helped and supported me through each of the numerous cell irradiations over the years.

A heartfelt thank you goes to Daniela Jung, throughout this journey, you have been an incredible friend, offering support, encouragement, and sometimes, simply a listening ear. Thank you for always being there.

I am also deeply grateful to Anna Isermann for her guidance during the initial phase of my PhD journey. Her support, particularly in helping me with the writing and language corrections of this thesis, has been invaluable. I sincerely appreciate her dedication and the time she has invested in helping me shape this project. I would also like to thank Zoe Schmal for the friendship we shared throughout this time made the challenging moments much more manageable and I always will remember the incredible sweets you can make.

In addition, of course, I cannot forget to thank my incredible friend Gargi Tewary for her support whether it was through late-night discussions, shared frustrations, or moments of celebration. Your friendship has meant the world to me. You helped me stay grounded and motivated, and I will forever cherish the times we spent together during this intense but rewarding process.

Special thanks or Shokran (in Arabic) are owed to Yvonne Lorat, whose extraordinary support has been a cornerstone throughout this journey. From the moment I met you, I knew I had encountered one of the kindest and most genuine people. Words cannot adequately express my gratitude. Your unwavering patience, encouragement, and belief in me, even during the most challenging times, provided the strength I needed to persevere. Your kindness and steadfast support have left a lasting impact on both my personal and academic life. You went beyond the academic aspects, offering guidance, reassurance, and a reminder of the bigger picture when I needed it most. I am profoundly grateful for your presence and the vital role you have played in this journey. Thank you for everything.

A special thank you is also reserved for Julia von der Lippe. Whether it was through a kind word, thoughtful advice, or simply being there when I needed you the most, your support has been invaluable. You have played an essential role not only in helping me

navigate my personal life but also in the successful completion of this thesis. I am profoundly grateful for everything you have done ありがとうございます.

I would also like to express my sincere gratitude to my new colleagues, Ruth and Nicolas, for their valuable support and contributions. I look forward to continuing our friendship and working together in the future.

I cannot forget to thank my friend Dr Abdul-salam Juhmani for tolerating all my complaints and frustrations. Even if you were so far, you never made me feel like it. Without your pieces of advice and our nice trips in Italy, I do not think I would have been able to finish anything in my PhD journey.

Lastly, I would like to express my deepest gratitude to my family and my beloved wife. Your unwavering love, support, and belief in me have been my greatest source of motivation and strength throughout this journey. This thesis is not only a product of my efforts but also a testament to the encouragement, patience, and sacrifices you have made. For that, I am forever grateful.

To everyone who has been a part of this journey, thank you from the bottom of my heart. This thesis would not have been possible without your contributions, and I am deeply grateful for the role each of you has played.

9. List of Tables

Table 1 Literature information of publication I	63
Table 2 Literature information of publication II	86
Table 3 Literature information of publication III	104
Table 4 Literature information of publication IV	118

10. List of Figures

Figure 1: DNA DSB repair pathways: non-homologous end joining (left), and homologous recombination (right).	15
Figure 2: Senescence triggers and characteristics: diagrammatic representation of various stimulators and biomarkers of senescent cells.	17
Figure 3: SAHFs formation in NT and H2A.J-KI fibroblasts before and after IR using IFM (left, red arrow) and TEM (right; white arrows).	29
Figure 4: TEM micrograph showing the cellular ultrastructure and morphological changes of the nuclear envelope before (left) and after (right) IR.	31
Figure 5: Automatic classification and segmentation of DNA density and the nanoparticles around LEDDs using HALO software.	34
Figure 6 (a) Photographic representation of WT and KO post 20 Gy radiation exposure, (b) TEM micrographic representation of lamin B1 in WT and KO dorsal skin samples post 20 Gy radiation exposure.	37